Optimization of a continuous-wave THz spectrometer for coherent broadband solid-state spectroscopy

Inaugural - Dissertation

zur

Erlangung des Doktorgrades

der Mathematisch-Naturwissenschaftlichen Fakultät

der Universität zu Köln

vorgelegt von

Holger Schmitz

aus Würselen

Köln, im April 2012

Berichterstatter:	Prof. Dr. M. Grüninger
	Prof. Dr. S. Schlemmer
Vorsitzender der Prüfungskommission:	Prof. Dr. A. Klein
Tag der letzten mündlichen Prüfung:	03.04.2012

Contents

1. Introduction **1**

2. Optical Spectroscopy **5**
2.1. Foundations 5
2.1.1. Fabry-Perot resonator 7
2.1.2. Drude-Lorentz model 9
2.2. Gaussian optics 9
2.2.1. SVE approximation 9
2.2.2. Gaussian beam 10
2.2.3. Gauss-Laguerre modes 13
2.2.4. Ray matrices 13
2.2.5. Beam transformation by a thin lens 14

3. Terahertz sources and detectors **17**
3.1. Realization of terahertz sources 17
3.1.1. Black body 17
3.1.2. Backward-wave oscillator 18
3.1.3. Gunn diode 19
3.1.4. Quantum-cascade laser 19
3.1.5. Free-electron laser 20
3.2. THz detectors 21
3.2.1. Bolometers 21
3.2.2. Golay cells 22
3.2.3. Pyroelectric detectors 22
3.3. Terahertz time-domain spectroscopy 22
3.3.1. Terahertz generation 22
3.3.2. Terahertz detection 24

4. Experimental setup: cw THz spectrometer **27**
4.1. Components 27
4.1.1. Near-infrared laser sources 28
4.1.2. External frequency control 30
4.1.3. Tapered amplifier 31
4.1.4. Photomixer and THz generation 32
4.1.5. Coherent detection 36

4.1.6. Fiber stretcher operation and settings . . . 41
4.1.7. Photocurrent correction . . . 43

5. Data Analysis **47**
5.1. Frequency-scan method . . . 47
5.1.1. Analysis based on the frequency-scan method . . . 49
5.1.2. Effective resolution . . . 54
5.1.3. Long-time performance . . . 55
5.2. Fiber-stretcher method . . . 58
5.2.1. Effective resolution . . . 59
5.3. Improvement of the phase accuracy by implementing a third laser . . . 60
5.3.1. Concept . . . 61
5.3.2. Extraction of information . . . 64
5.3.3. Performance of the correction . . . 67
5.4. Correction of the absolute value of L_{eff} . . . 70
5.5. Numerical analysis of n and κ . . . 71

6. Performance of the setup **77**
6.1. Signal-to-noise ratio . . . 77
6.2. Standing waves . . . 78
6.3. Frequency stability . . . 80
6.4. Amplitude stability . . . 83
6.5. Phase stability . . . 85
6.5.1. Improvement of the phase stability . . . 87

7. Beam profile and lens design **93**
7.1. Lens design . . . 93
7.1.1. Estimation of ray path parameters . . . 94
7.1.2. Lens material . . . 95
7.1.3. Lens design . . . 95
7.2. Beam profile . . . 96
7.3. Polarization . . . 101
7.3.1. Polarization dependence of cw THz sources . . . 101
7.3.2. Measurement of the polarization dependence . . . 102

8. Measurements on MgO **109**
8.1. Comparison between frequency-scan method and fiber-stretcher method 109
8.2. Comparison of 3-laser setup and 2-laser setup . . . 114

9. Measurements on silicon **123**
9.1. Room-temperature measurements of silicon . . . 123
9.2. Low-temperature measurements on silicon . . . 128
9.2.1. Cryostat layout . . . 129

9.2.2. Comparison of data obtained with and without the cryostat . 132
9.2.3. Comparison of the different cryostats 133
9.2.4. Results of the low-temperature measurements 137

10. Results on α-lactose monohydrate **149**
10.1. Sample preparation and measurement 149

11. Conclusion **157**

A. Appendix **161**
A.1. Scripts 161
A.1.1. Frequency-scan analysis 161
A.1.2. Inversion of $T(n, \kappa)$ and $\varphi(n, \kappa)$ 175
A.1.3. Piecewise Drude-Lorentz fit 177
A.2. Phase measurements 179
A.3. Beam profile 180
A.3.1. x-axis beam profile before collimating 180
A.3.2. y-axis beam profile before collimating 188
A.3.3. x-axis beam profile after collimating 193
A.3.4. x-axis beam profile at the focal spot 198
A.4. Polarization measurements 202
A.4.1. Polarizer angle of 0 ° 202
A.4.2. Polarizer angle of 45 ° 209
A.4.3. Polarizer angle of 90 ° 216
A.5. Measurements on MgO 225
A.6. Low-temperature data of silicon 229
A.6.1. Si measurements with the bath cryostat 229
A.6.2. Si measurements with the cold-finger cryostat 232

List of Publications **251**

Acknowledgements **253**

Abstract **255**

Kurzzusammenfassung **257**

Offizielle Erklärung **259**

1. Introduction

Research in solid state physics strongly relies on the availability of suitable probing techniques. Some prominent examples are microscopy, scattering techniques, and spectroscopy. The first spectroscopic experiments were absorption measurements employing visible light. Nowadays also elementary particles such as electrons or myons are used as probes. But also optical spectroscopy has been steadily improved by increasing the accessible frequency range as well as the resolution. The quantities found by those conceptually simple spectroscopy experiments open a way to study e. g. electronic excitations within the probed material if a suitable model is supplied. For a long time optical spectroscopy suffered from a gap in the probable frequency range. This blind spot, created by the lack of suitable sources in the range from 100 GHz to 1 THz, is called THz gap. Actually this frequency range can be covered since many years. However, available table-top setups still show a lack of either good enough resolution or wide frequency tunability, making experiments a difficult endeavor. Yet this particular area in the electromagnetic spectrum promises to unveil some of the most interesting phenomena in solid-state materials, as the following part will briefly motivate.

Phonon excitations in biomolecules and molecular solids have eigen modes at THz frequencies due to the large mass of the single sites [1–3]. In high-temperature superconductors the origin of the attractive interaction between electrons is not yet understood. The lowest energy excitation is the excitation over the so-called superconducting gap. The width of this gap corresponds to the binding energy of a Cooper pair which is in the order of some meV, i. e. some hundred GHz. Hence, THz spectroscopy is an important method to investigate high-temperature superconductors and other novel superconductors [4–8]. So-called heavy-fermion compounds are another candidate for THz investigations. Here, strong correlations in the partially filled f-orbitals as well as in the conduction band of rare earth or actinide ions lead to an effective mass m^* of electrons which is about a factor 1000 higher than the free-electron mass. Due to the high electron mass the damping constant γ of the free-carrier oscillation reduces. The width of the Drude peak lies in the range between some GHz and some THz so that THz spectroscopy is a suitable tool to study those materials [9–11]. Another field where THz spectrosopy is utilized, is investigations on multiferroics. Multiferroics are materials which possess more than one ferroic ordering in a certain phase [12]. Here, the interplay between ferroelectricity and ferromagnetism [13] is of particular interest for both fundamental science and industrial applications. In such materials it is possible to change the magnetization by an electric field or the electric polarization by a magnetic field due to coupling

between these order parameters. The coupling makes this class of materials potential candidates for the development of long-lasting, non-volatile computer memory which can be switched very fast by an electric field. The characteristic excitation in the multiferroic phase is a magnon that carries an electric dipole moment. This excitation is called electromagnon and its excitation energy lies in the THz range. Due to the magneto-electric coupling it is possible to probe this excitation with optical spectroscopy [14–20]. Also many molecules possess rotational and vibrational excitations at frequencies below 1 THz. The excitation energies are very characteristic for different molecules as they depend on their composition and structure. Therefore, the THz spectra of those molecules are often referred to as the molecules spectral fingerprint. This makes THz spectroscopy interesting for industrial applications. It is recommended for the detection and quantification of pollution [21]. Because many fabrics and plastics are transparent in the THz range it shows also a lot of promise for security applications. Thereby the utilization of THz spectroscopy for the identification of explosives or drugs [22–25] as well as THz imaging for the detection of hidden weapons have been demonstrated [26–30].

This explains the strong interest in closing the THz gap and it comes as no surprise that a lot of research and effort have been undertaken to achieve this goal. The first available sources were electronic devices like backward-wave oscillators and Gunn diodes. Later the quantum-cascade laser and the free-electron laser were developed. All these sources provide high output powers but only the free-electron laser has a wide tuning range. However, a free-electron laser can only be operated in large research facilities since relativistic electrons and high magnetic fields are needed.

A major breakthrough in the quest for broadband THz sources has been made by the invention of the laser-based THz generation. In time-domain terahertz spectroscopy (THz TDS), femto-second laser pulses are converted into broadband THz pulses by an electro-optical switch. This method can cover a frequency range up to the order of 10 THz [31]. The use of a second electro-optical switch offers a way of detection which preserves the phase information and provides a high signal-to-noise ratio. On the downside, femto-second lasers are quite expensive and the achievable resolution in THz TDS is rather low.

A rather young field in THz spectroscopy is the broadband continuous-wave THz spectroscopy (CW TS) based on photomixing. The frequency resolution is much higher than in THz TDS. Here, two near-infrared lasers are employed to generate beat signals with THz frequencies. The laser beat is converted into THz radiation by a so-called photomixer which basically acts as a low-pass filter. A second photomixer can be used for the coherent detection of the THz radiation. Since the measured photocurrent is proportional to the THz electric field, the phase information is preserved. This allows for the determination of both, real and imaginary part of the complex optical functions without the need of Kramers-Kronig transformation. More precisely the photocurrent is a product of the THz amplitude and the phase difference between laser beat and THz radiation at the detector. Extensive research in this field dealt with the increase of output power and bandwidth, i. e.

improving the antenna design and the semiconductor substrate [32–42]. However, the possibility to generate and detect THz generation is not enough for performing spectroscopy.

In the scope of this thesis a cw THz spectrometer is improved for solid-state spectroscopy to the effect that the complex optical functions can be precisely and reliably determined. Therefore, different methods to extract the amplitude and phase information most accurately from the photocurrent have to be checked for their precision, resolution, and performance. Since for a spectrum a sample and a reference measurement are needed, the stability of amplitude and phase is crucial and has to be checked. Possibilities to minimize or correct for instabilities have to be found. From the extracted transmittance and phase information the complex optical functions need to be determined. Here suitable numerical approaches are developed in the scope of this thesis. On the other hand the optical path needs to be optimized. Since many samples are single crystals and hence rather small, suitable optical elements are required to focus the THz beam onto the sample. The performance of the optical elements has to be analyzed by determination of the beam profile. Because of the long wavelengths of THz radiation the influence of standing waves on the measured data is also crucial and has to be minimized. This is essential when implementing a cryostat into the setup since it gives rise to diffraction and multiple reflection of the wave. All these issues will be addressed in the scope of this thesis which is organized as follows: In the following chapter, the fundamentals of optical spectroscopy are briefly introduced. Due to the fact that THz frequencies correspond to wavelengths in the millimeter range, Gaussian optics is reviewed.

Chapter 3 introduces the above-mentioned well-known THz sources and detectors in more detail. The setup installed in the scope of this thesis is discussed in chapter 4.

The different data-analysis methods developed in the course of this thesis are presented in chapter 5. In the first part the analysis of the photocurrent is shown, discussing the advantages and disadvantages of using the frequency-scan method or the fiber-stretcher method. A whole new method to correct for phase drifts is presented. For this, a third laser is implemented into the setup. Keeping two of the lasers at constant frequency and tuning the third one results in one stable and two tunable beat frequencies. In the ideal case, the phase φ_{ref} of the constant frequency should be stable. However, phase changes due to changes of the path length difference and frequency instabilities will change φ_{ref}. Knowing the drift of φ_{ref} gives the opportunity to correct the phases of the tunable beat frequencies. The determination of the complex optical functions from the measured transmittance and phase is discussed in the second part of chapter 5.

In chapter 6, the general performance of the setup is investigated. Data backing up the claim of a high signal-to-noise ratio is presented and the influence of standing waves in the beam path on the spectra is discussed. The accuracy of the interferometric frequency control and the amplitude and phase stability are investigated. Especially possibilities to minimize phase drifts are reviewed.

The optical elements designed in the scope of this thesis are described in chapter 7.

The determination of the beam profile of the radiation emitted by the photomixers and the performance of the optical elements are explained in detail. In the last part of this chapter, the polarization dependence of the photomixers is investigated.

In chapter 8, spectra of MgO are measured using all three methods discussed in chapter 5. MgO is almost non absorbing in the THz regime and the refractive index changes only slightly, making this material ideal to test the performance of the different measurement and analysis methods. Based on the results, the different methods are compared.

Chapter 9 deals with the implementation of a bath cryostat into the setup. A special design of the optical tail of the cryostat accounts for diffraction and standing waves. Measurements on Si have been performed down to temperatures of 2 K and compared to measurements using a cold-finger cryostat lacking the improvements of the optical tail.

To demonstrate the high performance of the setup, in the last chapter α-lactose monohydrate is investigated. Around 530 GHz it has the narrowest absorption line known for solid-state samples. Both resonance frequency and linewidth are determined very accurately removing doubts of previous measurements [43].

2. Optical Spectroscopy

Optical spectroscopy is a powerful and versatile tool to shed light on the optical and electronic properties of solids in a contactless and non-destructive manner. The dielectric properties of solids are described by the complex optical functions, e. g., the complex refractive index. However, the most commonly measured values are the frequency-dependent transmittance and reflectance from which the complex optical functions are determined. Two quantities are needed to determine the real and imaginary part of the complex optical functions. These can be transmittance and reflectance but also, e. g., transmittance and phase. Alternatively only one quantity can be measured and the Kramers-Kronig relation [44] can be applied to obtain the full complex optical function.

This chapter introduces the basics of optical spectroscopy. It is organized as follows: First it will be briefly explained how the optical functions can be obtained from the measured transmittance or reflectance. The influence of multiple reflections in the solid will be discussed. In the end, Gaussian optics will be introduced with special consideration for the large wavelength of THz frequencies.

2.1. Foundations

In optical spectroscopy the optical and electrical properties of materials are obtained by analyzing the frequency dependence of light reflected from or transmitted through a sample (see figure 2.1). As mentioned above, the measured values are often reflectance R and transmittance T. The reflectance is defined as the ratio of the reflected intensity I_R to the incoming intensity I_I. In the same way the transmittance is defined as the ratio between the transmitted I_T and the incoming intensity I_I. For a plane-parallel slab of thickness d they are given by:

$$R = |r|^2 = \frac{|E_R|^2}{|E_I|^2} = \frac{I_R}{I_I} \qquad \text{and} \qquad T = \frac{|E_T|^2}{|E_I|^2} = \frac{I_T}{I_I} = \frac{(1-R)^2 e^{-\alpha d}}{1-(Re^{-\alpha d})^2} \tag{2.1}$$

Here, E_I, E_R, and E_T are the electric field amplitudes of the incoming, reflected, and transmitted wave, respectively, and α denotes the absorption coefficient. The relation between the amplitude coefficients r and t is given by the Fresnel equations.

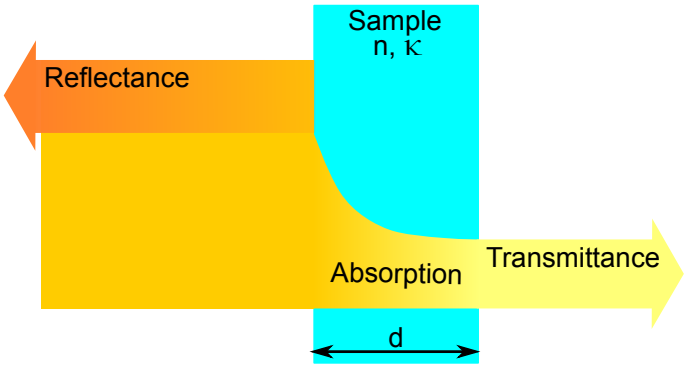

Figure 2.1.: Light is reflected by, absorbed by and transmitted through a sample

In case of normal incidence these equations read as

$$r = \frac{\tilde{n}_t - \tilde{n}_i}{\tilde{n}_t + \tilde{n}_i} \tag{2.2}$$

$$t = \frac{2\tilde{n}_i}{\tilde{n}_t + \tilde{n}_i} \quad , \tag{2.3}$$

where $\tilde{n}_i$ is the complex refractive index of the medium from which the electric field irradiates the second medium with the complex refractive index $\tilde{n}_t$. The complex refractive index is composed of the refractive index n and the extinction coefficient κ

$$\tilde{n} = n + i\kappa \quad , \tag{2.4}$$

which are unique properties of a material. The amount of transmitted or reflected light depends on these unique properties. Energy conservation dictates that $R + A + T = 1$, where A is the absorption. The refractive index n is defined as the ratio between the velocity of light in the material v and the velocity of light in vacuum c.

$$n = \frac{c}{v} \tag{2.5}$$

It is generally frequency-dependent and describes the change of the velocity and hence the wavelength of the light inside a certain medium, the so-called dispersion. The absorption can be described by the extinction coefficient κ. The extinction coefficient is not to be confused with the absorption coefficient α in Beer's law. Both coefficients are connected by:

$$\alpha = \frac{2\kappa\omega}{c} \tag{2.6}$$

An equivalent way to describe the material properties is the dielectric function $\varepsilon = \varepsilon_1 + i\varepsilon_2$. In linear response theory, the dielectric function relates the electric polarization induced in a medium to the applied external electric field.

$$\vec{P} = \varepsilon_0(\varepsilon(\omega) - 1)\vec{E} \tag{2.7}$$

The dielectric function and the complex refractive index are related in the following way:

$$\sqrt{\varepsilon(\omega)} = n + i\kappa \tag{2.8}$$
$$\varepsilon_1 = n^2(\omega) - \kappa^2(\omega) \tag{2.9}$$
$$\varepsilon_2 = 2n(\omega)\kappa(\omega) \tag{2.10}$$

Another way to describe a material is the optical conductivity. This gives the proportionality between the current density $\vec{j}$ and the applied electric field $\vec{E}$ in the general form of Ohm's law.

$$\vec{j}(\omega) = \sigma(\omega)\vec{E}(\omega) \tag{2.11}$$

The optical conductivity can be expressed by the dielectric function and consequently by the complex refractive index as,

$$\sigma_1(\omega) = \omega\varepsilon_0\varepsilon_2(\omega) = \omega\varepsilon_0 n(\omega)\kappa(\omega) \tag{2.12}$$
$$\sigma_2(\omega) = \omega\varepsilon_0\left(1 - \varepsilon_1(\omega)\right) = \omega\varepsilon_0\left(1 - n^2(\omega) - \kappa^2(\omega)\right) \quad . \tag{2.13}$$

The values of n and κ for a sample with known thickness d can be determined from R and T by solving the following system of equations:

$$R = \frac{(n-1)^2 + \kappa^2}{(n+1)^2 + \kappa^2} \quad , \tag{2.14}$$
$$T = \frac{(1-R)^2 e^{-\alpha d}}{1 - \left(Re^{-\alpha d}\right)^2} \quad . \tag{2.15}$$

These equations hold for the special case of a sample with plane-parallel surfaces in air ($n_{air} \approx 1$) and when the light is passing through the sample only once, which is a reasonable approximation for strongly absorbing material. In this case, the phase difference that is imparted to a wave with wavelength λ while traveling once through a medium with thickness d and refractive index n is given by:

$$\frac{\varphi_t}{2\pi} = \frac{L}{\lambda} = \frac{nd}{\lambda} \quad . \tag{2.16}$$

Here, L is the so-called optical path length $L = nd$. The more general case of multiple reflections within the sample will be discussed in the following section.

2.1.1. Fabry-Perot resonator

In the previous section it was assumed that part of the incoming light is reflected at the first surface while the rest of the light is passing through the sample being detected on the other side. However, a part of the light is reflected at the rear surface. Successive reflections between the two interfaces may generate non-negligible

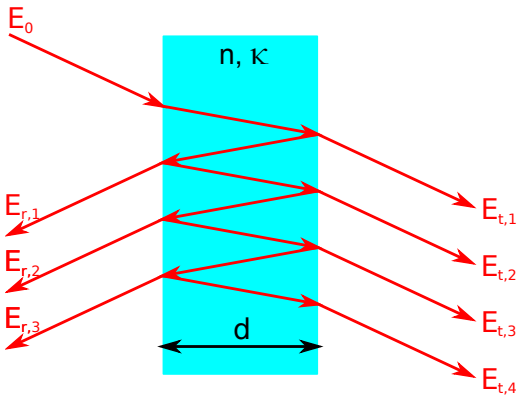

Figure 2.2.: Illustration of the different contributions to the transmitted field in weakly absorbing samples due to multiple reflections inside the sample.

interference effects as indicated in figure 2.2. Depending on the thickness, such interference has a pronounced effect on the transmittance for weakly absorbing samples. It can be accounted for by treating the sample as a Fabry-Perot resonator. In this case the transmittance is the sum over all contributions of the transmitted beams. For the sum it has to be considered that the amplitude decreases with every cycle due to absorption and light that leaves the resonator at each surface. Also, for every cycle the beam will experience a phase shift due to the additional pathlength. Taking these effects into account, the modified relation between transmittance and phase and the complex refractive index is given by [44]:

$$T = \frac{\left[(1-R)^2 + 4R\sin^2\phi_r\right] e^{-\alpha d}}{(1-Re^{-\alpha d})^2 + 4Re^{-\alpha d}\sin^2(\beta+\phi_r)} \tag{2.17}$$

$$\varphi_t = \frac{2\pi n d}{\lambda} - \arctan\left\{\frac{\kappa(n^2+\kappa^2-1)}{(\kappa^2+n^2)(2+n)n}\right\} + \arctan\left\{\frac{Re^{-\alpha d}\sin\{2(\beta+\phi_r)\}}{1-Re^{-\alpha d}\cos\{2(\beta+\phi_r)\}}\right\} \tag{2.18}$$

$$\phi_r = \arctan\left\{\frac{-2\kappa}{1-n^2-\kappa^2}\right\} \qquad \text{and} \qquad \beta = \frac{2\pi n d}{\lambda} \tag{2.19}$$

The phase shift φ_t is the absolute phase shift induced by the sample and R is the bulk reflectivity ($d \to \infty$) given by equation 2.14. In the transmittance, multiple reflections lead to a series of maxima and minima as a function of frequency due to constructive and destructive interference between the different rays. The period of this interference pattern is given by

$$\Delta\nu = \frac{c}{2nd} \quad , \tag{2.20}$$

where c is the velocity of light in vacuum. For a known sample thickness d these equations only depend on n and κ, i. e. the complex refractive index.

2.1.2. Drude-Lorentz model

To extract information from the measured transmittance or reflectance, a model is needed to connect the material properties with the spectrum. A common model to describe the frequency-dependent polarization of a solid is the Lorentz model, in which the complex dielectric function can be written as

$$\varepsilon(\omega) = \varepsilon_\infty + \sum_k \frac{\omega_{p,k}^2}{\omega_{1,k}^2 - \omega^2 - i\gamma_k\omega} \quad . \tag{2.21}$$

Here, k indexes the oscillators of the various contributions. The constant ε_∞ considers contributions from high-frequency electronic excitations. When the function is fitted to a set of data, the different resonance frequencies $\omega_{0,k}$, plasma frequencies $\omega_{p,k}$, and damping constants γ_k are the adapted parameters from which the properties of the material can be deduced.

2.2. Gaussian optics

In order to design optical elements to shape the beam, it is important to be able to describe its propagation. In many cases one can stick to geometrical optics where the beam is modeled in terms of rays. This approximation is valid if the wavelength is much smaller than the size of the optical elements. However, in the THz regime where the wavelength is of the order of millimeters, the size of the optical elements is only moderately larger than the wavelength. Here, the wave character of the light plays a role and diffraction cannot be neglected anymore. In this case the Gaussian beam approximation can be used to describe the beam propagation. This approximation is introduced in the following.

2.2.1. SVE approximation

When using ray optics one is actually talking about plane waves. Rays are the normals to the wavefronts which are parallel in case of a plane wave and are therefore used to describe its propagation. But a plane wave extends to infinity in the direction perpendicular to the propagation vector and hence is not suitable for description of real radiation. The SVE (Slowly Varying Envelope)[1] approximation takes a spatial restriction of the wave into account. For this approach, a spatial dependence of the amplitude is assumed:

$$\vec{E}(x,y,z) = \vec{E}_0(x,y,z)e^{ikz} \, . \tag{2.22}$$

The amplitude $E_0(x,y,z)$ is supposed to vary only slightly over one wavelength. This approach is inserted in the wave equation,

$$\frac{\partial^2 E_0}{\partial x^2} + \frac{\partial^2 E_0}{\partial y^2} + \frac{\partial}{\partial z}\left(\frac{\partial E_0}{\partial z} + 2ikE_0\right) = 0 \quad . \tag{2.23}$$

[1] Derivation according to [45]

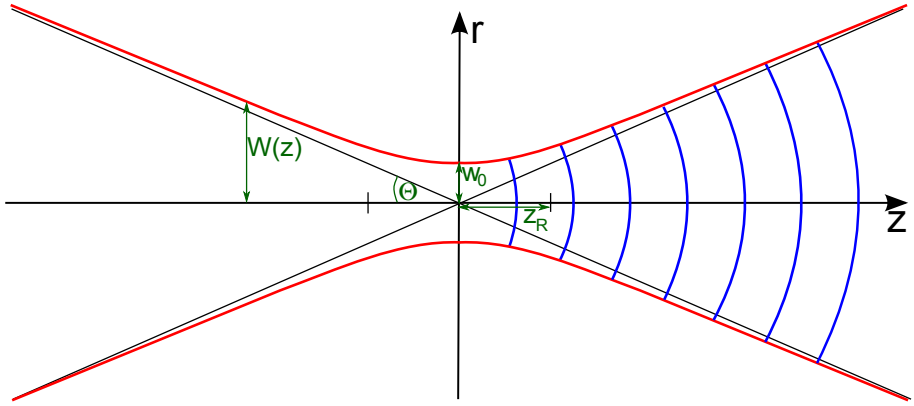

Figure 2.3.: Behavior of beam radius and wavefront of a Gausian beam.

The SVE approximation implies that the amplitude varies very slowly along the direction of propagation:

$$\frac{\partial E_0}{\partial z} \ll kE_0 \tag{2.24}$$

With this the wave equation in SVE approximation gives

$$\frac{\partial^2 E_0}{\partial x^2} + \frac{\partial^2 E_0}{\partial y^2} + 2ik\frac{\partial E_0}{\partial z} = 0 \quad . \tag{2.25}$$

In many cases it is convenient to assume a rotationally symmetric beam. In this case it is appropriate to change to cylindrical coordinates because under this condition E_0 is independent of φ. The wave equation in this particular case is

$$\frac{\partial^2 E_0}{\partial r^2} + \frac{1}{r}\frac{\partial E_0}{\partial r} + 2ik\frac{\partial E_0}{\partial z} = 0 \quad . \tag{2.26}$$

The simplest solution of this equation is the so-called Gaussian beam.

2.2.2. Gaussian beam

The lowest-order solution of the wave equation in SVE approximation (Equation 2.26) is the Gaussian beam or TEM_{00} mode given by the expression

$$\vec{E}(r,z) = \vec{E}_0 \frac{w_0}{w(z)} e^{-\frac{r^2}{w(z)^2}} e^{-i\{\omega t - \Psi_T(r,z) - \Psi_L(z)\}} \quad . \tag{2.27}$$

The name originates from the amplitude behavior which follows for all distances z a Gaussian profile in radial direction. The beam radius $w(z)$ denotes the distance from the central axis where the amplitude has fallen to $1/e$ of its maximum value. Unlike geometrical optics where the minimum beam waist is in principle infinitely small, the beam waist in Gaussian optics always has a finite size. The minimum

beam radius which can be achieved due to diffraction is conventionally labeled as w_0. The beam radius as a function of distance from the position of the beam waist is given by

$$w(z) = w_0\sqrt{1+\left(\frac{z}{z_R}\right)^2} \quad . \tag{2.28}$$

Due to diffraction, the beam radius is increasing with increasing distance from the beam waist. The Rayleigh length z_R, defined as the distance from the beam waist where cross-sectional area has doubled, is

$$z_R = \frac{\pi w_0^2}{\lambda} \qquad \text{and} \qquad w(z_R) = \sqrt{2}w_0 \quad . \tag{2.29}$$

The length $2z_R$ is called depth of focus. It gives the length over which the beam stays approximately focussed. For distances $z \gg z_R$, the beam radius $w(z)$ increases roughly linearly with distance. The angle between the line defined by $w(z)$ and the central axis is called far-field divergence angle Θ. It is given by

$$\Theta = \frac{w_0}{z_R} = \frac{\lambda}{\pi w_0} \, . \tag{2.30}$$

This is the smallest divergence angle that can be reached due to diffraction.

The second main difference to geometrical optics is that the wavefronts are not flat anymore but have a finite curvature. The surfaces of constant phase are rotational paraboloids. This is described by the transversal phase term which is given by

$$\Psi_T(r,z) = \frac{kr^2}{2R(z)} \qquad \text{with} \qquad R(z) = z\left\{1+\left(\frac{z_R}{z}\right)^2\right\} , \tag{2.31}$$

where $R(z)$ denotes the radius of the curvature. The radius of the curvature is increasing for increasing z and becomes infinite for $z \to \infty$ as well as for $z \to 0$. Together with the spreading of the beam with propagation this causes a diminution of the peak amplitude with increasing distance from the beam waist. The longitudinal phase term

$$\Psi_L(z) = kz - \arctan\frac{z}{z_R} \tag{2.32}$$

corresponds mainly to that of a plane wave. The additional term is called Gouy phase and provides a phase shift of π as the beam passes through the beam waist [46, 47]. Intuitively, this means that the sign of the phase front curvature changes.

The intensity of a beam is proportional to the square of the absolute value of the electric field $\vec{E}$

$$I(r,z) = \frac{\varepsilon_0\varepsilon}{2} c\vec{E}\vec{E}^* \, . \tag{2.33}$$

With this one gets for the intensity of a Gaussian beam

$$I(r,z) = \frac{\varepsilon_0\varepsilon}{2} c\vec{E_0}^{\,2} \frac{w_0^2}{w(z)^2} e^{-\frac{2r^2}{w(z)^2}} \equiv I_0(z) e^{-\frac{2r^2}{w(z)^2}} \quad . \tag{2.34}$$

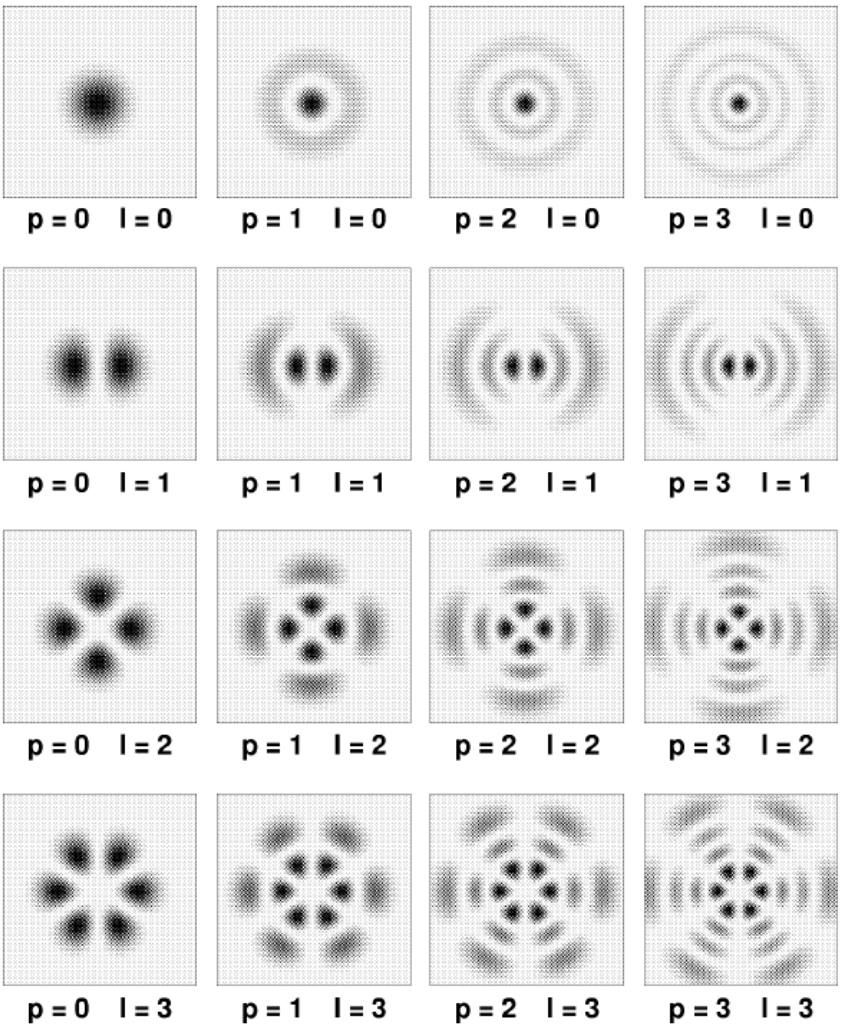

Figure 2.4.: Radial intensity distributions for some Gauss-Laguerre modes. Figure taken from [45]

The total transmitted power of the beam is obtained by integration over the intensity distribution. For the relation between the power and intensity one obtains

$$P = \int_0^\infty I(r,z) r dr = \frac{1}{4} w(z)^2 I_0(z) \quad . \tag{2.35}$$

If the definition of the beam radius $w(z)$ is put as the upper limit of the integral one finds that 86% of the total power lies within the beam radius.

2.2.3. Gauss-Laguerre modes

The Gaussian beam discussed up to this point is the simplest solution of the wave equation in SVE approximation in cylindrical coordinates. The general solution of this equation are the so-called Gauss-Laguerre modes

$$\begin{aligned} \vec{E}_p^l(r,\varphi,z) &= \vec{E}_0 \left(\frac{\sqrt{2}r}{w(z)}\right)^l \mathcal{L}_p^l\left(\frac{2r^2}{w(z)^2}\right) e^{-\frac{r^2}{w(z)^2}} e^{i\Psi} \begin{cases}\cos(l\varphi)\\ \sin(l\varphi)\end{cases} \quad , \quad p,l = 0,1,2,\ldots \\ \Psi &= kz - (p+l+1)\arctan\left(\frac{z}{z_R}\right) + \frac{zr^2}{z_R w(z)^2} \quad . \end{aligned} \tag{2.36}$$

Here, the $\mathcal{L}_p^l$ stands for the Laguerre polynomial

$$\mathcal{L}_p^l(u) = e^u u^{-l} \frac{d^p}{du^p}(e^{-u}u^{p+l}) \quad . \tag{2.37}$$

There are two different solutions which differ by a 90 ° rotation with respect to each other. Some examples for beam profiles of higher modes are shown in figure 2.4.

For these higher modes, the beam radius cannot be as easily defined as for the TEM_{00} mode. Because there is more than one maximum in the beam profile there can also be more than one radius where the amplitude is 1/e times the maximum value. In the case of higher modes, the outermost point of inflection is used as the beam radius.

2.2.4. Ray matrices

A very convenient way of describing the propagation and transformation of a beam is the use of ray matrices. The only requirement is a rotationally symmetric beam. In that case, the beam can be described by the distance r and the angle θ to the optical axis similar to linear optics. The parameters of the transformed beam in this approach are geometrical functions of the parameters of the input beam. Writing the beam parameters as vectors, these linear equations in matrix representation are

$$\begin{pmatrix} r_2 \\ \theta_2 \end{pmatrix} = \begin{bmatrix} A & B \\ C & D \end{bmatrix} \cdot \begin{pmatrix} r_1 \\ \theta_1 \end{pmatrix} \quad . \tag{2.38}$$

This matrix is called the ray transfer matrix. In this convention, the beam is always traveling from the left to the right. The parameters A, B, C, and D depend on the actual beam transformation. Consider a beam propagating a distance L. The propagation will not change the angle θ but the beam radius r will increase by $L \cdot \theta$ for small θ. In this case, the ray transfer matrix is given by

$$\begin{bmatrix} 1 & L \\ 0 & 1 \end{bmatrix} \quad . \tag{2.39}$$

The transformation by more than one optical element can be calculated by multiplying the different matrices in the order the ray passes them.

$$\begin{pmatrix} r_n \\ \theta_n \end{pmatrix} = M_n \cdot M_{n-1} \cdot \ldots \cdot M_2 \cdot M_1 \cdot \begin{pmatrix} r_1 \\ \theta_1 \end{pmatrix} \tag{2.40}$$

Defining the complex beam parameter q as

$$q = z + iz_R \quad \text{or} \quad \frac{1}{q} = \frac{1}{R(z)} - \frac{i\lambda}{\pi w(z)^2} \quad , \tag{2.41}$$

the so-called ABCD law can be applied, according to which the complex beam parameter transforms while passing through an optical system as given below:

$$q_{out} = \frac{Aq_{in} + B}{Cq_{in} + D} \tag{2.42}$$

2.2.5. Beam transformation by a thin lens

The ray transfer matrix for a thin lens is given by:

$$\begin{bmatrix} 1 & 0 \\ \frac{-1}{f} & 1 \end{bmatrix} \tag{2.43}$$

To describe the focusing of a Gaussian beam by a thin lens with focal length f, the propagation from the beam waist to the lens and from the lens to a distance z have to be considered. The total ray transfer matrix is then given by

$$\begin{bmatrix} 1 & z \\ 0 & 1 \end{bmatrix} \cdot \begin{bmatrix} 1 & 0 \\ \frac{-1}{f} & 1 \end{bmatrix} \cdot \begin{bmatrix} 1 & z_0 \\ 0 & 1 \end{bmatrix} = \begin{bmatrix} 1 - \frac{z}{f} & z + z_0 - \frac{zz_0}{f} \\ \frac{-1}{f} & 1 - \frac{z_0}{f} \end{bmatrix} \quad . \tag{2.44}$$

Using the ABCD law from equation 2.42 the beam waist w_{0f} behind the lens can be calculated from

$$-\frac{\lambda}{\pi w_{0f}^2} = \Im\left(\frac{1}{q(f)}\right) \quad . \tag{2.45}$$

Solving this equation results in

$$w_{0f} = \frac{w_0 \cdot f}{\sqrt{z_R^2 + (z_0 - f)^2}} \quad , \tag{2.46}$$

where w_0 denotes the beam waist before transmitting the lens. For object distances z_0 much larger than the focal length f, this equation can be approximated by

$$w_{0f} \approx \frac{w_0 \cdot f}{\sqrt{z_R^2 + z_0^2}} = \frac{w_0^2 f}{z_R w_0 \sqrt{1 + \frac{z_0^2}{z_R^2}}} = \frac{\lambda f}{\pi w_L} \quad , \tag{2.47}$$

where w_L is the beam radius at the position of the lens. The divergence angle of the Gaussian beam after the focal spot is given by

$$\Theta = \frac{w_L}{f} \quad . \tag{2.48}$$

From the simple equation 2.47 it can be seen that the beam waist decreases with increasing beam radius at the lens or with decreasing focal length.

3. Terahertz sources and detectors

For a long time, the spectral range between the infrared and the microwave regime was not accessible with spectroscopic methods. Due to the lack of satisfactory sources, this range between frequencies of 100 GHz and a few THz was often referred to as the THz gap [48, 49]. Many approaches to close the THz gap by developing powerful and widely tunable THz sources have been made. The most important methods of THz generation and THz detection are presented in this chapter.

3.1. Realization of terahertz sources

The first major progress was made in the 1960s by the invention of the backward-wave oscillator (BWO) [50]. After that there was almost no further improvement for the next 30 years. The interest in THz spectroscopy again increased with the progress in femto-second laser technology. Together with the development of ultra-fast photoconductive switches, this technique has become a common tool in THz spectroscopy. Nowadays a wide range of different THz sources from beamlines [51] and free-electron lasers to quantum-cascade lasers is available.

3.1.1. Black body

For spectroscopy in the far-infrared range, for example in a Fourier spectrometer, black-body-like sources are used. These sources radiate all frequencies in a characteristic, continuous spectrum which is described by Planck's law [52]

$$u(\nu, T) = \frac{8\pi h\nu^3}{c^3} \frac{1}{e^{\frac{h\nu}{kT}} - 1} \quad . \tag{3.1}$$

The spectral energy density $u(\nu, T)$ for different temperatures is shown in figure 3.1. Towards lower frequencies, the intensity is sharply decreasing to zero. Hence, the intensity in the range of a few THz is very low. Increasing the temperature results in an enhancement of the maximum intensity as well as in a shift of the maximum of $u(\nu, T)$ to higher frequencies. Therefore, the actual gain of intensity in the THz spectral range is small compared to the increase in temperature.

Because of the low optical power, detection of the radiation is very difficult. Detectors used in such experiments must be very sensitive to low intensities and thermal noise has to be accounted for.

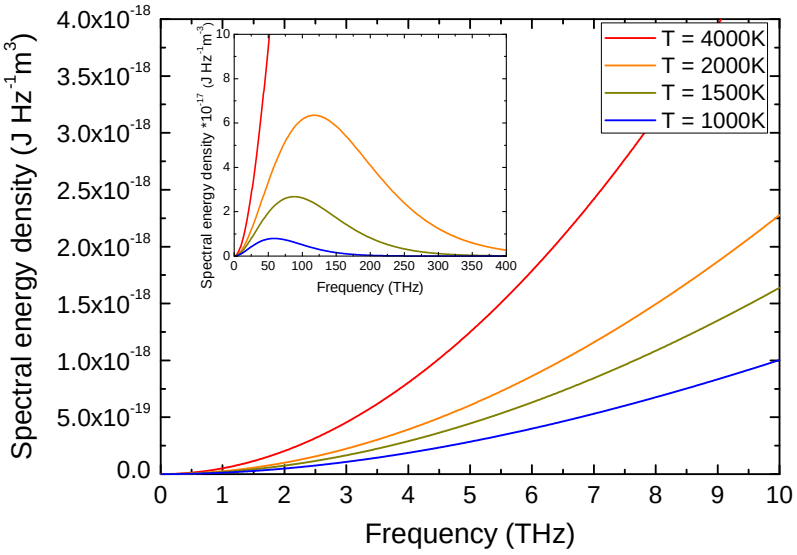

Figure 3.1.: Spectral density of a black-body source for different temperatures.

3.1.2. Backward-wave oscillator

For decades backward-wave oscillators (BWOs) were the main THz sources used for spectroscopic purposes. BWOs can cover the frequency range from 0.1 to 1.5 THz with an average output power of 10 mW but a single BWO can be tuned only ± 30% from its central frequency [50]. To cover the full THz spectral range, several BWOs are needed [53]. This is the major disadvantage since it is elaborate and time consuming to change in sequence between several BWOs in one experiment. Nevertheless BWOs are used successfully in spectroscopy [7, 54].

In principle, a BWO is an electro-vacuum diode. The schematic drawing is shown in figure 3.2. Electrons are emitted from the cathode by a heater and accelerated by a high voltage towards the anode. The electron beam is collimated by an external magnetic field. On its way from cathode to anode the electron beam flies through a comb-like electronic potential provided by a periodic metal structure. This causes the electrons to lose kinetic energy and to be bunched periodically. By this an electromagnetic wave is formed that moves in the opposite direction to the electron beam. With the help of wave guides, the radiation is coupled out. The frequency of the emitted electromagnetic wave depends on the electron velocity and thus on the strength of the acceleration field [50].

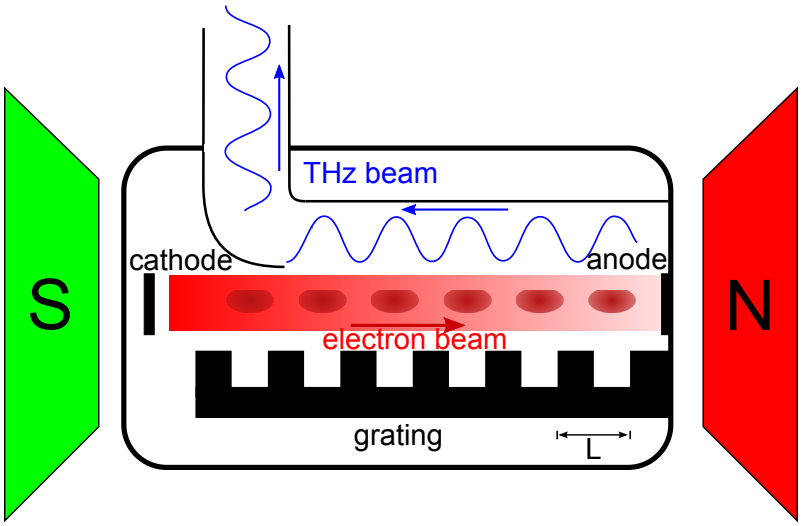

Figure 3.2.: Schematic diagram of a backward wave oscillator.

3.1.3. Gunn diode

A Gunn diode consists of three parts of n-doped semiconductor which are doped in different ways. The two outer parts are highly n-doped and the thin middle layer is only slightly n-doped. Due to the Gunn effect, these diodes exhibit a negative differential resistance region. Applying a high constant bias leads to fast statistical current fluctuations in the diode [55]. In short crystals these current fluctuations become coherent oscillations whose frequency is mostly determined by the thickness of the thin, slightly doped layer [56]. Gunn diodes provide a high output power in the range of 100 mW. Depending on the semiconductor material used, frequencies up to 3 THz can be reached but the tunability of a Gunn diode is only in the range of 10 GHz.

3.1.4. Quantum-cascade laser

A quantum-cascade laser (QCL) is a semiconductor-heterostructure laser [57]. One type of semiconductor acts as injector and the other type acts as active region [58]. When an external bias is applied to the superstructure, the electrons in the injection region undergo a intersubband transition to the active region. In the active region, the electron cascades down to a lower energy level, emitting a photon. The laser level scheme is usually a three-level system. To generate a population inversion for the lasing transition, level one has a long lifetime, while the electrons from level two decay very quickly as shown in figure 3.3. To maintain the process, the external bias has to be adjusted so that level three of the active region is aligned with level one of the next period in the superstructure. So the process repeats until the electron reaches the end of the superstructure.

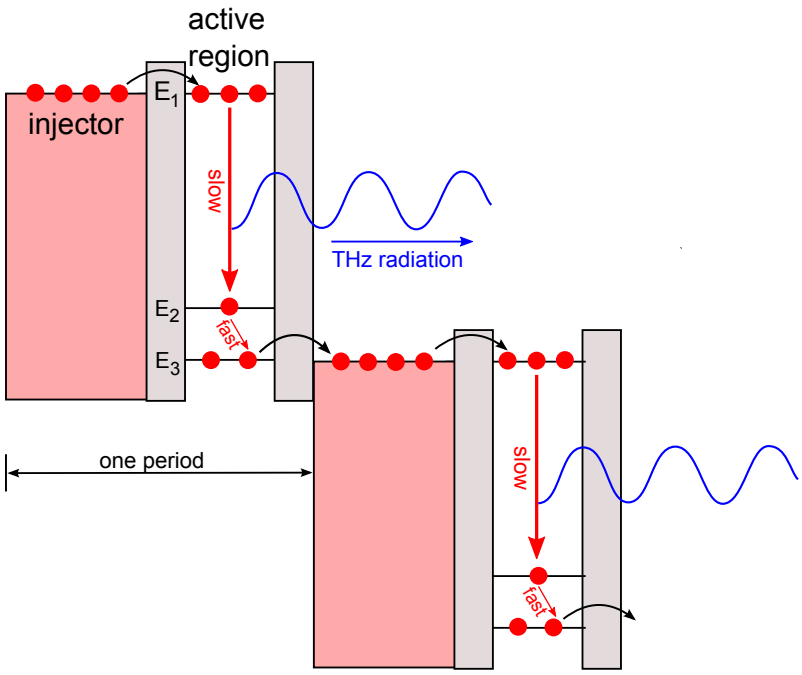

Figure 3.3.: Schematic illustration of the lasing process in the superlattice structure of a quantum-cascade laser.

There are many difficulties with this scheme. Because of the low energy of THz photons, the electron configuration can be easily disturbed by thermal excitations. To avoid this, the system has to be cooled to low temperatures, reducing the ease-of-use. The highest reported operation temperature of THz QCLs is in the range of 180 K [59]. Due to the long wavelength, it is difficult to confine the laser modes in a small volume. The lowest operation frequency reported so far is in the order of 1.4 THz [60]. The big advantage of the QCLs is that they have a high output power of 200 mW at liquid He temperatures [58] but the accessible frequency range is restricted by the size of the bandgap, which can only be tuned slightly.

3.1.5. Free-electron laser

In a free-electron laser (FEL), relativistic electrons are guided through a periodically alternating magnetic field of an undulator as shown in figure 3.4. This magnetic field forces the electrons on a sinusoidal trajectory. The oscillating electrons emit electromagnetic radiation. Its wavelength is determined by only a small number of parameters such as period, and strength of the magnetic field and the electron beam energy [58].

The big advantage of a FEL is its high output power and large tunability. On the other hand, it is very sophisticated to run, since an accelerator is needed to generate relativistic electrons. For generating high quality monochromatic radiation, a few

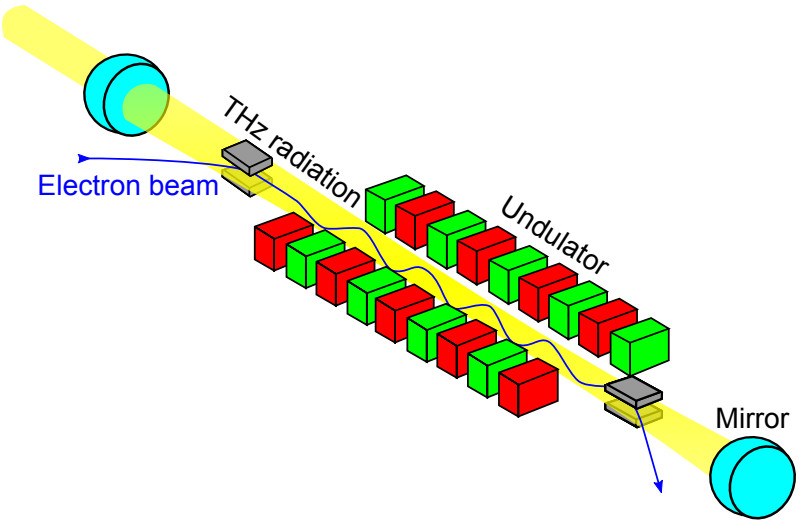

Figure 3.4.: Schematic diagram of a free-electron laser.

hundred superconducting magnets are necessary which add up to a length of several meters and have to be cooled continuously with liquid helium. Due to its size and high costs, a FEL can only be operated at a large research facility. This means limited access to the experiment.

3.2. THz detectors

At such low energies, widely used detectors measure the optical power by an increase of the temperature of an absorber. The used absorbers must have a very low heat capacity to be sensitive to even small optical powers. There are different ways to measure the increase in temperature which results in different detector types. A few of them are briefly explained in the following.

3.2.1. Bolometers

A bolometer is the most prevalent detector for THz frequencies [61]. The temperature change is measured via a change of resistance. The absorber is a thin layer on, e.g., silicon which serves as thermal mass whose resistance is measured. To be sensitive to small increases in temperature, the silicon is cooled to liquid He temperature which makes the device somewhat more elaborate. Dissipation of the heat is provided by the connection to a heat sink. The speed of the detector is proportional to the ratio of the heat capacity of the thermal load and the thermal conduction between load and heat sink.

3.2.2. Golay cells

In a Golay cell [62], the absorber is a window attached to a small volume of gas. Due to heating of the window, the gas expands. Because of the increasing pressure, a flexible mirror on the other side of the enclosed gas cell is deformed. The deformation is optically detected via the misalignment of a light beam. Unlike a bolometer, a Golay cell can be operated at room temperature. However, due to a missing heat sink, the incoming signal has to be chopped and the response is rather slow.

3.2.3. Pyroelectric detectors

A pyroelectric material is a material with a spontaneous electric polarization. The polarization is the finite macroscopic dipole-moment density of the crystal and hence there are non-zero surface charges. These charges are compensated by free carriers in the material. In a pyroelectric detector, the surfaces perpendicular to the polar axis are coated with electrodes which are connected via an ampere meter. Incoming radiation heats up the pyroelectric material and due to the temperature change, the polarization changes. To compensate the surface charges, carriers are flowing between the electrodes and this current is measured. A pyroelectric detector can also be operated at room temperature. This kind of sensors responds to changes in the intensity so that there is no underlying offset signal.

3.3. Terahertz time-domain spectroscopy

THz time-domain spectroscopy (THz TDS) has developed rapidly in last years and has become a common method for THz spectroscopy. Here, a very short electromagnetic pulse is applied to excite the sample. The response is recorded as a function of time and the corresponding spectrum obtained by Fourier transformation. The concept of generation and detection will be explained in more detail in sections 3.3.1 and 3.3.2, respectively.

3.3.1. Terahertz generation

In THz TDS, femtosecond lasers, usually titanium:sapphire lasers, are employed to generate very short optical pulses. However, these laser pulses are not yet sufficient to probe excitations at THz frequencies. They have to be converted into THz pulses by an electro-optic switch [63] which is schematically drawn in figure 3.5. In the simplest case, this switch consists of a metallic structure placed on a high-resistivity semiconductor. This realizes a coplanar transmission line, but more complex designs are also possible [64–66]. The metal striplines are biased with a DC voltage. The laser pulse irradiating the semiconductor between the striplines creates free charge carriers which are accelerated towards the stripline structure due to the applied bias voltage, giving rise to a time-dependent current (see figure 3.6 (a)). According to

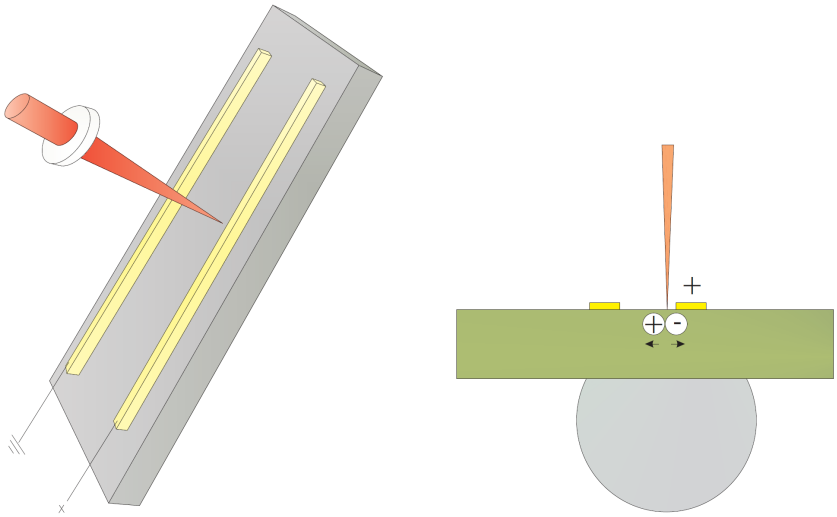

Figure 3.5.: Schematic drawing of a photoconductive switch. The laser pulse is focused on a semiconductor between two biased metal electrodes. The created free carriers are accelerated to the electrodes and thereby emit THz radiation. Figure taken from [2].

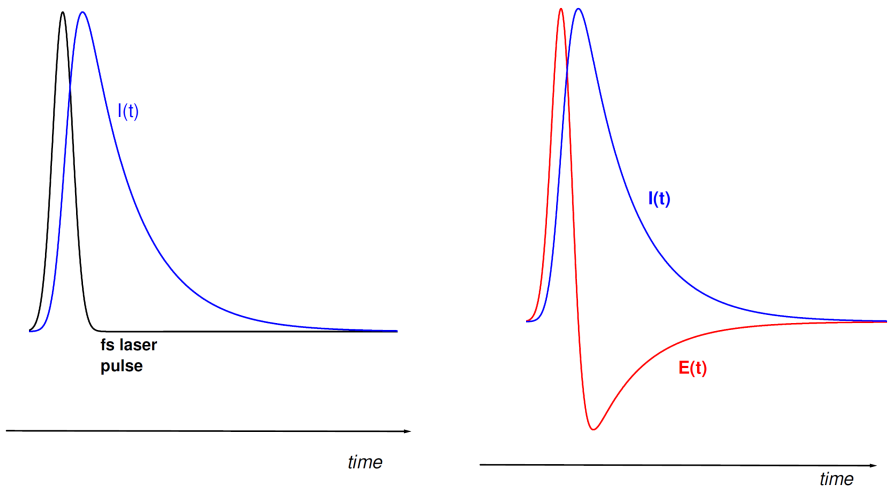

(a) (b)

Figure 3.6.: Schematic drawing of the THz generation process: (a) The laser pulse creates free carries and induces a current between the electrodes. (b) The temporal current leads to emission of an electromagnetic wave packet. Figure taken from [2].

Maxwell's law, the accelerated charges give rise to a time-dependent electromagnetic field of which the amplitude is proportional to the first time derivative of the current [50].

$$E(t) \propto \frac{\partial I(t)}{\partial t} \tag{3.2}$$

The temporal behavior of current and electric field is depicted in figure 3.6 (b).

The frequency range that can be probed with the pulse is mainly determined by the steepness of the field slope. The decay time of the current is determined by carrier lifetime in the semiconductor and is desired to be very short. With novel semiconductor materials, frequencies of more than 10 THz can be reached [31].

3.3.2. Terahertz detection

The detection of THz radiation works very similar to the generation [67, 68]. Again, an electro-optic switch is utilized, but with an electrode structure that is a little more complicated than for the emitter [69]. For detection, the electrodes are not biased but connected via an ampere meter as shown in figure 3.7 (a). In analogy to the emitter the semiconductor between the electrodes is irradiated by a laser pulse which generates free carriers. If the arrival of the THz pulse coincides with the arrival of the laser pulse, the carriers generated by the laser are accelerated by the THz pulse and the current flowing through the electrodes is measured. Since the width of the laser pulse is much smaller than the width of the THz pulse, the time delay between the THz pulse and the laser pulse has to be varied by a delay line in the laser path to measure the full time dependence of the THz electric field (see figure 3.7 (b)). This delay line is the limiting factor for the spectral resolution. Due to the small dimensions of the photoconductive switch, any misalignment induced by the delay line results in a misalignment between laser pulse and the active region of the photoconductive switch and hence the signal is not recorded any longer. The resolution of THz TDS systems is therefore limited to the order of 10 GHz [70].

The measured photocurrent density $j(\tau)$, where τ is the time delay between the two pulses, is a convolution of the THz electric field $E(t)$ and the detector response $D(t)$ [50]

$$j(\tau) = \frac{1}{T} \int_0^T E(t) D(t-\tau) dt \quad . \tag{3.3}$$

By Fourier transform, the signal is transferred from the time domain to the frequency domain. The convolution becomes a product and the detector response function cancels out when dividing sample measurement by reference measurement. Because the measured current is directly proportional to the electric field of the THz pulse, the phase information is preserved. It is thus possible to directly measure amplitude and phase and there is no need for Kramers-Kronig transformation. Another advantage is that the detection is gated. The detector is only switched on

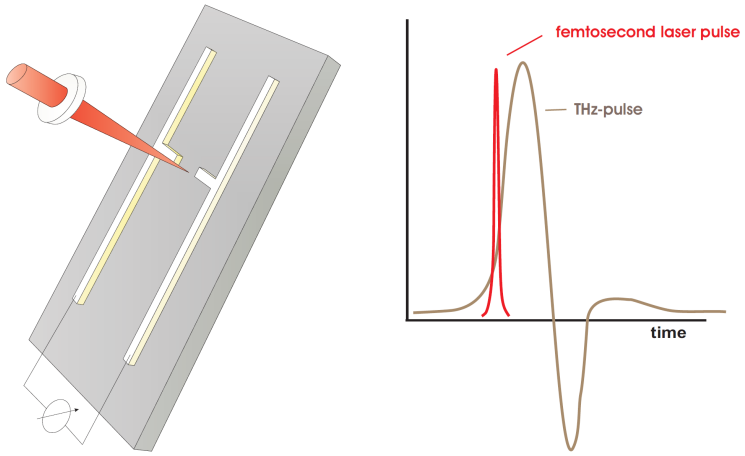

Figure 3.7.: (a) The THz receiver works similar to the THz emitter. The electrodes are not biased but connected via an ampere meter. (b) To record the entire waveform the laser pulse is moved over the THz pulse by utilizing a delay line. Figure taken from [2].

by the laser pulse when the THz pulse is reaching the detector. This provides a very high signal-to-noise ratio [50].

Another common method for the coherent detection of THz radiation is the so-called electro-optic sampling [71, 72]. Here, the THz pulse and a linearly polarized laser probe beam are guided through a birefringent crystal, for example ZnTe. The electric field of the THz pulse changes the birefringence of the crystal. Because of this, the polarization of the laser beam changes from linear to elliptical. The magnitude of the polarization change is directly proportional to the THz field. The laser beam is detected with a balanced detector which measures the magnitude of the two half-axes of the ellipse.

The change in polarization is typically very minor ($10^{-4} - 10^{-5}$). Nevertheless the signal-to-noise ratio is comparable to that of electro-optical switches and the bandwidth is much higher for electro-optical sampling [73].

THz time-domain spectroscopy has proven to be a powerful technique and has become common in the last few years. Nonetheless, a great deal of progress is still happening in the field of laser-based THz spectroscopy. One new technique is continuous-wave THz spectroscopy, which provides a much higher resolution, among other advantages. These systems are also much cheaper since they operate with commercial diode lasers instead of femto-second lasers. Since the spectrometer installed within the scope of this work is a continuous-wave spectrometer, it will be introduced in detail in the next chapter.

4. Experimental setup: cw THz spectrometer

Laser-based continuous-wave sources are a recent development in THz spectroscopy. It can be seen as the frequency-domain counterpart to THz TDS. This method deploys two near-infrared lasers to generate a beat signal that lies in the THz frequency range. The beat signal is converted into THz radiation by a so-called photomixer which acts as a transmitter. The signal is coherently detected by a second photomixer, the receiver. Every photomixer can thereby act as transmitter or receiver.

Continuous-wave THz generation was first applied by the group of Brown *et al.* [74–78]. Coherent detection of cw THz radiation was demonstrated shortly after that [79]. This method offers several advantages such as a broad accessible frequency range, frequency selectivity, and a much higher resolution than THz TDS. The photomixing procedure has experienced a huge development over the last years and is on its way to become a powerful method for THz spectroscopy [35, 36, 80–82]. As the first part of this thesis a cw THz spectrometer was installed in cooperation with Toptica Photonics. The setup and its components are introduced in the following.

4.1. Components

A schematic of the setup used in this work is shown in figure 4.1. The whole setup is fiberized. Two tunable diode lasers (Toptica DL-DFB 100) are used as light sources. Each laser contains a 60 dB optical isolator to prevent light which is not coupled into the fiber from reflecting back into the laser diode. The laser beams are superimposed in a fiber array from which 1% of the power of each laser is guided to an interferometric frequency detector. This provides frequency stabilization and control. The superimposed laser beams are amplified by a tapered amplifier (Toptica BoosTA 850). In a second fiber array the laser beat is split into two parts of equal powers. One part is guided to the photomixer that acts as transmitter while the other part is guided to the receiver photomixer. The employed photomixers are made of high-energy ion-implanted GaAs and possess a self-complementary antenna with log-periodic structure. All parts of the setup as well as the THz generation and detection process are elaborated in the following sections.

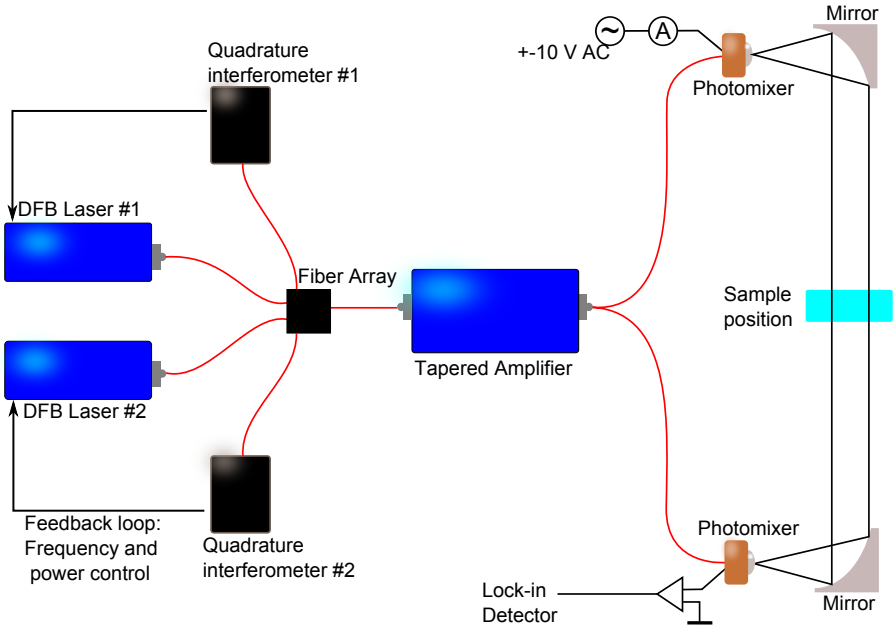

Figure 4.1.: Sketch of the continuous-wave terahertz spectrometer. Two near-infrared laser beams are superimposed to generate a beat frequency in the THz range. Stabilization of the laser frequency is achieved by two quadrature interferometers. The laser beat is amplified by a tapered amplifier and guided to the transmitter and receiver photermixer, respectively.

4.1.1. Near-infrared laser sources

In CW TS, the frequency resolution is determined by the quality of the laser beat and therefore depends on the stability and linewidth of the lasers. Hence, lasers with very high frequency stability and narrow lines are required. The use of diode lasers is favorable because of their low costs and easy maintenance, but they emit in multiple modes. Two components of a laser select the frequency, namely the laser cavity and the active medium. The modes supported by the laser are always a convolution of the modes supported by the active medium and the ones supported by the cavity. Due to interference caused by multiple reflections in the laser cavity only wavelengths that are an integer multiple of two times the cavity length L are sustained:

$$2 \cdot L = n \cdot \lambda \qquad n = 1, 2, 3, \ldots \tag{4.1}$$

These frequencies are called the eigen-modes of the resonator (blue lines in figure 4.2).

The active medium is the source of the optical gain. To be able to lase, a population inversion must be induced, meaning there have to be more electrons in an excited state than in the ground state. In diode lasers this population inversion is induced by an external current applied to the active medium. Lasing can occur on all resonator modes which have the appropriate frequency to cause stimulated

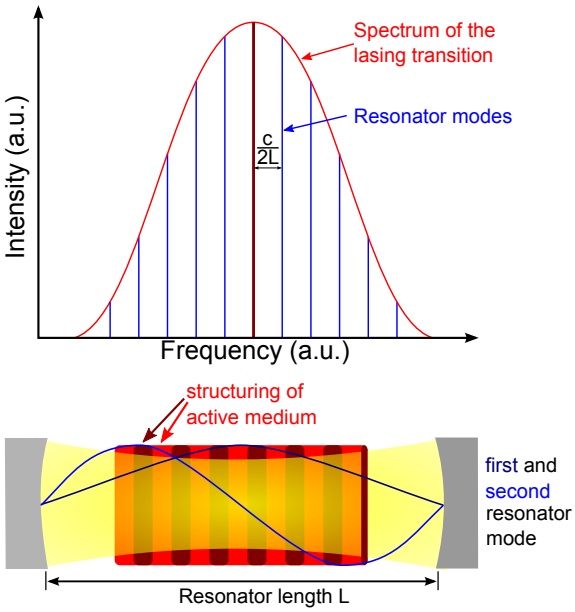

Figure 4.2: Upper part: The lasing transition is broad and supports several resonator modes. Lower part: Laser resonator alone cannot select a single mode. Additionally the active medium is periodically structured and serves as a Bragg grating.

emission. Because the width of the lasing transition is broader than the spacing of the resonator modes, the laser is usually multimodal, as is illustrated in the upper part of figure 4.2. In order to select only one mode an additional Bragg grating can be utilized. The Bragg grating can be employed outside or inside the cavity. If it is installed outside the cavity, different laser modes can be selected and hence the configuration is more flexible.

For the lasers used in this work, a different solution is applied. The Bragg grating is deployed in the laser cavity by texturing the active medium with a periodic structure as shown in the lower part of figure 4.2. One loses the flexibility of selecting different modes but the stability increases. The laser frequency can be tuned by the temperature of the active medium because the period of the Bragg grating changes due to thermal expansion. However, temperature fluctuations can cause frequency drifts and the frequency control by temperature is rather slow. A faster way to change the frequency is to change the pump current. The pump current changes the number of free carriers in the active medium and thereby its refractive index. With the refractive index the optical path length in the medium $n \cdot d$ changes. Note that the free carriers mainly change the refractive index in the frequency range below about 1 THz. Nevertheless, the change of n at the laser frequency (780 nm $\approx$ 380 THz) is still of the order of 10^{-6}, which is the same order as the linear expansion coefficient of the active medium. Thus, the frequency can be controlled by two parameters, temperature and current.

The laser beat and hence the THz frequency is tuned by heating one laser diode and cooling the other one. Both lasers are always tuned by the same amount but in different directions. If one considers only the laser beat itself, the lowest THz frequency given by the laser linewidth, which is actually in the range of some MHz.

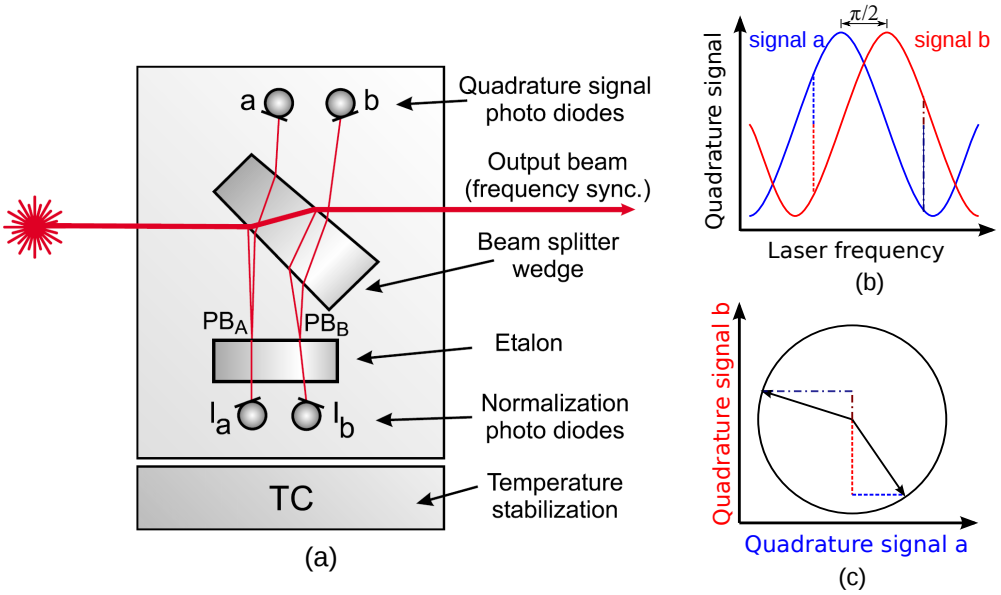

Figure 4.3.: (a) Sketch of the quadrature interferometer, taken from [83]. (b) The interference pattern of the two diodes a and b is shifted by $\pi/2$ with respect to each other. (c) Position of the combined quadrature signal on the circle for two examples.

The laser beat can thus be generated continuously from zero frequency onwards. The upper frequency limit is determined by the mode-hop-free tuning range of the laser diodes and their non-destructive maximum heating and cooling temperature of 50 °C and 0 °C, respectively.

In the scope of this thesis two different sets of laser diodes were used. One set has a center wavelength of about 780 nm, the other one 850 nm. The latter one cannot be used if the photomixers are cooled down, due to the temperature dependence of the band gap of GaAs. For the 780 nm set, only diodes with identical center frequencies were available at the time of this work. This allows for a maximum THz frequency of 1.3 THz. However, with two diodes of 853 nm and 855 nm, the beat frequency can be varied up to 1.8 THz. The laser power after the 60 dB optical isolator and fiber coupling amounts to about 20 mW per laser.

4.1.2. External frequency control

The external frequency control and stabilization of each laser is achieved by a quadrature beam interferometer (in the following denoted as iScan) [83]. A schematic drawing of the iScan is shown in figure 4.3 (a). A wedge-shaped beam splitter generates two low-power probe beams out of the incoming laser beam which pass through a low-finesse etalon at slightly different angles. The position and shape of the beam splitter is chosen such that the two interference signals, created by multiple reflec-

tions in the etalon, have a phase shift of $\pi/2$ with respect to each other as depicted in figure 4.3 (b). Each interference signal is detected by two photo diodes. One pair of photo diodes (I_a and I_b) measures the laser power. This is necessary since the quality of the fiber coupling of the lasers changes with frequency due to the change in laser temperature and the involved change in pointing. At the same time, their signal is used to normalize the signal of the diodes a and b which serve for frequency control. Their signals are combined into a quadrature signal: The measured voltages of the two diodes are drawn in an x-y graph with signal a on the x axis and signal b on the y axis. Due to the relative phase shift of $\pi/2$ the combined signal lies on a circle and the angle between starting position and actual position is a linear function of frequency. Two examples are shown in figure 4.3 (c). The control loop compares the signals of the diodes to a computed reference value and sends the resulting error signal back to the laser control where laser temperature and current are corrected. However, since the signals a and b are not exactly cosine-shaped, the x-y graph is not an exact circle. This leads to deviations between the set frequency and the real frequency as will be shown in the discussion of the frequency stability in section 6.3.

The use of two interference signals crucially increases the precision of the control. At an extremum of the interference pattern the slope is very small and hence a change in frequency will only result in a small change of signal. By using two interference signals with a phase shift of $\pi/2$, the second interference pattern always has a large slope at the position where the first pattern has its extremum and vice versa. Of course, the larger the slope the more precise the frequency adjustment. But making the slope large by decreasing the frequency period increases the risk of slipping by one whole period.

For the iScans used here, the period of each interference pattern is 8 GHz. The temperature of each laser diode is controlled in the range of 0 °C to 50 °C with a precision in the mK range which in the end leads to a long-term frequency stability in the MHz range [83].

4.1.3. Tapered amplifier

After superposition, the laser beams are amplified by a tapered amplifier, which is in principle nothing more than an active medium with a particular geometry. The incoming laser beam is amplified by stimulated emission over the whole length of the active medium. The population inversion is maintained by continuously pumping the active medium with an external current. To optimize the performance of the tapered amplifier, the active medium has a tapered shape which is the origin of the name for this type of amplifiers (see figure 4.4). The increase of the cross section of the active medium increases the laser gain. At the same time the larger surface provides a better heat dissipation. One thing to be taken into account is that the amplification is frequency dependent due to the different extent of population inversion.

Due to the low breakdown power of the photomixers, the laser beat is amplified

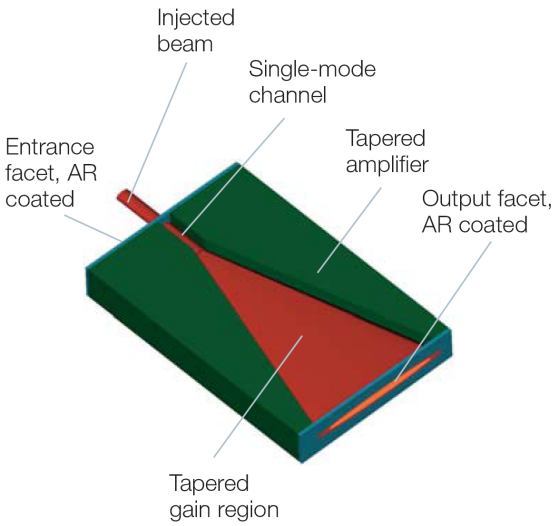

Figure 4.4: Sketch of the geometry of a tapered amplifier. Figure taken from [84]

only moderately, so that each photomixer is illuminated by about 35 mW.

4.1.4. Photomixer and THz generation

The photomixers are the centerpiece of the cw THz setup. In this section the generation of THz radiation as well as the properties and structure of the photomixers are described in detail.

The photomixer consists of a GaAs substrate, with one side featuring a thin low-temperature grown GaAs layer and an antenna structure. The other side of the substrate has a hyperspherical Si lens attached, which is needed to couple the generated THz radiation to air, as will be shown later. A scheme of the profile is depicted in figure 4.5.

We start from two linearly polarized superimposed laser beams. When the phase difference is assumed to be zero, the electric field of the superimposed beam is given by

$$E = E_0 \cos(\omega_1 t) + E_0 \cos(\omega_2 t) \tag{4.2}$$

$$E = 2E_0 \cos(\omega_{mod} t) \cos(\omega_{beat} t) \tag{4.3}$$

$$\omega_{mod} = \frac{1}{2}(\omega_1 + \omega_2) \qquad \omega_{beat} = \frac{1}{2}(\omega_1 - \omega_2) \tag{4.4}$$

where ω_{mod} is the so-called modulation frequency and ω_{beat} is the beat frequency. This beam irradiates the photomixer with an intensity

$$I \sim E^2 \sim 4E_0^2 \cos^2(\omega_{mod} t) \cos^2(\omega_{beat} t) \tag{4.5}$$

The structure of the photomixer is similar to that of the electro-optical switches used for THz TDS. Instead of a stripline, it consists of a metallic broadband antenna with

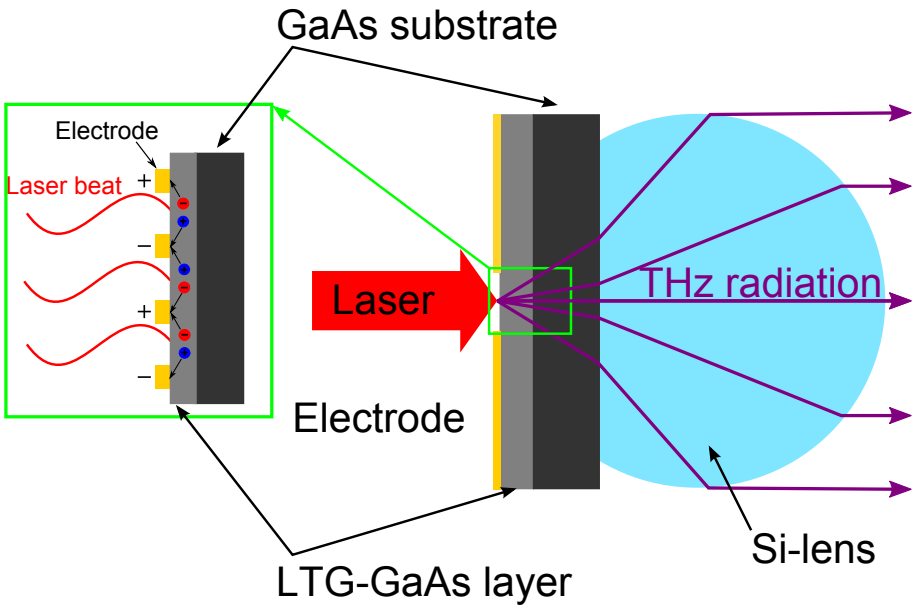

Figure 4.5.: Schematic profile of a photomixer.

a small gap in its center, deposited on GaAs [36, 85]. But the requirements on the semiconductor material are much higher for cw THz generation than for THz TDS, as will be discussed below. For cw THz generation the photomixer is biased, meaning there is a constant electric field in the semiconductor gap between the two halves of the antenna. The incoming laser beam excites electrons over the band gap and the semiconductor becomes conducting. Due to the applied bias, the charge carriers are accelerated towards the electrodes as shown in the inset of figure 4.5. The photomixer acts as a low-pass filter which lets only the beat frequency pass (see figure 4.6) and blocks optical frequencies. Just to raise the cutoff frequency to the THz range, the lifetime of the carriers in the semiconductor must already be very short. Usually the lifetime of the excited carriers in the materials used is in the order of less than a picosecond. In this case, the modulation frequency ω_{mod} varies much faster than the free-carrier lifetime, and therefore the electrons cannot follow it. This means that the term with ω_{mod} in equation 4.3 can be replaced by a time-averaged constant. The intensity the electrons can react to is given by

$$I \sim \cos^2(\omega_{beat} t) = \frac{1}{2}\{1 + \cos[(\omega_1 - \omega_2)t]\} \tag{4.6}$$

which means that only the difference frequency[1] of the two lasers plays a role. The number of created charge carriers is proportional to the intensity of the laser beat, and so are the conductivity σ and the current density j, since they are proportional to the number of free charge carriers,

$$\vec{j} = \sigma \vec{E} = nqv_D. \tag{4.7}$$

[1]For simplicity, in the following the difference frequency will also be referred to as beat frequency.

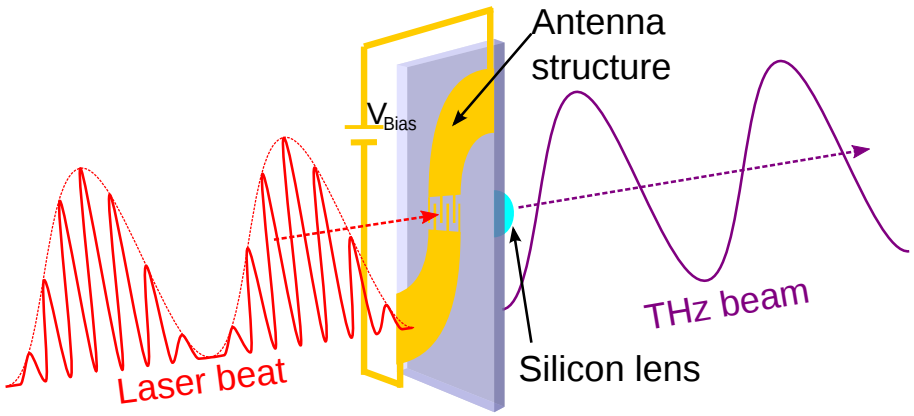

Figure 4.6.: The incoming laser beat modulates the conductivity of the antenna gap. Due to the biased electrodes, a time-dependent current is flowing in the antenna which then radiates an electromagnetic wave of the beat frequency.

Here q is the charge and v_D is the drift velocity of the charge carriers. The current flowing through the antenna structure therefore oscillates with the beat frequency of the two lasers and the electromagnetic wave emitted from this antenna structure has the frequency $\omega_{\mathrm{THz}} = \omega_1 - \omega_2$. The process is shown schematically in figure 4.6.

A short lifetime of the free carriers must be guaranteed so that the number of free carriers at time t is always proportional to the laser intensity at time t. If the lifetime exceeds the timescale where the beat intensity changes, the correlation between beat intensity and current density j is lost and the emitted wave does not have a defined THz frequency. Therefore the performance of the photomixer in the case of high frequencies is restricted by the carrier lifetime [36].

The material of choice for the semiconductor is GaAs because of its short electron-hole recombination time [36]. But the intrinsic carrier lifetime is still too large and has to be further decreased by the introduction of additional defects. The required lifetime in the sub-ps range can be achieved by growth of GaAs at relatively low temperatures (around 300 °C) and/or post-growth ion implantation [42, 86, 87]. In both cases additional defects are induced in the semiconductor. By growing the GaAs at low temperatures, the ions do not have the mobility to settle in the right way resulting in As ions located at Ga sites and Ga vacancies. Both defects provide a large capture cross-section for electron-hole pairs. Subsequently, the low-temperature grown GaAs (LT-GaAs) is usually annealed to increase the resistivity, even though the lifetime is slightly increased by this process [34]. The increase of the resistivity gives rise to a larger output power, as discussed later in this section. The other method, ion implantation, creates defects by destroying the GaAs lattice structure. It is important to note that in the photomixers used here, the As ions are implanted below the photoactive volume, so that the ions do not by themselves change the GaAs properties [42]. The advantage of high-energy ion implantation is the high reproducibility of the material properties compared to low-temperature

growth.

Apart from the short carrier lifetime of LT-GaAs, two other important properties make it very suitable for use in photomixers. On the one hand LT-GaAs provides a high carrier mobility, so that despite the low carrier lifetime as many carriers as possible can reach the metal electrodes. The current flowing through the antenna structure can then be as high as possible. On the other hand, the breakdown voltage of LT-GaAs is relatively high, allowing a high electric field to be applied, which also results in a higher current.

It was found that the potential difference drops very fast as a function of the distance from the electrodes [88]. To enhance and homogenize the electric field and keep the active area the same, the electrodes are fabricated with an interdigitated finger structure as shown in figure 4.7. Generally the electromagnetic power emitted by the photomixer can be described by [36]:

$$P_{\mathrm{THz}}(\omega) = 2\frac{R_A V_B^2}{A}\left[\frac{\eta\mu e\tau}{rh\nu}\right]^2 \frac{mP_1P_2}{[1+(\omega\tau)^2][1+(\omega R_A C)^2]} \tag{4.8}$$

The used symbols are given in table 4.1. Some important dependencies can be seen from this formula. At high frequencies the power drops with $P_{\mathrm{THz}} \sim \omega^{-4}$. In this region the performance of the photomixer is limited by the carrier lifetime τ and the capacitance of the gap C. For frequencies $\omega\tau \gg 1$, the modulation is reduced like described before and, additionally, the heating of the device is increased due to charge accumulation. Also, for frequencies $\omega R_A C \gg 1$, there occurs charge accumulation at the electrodes due to the finite capacitance of the gap which also reduces the modulation. The output power depends quadratically on the bias voltage V_B

Table 4.1.: Parameter explanation of equation 4.8

Symbol	Explanation
P_1	power of laser one
P_2	power of laser two
m	laser overlap parameter (1 for perfect overlap, 0 for no overlap)
R_A	antenna resistance
V_B	bias voltage
A	active (laser spot) area
r	width of the antenna gap
η	number of charge-carrier pairs created per photon
$h\nu$	mean laser photon energy
μ	effective carrier mobility
e	electron charge
τ	mean charge-carrier lifetime
C	capacity of the antenna gap
ω	laser beat frequency

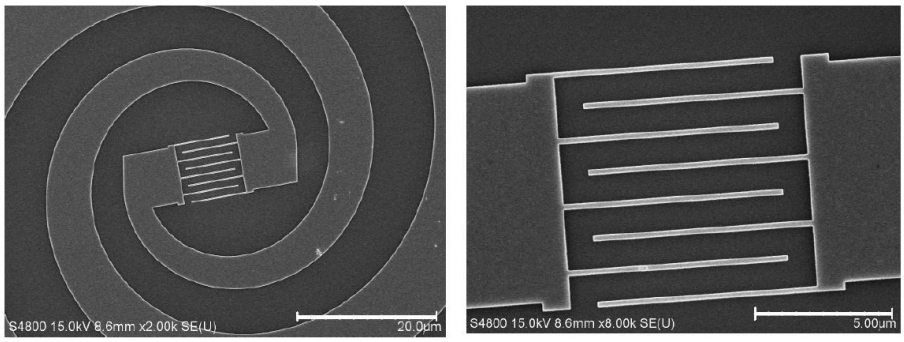

Figure 4.7.: Scanning electron microscope (SEM) picture of the self-complimentary log-periodic spiral antenna structure and the interdigitated finger structure. Picture taken from [91].

and therefore on the electric field between the electrodes. The interdigitated finger design increases the output power by increasing the applied field but simultaneously increases the capacitance C and therefore further limits the high-frequency performance [76]. Finally, the outcoupled THz power depends not only on the shape and design of the interdigitated finger structure but also on the shape of the antenna itself and the antenna impedance which are expressed in R_A [36, 89, 90].

Due to the high refractive index of GaAs, the main part of the THz radiation is radiated into the substrate. To couple as much of the THz radiation as possible out to free space at the opposite side of the GaAs, a Si lens is employed which has a dielectric constant in between those of GaAs and air. It collects and collimates the emitted THz radiation and by this increases the efficiency [92]. Still, the efficiency of the photomixers is low. For the photomixers used in this work the radiated THz power is in the range of some tens of nW [42]. The properties of the THz radiation in terms of the beam profile and the polarization are investigated in sections 7.2 and 7.3. The photomixers used in this work were fabricated at the Max-Planck-Institute for Radioastronomy in Bonn by Dr. Iván Cámara Mayorga. They consist of a high-energy ion implanted GaAs substrate with a self-complimentary log-periodic spiral antenna structure. A picture of the antenna and the finger structure is shown in figure 4.7. The active mixing area contains an interdigitated finger structure and has a size of $9 \times 9\mu\text{m}^2$ [41].

4.1.5. Coherent detection

The emitted THz signal is detected with a second photomixer via homodyne detection. In the detection scheme, the electrodes of the photomixer are not biased but connected by an ampere meter as shown in figure 4.8. As for the transmitter, the incoming laser beat generates free carriers in the semiconductor material, giving rise

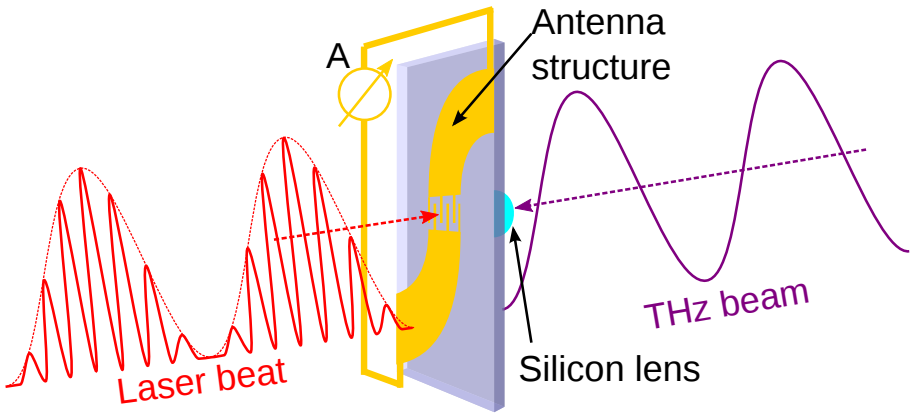

Figure 4.8.: The free charge carriers created by the laser beat are accelerated by the THz electric field. The current flowing through the antenna is then detected by an ampere meter.

to a time-dependent charge-carrier density

$$n(t) \propto 1 + \cos(\omega_{beat} t) \quad . \tag{4.9}$$

The charge carriers are accelerated by the incident THz electric field

$$E(t) \propto A \cos(\omega_{beat} t + \varphi) \quad , \tag{4.10}$$

where φ is the phase difference between the laser beat and the THz radiation. The current flowing in the receiver is hence proportional to

$$j(t) \propto (1 + \cos(\omega_{beat} t)) \cdot A \cdot \cos(\omega_{beat} t + \varphi) \quad . \tag{4.11}$$

It is important to note that the current density is proportional to the electric field of the THz radiation and not to the intensity, which means that the phase information is preserved. Nevertheless, the oscillation of the current is too fast to be resolved by the ampere meter, so that the measured value is a temporal average

$$\langle j \rangle \propto \frac{A}{2} \cos(\varphi) \quad . \tag{4.12}$$

The measured current (denoted as THz photocurrent I_{ph}) is a product of the THz amplitude A and the relative phase φ between the laser beat and the THz radiation. The amplitude of I_{ph} depends on ν as discussed in section 4.1.4. It extends from $I_{ph} \approx 200$ nA at 100 GHz to $I_{ph} \approx 0.5$ nA at 1.3 THz. To detect such small currents, a lock-in detection technique is used. The current is first pre-amplified by a transimpedance amplifier. The THz signal is modulated by applying a square-wave voltage as bias voltage. The modulation frequency and amplitude amount to 220 Hz and ± 10 V, respectively. For lock-in detection, a Toptica TeraControl 110 digital lock-in module based on a field-programmable gate array (FPGA) is employed.

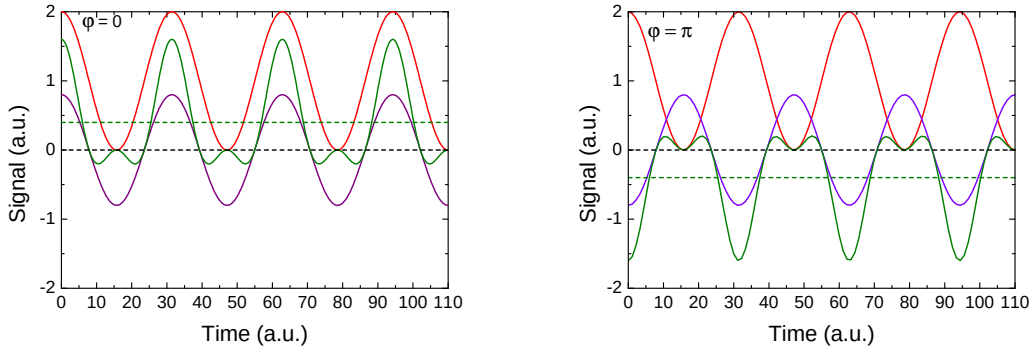

Figure 4.9.: The left-hand side shows the behavior of the photocurrent (green) for laser beat (red) and THz radiation (purple) arriving in phase at the receiver. The right-hand side shows the behavior for a phase shift of π between laser beat and THz radiation.

Before discussing how the amplitude and phase information are separated, the behavior of the photocurrent for two special cases is briefly shown. The optical path length of the laser beat and the THz radiation are usually different which means that the two beams exhibit a phase shift with respect to each other.

In the first case it is assumed that the laser beat and the THz radiation are in-phase ($\varphi = 0$). This case is shown in the left side of figure 4.9. When the laser intensity is high, the THz electric field is positive which means that a relatively high current, shown in green, is flowing in positive direction. On the other hand, when there is a negative THz electric field, the number of charge carriers is small due to the low laser intensity. As a consequence, there is almost no current flowing in the negative direction. Hence the temporal average of the photo current I_{ph} is at its positive maximum as shown by the green dotted line in figure 4.9.

In the second case it is assumed that the laser beat and THz electric field are out of phase ($\varphi = \pi$). This example is shown in the right side of figure 4.9. In this case things are the other way round. When the number of charge carriers excited by the laser beat is high, there is a negative THz electric field and when there is a positive THz electric field the number of charge carriers is low. Hence the flowing current is mainly negative which means that also the temporal average is at its negative extremum. For relative phase shifts in between, the measured photocurrent does not have its maximum value and therefore is not proportional to the maximum THz amplitude.

To get the maximum photocurrent that is proportional to the THz electric field an additional phase shift $\Delta\varphi$ can be implemented

$$\langle j \rangle \propto \frac{A}{2} \cos(\varphi_0 + \Delta\varphi) \quad . \tag{4.13}$$

By varying $\Delta\varphi$ such that one gets maximum amplitude the THz amplitude and

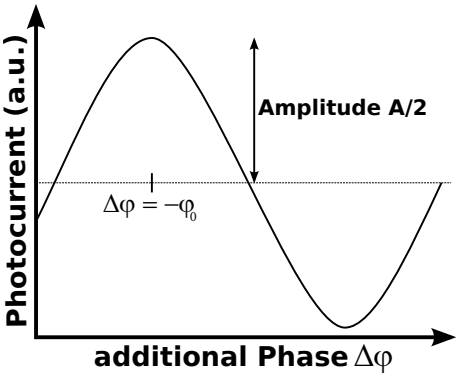

Figure 4.10: The photocurrent as a function of the additional phase shift $\Delta\varphi$ shows a sinusoidal behavior due to alternating constructive and destructive interference. Both the amplitude A and the phase φ can be extracted from the extrema.

phase can be extracted (see figure 4.10).

The variation of $\Delta\varphi$ can be implemented by varying the frequency in small steps or actively changing the optical path-length difference

$$\Delta L = (L_S + L_{\mathrm{THz}}) - L_D \quad , \tag{4.14}$$

where L_S and L_D are the path of the laser beat to the transmitter and receiver photomixer, respectively, and L_{THz} is the THz beam path. Both methods are investigated and compared in the scope of this thesis.

Varying the frequency in small steps is easy to accomplish and a very stable method since no moving parts are present. The relative phase between the laser beat and the THz radiation at the receiver changes with frequency for $\Delta L \neq 0$. As a consequence, the phase shift between laser beat and THz radiation will alternate between zero and π which means that the measured photocurrent will oscillate as a function of frequency as indicated in equation 4.12. This method was also applied by Mouret *et al.* [93]. Amplitude and phase information are extracted from the envelope and the positions of the extrema. The data analysis deployed for this method is discussed in detail in section 5.1.

A change of the optical path length can be either implemented in the THz light path L_{THz} or in the laser path L_S and L_D. A change of the THz optical path can for example be realized with a mechanical delay stage [96, 97]. However, this is not favorable since in this case the amplitude depends on L_{THz} due to standing waves. Consequently, the measured photocurrent $I_{ph}(L_{\mathrm{THz}})$ deviates from the expected sinusoidal behavior which is shown in figure 4.11. A delay line in the laser beam path can either be implemented before or after the superposition of the lasers. To accurately extract amplitude and phase, the minimum modulation of the path length difference Δs provided by the delay line should be half a wavelength of the lowest THz frequency (see figure 4.10), i. e., a phase difference of π. For a frequency of 50 GHz, this corresponds to 3 mm. Such a distance can be easily provided by a conventional delay stage which requires a free optical beam [79, 93, 96, 98–100].

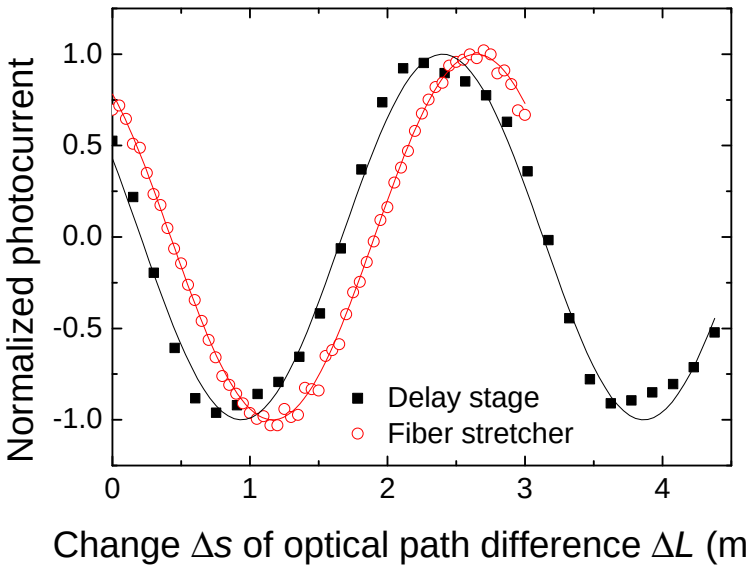

Figure 4.11.: Photocurrent at 100 GHz as a function of optical path-length difference ΔL. On the one hand the path-length difference was modulated by a fiber stretcher in the laser path (red symbols) and on the other hand by a mechanical delay stage in the THz path (black symbols). The cosine fits are shown as solid lines. The phase shift between the two data sets is due to a difference in ΔL for $\Delta s = 0$. Small deviations between the cosine fit and the data of the mechanical delay stage can be observed. Picture taken from [94]. See also reference [95]

However, a mechanical delay stage is rather slow and contrary to a compact fiberized setup. Implementing the delay line in only one of the laser beam paths, i. e., before superposition, decreases the needed delay length [101–103]. Due to the much smaller wavelength of the near-infrared laser (780 nm), the required stretch length for a phase difference of π is much smaller. It is in the order of 1 μm, which can be easily provided by an electro-optic modulator. This also has the advantage of a fast scanning speed. However, the length changes in the modulator due to thermal drifts are in the same order of magnitude. Without elaborate stabilization, the accuracy and stability is strongly affected by the electro-optic modulator.

Therefore, the setup used in this work employs a fiber stretcher for phase modulation. This ensures both fast modulation and high stability while keeping the advantage of an all-fiber-based setup. The data analysis deployed for the use of the fiber stretcher is described in section 5.2. Additionally, a way to correct drifts of the photocurrent amplitude is implemented into the setup. The so-called photocurrent correction (PCC) is discussed in section 4.1.7[2]. Both the operation of the fiber

[2]The concept of the fiber stretcher as well as the photocurrent correction were developed and

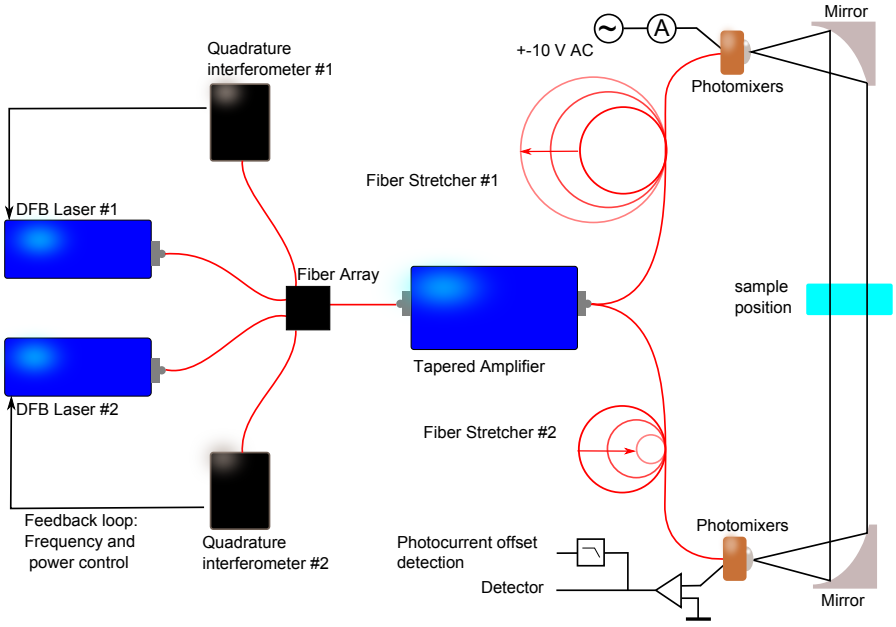

Figure 4.12.: Two fiber stretchers were implemented into the setup, one in the transmitter path L_S and the other in the receiver path L_D. Both fiber stretchers work anti-symmetrically gaining twice the path-length difference as for a single fiber stretcher.

stretcher and the concept of the photocurrent correction will be briefly introduced in the following.

4.1.6. Fiber stretcher operation and settings

Two identical fiber stretchers were implemented in the setup. One in the transmitter arm L_S and the other in the receiver arm L_D, as indicated in figure 4.12. The fiber stretchers employed here were fabricated by Optiphase (Optiphase PZ2-PM3-APC-E-850P). Each fiber stretcher consists of 60 meters of polarization maintaining fiber wound around a cylindrical piezo, with the expansion of the fiber being a linear function of the applied voltage. This has two big advantages: (i) By letting the two fiber stretchers work antisymmetrically, i.e. one fiber stretcher contracts while the other one expands, the modulated path length Δs of ΔL is twice as large than using only one fiber stretcher. (ii) Thermal drifts are minimized since length changes due to any thermal drift occurring in both fiber stretchers will cancel out (compare equation 4.14) and ΔL is kept small.

The maximum modulation frequency of the piezos is limited by the maximum output current (here 200 mA) due to the capacitance of the fiber stretchers of 100 nF each. The proportionality constant ζ between applied voltage U and resulting length

implemented into the setup by Axel Roggenbuck within the scope of his PhD thesis [94].

difference Δs was determined by analyzing the phase change per fiber-stretcher voltage at a fixed frequency. Between two adjacent maxima of the photocurrent Δs changes by one wavelength λ. Thus, ζ is given by

$$\zeta = \frac{\lambda}{\Delta U} = \frac{\Delta s}{\Delta U} \quad , \tag{4.15}$$

where ΔU is the voltage change between two maxima. Taking the refractive index of the fiber into account, $\zeta = 17.77\ \mu$m/V is found for our setup. Note that ζ was measured for the combination of both fiber stretchers. For the desired path difference of $2\Delta s_0 = 3$ mm, corresponding to half the wavelength at a frequency of 50 GHz, the required voltage can now be determined:

$$2\Delta s_0 = 2 \cdot 17.77 \mu\text{m/V} \cdot U_0 \tag{4.16}$$

$$\Rightarrow U_0 = \frac{3\text{mm}}{2 \cdot 17.77 \mu\text{m/V}} \approx 85\ \text{V} \tag{4.17}$$

In principle, the fiber stretcher can be operated in two different modes. In the first mode, the modulation frequency of the stretcher is set below the frequency of the lock-in modulation applied to the transmitter bias. This mode is similar to the operation of a conventional mechanical delay line. It still allows for the usage of lock-in detection which provides a high sensitivity. However, as the fast modulation of the transmitter bias affects the measurement of the transmitter photocurrent (see section 4.1.7), we prefer a different method.

The second mode is to apply high modulation frequencies to the fiber stretcher, in this case 800 Hz. To increase the quality of the data, about 240 stretcher cycles are averaged before fitting, and thus the time to measure one frequency point is about 300 ms. Additionally, the fit is improved for higher frequencies since the number of periods also increases with frequency due to the constant value of $2\Delta s_0$. This is favorable since the efficiency of the photomixers decreases with increasing frequency.

In this mode, the previous switching of transmitter bias is in principle not needed, but still useful at much lower rates to correct disturbances introduced by the fiber stretcher modulation, for example small variations of the optical power emerging as a function of stretched length [94]. The switching frequency of the transmitter bias was set to be an integer factor of the stretcher modulation frequency:

$$2f_{T_x} = \frac{f_{stretcher}}{m} \tag{4.18}$$

When $m = 5$ is chosen, $f_{T_x} = 80$ Hz and the bias voltage is inverted every five stretcher cycles as depicted in figure 4.13. While a change in sign of the bias voltage also switches the sign of the recorded THz signal, the variations remain unchanged. For calculating the average the recorded signals are multiplied with the sign of the bias voltage. Thereby the sign of the disturbances changes and hence by averaging the effect should cancel out. Note that the stretcher cycles which coincide with the switch of the bias voltage at the photomixer as shown in gray in figure 4.13 are not considered for the average.

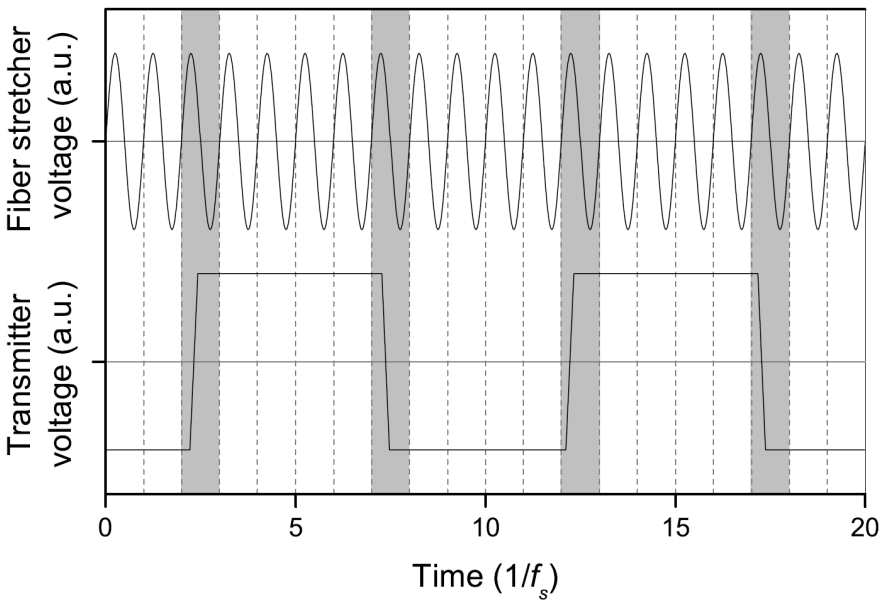

Figure 4.13.: The figure shows both the fiber stretcher voltage and transmitter bias voltage as a function of time. The bias voltage of the transmitter switches sign every 5 stretcher cycles. Stretcher cycles where the bias voltage changes are not used for the average and fit. Picture taken from [94].

4.1.7. Photocurrent correction

The photocurrent correction (PCC) enables the correction of potential drifts of the photocurrent amplitude. All parameters given in table 4.1 that are influenced by the environment can be described as a variation of the laser power at the transmitter or receiver. Mechanical stress for instance can lead to a small bending of the fiber. As a consequence not the whole antenna gap is illuminated by the laser beat and hence the radiated THz power decreases. Starting from equation 4.12 the photocurrent measured at the receiver can be rewritten as

$$I_{ph} = R_{Tx} R_{Rx} \sqrt{P_{1,Tx} P_{1,Rx} P_{2,Tx} P_{2,Rx}} \cos\varphi \tag{4.19}$$

substituting the THz electric field by the power of the two lasers at the transmitter ($P_{1,Tx}$ and $P_{2,Tx}$) and at the receiver ($P_{1,Rx}$ and $P_{2,Rx}$), respectively. R_{Tx} and R_{Rx} denote the efficiency to convert the laser power to THz power at the transmitter and to convert the THz power to a THz photocurrent at the receiver. Instabilities of these laser powers can for example be induced by mechanical displacement of the optical fiber due to temperature fluctuations. Thermal expansion also leads to a change of polarization. Polarization is also affecting the measured photocurrent since the interdigitated finger structure of the antennas can act as a sort of polarizer and reflect more of the incoming laser light when it is polarized along the finger structure than polarized perpendicular to it. It is important to note that in principle all four

parts of the laser power can change independently. A change in one of the laser arms before superimposing will for instance change either $P_{1,Tx}$ and $P_{1,Rx}$ or $P_{2,Tx}$ and $P_{2,Rx}$. A change of polarization will in contrast affect the laser beat in either the transmitter or receiver path and hence change either $P_{1,Tx}$ and $P_{2,Tx}$ or $P_{1,Rx}$ and $P_{2,Rx}$. Controlling all the parts is complex and elaborate so that it is more efficient to record the laser power at both the transmitter and receiver and correct the measured data after the measurement.

Due to their construction the photomixers can act as photo diodes. As mentioned in chapter 4.1.4, for a biased photomixer the number of carriers and hence the current density in the semiconductor gap of the antenna structure is directly proportional to the laser intensity. By applying a DC voltage and measuring the DC part of the photocurrent it is possible to measure the laser power at the photomixers. At the transmitter, a DC bias is applied by default and hence a DC current is already flowing. The receiver side is typically unbiased. To be able to measure a DC current at the receiver a small bias voltage is applied which adds an offset to the THz photocurrent. In the analysis, this offset is subtracted from the THz photocurrent. Note that there is a small self-induced offset voltage at the receiver due to inhomogeneous illumination and asymmetries in the antenna structure which lead to contact voltages. To get reliable values of the DC photocurrent, the applied bias voltage has to be significantly larger than the default offset [94]. The self-induced offset voltage is different for every photomixer and is typically in the range of ∼10 mV. For the reliable measurement of the DC current a minimum bias of ∼30 mV is required. It is important to note that this bias voltage does not change the linear response of the photomixer [94]. The receiver bias is provided by the transimpedance amplifier (Femto DLPCA-200) which also pre-amplifies the THz photocurrent.

For every frequency point the DC currents at transmitter and receiver, respectively (in the following denoted as I_{Tx} and I_{Rx}), are recorded. These values are used to correct the drifts:

$$E_{\mathrm{THz,Norm}} = E_{\mathrm{THz}} \frac{I_{Tx,0}}{I_{Tx}} \frac{I_{Rx,0}}{I_{Rx}} \tag{4.20}$$

Here $I_{Tx,0}$ and $I_{Rx,0}$ are the mean values of the recorded I_{Tx} and I_{Rx}. In the correction of a measured spectrum we assume the mean values of the DC currents $I_{Tx,0}$ and $I_{Rx,0}$ to be the same in sample and reference measurement since the average laser power does not change.

$$T = \left(\frac{E_{\mathrm{THz,sample}}}{E_{\mathrm{THz,ref}}} \frac{I_{Tx,\mathrm{ref}}}{I_{Tx,\mathrm{sample}}} \frac{I_{Rx,\mathrm{ref}}}{I_{Rx,\mathrm{sample}}} \right)^2 \tag{4.21}$$

It is important to note that the DC currents are proportional to the sum of the laser powers at the transmitter and receiver, respectively,

$$I_{Tx} = R_{Tx} P_{Tx} = R_{Tx}(P_{1,Tx} + P_{2,Tx}) \tag{4.22}$$

$$I_{Rx} = R_{Rx} P_{Rx} = R_{Rx}(P_{1,Rx} + P_{2,Rx}) \tag{4.23}$$

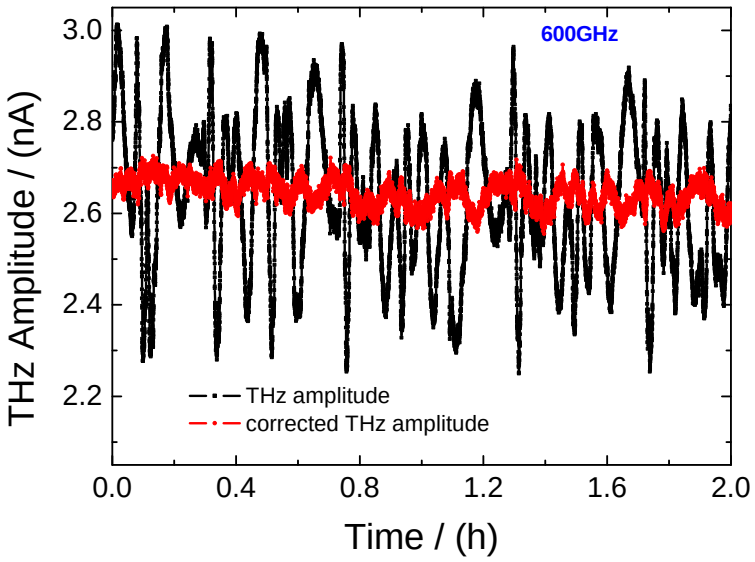

Figure 4.14.: Measurement of the THz amplitude at fixed frequency (600 GHz) as a function of time. Temperature fluctuations of $\pm 1\,^{\circ}\mathrm{C}$ were intentionally induced using the air-conditioning system. The large fluctuations of the THz amplitude are corrected reasonably by the photocurrent correction. Picture taken from [94]

whereas the THz photocurrent is proportional to the product of the laser powers (see equation 4.19). The correction is nonetheless valid as long as both laser powers do not change differently [94]. Figure 4.14 shows the THz amplitude at a constant frequency of 600 GHz as a function of time measured by the fiber-stretcher method. During the measurement, temperature fluctuations of $\pm 1\,^{\circ}\mathrm{C}$ were intentionally induced by the air-conditioning system. The amplitude before applying the photocurrent correction shows fluctuations of $> \pm 10\%$ whereas after the photocurrent correction the fluctuations are only in the order of 3%. To demonstrate the capabilities of the photocurrent correction, several reference measurements were performed in sequence also using the fiber-stretcher method. The amplitude ratios of succeeding measurements were calculated. Changes in the environmental conditions can change the mechanical stress of the fibers and hence the polarization of the laser beat is influenced (see section 4.1.4). Separation of the two fiber arms and rolling up the fibers that guide the laser beat to transmitter and receiver will increase the effect. Due to bending, there is stress on the fibers and thermal expansion of the fibers changes this stress and hence the polarization. Because of the separation, the change will be different in each fiber arm. Two exemplary amplitude ratios before and after the photocurrent correction are depicted in figure 4.15. The measurements were performed such that the frequency was first varied from 60 GHz

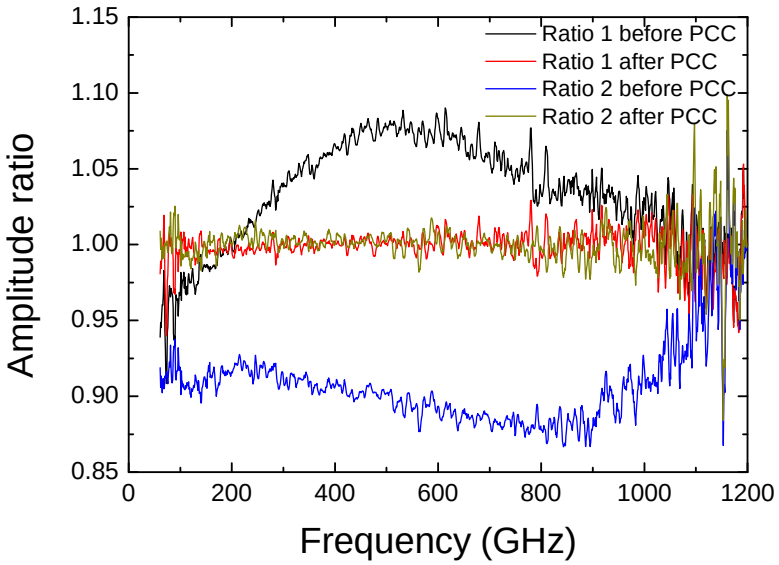

Figure 4.15.: The two amplitude ratios of successive measurements before the photocurrent correction show deviations of 10% from the expected 100% line. After the photocurrent correction the deviations are only in the range of ±2%.

to 1.2 THz and then again back to 60 GHz. Therefore the time difference between the measurements is smallest for high frequencies and despite the large fluctuations this region is closest to the 100% line. The time to measure one spectrum was about 20 minutes, hence the time scale of this measurement is much shorter than the one presented in figure 4.14. Note that for the measurement of the amplitude ratio no temperature variation was induced. Before photocurrent correction, the ratios exhibit a large deviation of up to ±10% from the expected value. After the photocurrent correction, the deviations are only in the range of ±2% demonstrating the high level of performance. However, this is an extreme case to show the capability of the photocurrent correction. In the discussion of the amplitude stability in section 6.4 it is shown that the time-dependent amplitude stability is much higher if the two fiber arms were kept in close vicinity and unnecessary bending of the fibers is avoided.

5. Data Analysis

Depending on which method is used, scanning the frequency while keeping ΔL fixed or modulating ΔL at fixed frequency, different ways to extract amplitude and phase from the measured photocurrent are employed. In this chapter the different methods are discussed concerning their advantages and disadvantages. Furthermore different solutions to obtain the complex optical functions from the transmission and phase data are presented.

5.1. Frequency-scan method

In the frequency-scan method, ν is varied in small steps for a fixed ΔL. As discussed in section 4.1.5 this results in a photocurrent which oscillates as a function of frequency. To obtain transmittance and phase, the sample measurement has to be compared to a reference measurement, i. e. a measurement without sample where the refractive index ($n_{air} \approx 1$) is independent of frequency. Inserting a sample into the THz path leads to two effects. First the amplitude of the THz radiation is di-

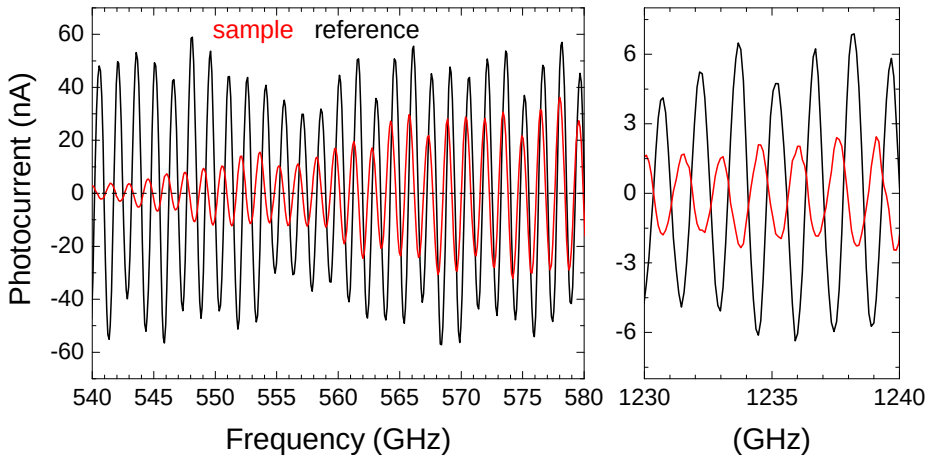

Figure 5.1.: An example of the detected photocurrent with and without sample. The sample investigated here was α-lactose monohydrate. The photocurrent is shown at the first absorption line around 530 GHz and at high frequencies where the amplitude is low.

minished due to absorption within the sample. Secondly the finite refractive index of the sample increases the optical path length in the THz beam path. Hence these two effects lead to a decrease and a shift of the extrema in the photocurrent with respect to the reference measurement. This is shown in figure 5.1 on a sample and reference measurement in the vicinity of an absorption line. The sample used here is α-lactose monohydrate. A detailed discussion of this measurement is given in chapter 10.

For calculating the transmittance the envelopes of sample and reference measurements have to be determined. The transmittance is then calculated by dividing the squared interpolated envelopes:

$$T(\omega) = \left(\frac{I_{ph}^{\text{sample}}(\omega)}{I_{ph}^{\text{ref}}(\omega)} \right)^2 \tag{5.1}$$

The phase information in this case can be obtained from the shift of the extrema and/or zero crossings between sample and reference measurement. In the following this will be explained based on the maxima in the photocurrents. As already mentioned before, maxima in the photocurrent occur if the path difference between the laser beat and the THz beam path is an integer multiple of the wavelength. Comparing the wavelengths λ_s and λ_r of the maxima of the same order m from sample and reference measurement one obtains

$$\frac{\Delta r}{m\lambda_r} = 1 = \frac{\Delta s}{m\lambda_s} \quad , \tag{5.2}$$

where Δr and Δs denote the path-length difference in the reference and sample measurement, respectively. The path-length difference in the sample measurement can be expressed in terms of Δr. Assuming the light passes through the sample only once, a sample with thickness d and refractive index $n(\omega)$ changes the optical path length by $(n(\omega) - n_{air})\, d$. Hence the optical path-length difference in the sample measurement can be described by the sum of the path-length difference of the reference measurement and the change by the sample:

$$\Delta s = \Delta r + (n(\omega) - n_{\text{air}})\, d \tag{5.3}$$

Inserting this equation into equation 5.2 and substituting $\lambda_{r,s} = c/\nu_{r,s}$ one obtains:

$$\Delta r \cdot \nu_r = [\Delta r + (n(\omega) - n_{\text{air}})\, d]\, \nu_s \tag{5.4}$$

$$\Delta r\, (\nu_r - \nu_s)\, /\nu_s = (n(\omega) - n_{\text{air}})\, d \approx \Delta L \tag{5.5}$$

The path-length difference in the reference measurement Δr is related to the spacing between adjacent maxima by $\Delta\nu = c/\Delta L$ (see equation 5.12). With this one finally finds the equation which yields the refractive index n from the maxima of the photocurrent.

$$\left(\frac{\nu_r}{\nu_s} - 1 \right) \frac{c}{\Delta\nu_r} = (n(\omega) - n_{air})\, d \tag{5.6}$$

The phase difference $\Delta\varphi$ of two beams with same wavelength λ corresponds to a relative path-length difference ΔL given by:

$$\frac{\Delta\varphi}{2\pi} = \frac{\Delta L}{\lambda} \qquad \text{with} \quad \Delta L \approx (n(\omega) - n_{\text{air}})\, d \tag{5.7}$$

By combining equations 5.6 and 5.7 one can finally obtain the phase. A detailed description of the numerical analysis is given in the next section.

5.1.1. Analysis based on the frequency-scan method

The amplitudes and positions of the photocurrent extrema as well as the positions of the zero crossings are determined numerically by an inhouse-developed program. Prior to this, data are filtered and corrected as discussed in detail below.

Frequency correction

In section 4.1.2 we showed that the frequency is controlled by measuring the intensity of two interference signals that are shifted by $\pi/2$ with respect to each other. The x-y graph of the two signals only yields a perfect circle if the interference signals show a cosine shape. However, the behavior of the interference signal is described by the Airy function and hence the x-y graph does not have a perfect circle shape. As a result also the angle between two positions on the circle is not a linear function of frequency any more but there are small deviations. This is discussed in detail within the frequency stability in section 6.3. For the correction of these deviations, the reference measurement is used. Assuming a non-dispersive medium n in the beam path, ΔL is independent of frequency. In this case the extrema of the photocurrent are equally spaced in frequency. Any deviation in the spacings can then be referred to as a frequency error. To apply the correction, all the frequencies of the extrema are determined. The data is searched point by point for local maxima or minima. For a maximum it is checked if the amplitude is positive and if the neighboring points are smaller than the actual point. To check for a minimum this method is simply reversed. After a maximum or minimum is found, the peak position is extracted by analytically calculating the parabola that is determined by the three points closest to the extremum. A parabola is a good approximation of a sinusoidal curve in the proximity of the extremum. If the measured data is noisy the position of an extremum can also be determined by fitting a parabola to more points around the extremum. Note that for the frequency correction only the peak position is needed. Alternatively the noisy data can be slightly smoothed with a Savitzky-Golay algorithm to remove spikes. The frequency of the extrema is then plotted as a function of the counting index as shown in figure 5.2 (a). For equally spaced extrema this results in a straight line and any deviation from that is due to frequency errors. To quantify the deviations, a linear fit is made to this data. The deviation between data and fit can be seen in the inset of figure 5.2 (a). Subsequently the straight line

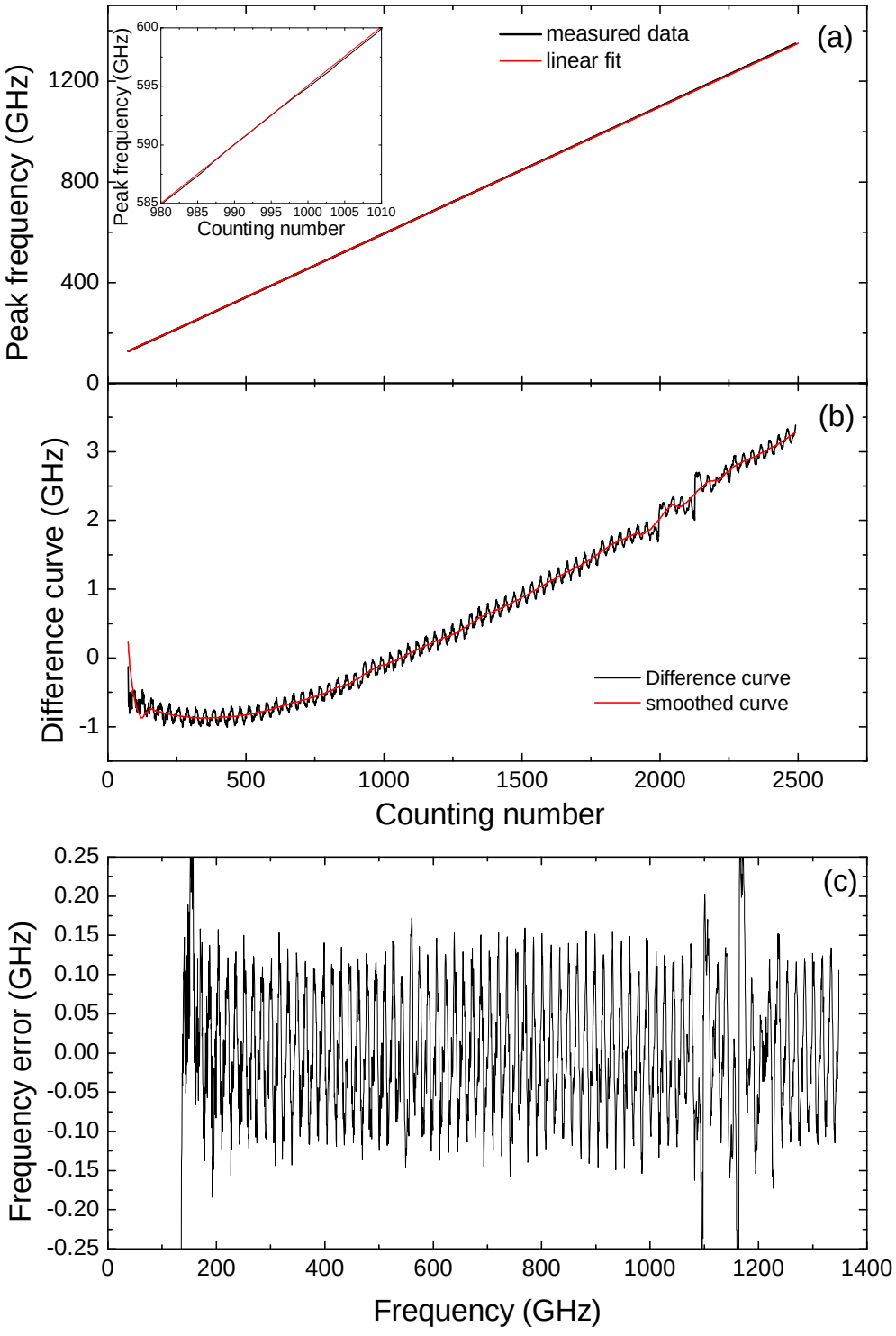

Figure 5.2.: (a) The frequency of the extrema is plotted as a function of the counting index. A linear fit is made and the fitted line is subtracted from the data. (b) The difference curve still contains the influence of the dispersive media in the beam path. To get rid of these effects, the difference curve is strongly smoothed and the smoothed curve subtracted from the difference curve. Away from the water absorption lines, the result shown in (c) is the frequency error due to the iScan.

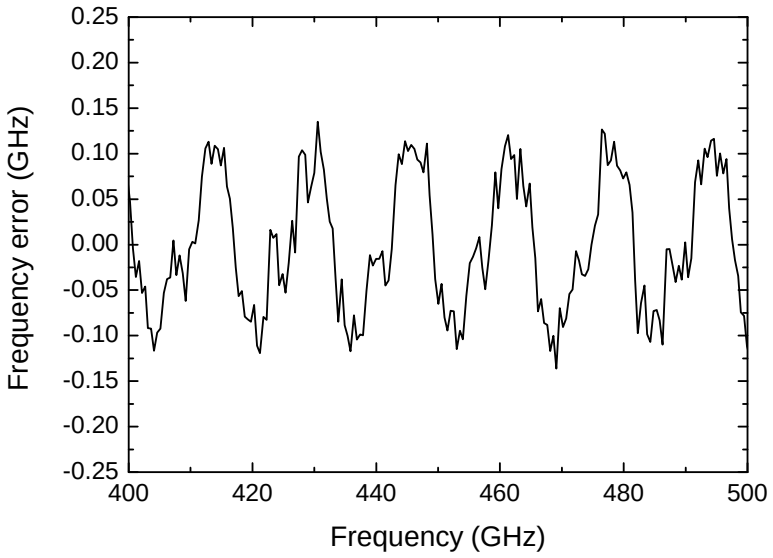

Figure 5.3.: Frequency error in the frequency range between 400 GHz and 500 GHz.

of the fit is subtracted from the data. The difference curve shows an oscillation with a period of 16 GHz which corresponds well with the combined free spectral range of both iScan interferometers (see chapter 6.3). This oscillation mainly is due to the frequency error of the iScans. At e. g. 1100 GHz and 1160 GHz absorption lines of water vapor in L_{THz} are clearly visible. Additionally a nonlinear progression due to the dispersive media in the beam path is present (see figure 5.2 (b)).

Since the Si lenses and the GaAs substrate are part of the optical path, the simple assumption of a non-dispersive medium in the beam path is not valid. Additionally other dispersive optics are usually used to define the parameters of the optical beam. This affects the frequency dependence of the optical path and hence the spacing of the extrema. The nonlinearity induced by the dispersive media is more pronounced than the changes due to the frequency error. Thus, these effects have to be accounted for in the frequency correction.

To get rid of these effects the difference curve is strongly smoothed to obtain the average behavior (red curve in figure 5.2 (b)). This curve is subtracted from the difference curve. The result mainly gives the frequency error of the iScans, see figure 5.2 (c). In a last step the frequency error is plotted as a function of frequency by replacing the counting index by the corresponding peak frequency. Figure 5.3 shows the frequency error in range between 400 GHz and 500 GHz where the period of 16 GHz can be clearly observed. The amplitude of the oscillation is smaller than 200 MHz. This is a systematic error of the iScans. A statistical error due to temporal fluctuations does contribute additionally and will be discussed in section 6.5. The frequency axis finally is corrected by means of the obtained deviations. Note that

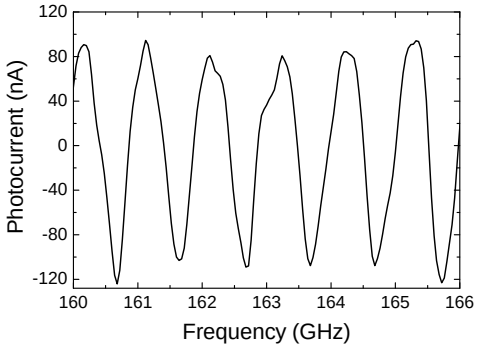

Figure 5.4: Photocurrent of a reference measurement ($n = \text{const.}$) at low frequencies for a constant ΔL. Deviations from the sinusoidal shape are due to standing waves in the beam path.

the frequency axis of the sample measurement is also corrected using the frequency error obtained from the reference measurement since the error originates from the iScan only and is reproducible for every frequency sweep.

Evaluation of extrema and zero crossings

With the frequency axis corrected as described above, the extrema and the zero crossings of the photocurrent are determined. Note that for the frequency correction only the frequency of the extrema is important. For the calculation of the transmittance it is crucial to determine both frequency and amplitude with sufficient precision. In the ideal case the photocurrent has a sinusoidal form as a function of ν for a fixed path-length difference ΔL and the best result should be obtained by fitting a cosine function to the extrema. Concerning the materials used for THz optics, the absorption decreases with increasing wavelength, thus pronounced standing waves are formed in the beam path at low frequencies. These standing waves affect the frequency dependence of the photocurrent curve since the amplitude is influenced by the interference due to multiple reflections. Because of the large wavelength, the perturbation of the sinusoidal shape is especially pronounced at low frequencies (below 200 GHz). An example of the photocurrent of a reference measurement at low frequencies is shown in figure 5.4. Because of the perturbation of the sinusoidal behavior, the determination of the peak frequency and amplitude is again restricted to a few points around the maximum as described in section 5.1.1. Figure 5.5 shows an example of the obtained parabolas. Both frequencies and amplitudes of the photocurrent extrema are determined very well by the parabolas. The photocurrent and the determined envelope are shown in figure 5.6. The envelope precisely matches the calculated extrema.

In addition to the extrema, the zero crossings of the THz photocurrent are also obtained. Data points between which a change in sign takes place are searched and the zero-crossing frequency is determined by linear interpolation between these points. For noisy data there might be more than one change in sign at a particular zero crossing. To account for that, the distance between adjacent zero-crossings is

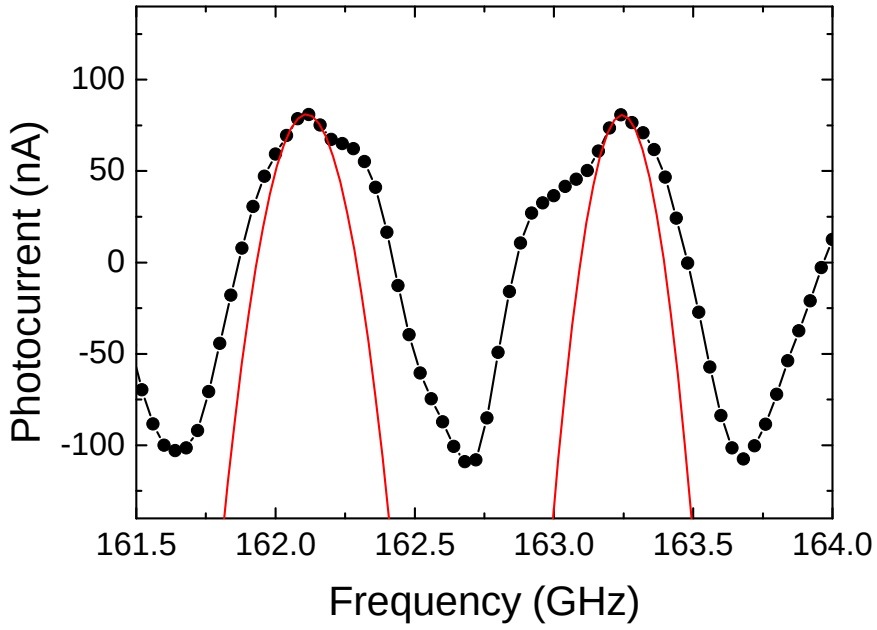

Figure 5.5.: Segment of the photocurrent together with the parabolas calculated for the maxima determination.

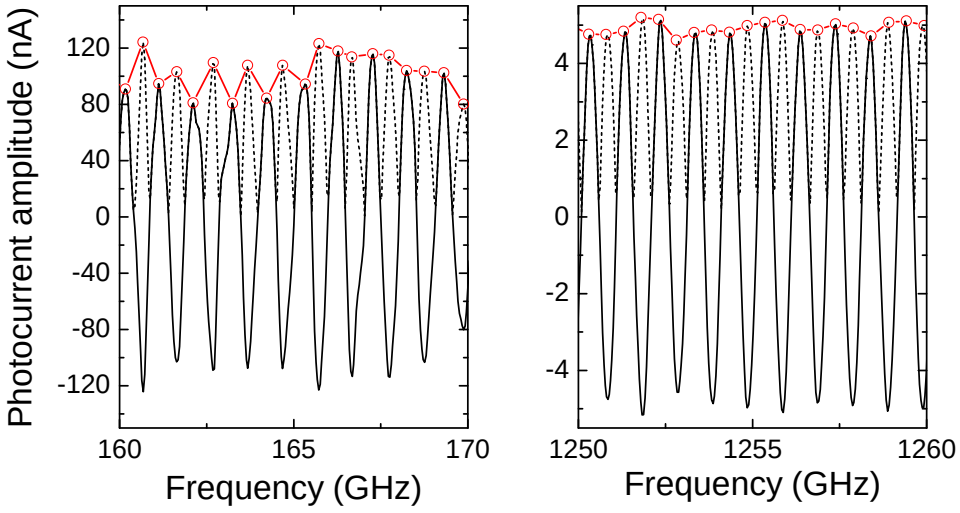

Figure 5.6.: The calculated extrema frequencies (red curve) agree very well with the absolute value of I_{ph} (black curve). Dotted line: $|I_{ph}|$.

compared to the period of the photocurrent. If it is smaller than a certain limit, all the zero crossing points found in this limit are averaged and then a straight line is fitted to points in a certain vicinity of this average. The actual zero crossing is extracted from the linear fit.

Calculating transmittance and refractive index

The transmittance is calculated from the ratio of the squared envelopes defined by the extracted extrema points of sample and reference as given in equation 5.1. Due to the phase shift induced by the sample, the extrema of sample and reference measurement are shifted in frequency with respect to each other. For a point-by-point division of both data sets, one of the curves has to be interpolated. Usually the reference measurement is interpolated since it comprises less spectral features. However, this will introduce errors because it does not reproduce the correct behavior but just assumes a polynomial between two points (see discussion of the analysis based on the fiber-stretcher method in section 5.2).

The refractive index can either be obtained from the shift in the zero crossings or from the shift in the extrema using equation 5.6. In the following we will just talk about the extrema but the same is also valid for the zero crossings. The first step is to compare the corresponding extrema of sample and reference measurement. Since the photocurrent data does not start at zero frequency, the order of the peaks has to be estimated. The frequencies of peaks of the same order m are generally different for sample and reference measurement. This also introduces a small error in the analysis. In equation 5.3 the path-length difference Δs in the sample measurement is expressed in terms of the path-length difference Δr in the reference measurement which is only correct if both are taken at the same frequency. This is usually not the case. Due to the Si lenses, Δr is also not independent of frequency. To minimize the uncertainty originating from the frequency dependence of the path-length difference, it is preferable to compare the frequency $\nu_{s,m}$ of the extremum of the sample measurement which has the order m to that extremum frequency $\nu_{r,q}$ of reference measurement of the order q which is the closest in frequency. As compensation for the wrong order, multiples of the photocurrent period $\Delta\nu_r$ are added to the frequency of the reference photocurrent extremum.

$$\left(\frac{\nu_{r,q} + |m-q| \cdot \Delta\nu_r}{\nu_{s,m}} - 1\right) \frac{c}{\Delta\nu_r} = (n(\omega) - n_{air})\, d \tag{5.8}$$

5.1.2. Effective resolution

The effective resolution in this method is determined by the distance $\Delta\nu$ between two adjacent extrema because only at these points the amplitude can be read off. The distance between two maxima is determined by the difference in the optical path length ΔL. The photocurrent at a frequency ν_1 is maximum if the path difference

between the laser beat and the THz beam is an integer multiple of the wavelength λ,

$$\Delta\varphi = n \cdot 2\pi = 2\pi \frac{\Delta L}{c} \nu_1 \quad . \tag{5.9}$$

At the next higher frequency where a maximum occurs, the relative phase is

$$\Delta\varphi = (n+1) \cdot 2\pi = 2\pi \frac{\Delta L}{c} \nu_2 \tag{5.10}$$

From equations 5.9 and 5.10, the spacing between two adjacent maxima is given as

$$(n+1) - n = \frac{\Delta L}{c} (\underbrace{\nu_2 - \nu_1}_{\Delta\nu}) \tag{5.11}$$

$$\Rightarrow \Delta\nu = \frac{c}{\Delta L} \tag{5.12}$$

However, the actual resolution, i. e. the frequency steps, have to be small enough to resolve the photocurrent period. In this work a photocurrent period of about 1.5 GHz is applied. Since transmittance and phase are obtained from the extrema, the resolution is ~ 1.5 GHz$/2 = 750$ MHz. When using the extrema as well as the zero crossings, the resolution for the phase data is ~ 1.5 GHz$/4 = 375$ MHz. For these measurements a frequency step size $\Delta\nu = 50$ MHz was used. With a lock-in integration time of about 300 ms per frequency point, sweeping the whole frequency range takes several hours which makes this method very time consuming.

5.1.3. Long-time performance

To keep the time difference between the sample and reference measurement short, the measured frequency range is split into smaller parts. For the purpose of testing, first a small frequency range of 20 GHz was chosen. Several reference measurements were performed where a single measurement took about three minutes. Each measurement with odd number was divided by the subsequent even-numbered measurement so that every measured photocurrent was used only for one ratio. The results are shown in the inset of figure 5.7. Except for some spikes, the deviations are smaller than $\pm$ 2% from the 100% line. By averaging the amplitude ratios, the 100% line can be reproduced very well. As a quantitative value, the sum of the squared residuals S was calculated as a function of the number of averaged curves,

$$S = \frac{1}{N} \sum_{i=1\ldots N} (y_0 - y_i)^2 \qquad \text{with} \quad y_0 = 1 \quad . \tag{5.13}$$

The function S decreases with increasing number of averaged spectra, as shown in figure 5.7. After an average of about 25 spectra the deviations from the 100% line are less than 1% (see orange line in the inset of figure 5.7).

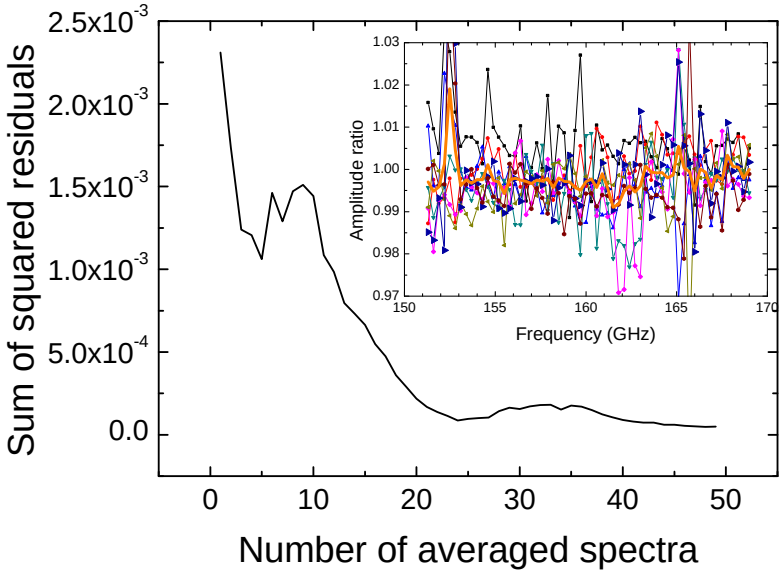

Figure 5.7.: The sum of squared residuals decreases with increasing number of averaged spectra. The inset shows 8 exemplary ratios. Except the spikes the deviation from the 100% line is in the order of 2%. The quality of the result is significantly increased by averaging. The average is shown as a thick orange line.

The above considerations show that the quality of a measured spectrum can be significantly increased by measuring short frequency ranges and averaging over several spectra. Nevertheless, the whole advantage of broadband spectroscopy is lost by doing so. Changing between sample and reference more often also introduces other instabilities. Performing a complete measurement becomes more time consuming as different frequency ranges have to be measured several times with a certain overlap to the next range. Therefore a compromise between data quality and measurement time has to be found. A frequency range of 20 GHz is too small for standard use. Therefore the frequency range per measured spectrum was increased to 135 GHz. Again several reference measurements were performed and the amplitude ratios calculated as described above. Figure 5.8 shows the sum of the squared residuals as a function of the number of averaged spectra. As can be seen, S decreases fast with increasing number of averaged spectra and an average over five spectra shows a very good result. For $N = 5$ the values of S obtained for the frequency ranges of 20 GHz and 135 GHz, respectively, are in the same order of magnitude. The different averages obtained are shown in the inset of figure 5.8. For the average of only two spectra the deviation from the 100% line is in the order of 4%. With increasing number, the spectrum approaches more and more the 100% line. By averaging over 5 spectra, the deviation from the 100% line is reduced to about 0.5%.

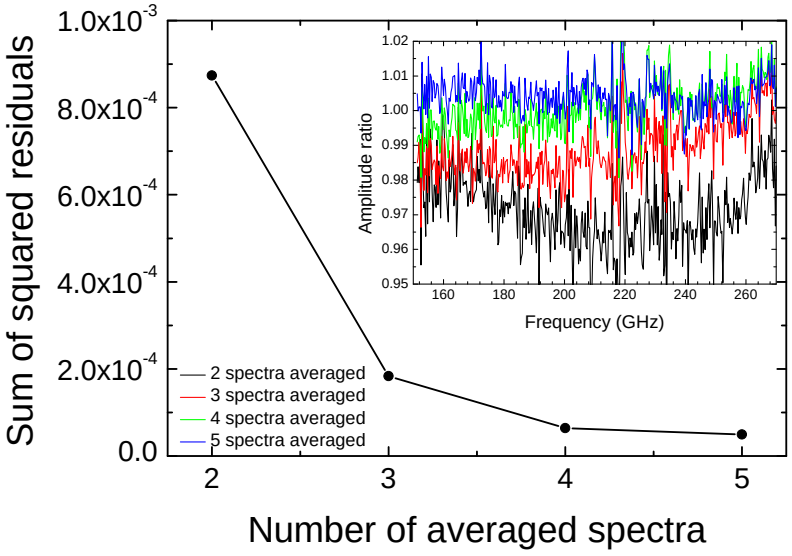

Figure 5.8.: The sum of the squared residuals decreases with increasing number of averaged spectra. The inset shows the corresponding spectra that belong to different number of averages. With increasing number, the spectrum approaches more and more the 100% line.

Measurements on α-lactose monohydrate employing this procedure were performed. The frequency range of 135 GHz was used for each frequency sweep. Between adjacent frequency ranges an overlap of 30 GHz was considered. For each frequency range, six spectra were measured by alternately switching between sample and reference. Considering the 15 minutes per frequency sweep, two frequency ranges per day could be measured. Measuring the full spectral range of 1800 GHz takes more than one week. Figure 5.9 shows the overlap regions of two different frequency ranges. The range from 140 GHz to 175 GHz and from 340 GHz to 370 GHz are shown in figure 5.9 (a) and (b), respectively. It is important to note that the two overlapping spectra were measured with a 24 hour gap between them. Despite that, the agreement between the averaged spectra is very good. Even the features of the fine structure in the spectra caused by standing waves and the emission characteristic of the photomixers are reproduced. The ratio of the overlapping spectra is plotted in figures 5.9 (c) and 5.9 (d), respectively. On average the ratios are unity. The large noise is due to errors induced by interpolation between the extrema (see section 5.1.1).

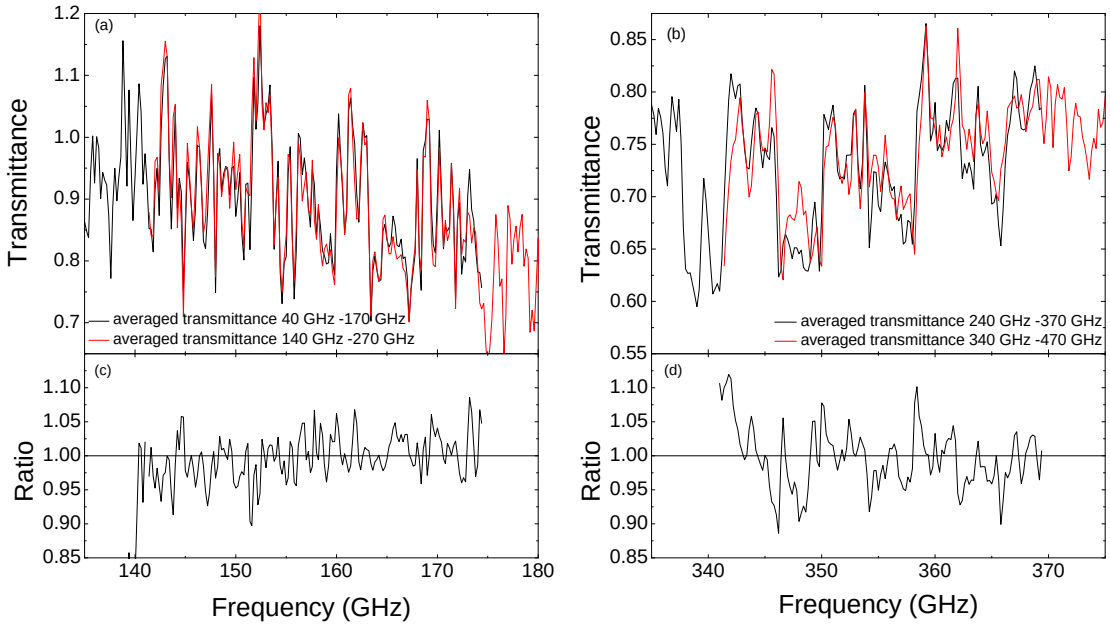

Figure 5.9.: Overlap of two averaged transmission spectra measured on α-lactose monohydrate at two different frequency ranges. In (a) between 140 GHz and 175 GHz and in (b) between 340 GHz and 370 GHz. The overlapping spectra were measured with a 24 hour gap. Also the fine structure of transmittance is reproduced well especially in the low-frequency part.

5.2. Fiber-stretcher method

In the fiber-stretcher method[1], ΔL is varied for a constant frequency as explained in section 4.1.6. Via the change of ΔL and hence the phase $\Delta\varphi$ at the detector, a sinusoidal photocurrent is recorded as function of stretcher length or voltage. An example for the recorded data at 600 GHz is shown in figure 5.10. Amplitude and phase are extracted by fitting a cosine function (red line). Note that the frequency is given as a known parameter to the fit.

The advantage of this method is that amplitude and phase can be determined at every frequency. This enables to measure amplitude and phase of sample and reference at the same frequencies. Thus, an interpolation between adjacent data points like for the frequency-scan method is not needed (see 5.1). This is especially important at low frequencies where standing waves are pronounced and the interpolation causes mistakes as shown in figure 5.11. Here, the frequency-scan method and the measurement with fiber stretcher are compared. The frequency steps in both measurements are 30 MHz. The amplitude determined with the fiber stretcher coincides

[1]The concept of this method was developed and implemented by Axel Roggenbuck within the scope of his PhD thesis (see reference [94])

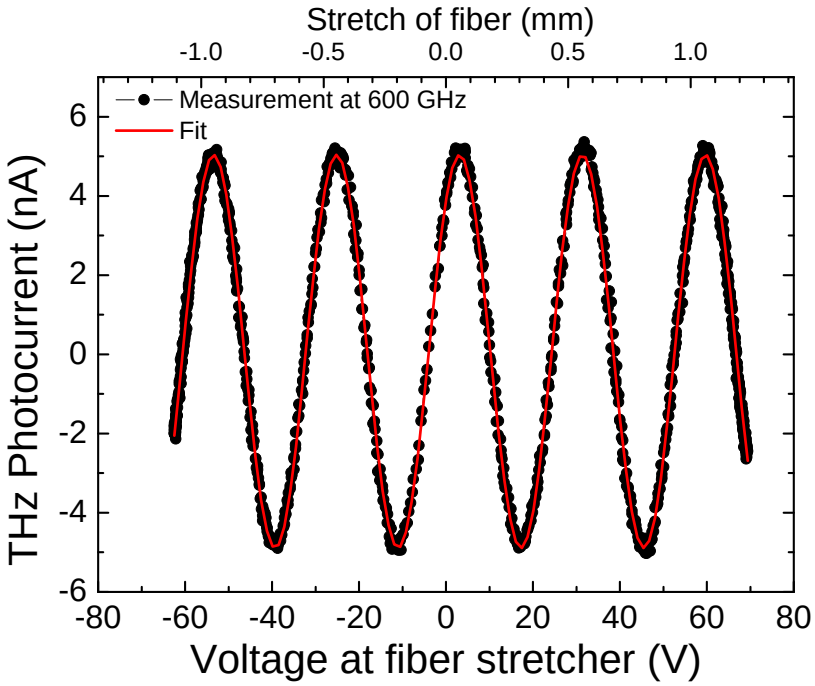

Figure 5.10.: The THz photocurrent amplitude as a function of stretcher voltage (bottom x axis) and stretcher length (top x axis). A sinusoidal fit is shown in red.

with the maxima of the photocurrent for higher frequencies. At low frequencies it can be clearly seen that the behavior of the envelope is not smooth as for high frequencies due to the pronounced standing waves. Here, the fiber-stretcher method improves the accuracy of the determined transmittance due to the fact that interpolation is not needed. Additionally it can be seen that the maxima of the oscillating photocurrent coincide with $\Delta\varphi = 0$ determined by the fiber-stretcher measurement. This shows that the phase can be measured precisely with both methods, but in the frequency-scan method the phase can only be determined where it is a multiple of 2π, π or $\pi/2$.

5.2.1. Effective resolution

The effective resolution is determined by the frequency-step size, i. e. the spacing between adjacent frequency points. This can in principle be chosen arbitrarily in the Toptica Teracontrol software. Note that the smallest reasonable value of $\Delta\nu$ is determined by the laser stability as discussed in chapter 4.1.1. However, since the excitations investigated in solid-state spectroscopy typically have linewidths in the order of some tenth of GHz, the small frequency-step size of 50 MHz used in the frequency-scan method to resolve the oscillating photocurrent is not needed. Therefore, in the fiber-stretcher method a larger frequency-step size is chosen. By

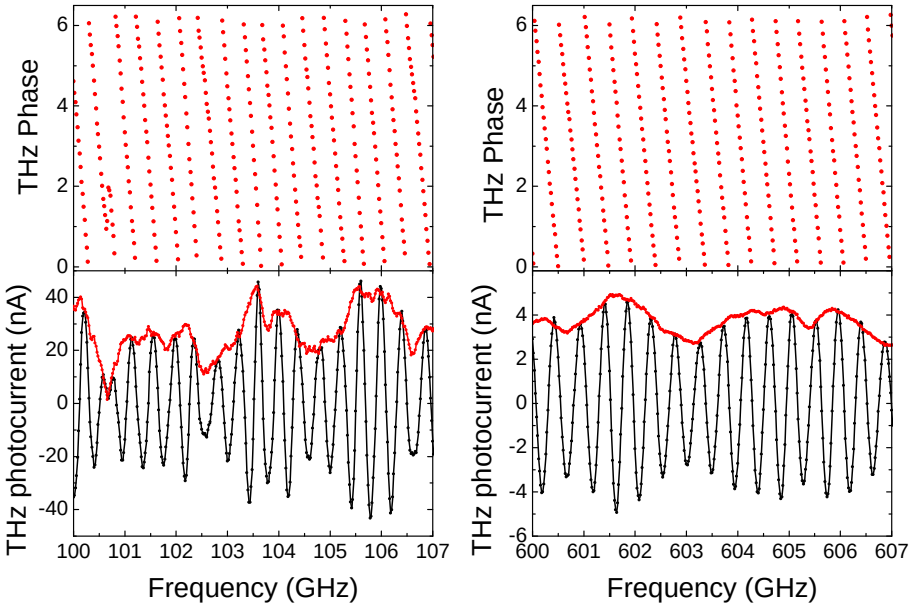

Figure 5.11.: The lower panels show a comparison between the photocurrent of a reference measurement with (red) and without fiber stretcher (black), respectively, for two different frequency ranges. In the upper panels the phase data obtained with the fiber-stretcher method is shown. The maxima of the oscillating photocurrent coincide very well with the minima of the phase measured with the fiber-stretcher method. Figure taken from [94]. See also reference [95]

increasing $\Delta\nu$ the time to perform a frequency scan is decreased. With $\Delta\nu = 1$ GHz one frequency sweep takes about ten minutes. Thus, as an additional advantage, the time between sample and reference measurement is kept short.

5.3. Improvement of the phase accuracy by implementing a third laser

As described in section 4.1.7, the DC current of the photomixers is recorded to correct fluctuations of the laser power and hence the measured amplitude. In section 6.5.1 it is discussed that the precision of L_{eff} is about 20 μm since even small fluctuations in the environmental conditions have a significant influence on ΔL as shown in section 6.5. Although this uncertainty may sound small, it is still relatively large for an accurate phase determination. To increase the precision it would be important to also have the possibility to record and correct for fluctuations of the phase. The

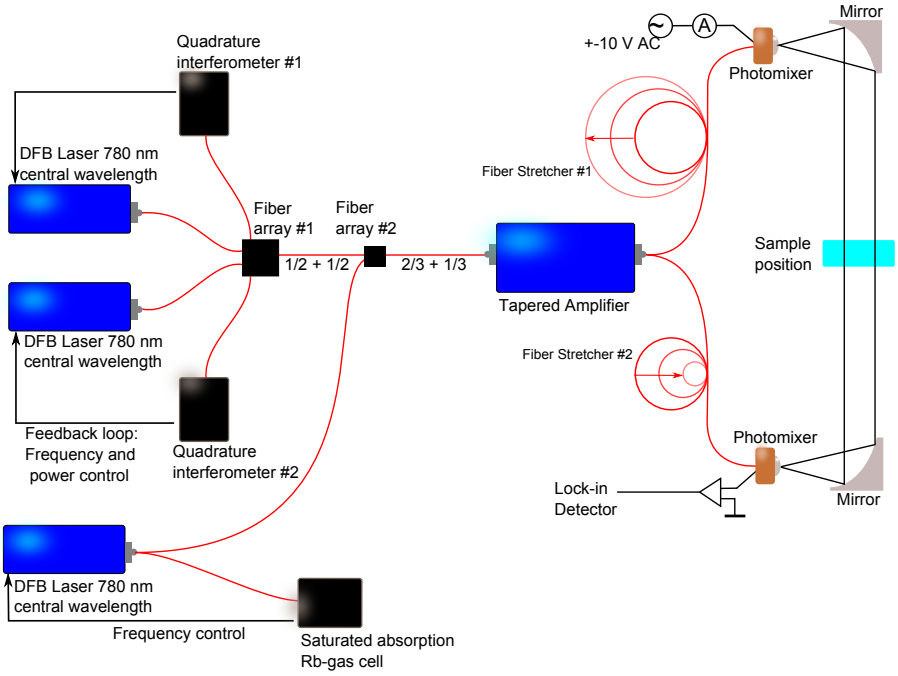

Figure 5.12.: Schematic drawing of the setup with three lasers. The third laser is locked to a Doppler-free Rb absorption line and superimposed with the beat of the other two laser at the ratio of 1/3 to 2/3.

idea for a new method for the correction of phase fluctuations has been developed by Markus Grüninger, Joachim Hemberger, and Axel Roggenbuck at the University of Cologne [104]. This method is presented in detail in the following section.

5.3.1. Concept

For this correction a reference phase value $\Delta\varphi_{\mathrm{ref}}$ is needed that records the phase drift due to changes in ΔL induced by fluctuations of the environmental conditions. To achieve this goal, a third laser is added to the setup (see figure 5.12)[2]. Three lasers generate three different beat frequencies. Two lasers are kept at a constant frequency while the third laser is tuned, resulting in one constant beat frequency ω_{ref}, provided the laser frequencies are not drifting, and two tunable beat frequencies ω_{tb1} and ω_{tb2}. If ω_{ref} is constant also the corresponding phase $\Delta\varphi_{\mathrm{ref}}$ should be constant. However, due to fluctuations of ΔL, $\Delta\varphi_{\mathrm{ref}}$ changes. In the experiment $\Delta\varphi_{\mathrm{ref}}$ is recorded together with $\Delta\varphi_{\mathrm{tb1}}$ and $\Delta\varphi_{\mathrm{tb2}}$. Relative phase fluctuations can then be read off from $\Delta\varphi_{\mathrm{ref}}$ and used to correct $\Delta\varphi_{\mathrm{tb1}}$ and $\Delta\varphi_{\mathrm{tb2}}$. For the correction the time-dependent drift of $\Delta\varphi_{\mathrm{ref}}$ from a constant reference value is calculated. Since only relative fluctuations can be corrected, this reference value can be chosen arbitrarily.

[2]The third laser was implemented and first measurements on MgO and Si were performed in collaboration with Ernesto Vidal (see [105]).

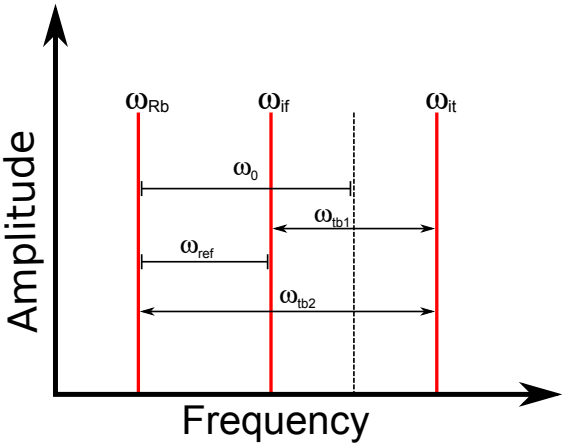

Figure 5.13: Assignment of the three beat frequencies with respect to the different lasers. The dotted line denotes the initial position of laser 1 and laser 2 where both have the same frequency

For instance the first value or the average of the time-dependent $\Delta\varphi_{\mathrm{ref}}$ can be chosen. Since the time-dependent change of ΔL is the same for all frequencies, the time-dependent variation of $\Delta\varphi_{\mathrm{ref}}$ can be used to correct $\Delta\varphi_{\mathrm{tb1}}$ and $\Delta\varphi_{\mathrm{tb2}}$. Note that the correction is performed on the values of ΔL calculated from the phases. In the actual measurement also drifts of the beat frequencies arise due to the finite stability of the lasers. These drifts also influence the phase as discussed in the context of the coherent detection (see section 4.1.5). However, the correction is still valid if all lasers drift the same way.

To implement the correction for phase drifts, a diode laser locked to a Doppler-free Rb absorption line was installed as third laser. Rubidium is particularly suited since it has very sharp absorption lines around 780 nm which is the center frequency of the used diode lasers. The $5S_{1/2} - 5P_{3/2}$ transition used here has a vacuum wavelength of 780.241 nm and a Doppler-free linewidth of about 6 MHz [106, 107]. The frequency stability of ω_{Rb} is in the range of 1 MHz. The Doppler-free line shape is achieved by a saturated absorption scheme [108]. Here a tunable laser is divided into two parts, a strong pump beam and a weak probe beam, that are guided through the gas with nearly opposite directions. Because of the Doppler effect atoms with different velocities will absorb different wavelengths. Only for static atoms both rays are absorbed in the same way. Since the pump beam has a much higher intensity than the probe beam, almost all states are excited so that the weaker probe beam is nearly not absorbed. The Doppler-free linewidth appears then as a dip in the absorption spectrum of the weak ray. The frequency ω_{Rb} is stabilized to this dip in the absorption spectrum. More information on the exact locking procedure is discussed in [105].

The second stable laser is provided by one of the iScan-controlled lasers. The frequency of the stabilized laser is in the following denoted as ω_{if} and the one of the tuned laser as ω_{it}. To set the stable beat frequency $\omega_{\mathrm{ref}} = \omega_{\mathrm{if}} - \omega_{\mathrm{Rb}}$ to a desired value, first the difference frequency $\omega_{\mathrm{tb1}} = \omega_{\mathrm{if}} - \omega_{\mathrm{it}}$ is adjusted to a certain THz frequency using the Toptica Teracontrol. Note that both ω_{if} and ω_{it} are tuned by the same

frequency steps but with opposite sign as discussed in section 4.1.1. Initially only the difference frequency ω_{tb1} is known. Still the beat frequency ω_{ref} of the two stable lasers can be determined with the help of ω_{tb1} as will be described in detail in section 5.3.2. The frequency ω_{if} is then stabilized by fixing the control parameters of the iScan, i.e. temperature and current, to the actual values while they are doubled for ω_{it} to compensate for the non-tuning laser. In short, the value of ω_{ref} depends on the choice of ω_{if} which is set by choosing a starting value of $\omega_{\mathrm{tb1}} = \omega_{\mathrm{it}} - \omega_{\mathrm{if}}$ as described above. Note that the second tunable beat frequency is $\omega_{\mathrm{tb2}} = \omega_{\mathrm{it}} - \omega_{\mathrm{Rb}}$ as schematically shown in figure 5.13.

It is preferable that the output powers of all three lasers are the same. Different output powers would lead to a finite non-modulated intensity. This non-modulated intensity will generate a DC current in the photomixer, i.e. a heating of the photomixer. This decreases the highest possible output power since not all of the laser power is converted into THz power. The loss of THz power due to the non-modulated laser intensity cannot be compensated for by increasing the laser power since the photomixers can be damaged when the heating is too much. Assuming all laser powers to be the same ($P_1 = P_2 = P_3 = P_0$), a 1/3 - 2/3 fiber array is the ideal choice to generate three beat frequencies with equal powers (see figure 5.12). The frequencies ω_{if} and ω_{it} are first superimposed by a 1/2 - 1/2 fiber array so that the power at the output of this fiber array is $1/2P_{\mathrm{if}} + 1/2P_{\mathrm{it}}$. Introducing the third laser after that with the ratio of 1/3 to 2/3 will ensure that all lasers have the same power.

$$\begin{aligned} P_{\mathrm{tb1}} &= \frac{1}{2} \cdot \frac{2}{3} P_0 = \frac{1}{3} P_0 \\ P_{\mathrm{tb2}} &= \frac{1}{2} \cdot \frac{2}{3} P_0 = \frac{1}{3} P_0 \\ P_{\mathrm{ref}} &= 1 \cdot \frac{1}{3} P_0 = \frac{1}{3} P_0 \end{aligned}$$

In reality the different lasers have different output powers. In fact the output power P_{Rb} is about 38 mW which is nearly twice as large as the output power of the other lasers (about 23 mW). Adjustment of these powers via the current of the laser diode is not trivial since on the one hand the iScans and especially the Rb-gas cell need a certain minimum power to operate and on the other hand the laser diodes can only handle a certain maximum current which is different for each diode. The laser power of ω_{it} and ω_{if} could not be increased since they are already operating near the maximum diode pump current. The powers of the different beat signals have to be considered. Calculating the superposition of three frequencies where two frequencies have amplitude A_0 and the third frequency has amplitude B_0, the powers of the beat signals are proportional to A_0^2 for the beat between the frequencies with

same amplitude and A_0B_0 for the other two.

$$\begin{aligned} I &\propto (A_0\cos(\omega_{\mathrm{it}}t+\Delta\varphi_{\mathrm{it}})+A_0\cos(\omega_{\mathrm{if}}t+\Delta\varphi_{\mathrm{if}})+B_0\cos(\omega_{\mathrm{Rb}}t+\Delta\varphi_{\mathrm{Rb}}))^2 \\ &\propto A_0^2\cos(\omega_{\mathrm{tb1}}t+\Delta\varphi_{\mathrm{tb1}})+A_0B_0\cos(\omega_{\mathrm{tb2}}t+\Delta\varphi_{\mathrm{tb2}})+ \\ &\quad +A_0B_0\cos(\omega_{\mathrm{ref}}t+\Delta\varphi_{\mathrm{ref}}) \end{aligned} \tag{5.14}$$

Equation 5.14 is derived analogous to the case of two lasers described in section 4.1.4.

In our case, the amplitude A_0 is proportional to $\sqrt{23\ \mathrm{mW}}$ and B_0 to $\sqrt{38\ \mathrm{mW}}$. For the power of the beat signals behind the fiber arrays this results in $A^2 \sim (1/2 \cdot 2/3 \cdot A_0^2) \sim 7.7$ mW and $AB \sim (1/2 \cdot 2/3 \cdot A_0^2)^{\frac{1}{2}} \cdot (1/3 \cdot B_0^2)^{\frac{1}{2}} \sim 9.9$ mW. In the three-laser setup, the total laser power at the photomixer is about the same as for the two-laser setup. Since the single laser powers are not equal, now a certain amount of power is transformed into Joule heat.

5.3.2. Extraction of information

When using two lasers, only one beat frequency is present and amplitude and phase can be extracted relatively easy from a sinusoidal fit since the beat frequency is known. Adding a third laser increases the number of parameters, namely three amplitudes and three phases have to be determined. As already mentioned, not all beat frequencies are known. Since only ω_{tb1} and not ω_{it} and ω_{if} are known, ω_{tb2} and ω_{ref} have to be determined. Nevertheless, ω_{tb2} and ω_{ref} are related via ω_{tb1} by $\omega_{\mathrm{tb2}} = \omega_{\mathrm{ref}} - \omega_{\mathrm{tb1}}$, so that in principle only one frequency has to be determined.

Numerical simulations

With three lasers, the data measured with the fiber stretcher, i. e. the intensity as a function of path-length difference is a superposition of three sinusoidal curves. Due to the different laser powers and the frequency-dependent efficiency of the photomixers, the amplitudes of the different beat signals can exhibit large differences. Therefore a numerical test was performed for the reliable extraction of the six parameters in case of large amplitude differences. For this purpose a superposition of three sinus functions was calculated and provided with white noise. This curve was subsequently fitted with a superposition of three sinus functions by a Levenberg-Marquardt algorithm and the extracted parameters were compared to the initial ones. Note that the frequencies were not fit parameters in this simulation. The amplitude-frequency relation as well as the fitted range was chosen in agreement with the experimental conditions[3]. Two different scenarios were simulated, namely two equally large and one small amplitude as well as three different amplitudes [105]. The noise level was set to 0.1 a. u. which was chosen to test the limits of the fit. In figure 5.14, the differences between the set values and the extracted amplitudes and

[3]The simulations were performed in the scope of the master thesis of Ernest Vidal

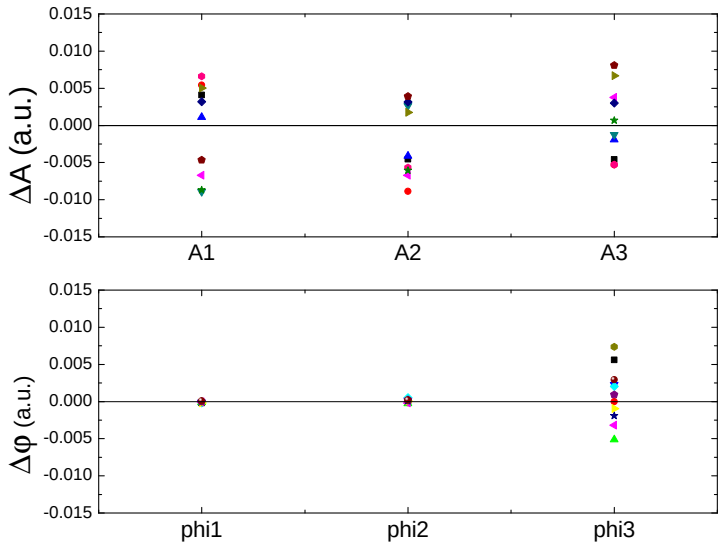

Figure 5.14.: Difference between set and extracted values of amplitude and phase. The data was simulated and fitted ten times in a row (different symbols) to have a measure of the precision of the fit. Deviations between set and extracted values and between the different fits are very small, hence the fit is a reliable and precise method to extract amplitude and phase data. The set values are $A_1 = 50$ a. u., $A_2 = 20$ a. u., and $A_3 = 1$ a. u. and $\varphi_1 = 0$, $\varphi_2 = \pi/2$, and $\varphi_3 = \pi$ and the white noise is $\delta A = 0.1$ a. u..

phases for the case of three different amplitudes are shown. The frequencies of the simulated curve were 100 GHz, 500 GHz, and 800 GHz. The according amplitudes and phases were chosen to be $A_1 = 50$ a. u., $A_2 = 20$ a. u., and $A_3 = 1$ a. u. and $\varphi_1 = 0$, $\varphi_2 = \pi/2$, and $\varphi_3 = \pi$. To look into more detail the curve was simulated and fitted ten times in a row (every time the white noise changes) to extract the uncertainty of the fit. The differences between the fit results and the set values are one order of magnitude smaller than the provided white noise although the uncertainty in the phase data increases with decreasing amplitude. Thus the fit scheme shows very good performance in the case of three different frequencies. A disadvantage of this method is that the start parameters for the fit have to be somewhat close to the actual values. However, if small frequency steps are used in a measurement, the fit results of a frequency i can be given as start parameters to the frequency $i+1$. The method of multi-linear regression to analyze the simulated data was tested [105]. The precision of both methods is comparable. However, the multi-linear regression has the disadvantage that all three frequencies have to be known, and therefore it was not employed for the analysis [105].

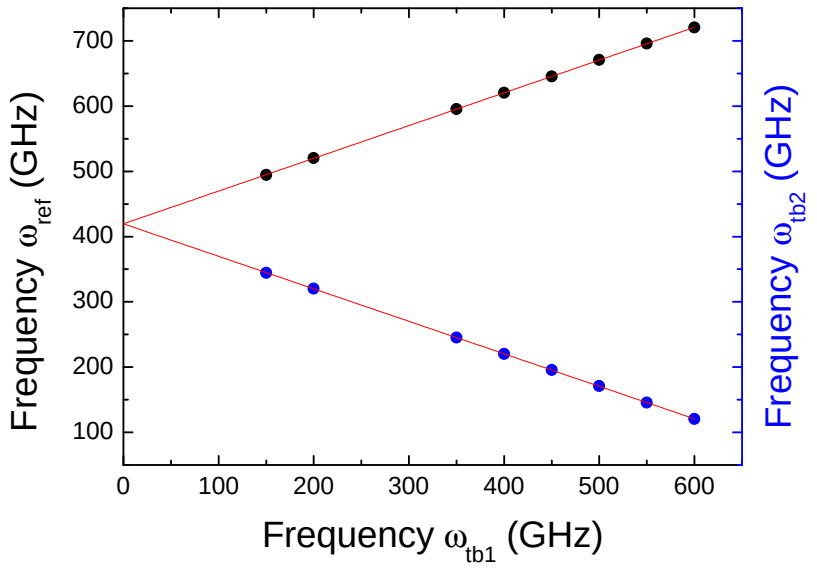

Figure 5.15.: Both ω_{tb2} and ω_{ref} are plotted as a function of ω_{tb1}. The y intercept of these curves defines the frequency offset between ω_{ref} and the initial position of ω_{tb1} and ω_{tb2}.

Realization of data extraction

For the analysis of a measurement, the intensity data as a function of fiber stretch is directly exported. This curve will in the following be termed interferogram because of the similarities to Fourier spectroscopy. To extract amplitude and phase as precisely as possible it is inevitable to give the frequencies as known parameters to the fit. An uncertainty in frequency automatically results in an uncertainty in all the other parameters, i. e. amplitude and phase. Fitting the frequencies for every interferogram leads to different uncertainties in every fit. Therefore, the three beat frequencies were included as fixed parameters in the fit. Consequently the uncertainty in amplitude an phase induced by the uncertainty in the frequencies is a systematical error.

To include the frequencies as known parameters to the fit, the beat frequencies ω_{ref} and ω_{tb2} have to be determined. This was done the following way: Both iScan-controlled lasers were operated in the normal mode, i. e. the frequency of both lasers is tuned in the same way but in different directions. For each set frequency of ω_{ref} determined by ω_{tb1} the interferograms were collected over half an hour. Besides the amplitudes and phases also ω_{tb2} was fitted. Note that ω_{tb1} is known and hence given as fixed parameter to the fit and ω_{ref} is determined by $\omega_{\mathrm{tb2}} - \omega_{\mathrm{tb1}}$. The extracted frequencies ω_{ref} and ω_{tb2} were averaged for every set of frequencies. Both ω_{ref} and ω_{tb2} were then plotted as a function of ω_{tb1} and fitted by a straight line. For the

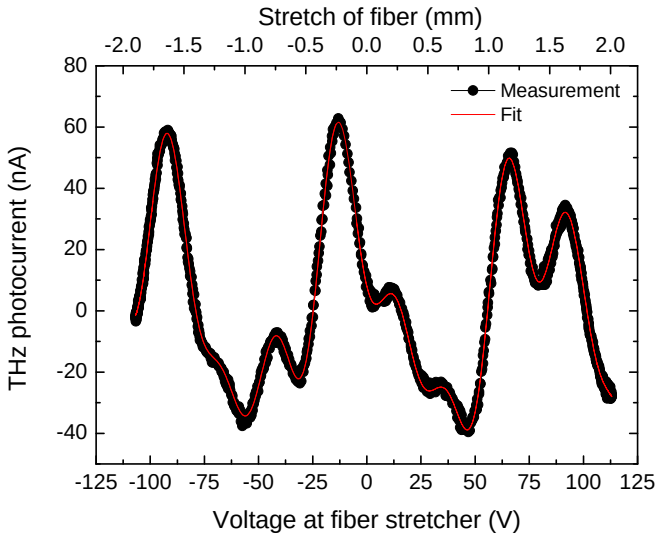

Figure 5.16.: THz photocurrent as a function of stretcher voltage (bottom x axis) and stretcher length (top x axis) for the three-laser setup. A fit is shown in red.

fit the slopes were set to 0.5 and -0.5, respectively, since ω_{ref} and ω_{tb2} change half as much as ω_{tb1}. The y intercept gives the offset frequency ω_0 between ω_{Rb} and the initial frequency of ω_{it} and ω_{if}, i. e. between ω_{Rb} and the dotted line in figure 5.13. Figure 5.15 shows an example for the determination of ω_0. From the linear fits shown in figure 5.15, the y intercept was determined to be 420.3 GHz $\pm$ 0.2 GHz. The values ω_{ref} and ω_{tb2} are then determined by ω_0 and ω_{tb1}:

$$\omega_{\mathrm{ref}} = \omega_0 - \frac{\omega_{\mathrm{tb1}}}{2} = \omega_{\mathrm{tb2}} - \omega_{\mathrm{tb1}} \tag{5.15}$$

$$\omega_{\mathrm{tb2}} = \omega_0 + \frac{\omega_{\mathrm{tb1}}}{2} \tag{5.16}$$

Note that the value of ω_0 changes due to changes in the initial position of ω_{it} and ω_{if} and also uncertainties in the fit which means that this value has to be determined on a daily basis. Since ω_{tb1} is always known, ω_0 can be determined from equation 5.16 by performing a reference measurement. For the first frequencies the interferograms can be fitted with ω_{tb2} as a fit parameter as described above. In the end averaging over all calculated values gives ω_0. However, a precise determination of ω_0 is crucial for precise measurements. Improper determination of ω_0 leads to a frequency offset between the two tuned THz frequencies. This fact can be used to check the accuracy of the determined ω_0. A more detailed discussion is given in Appendix E of [105].

5.3.3. Performance of the correction

Being able to include the frequencies as fixed parameters in the fitting procedure, the performance of the phase correction was investigated. Therefore test measurements

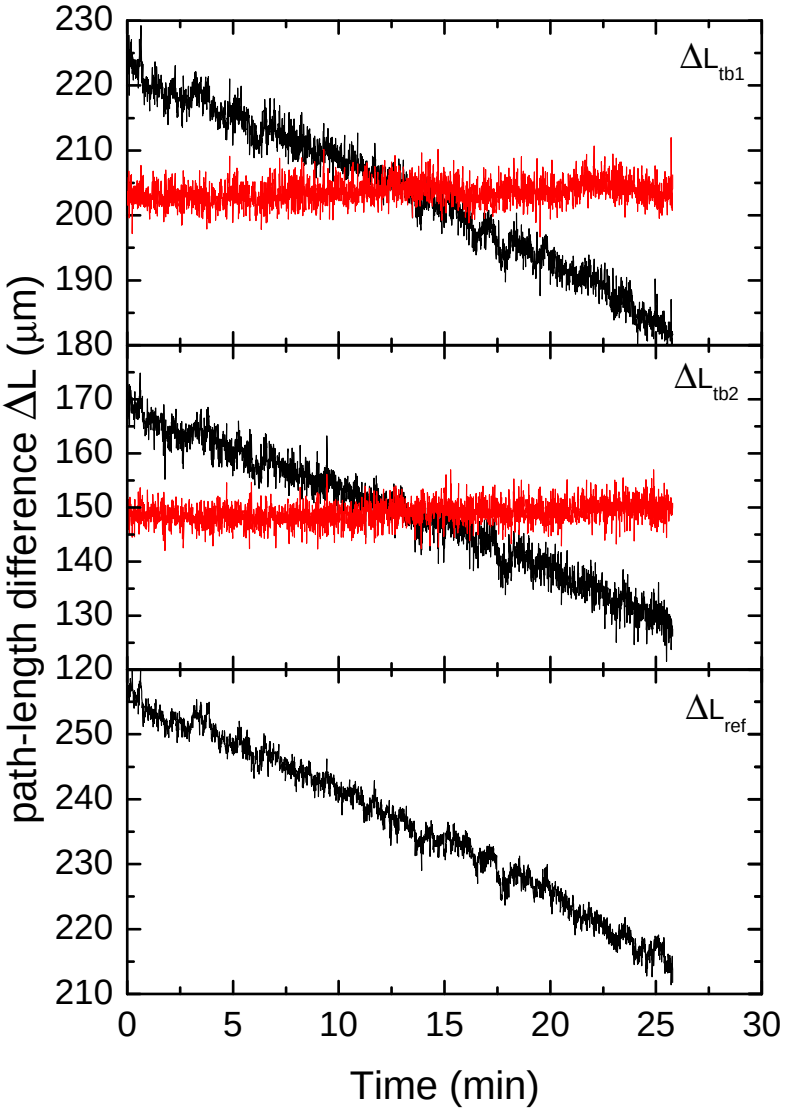

Figure 5.17.: Path-length differences ΔL for the three THz frequencies before and after the correction. Before the correction all ΔL_i show a strong long-term drift of around 40 μm which is corrected effectively by the correction. The short-term fluctuations in ΔL_i due to fluctuations in φ cannot be corrected. They are about 5 μm which is comparable to the result of the two-laser setup (see section 6.5.1).

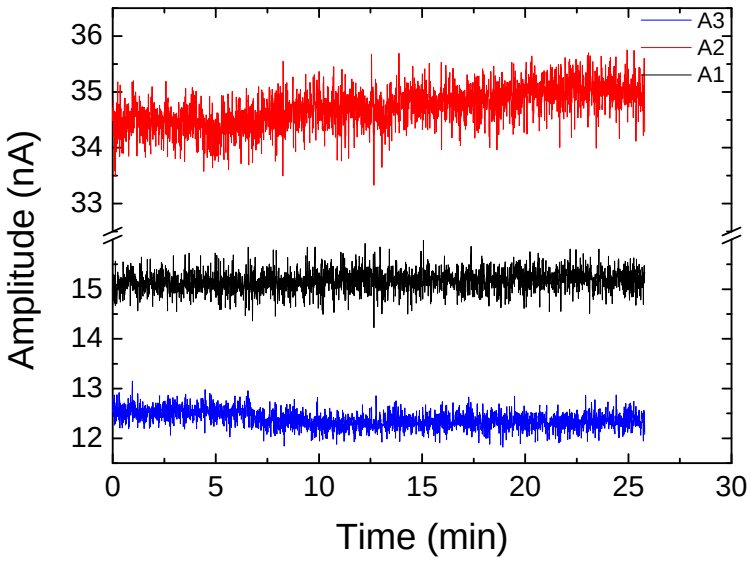

Figure 5.18.: The amplitudes of the three THz frequencies are shown as a function of time. The uncertainty is in the range of 3% which is comparable to those discussed in section 6.4 for the two-laser setup.

where all three frequencies are constant, were performed. The frequency ω_{tb1} was set to 450 GHz and thus $\omega_{\mathrm{tb2}} = 195.6$ GHz and $\omega_{\mathrm{ref}} = 645.6$ GHz as described in the previous section. An example of the measured interferogram and the corresponding fit is shown in figure 5.16.

By measuring at constant frequencies, both the uncertainties in the amplitude and phase are determined and the correction of the phases can be tested easily since for constant frequencies, the phases should also be constant. Changes in ΔL due to fluctuations in the environmental conditions should be the same for all frequencies. After the correction the phases φ_{tb1} and φ_{tb2} should be constant as a function of time. An example of the three path length differences ΔL, before and after correction is shown in figure 5.17. Before the correction, all three values of ΔL show a strong long-term drift of about 40 μm within half an hour. Here, ΔL of ω_{ref} was used for the correction which was performed as described in section 5.3.1. After the correction, the path-length differences are constant as expected. The short-term fluctuations due to the uncertainty of φ cannot be correct within this method. These short-term fluctuations are about 5 μm which is in the same range as for the two-laser setup described in section 6.5.1.

Figure 5.18 shows the corresponding photocurrent-corrected amplitude values. The uncertainty in these values is about 3% which is also comparable to those discussed in section 6.4. These results show that determination of amplitude and phase from the fit of three sinusoidal functions with different magnitudes is very

reliable. The precision of the phase data is increased a lot by the use of one constant frequency as a measure for long-term drifts in ΔL and the associated correction. However, in the above-described method the phase correction only accounts for relative changes of the phase. The precision of the absolute value to which one has to refer is not improved by this method. Nevertheless, the knowledge of the absolute phase value is mandatory for a precise determination of the complex optical functions. The correction of the absolute phase value is explained in the next section.

5.4. Correction of the absolute value of L_{eff}

The aim of spectroscopy is the precise determination of the complex optical functions, for example n and κ. Here n and κ are extracted from the measured T and $\Delta\varphi$ (see section 5.5). From the phase measurement, $L_{\text{eff}} \approx (n-1)d$ is obtained. The uncertainty in the absolute value of ΔL is around 20 μm (see section 6.5.1). For the 0.5 mm thick silicon wafer investigated in chapter 9, $L_{\text{eff}} \approx 1200$ μm is found. In this case the uncertainty $\delta L \approx 20$ μm of ΔL means an uncertainty of L_{eff} of about 2%. Hence also the determination of n is rather inaccurate.

However, one can make use of the Fabry-Perot fringes induced by the sample to correct the absolute value of L_{eff}. At the maxima of the Fabry-Perot fringes, the exact value of the phase is known. Here the wave interferes constructively after undergoing multiple reflections within the sample. The optical path length in the sample is nd, thus the condition for constructive interference is $2nd = m \cdot \lambda$ where m is the order of the maximum. The frequency of the maxima can generally be determined with an accuracy of $\Delta\nu \approx \pm 1$ GHz. For high orders of m, nd can be determined very precise. Typically m is of the order of 10 at frequencies of 1 THz and hence the uncertainty of nd is in the order of 0.1% for these frequencies. With the mechanically measured thickness, n can be obtained with high accuracy at the frequencies of the maxima. The refractive index obtained approximately from L_{eff} is shifted to coincide with the one obtained from the maxima of the Fabry-Perot fringes. Then the accurate phase values are inferred from the corrected refractive index. Figure 5.19 shows an example of the correction for a measurement on MgO. The refractive index n_T obtained from the maxima is shown as green dots. The refractive index n_φ obtained from L_{eff} by the simple use of equation 5.7 is shown in black. For both the mean values $\overline{n_T}$ and $\overline{n_\varphi}$ are calculated and indicated as blue and red line, respectively, in figure 5.19. To correct n_φ it is shifted by the constant offset $\overline{n_T}$-$\overline{n_\varphi}$ such that both mean values coincide (see arrow in figure 5.19).

Alternatively the parameters extracted from a fit to the data can be used for the correction. With the thickness known, the high-frequency refractive index $n = \sqrt{\varepsilon_\infty}$ can be determined very precisely from the fit of the transmittance data. The measured L_{eff} is then shifted by an constant offset to coincide with the L_{eff} obtained from the fit of the transmittance.

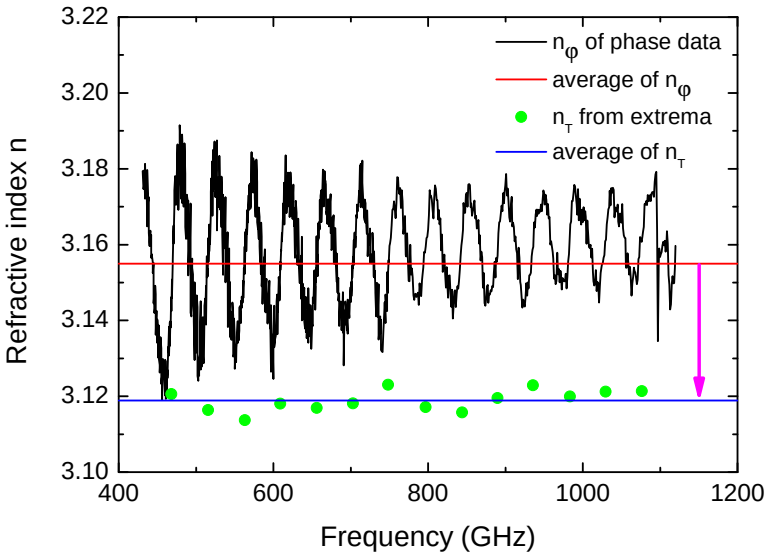

Figure 5.19.: Refractive index of MgO obtained from the maxima of Fabry-Perot fringes (green) and L_{eff} (black). For the correction n_φ is shifted such that both mean values (red and blue) coincide.

5.5. Numerical analysis of n and κ

From the measured transmittance T and phase difference $\Delta\varphi$ the complex optical functions can be obtained. To achieve this, a model containing different Lorentz oscillators can be fitted to the data and the complex optical functions can then be calculated from the fitted $\nu_{0,i}$, $\nu_{p,i}$, and γ_i. Alternatively, n and κ can be calculated directly from the measured values using equations 2.17 and 2.18. This method has the advantage, that no model has to be assumed. Note that equation 2.18 gives the absolute phase induced by traveling optical path nd. However, measured is the phase shift of the sample with respect to the reference which is proportional to $(n-1)d$. The absolute phase shift of the sample can then be calculated by adding the reference phase again, i. e. by adding the optical path through air with the length of the sample thickness d:

$$\varphi_{abs} = \Delta\varphi + \varphi_{\text{ref}} = \Delta\varphi + \frac{\omega d}{c} \tag{5.17}$$

This induces an error due to the uncertainty in the sample thickness d, but the error is assumed to be small since the sample thickness can be measured mechanically with a precision of about ± 2 μm. Taking the mechanically determined thickness, the only unknown parameters are n and κ. Thus, in a first attempt, equations 2.17 and 2.18 were treated as a system of nonlinear equations. The solution of this set of equations was obtained numerically for every single frequency.

To test the analysis, transmittance and phase data of MgO obtained by the fiber-stretcher method was used (see section 8.1). MgO is almost non absorbing in the THz spectral range. Only the tail of phonons at higher frequencies slightly changes the optical functions [109]. Hence this sample is ideal to test whether the small changes in the refractive index or the small values of the extinction coefficient can be determined reliably.

Figure 5.20 shows n and κ obtained from the solution of the system of nonlinear equations as well as the ones obtained from fitting a Drude-Lorentz model to transmittance and phase data (see section 8.1). For n, the result from a simple calculation of the effective sample thickness $L_{\text{eff}} = L_{\text{sample}} - L_{\text{ref}} \approx (n-1)d$ is shown which does not take multiple reflections into account as described in 5.1 (green curve in figure 5.20). The refractive index calculated from the numerical solution is reasonable but the uncertainty is of the same order as the oscillations in the simple calculation. It is assumed that these deviations are due to the uncertainty in the measured transmittance and phase. Even if the data is smoothed, small deviations can prevent that a common solution for both equations is found. Additionally it turns out that the variation of κ has only little influence on the value of φ_{abs}. As a consequence, κ is nearly undetermined as can be seen in the lower part of figure 5.20. Most of the data points do not move from there starting value and the others are scattered over a range of about 0.1.

In order to get a reasonable result, it is not sufficient to consider a single frequency but the behavior in the vicinity of this frequency has to be studied. Therefore, the data were analyzed by fitting equations 2.17 and 2.18 simultaneously to a small frequency range. This method will in the following be denoted as inversion method. It is important to note that n and κ are assumed to be constant over the fitted range. The simultaneous fit is realized by combining the two equations 2.17 and 2.18 to

$$f_{fit}(\omega, n, \kappa) = T(|\omega|, n, \kappa) \cdot (1 - \Theta(\omega)) + \varphi(\omega, n, \kappa) \cdot \Theta(\omega) \quad , \tag{5.18}$$

where Θ is the Heaviside function. The measured values are combined in the same way and fitted by function 5.18. The extracted behavior of n and κ for different sizes of the fitted range is shown in figure 5.20. For a size of the fitted range of 50 GHz which corresponds to roughly one period of the Fabry-Perot oscillations, n is determined very well. The small increase of the refractive index of about 0.01 with increasing frequency due to the tail of phonons at higher frequencies is very well seen in the calculated data. The precise determination of κ is difficult since the absorption in MgO is very low. Additionally the influence of κ on the phase data is small so that the information of $\Delta\varphi$ does not provide a precise determination of κ. Still, from figure 5.20 (b) it can be seen that the behavior of the extinction coefficient κ can be reasonably determined down to the order of 10^{-3}. At low frequencies the deviations increase due to the pronounced influence of standing waves in the optical path which are not taken into account in the analysis. Expanding the fitted range to

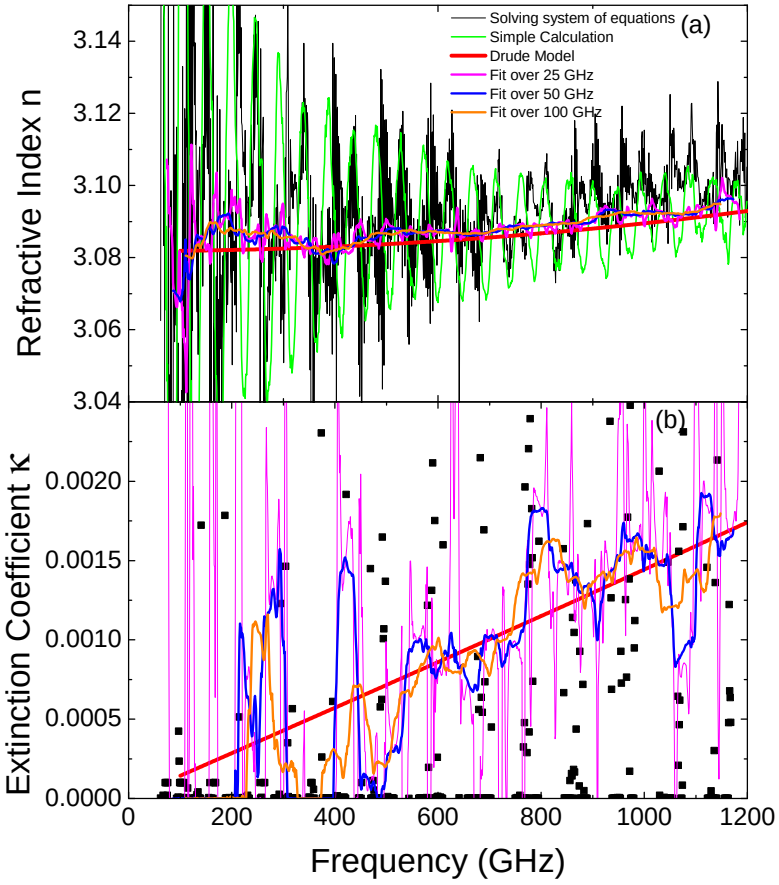

Figure 5.20.: Panel (a) shows the refractive index and (b) the extinction coefficient of MgO calculated with different methods from transmittance and phase data. The Drude-Lorentz model based on the parameters from reference [109] is shown as red curve.

more than one period of the Fabry-Perot fringes does not lead to any improvement. The great advantage of this method is that no model has to be assumed. However, on the downside the approach assumes the refractive index n and the extinction coefficient κ to be constant within the fitted range. Thus using this method in the vicinity of absorption lines is difficult. Nevertheless, in chapter 10 it is shown for the measurements on α-lactose monohydrate, that also in this case both n and κ can be determined well with this method.

To overcome the disadvantage of assuming a constant n and κ over the fitted

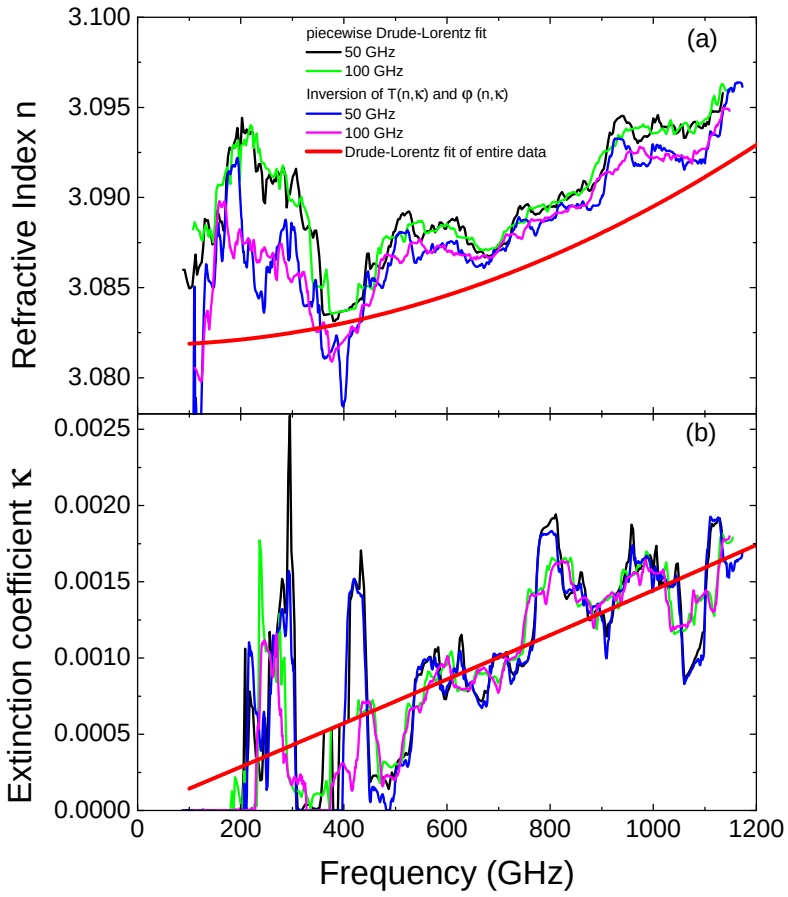

Figure 5.21.: Panel (a) shows the refractive index and (b) the extinction coefficient of MgO determined by either the inversion method or by the PDL fit. The values extracted from the Drude-Lorentz fit of the entire frequency range are shown in red.

range, transmittance and phase have to be fitted by a Drude-Lorentz model[4]. Fitting the model only to a small data range as done for solving the nonlinear system of equations leads to a very good agreement between data and model. Although the obtained parameters ν_0, ν_p, and γ do not have to resemble the real properties of the material, the complex optical functions calculated from these parameters resemble the actual properties of this frequency range. Figure 5.21 compares the results of

[4]All Drude-Lorentz fits (piecewise or over the whole frequency range) are performed using the program RefFIT 1.2.84 by A. Kuzmenko (Département de Physique de la Matiére Condensée, Université de Genéve, Switzerland)

the inversion method and the piecewise Drude-Lorentz fit (PDL fit). The fitted range of one period of the Fabry-Perot fringes was the same for the two methods. Due to the fact that ν_0 of the oscillator is much higher than the frequencies of the measured range [109], ν_0 was considered as fixed parameters in the Drude-Lorentz model and ε_∞, ν_p, and γ were fitted. Note that for the results shown in figure 5.21 the thickness $d = 1.035$ mm obtained by the Drude-Lorentz fit of the entire data range was also a fixed parameter in the fit. Both, the refractive index and the extinction coefficient obtained by both methods are nearly identical showing the consistency of both approaches. For both methods the slight increase of n is revealed nicely and κ can be determined down to the order of 10^{-3}. Exceeding the fitted range to more than one period of the Fabry-Perot fringes does not considerably improve the determined n and κ. The example of MgO shows that the complex optical functions can be determined very precisely from the measured transmittance and phase data.

6. Performance of the setup

For a reliable and precise determination of amplitude and phase, the stability of the setup is very important. A high signal-to-noise ratio is preferable for a precise analysis of the measured data. In this chapter the signal-to-noise ratio as well as the amplitude and phase stability are investigated using the different methods discussed in chapter 5. Also the frequency error induced by the iScans is investigated in more detail. Different possibilities to increase the phase stability apart from the correction of the three-laser method are shown.

6.1. Signal-to-noise ratio

The signal-to-noise ratio (SNR) is a measure that compares the level of a desired signal to the noise level. As already pointed out, the detected photocurrent is proportional to the THz electric field. Hence the measured THz power is proportional to the squared photocurrent ($P_{THz} \propto I_{ph}^2$). In the following, the SNR is given as the dynamic range which is the ratio between the highest signal and the lowest signal that can be detected. The dynamic range in decibels (dB) is given as

$$DR = 10 \log_{10} \left(\frac{P_{ph}}{P_{noise}} \right) = 20 \log_{10} \left(\frac{I_{ph}}{I_{noise}} \right) \tag{6.1}$$

where I_{noise} is the photocurrent measured with blocked detector and I_{ph} is the photocurrent measured through an empty beam path, i. e. the maximum detectable photocurrent. The SNR curve shown in this section was measured by Toptica Photonics. The measurement of both I_{ph} and I_{noise} were performed with a bias modulation frequency of 5 kHz and an integration time of 300 ms. For I_{noise} a value of about 4 pA was measured independent of frequency. The signal I_{ph} is frequency dependent as described in sections 4.1.4 and 4.1.5. Amplitudes range from $I_{ph} >$ 100 nA at 100 GHz to $I_{ph} \leq 0.5$ nA at 1.8 THz which results in a dynamic range from ∼90 dB at 100 GHz down to ∼40 dB at 1.8 THz. The complete frequency behavior of the dynamic range is shown in figure 6.1. Due to the THz beam path of about 35 cm in air, water vapor absorption lines are visible in the dynamic range. Note that these narrow absorption lines are very well resolved as can be seen in the inset of figure 6.1. The frequencies of the water vapor absorptions are in agreement with references [110, 111].

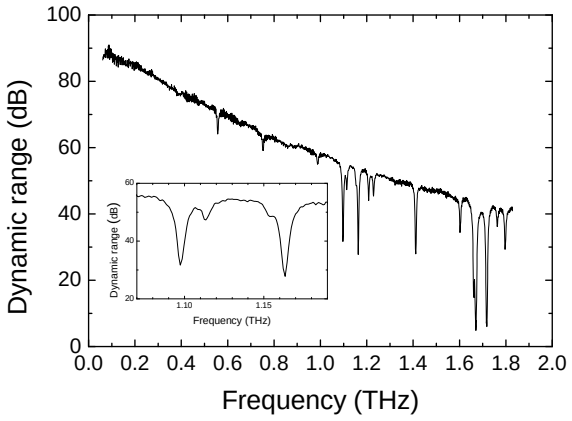

List of water absorption lines after references [110, 111]

line number	resonance frequency
1	577 GHz
2	752 GHz
3	988 GHz
4	1097 GHz
5	1113 GHz
6	1163 GHz
7	1208 GHz
8	1229 GHz
9	1411 GHz
10	1602 GHz
11	1661 GHz
12	1669 GHz
13	1717 GHz
14	1762 GHz
15	1795/1797 GHz

Figure 6.1.: Frequency dependence of the dynamic range between 100 GHz and 1.8 THz. The absorption lines are due to water vapor in the THz beam path of about 35 cm. Their corresponding resonance frequencies are listed in the table. The data shown was measured by Toptica Photonics, see also [112].

6.2. Standing waves

Due to the low absorption at large wavelengths in the materials used for THz optics, standing waves play a critical role in THz spectroscopy. They cause additional Fabry-Perot fringes that might conceal actual features of the investigated sample. In THz TDS these standing waves are completely removed by cutting off the interferogram before the first pulse reflected within the sample arrives at the detector. However, this strongly limits the resolution especially for thin samples. In the frequency domain, it is however not so easy to completely suppress standing waves. Therefore it is important to know how the standing waves influence the measurement and, if possible, to suppress them. Figure 6.2 shows a section of the transmittance and the effective sample thickness $L_{\text{eff}} = L_{\text{Sample}} - L_{\text{Ref}} \approx (n-1)d$ of silicon. The results of three successive measurements are shown. On a first glance this data seems to be very noisy especially on the positive slopes of the Fabry-Perot fringes. However, the peaky structure is very reproducible in all the curves. Also it is periodic with a period of roughly 2 GHz indicating that this peaky structure is a Fabry-Perot oscillation. This is supported by the fact that the period of 2 GHz translates into an etalon length of 7.5 cm which is the distance between the photomixer and the sample position in this experiment. When comparing the effective sample thickness with the transmittance data, the less pronounced standing-wave patterns on the ascending slopes coincide with the maxima in the transmittance as indicated by the red arrows in figure 6.2. A low transmittance in contrast means a high reflectance and thus pronounced standing waves. The magnitude of this standing-wave pattern is up to 100 μm which is much larger than the drift between the individual runs.

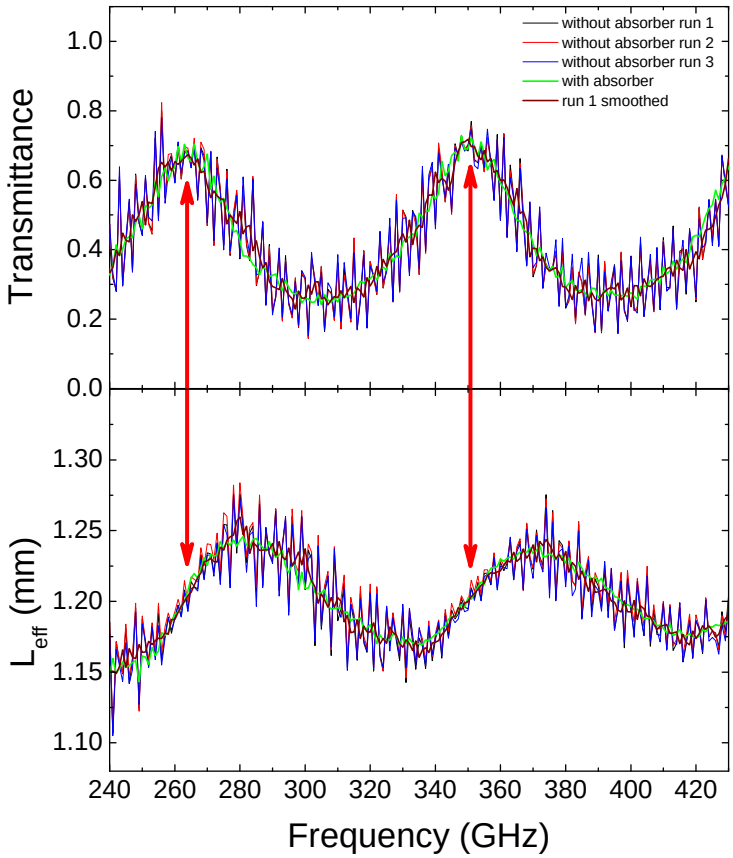

Figure 6.2.: Upper panel: Three transmittances of Silicon measured without absorbers in the beam path. For comparison a transmittance measured with absorbers and a smoothed transmittance are shown. Lower panel: The according effective sample thickness calculated from the phase data. Indicated by the red arrows is the correlation between high transmittance and less pronounced standing waves. The standing-wave pattern can be reduced by smoothing or measuring with absorbers in the THz path.

Suppressing these standing-wave patterns would increase the quality of the data significantly. This can be achieved by either absorbing or guiding reflected waves out of the beam path. As indicated before, very pronounced standing waves are formed between the sample holder and the photomixers. To suppress standing waves between these components, paper can be used as absorber. Paper is weakly absorbing in the THz range so that the standing waves are suppressed and at the same time as much intensity as possible reaches the receiver. Additionally, the magnitude of absorption can be easily adjusted by changing the paper thickness. Tilting the absorber by 45° with respect to the beam path should prevent additional standing

waves between them and the other components. Two absorbers were implemented in the setup, one between the sample and transmitter and the other between sample and receiver. Since the absorbers reduce the overall intensity, the whole accessible range cannot be measured in one frequency sweep. At high frequencies where the intensity is low it has always to measured without absorbers. If the period of the standing-wave pattern is much smaller than the period of the Fabry-Perot fringes induced by the sample, the data can be smoothed by adjacent averaging over a small range to reduce the standing-wave pattern. In figure 6.2 both methods are compared. For the measurement with absorbers in the beam path, two sheets of 2.5 mm thick cardboard were used (see chapter 9). One of the measurements without absorbers was smoothed by adjacent averaging over 6 GHz for the comparison. It can be seen that both methods decrease the standing-wave pattern by one order of magnitude. The usage of absorbers shows a slightly better performance than the smoothing as can be seen at the slopes with pronounced standing-wave patterns. Unlike the smoothing this method does not decrease the resolution.

6.3. Frequency stability

As mentioned in section 4.1.2 the interference signals of the iScan do not show a perfect cosine shape and thus the x-y graph of the two signals is not a perfect circle. However, to get as close to the circular shape as possible, the signal levels at the different photo diodes of the iScan have to be adjusted. Thereby the x-y graph of the measured signals is aligned to match the one of the reference values. The better the adjustment and hence the circular shape is, the smaller is the frequency error. For the alignment the x-y graph is displayed on an oscilloscope. The precision is determined by the reading error of the voltages. A much more precise check of the alignment can be obtained by looking at the experimentally determined frequency error.

The determination of the frequency error using the frequency-scan method was described in section 5.1.1. For the fiber-stretcher method a similar approach is used. Here, the frequency error is extracted by calculating the frequency-dependent deviation of the reference phase from a straight line analogous to the description in 5.1.1. Figure 6.3 shows the frequency error obtained from a frequency-scan and a fiber-stretcher measurement. Note that this data was measured using the 780 nm laser diodes. It is clearly seen that the obtained frequency error is the same for both methods which shows that this is no artifact of the data analysis. However, the maximum frequency error of about $\pm$ 600 MHz is much larger than the frequency error obtained using the 850 nm laser diodes (see section 5.1.1). As discussed in section 5.1.1 the observed period of 16 MHz corresponds to the free spectral range of both iScans. The origin of the larger period of about 400 GHz is not yet clear. Since the free-spectral ranges of the two iScans are not exactly the same, a beat is expected. For some frequencies the signals of both iScans are in phase, hence the

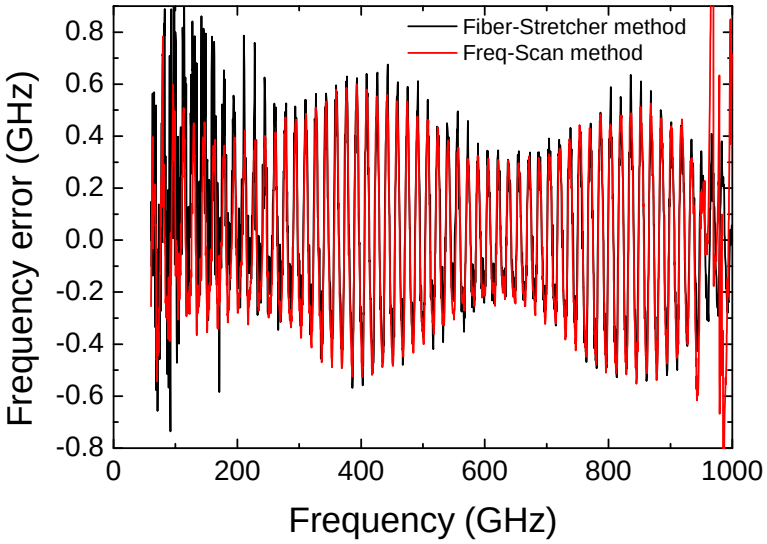

Figure 6.3.: Frequency error obtained by the frequency-scan method and the fiber-stretcher method using the 780 nm laser diodes.

error adds up, and for other frequencies the signals are out-of-phase. However, the difference between the free-spectral ranges is about 40 MHz. This results in a beat frequency of 1.6 THz which is a factor of 4 larger than the observed 400 GHz. Below 200 GHz the frequency error obtained from the fiber-stretcher measurement is larger than the one of the frequency-scan measurement. Here, the number of periods in the interferogram is quite small and thus the phase is not determined as precisely as for higher frequencies.

The frequency error can increase with time due to long-term drifts within the system. Hence, the frequency error has to be checked from time to time and if necessary the iScan parameters readjusted. Figure 6.4 shows the frequency error measured with the frequency-scan method and the 780 nm laser diodes before and after the alignment of the x-y graph. It can be seen that the frequency error around 400 GHz and 800 GHz is considerably reduced by the alignment. However, around 150 GHz, 600 GHz, and 900 GHz the frequency error does not change. Still, the maximum frequency is reduced to about 300 MHz by the alignment showing the importance of a good adjustment of the iScan parameters. Note that due to the fact that the interference signals of the iScans do not follow a perfect cosine behavior, the x-y graph can never be aligned to a perfect circle. Thus a certain frequency error cannot be avoided.

Figure 6.5 shows an example of the minimum frequency error that could be reached using the 850 nm diodes. The two frequency errors shown are obtained from two different reference measurements. The maximum frequency error for this alignment

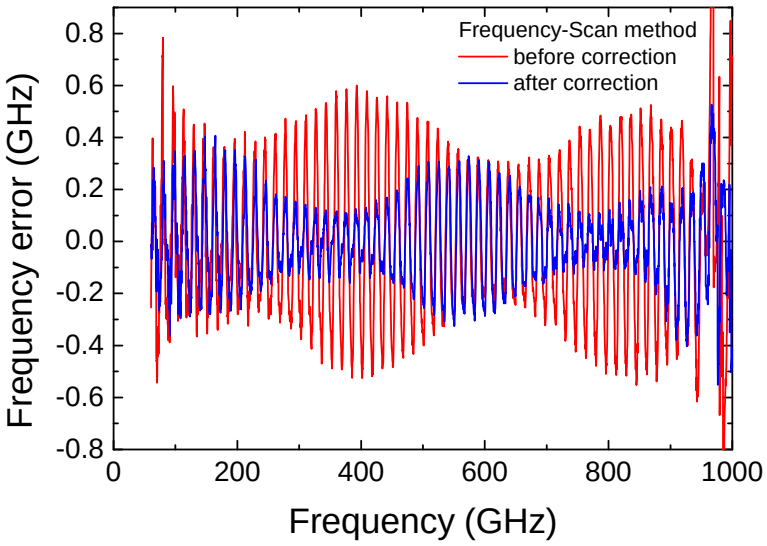

Figure 6.4.: Frequency error obtained by the frequency-scan method before and after the alignment of the x-y graph using the 780 nm laser diodes.

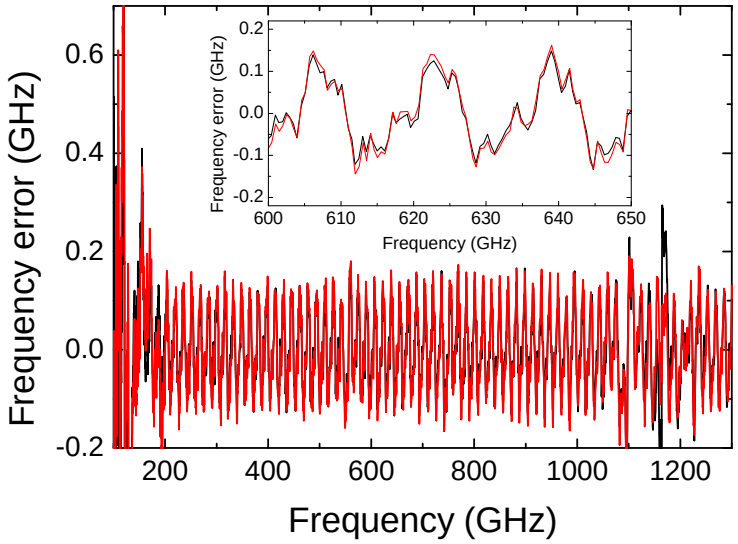

Figure 6.5.: Frequency error of two successively measured references obtained by the frequency-scan method . The measurement was performed using the 850 nm diodes.

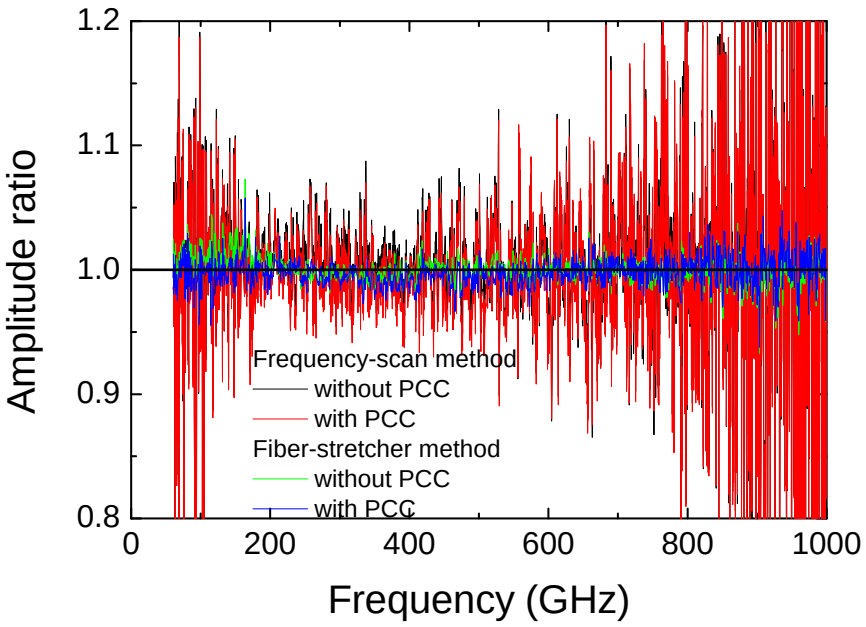

Figure 6.6.: Comparison of the amplitude ratios obtained with the frequency-scan method and the fiber-stretcher method. The larger noise in the frequency-scan method is due to the error induced by interpolating between the extrema.

is about ±200 MHz which is about 100 MHz smaller than shown in figure 6.4. In the inset of figure 6.5, a small range of the frequency error is shown. It can be seen that the agreement between the curves is very good showing that the frequency error is very reproducible. In the frequency error presented in figure 6.5 only the period of 16 GHz of the iScan free spectral range is observed.

6.4. Amplitude stability

To obtain transmittance and phase, a sample and a reference measurement are required which have to be performed in sequence. Changes in the laboratory conditions between or even during a single measurement affect the amplitude and hence the transmittance. To see how strong the amplitude changes between two measurements and how efficiently the drifts are reduced by the photocurrent correction (see section 4.1.7), several reference measurements were performed in succession and the amplitude ratios of consecutive measurements were calculated. Since the amplitude stability depends on the polarization of the laser beat, the two fiber branches were put in close vicinity to minimize temperature differences between them. Additionally strong bending of the fibers such as rolling up was avoided. Figure 6.6 shows

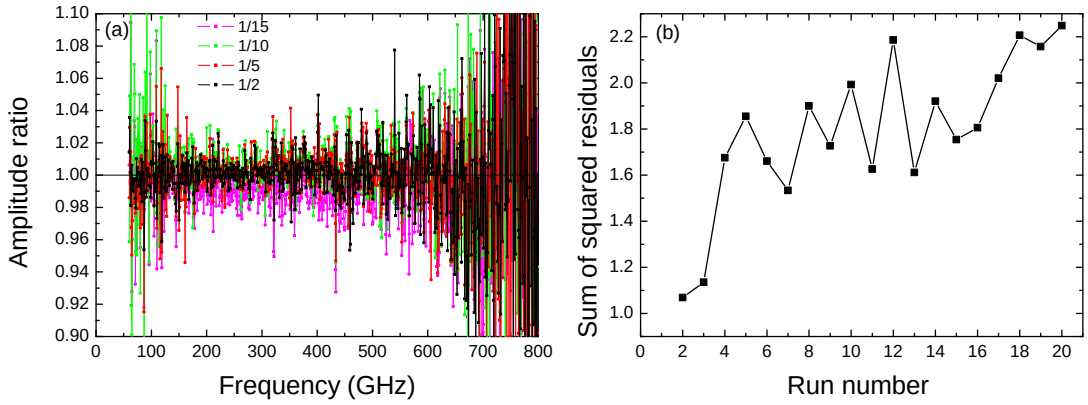

Figure 6.7.: (a) Amplitude ratio between successive frequency sweeps and the first sweep. Even for large temporal distances the deviations are in the order of ±2%. (b) Sum of squared residuals as function of the run number taken for the ratio.

amplitude ratios measured with the frequency-scan method and the fiber-stretcher method. Note that both ratios were measured in direct succession. The influence of the photocurrent correction is small showing the good amplitude stability of the system. Note that the amplitude stability is much better than shown in section 4.1.7 where the photocurrent correction was tested under extreme conditions. Nevertheless, the amplitude ratio measured with the fiber-stretcher method is improved by the photocurrent correction below 200 GHz. The 100% line is reproduced very well by both methods. However, the noise is much larger in the frequency-scan method due to the error caused by interpolating between the extrema (see section 5.1.1). Above 200 GHz it is in the range of ±5% but increases with increasing as well as with decreasing frequency. The increase on the low-frequency side is due to standing-wave effects. At high frequencies the signal-to-noise ratio decreases and therefore the precision in the determined extrema decreases. For the fiber-stretcher method the short-term fluctuations are only in the range of ±2%.

For further investigations, the ratios of different reference measurements with respect to the first measurement are plotted in figure 6.7 (a). Note that these measurements were obtained using the fiber-stretcher method and all references were photocurrent corrected before calculating the ratio. The deviation of the ratio of the first successive runs is in the order of ±2% like above. This is still the case for the ratio of the first and the tenth run. For the ratio between the first and the fifteenth run the deviation is only marginally larger. Figure 6.7 (b) shows the sum of the squared residuals S as a function of the measurement number taken for the ratio. After the third run there is a relatively strong increase of S but for all further sweeps S is increasing only slightly. This shows that with the fiber-stretcher method a amplitude stability of ±2% can be achieved even for long measurements.

6.5. Phase stability

Alongside a precise amplitude measurement, a precise phase measurement is also necessary for the determination of the complex optical functions. Temperature fluctuations in the environment can affect the phase measurement. Since both fiber branches do not have exactly the same length, temperature fluctuations change the optical path of both fiber branches differently and hence affect ΔL. The main contribution is thereby expected from the temperature dependence of the refractive index n ($\frac{\partial n(SiO_2)}{\partial T} = 10^{-5}/K$) [113] which is about one order of magnitude larger than the thermal expansion ($\alpha_{SiO_2} \approx 0.5 \cdot 10^{-6}/K$) [114]. Small temperature differences between the fiber branches do also affect the phase stability. To minimize temperature differences, the fiber stretchers are mounted in close vicinity. However, the fibers leading from the fiber stretchers to the photomixers are spatially separated.

To estimate how strong the measurement of the phase is influenced by the environmental conditions, the overall change of the phase at a fixed frequency with varying laboratory temperature was observed. This was done at three frequencies, namely 200 GHz, 600 GHz, and 800 GHz. A variation of the laboratory temperature between 22 °C and 24.5 °C was induced by the air conditioner. The temperature was measured close to the fiber stretchers using a thermocouple. Figure 6.8 shows the measurement for 600 GHz where temperature and phase are shown as black and blue lines, respectively. The phase is given in units of radians. It can be seen that the phase is changing according to the temperature between 4.25 and 4.55 which is nearly a change of 10%. For most of the further considerations we will use equation 5.7 to translate the phase change into a change of the path-length difference ΔL. In other words, the length change between the transmitter branch ($L_S + L_{THz}$) and the receiver branch (L_D) that causes the observed phase shift. Hereafter, the change in ΔL is denoted as δL. It is important to note that the value of ΔL for the setup was about 7 cm during these measurements.

In the example shown in figure 6.8, the phase change of 0.3 radians translates into $\delta L \approx 24$ μm. For the other two frequencies of 200 GHz and 800 GHz (the curves are shown in Appendix A.2), the total phase change was 0.1 and 0.35, respectively, which results in $\delta L \approx 27$ μm and 21 μm. Taking the temperature change of 2.5 °C into account, this results in a change of ΔL with temperature of $\Delta L/\Delta T \sim 10\mu$m/K. This value looks rather small but the phase drift has a crucial influence on the analysis of n and κ (see section 5.5). Note that the air conditioner in the laboratory is normally not in use.

Before looking at the phase stability at experimental conditions, meaning at room temperature without air conditioning, it was investigated whether the 120 m of fiber in the fiber stretcher or the remaining fiber pieces are mainly contributing to the value δL. The fiber length in the fiber stretcher is the far largest amount in the whole setup but it is implemented in a metal casing which seals it off from the environment. However, the remaining fiber parts are external and hence more susceptible for changes of the laboratory conditions. To determine whether the

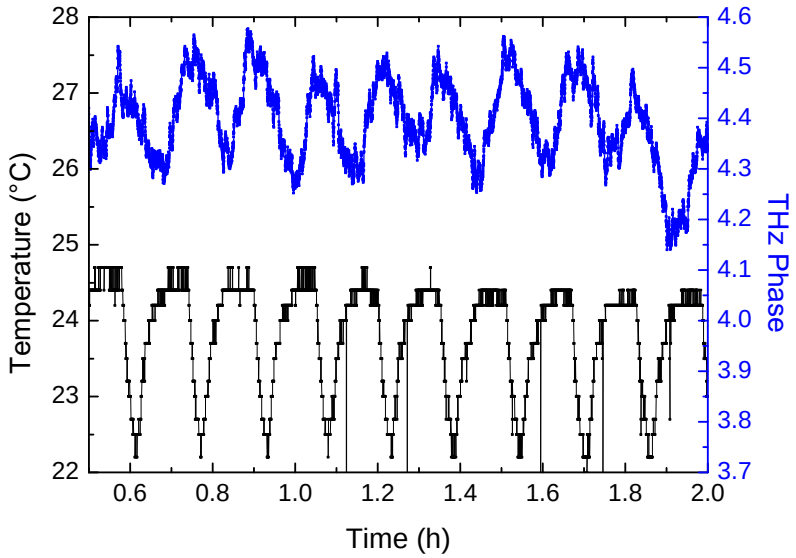

Figure 6.8.: The phase measured at a constant frequency (600 GHz) is varying according to the induced temperature fluctuations. For a temperature change of 2.5 °C, the phase changes by about 0.3 radians

120 m of fiber from the fiber stretcher is increasing the phase instability or not, the phase drift with and without the fiber stretcher in the optical path was measured using the frequency-scan method as described in section 5.1. Since this method does not provide the phase determination at one fixed frequency, a small frequency range was measured repeatedly and δL calculated from the shift of the extrema. A temperature modulation between 22.2 °C and 24.2 °C was again induced by the air conditioner. Figure 6.9 shows the measurements both with and without fiber stretcher. A frequency range from 590 GHz to 610 GHz was measured successively. During one temperature cycle, nine frequency sweeps were measured. The phase drift was analyzed by determining the maximum shift of the zero-crossing frequencies $\delta\nu_{zero}$ of the oscillating photocurrent. With fiber stretcher in the optical path, the zero-crossing frequencies drifted by about 180 MHz. Without fiber stretcher, the drift was about 370 MHz which is even larger. Note that the period $\Delta\nu_{I_{ph}}$ of both photocurrents is not the same as the two fiber stretchers do not contain exactly the same fiber length. The length difference between the two fiber stretchers estimated from the photocurrent periods is about 3 cm.

The phase drift $\delta\varphi$ can be calculated from $\delta\nu_{zero}/\Delta\nu_{I_{ph}}$ and from this again the change in the optical path difference can be calculated using equation 5.7. As result one gets $\delta L \approx 20 \pm 3$ μm and $\delta L \approx 26 \pm 3$ μm with and without fiber stretcher, respectively, over a period of ten minutes. This shows that the drift is approximately the same with and without fiber stretcher. The small difference might be due to the

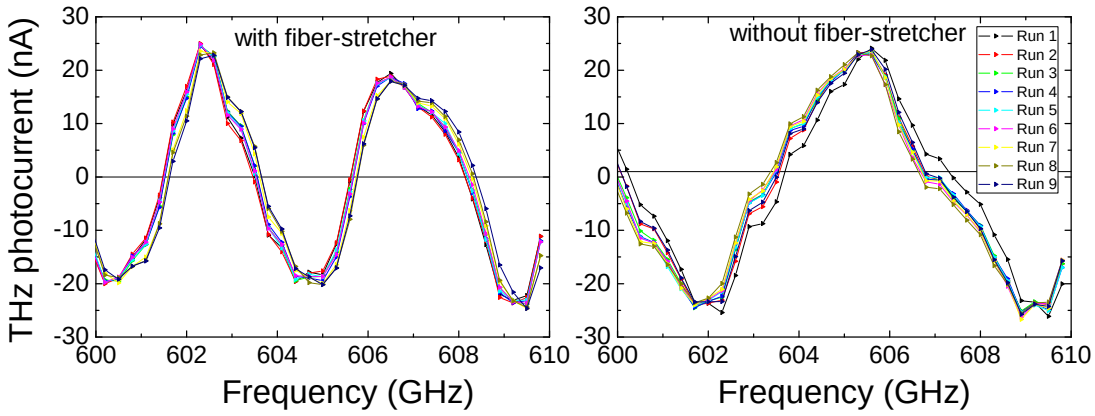

Figure 6.9.: Left: Photocurrent in the range from 600 GHz to 610 GHz measured with fiber stretcher in the laser beam path. Right: Photocurrent in the same range measured without fiber stretcher in the laser beam path. In both plots the photocurrent was measured over one temperature cycle.

fact that although the temperature modulation was the same the overall conditions in these two experiments could differ. In the following, the frequency dependence of the drift will be considered. To measure really the frequency dependence and not the time dependence the conditions have to be the same for all frequencies. This can be realized simply by measuring all frequencies at more or less the same time. Before doing so, the minimization of the phase drift is considered.

6.5.1. Improvement of the phase stability

As discussed in section 4.1.5 either the frequency or the path difference can be varied to extract amplitude and phase information. But these parameters also cause uncertainties in the phase determination. Drifts of the THz frequency and the above-mentioned changes in the path difference lead to a phase shift of the THz beam with respect to the laser beat at the receiver as discussed in section 4.1.5. In case of frequency instabilities, the mismatch between the actual and the fitted frequency gives an additional error of the phase. In a first step it was estimated based on calculations which of these effects has more influence on the reliability of the phase detection. For this calculation we assumed that the THz optical path does not change. This is reasonable since the THz path length L_{THz} is much shorter than the laser beam paths to the transmitter L_S and the receiver L_D ($L_{THz} \ll L_S, L_D$) and a change of the refractive index of air with temperature is much smaller than for the SiO_2 based fibers. With this assumption the drift of ΔL can be expressed as:

$$\delta L = \left(\Delta L \cdot \frac{\delta\nu}{\nu}\right) + (\underbrace{\Delta L - L_{THz}}_{=L_S - L_D}) \cdot \alpha\delta T \quad , \tag{6.2}$$

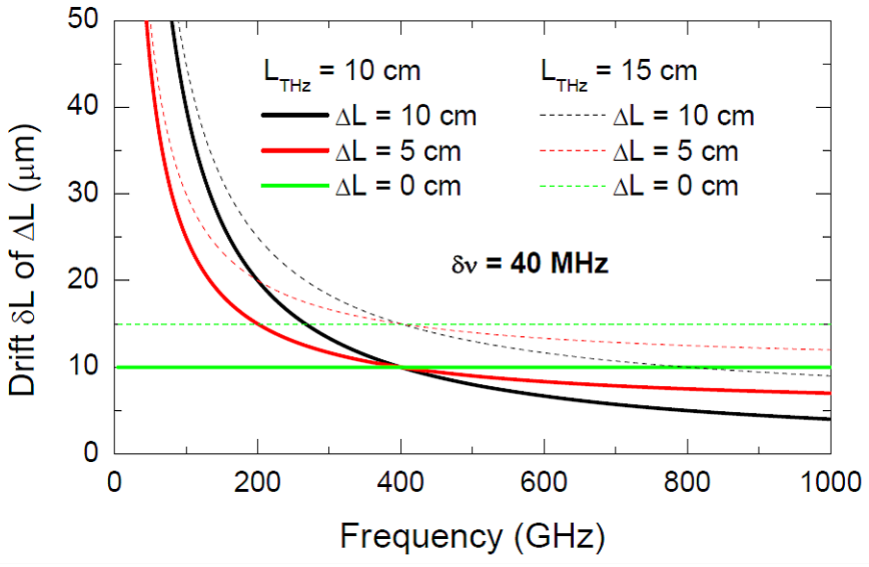

Figure 6.10.: The calculated frequency-dependent drift of ΔL according to equation 6.2.

where $\delta\nu$ and δT denote the maximum change of the frequency ν and the temperature T, respectively, and α denotes the thermal expansion coefficient. The first term describes the drift due to frequency instabilities and the second term the drift due to temperature instabilities. For the calculations, constant values of $\delta\nu = 40$ MHz which is the maximum reachable stability of the THz frequency and $\delta T = 1$ K are used. Two values for the THz path of $L_{THz} = 10$ cm and $L_{THz} = 15$ cm were considered. Figure 6.10 shows the result of equation 6.2 for three different values of ΔL. In case of $\Delta L = 0$ the drift is frequency independent which can be seen from equation 6.2. By increasing ΔL also the drift δL increases especially for low frequencies. The drift increases also with $(\Delta L - L_{THz})$. This can be explained by the fact that for $\Delta L = 0$ (for increasing L_{THz}) the imbalance between the two fiber paths L_S and L_D gets stronger. Hence, it is evident that the phase drift is minimized by adjusting ΔL to zero and choosing L_{THz} as small as possible. Keeping L_{THz} and hence the difference between L_S and L_D small minimizes the thermal contribution to the drift. In the ideal case when both fiber paths have the same length, the equal changes in both fibers will cancel out and therefore minimize thermal drifts. Setting ΔL to zero minimizes the frequency contribution of the drift. Figure 6.10 shows that the frequency has a stronger influence than the thermal contribution to the drift. Furthermore, the adjustment of ΔL is more practical than the adjustment of $L_S - L_D$ where one has to implement fiber pieces with certain length either by splicing or by additional fiber-fiber couplers. For the following experiments, ΔL was set to zero by adjusting L_{THz}. Figure 6.11 shows data for $\Delta L \approx 0$ with $L_{THz} \approx 12$ cm. The phase has been measured at different frequencies as a function of time. To provide the same conditions for all frequencies, they are measured at more or less

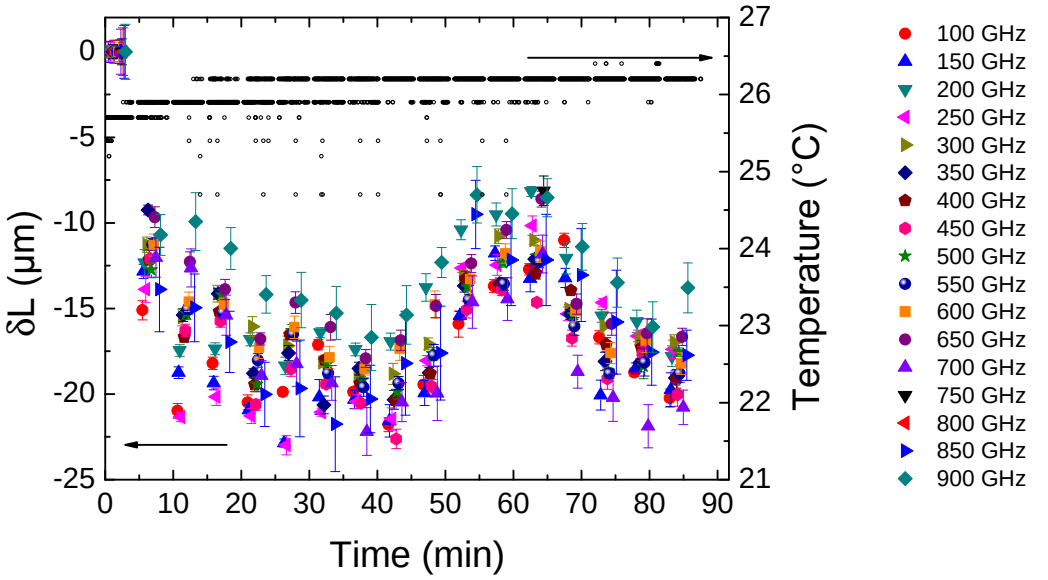

Figure 6.11.: Drift δL of ΔL measured for different frequencies as a function of time. All frequencies show the same drift of the order of about 20 μm. Fluctuations within one frequency cycle of about 3 μm are due to the overall precision of the sinusoidal fit.

the same time. This was realized by measuring at a certain frequency for some seconds then moving to the next frequency. When reaching the highest frequency the software moved to the lowest frequency again and proceeded. In the small time steps between the different frequencies the environment changes only slightly and therefore the drift of all frequencies over time can be recorded under comparable conditions. No deliberate temperature modulation was used for this measurement. In Figure 6.11, the drift δL is plotted as a function of time. Different frequencies are indicated by different colors. The error bars give the standard deviation of the measured values of δL. All values were normalized to the starting point which was set to zero. The uncertainty increases for increasing frequency since the emitted power and hence the signal-to-noise ratio drops with increasing frequency. Thus the performance of the sinusoidal fit decreases. The uncertainty of δL is about 3 μm at low frequencies and about 5 μm for the highest frequency. It can be seen that the temperature was not yet stable in the beginning of the measurement due to the heating up of the electronic control units. The increase of temperature leads to a relatively sharp drop of δL compared to the later measurements where the temperature is more stable. In the interval between 20 and 90 minutes the drift of ΔL is smaller than 20 μm. To really demonstrate that the choice of ΔL has a crucial influence on the phase stability, ΔL was increased to about 45 cm. The result is depicted in figure 6.12. Here two clear differences from the earlier measurement can

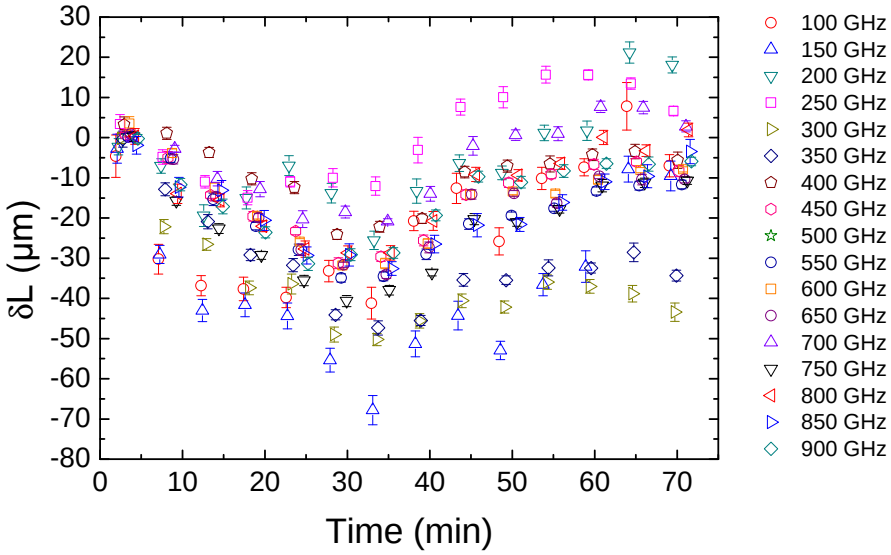

Figure 6.12.: Drift δL of ΔL measured for different frequencies as a function of time with $\Delta L = 45$ cm. The lower frequencies show a stronger drift since now frequency uncertainties play a role. Also the overall magnitude of the drift is much larger than in the case of $\Delta L = 0$ (see figure 6.11).

be seen. On the one hand, δL is not frequency independent any more. At lower frequencies δL shows the same general behavior as for the higher frequencies but the drift is stronger. On the other hand, the overall change is much larger than in the case of $\Delta L = 0$. For a frequency of 150 GHz the drift amounts to nearly up to 80 μm. Also for higher frequencies the drift is about 40 μm which is nearly twice as large as for $\Delta L = 0$.

Nevertheless, figure 6.11 shows that the drift is the same for all frequencies as expected for $\Delta L = 0$. This gives the opportunity to correct the phase drifts using the three-laser setup as described in section 5.3 and to reduce the drift of 20 μm even more. Figure 6.13 shows the drift δL of the corrected ΔL exemplary for two different frequencies as a function of time. The drift over half an hour is reduced to ~ 2 μm. Hence the phase correction applied within the 3-laser method improves the stability of ΔL by one order of magnitude. In section 8.2 it is demonstrated, that due to the phase correction the precision in the measured complex optical functions is increased significantly.

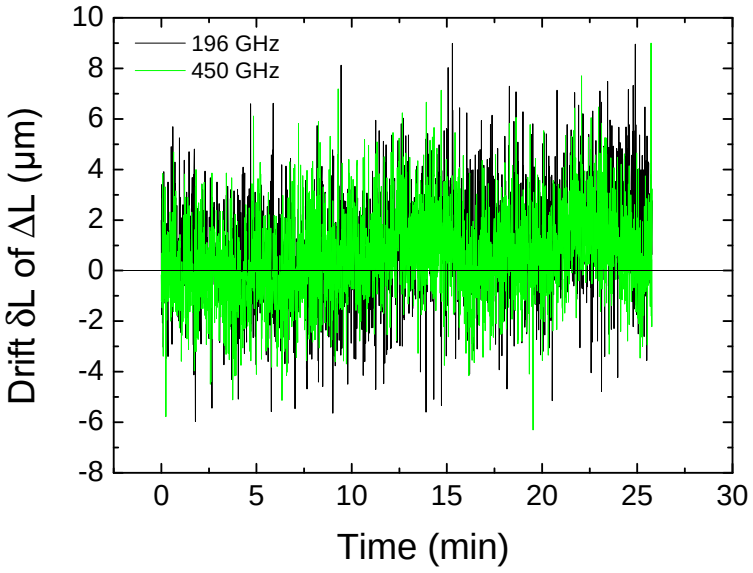

Figure 6.13.: Drift δL of ΔL after the correction of the phase drift using the 3-laser method for two exemplary frequencies. The drift over half an hour is reduced to about 2 μm.

7. Beam profile and lens design

The Si lens of the photomixer mediates between the refractive indices of the GaAs substrate and air. It collects and pre-collimates the emitted THz radiation. Since the active region is not exactly in the focal spot of the hyperspherical lens, the outgoing radiation is not completely collimated but still exhibits a finite opening angle. To collimate and focus the radiation, additional optical elements have to be applied. This can either be lenses or mirrors. Lenses have the advantage of being easily adjustable but cause additional reflections and absorptions in the beam path. Mirrors on the other hand are non-absorbent but the alignment is rather difficult. In a first attempt we decided for lenses since the absorption can be used to suppress the standing waves between sample and transmitter or receiver. Standing waves caused by the lenses are avoided by slightly tilting them. Because of the large wavelength, the influence of the tilting on the beam path is negligible.

7.1. Lens design

A four-lens setup was proposed as sketched in figure 7.1. The first lens collimates the divergent beam from the transmitter, the second one focusses the beam onto the sample, while the third recollimates the beam. The fourth lens collects the collimated light and focusses it on the receiver. Since commercial lenses have relatively small diameter and few choices of focal lengths, the lenses were self-fabricated. For the design it has to be considered that the diameter of the focal spot is well suited for the size of the investigated samples. As described in section 2.2.5, the focal length and the size of the focal spot are connected. Also one needs to find a material which can be used for lenses in the THz spectral range. These steps are discussed in more detail in the following.

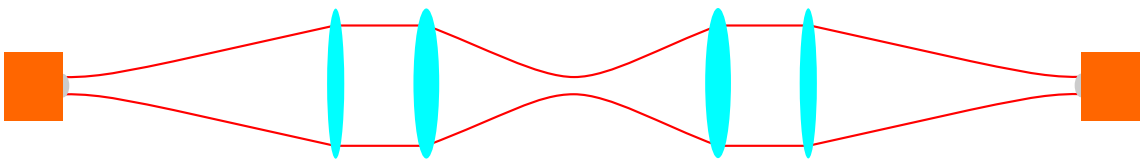

Figure 7.1.: Schematic drawing of the four-lens setup.

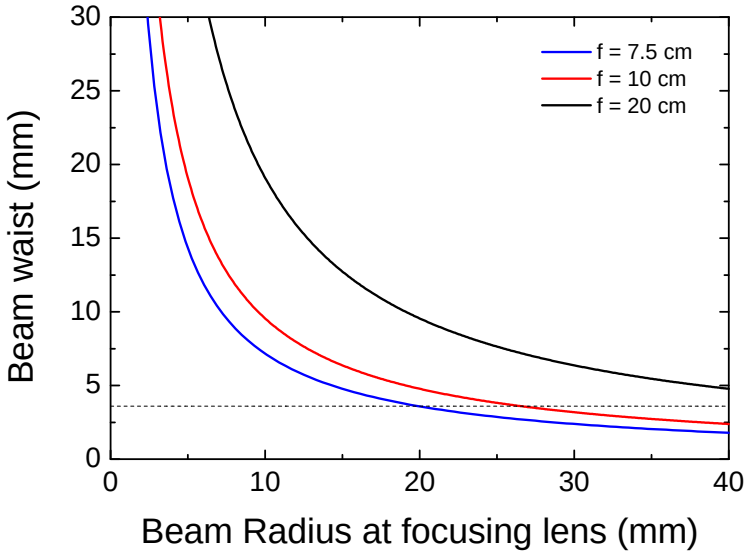

Figure 7.2.: Correlation between the radius of the parallel beam before focusing and the beam waist for different focal lengths at 100 GHz.

7.1.1. Estimation of ray path parameters

The samples that are investigated with this setup are mostly single crystals whose size is predetermined. Hence a beam diameter smaller than 1 cm is preferred. As discussed in section 2.2.5, the beam waist w_0 can be reduced by either increasing the beam radius w_L at the position of the focusing lens or decreasing the focal length f. To increase the beam radius at the position of the focusing lens, the focal length of the collimating lens and hence the path of the divergent beam can be increased. However, this increases also the distance the beam has to pass through air and hence the absorption due to water vapor. Decreasing the focal length of the focusing lens on the other hand increases the lens thickness and thereby the absorption due to the lens material. Furthermore, the focal length cannot be chosen too small since a sample holder or cryostat has to be placed in between.

For the estimation, a half-opening angle of the photomixers of 7.5° at 100 GHz was assumed. Note that in the following always the half-opening angles are given. The focal length of the focusing lenses was chosen to be 10 cm to have enough space so that a cryostat and polarizers can be placed in between. Figure 7.2 shows the radius of the focal spot as a function of the beam radius at the focusing lens for a frequency of 100 GHz. For comparison also other focal lengths are shown. To make the THz path not too long, the focal length of the collimating lenses was chosen to be 20 cm. Considering the assumed opening angle for 100 GHz, this results in a beam radius before focusing of about 26 mm which in the end gives a beam waist of about 3.6 mm as indicated by the dotted line in figure 7.2. Note that the

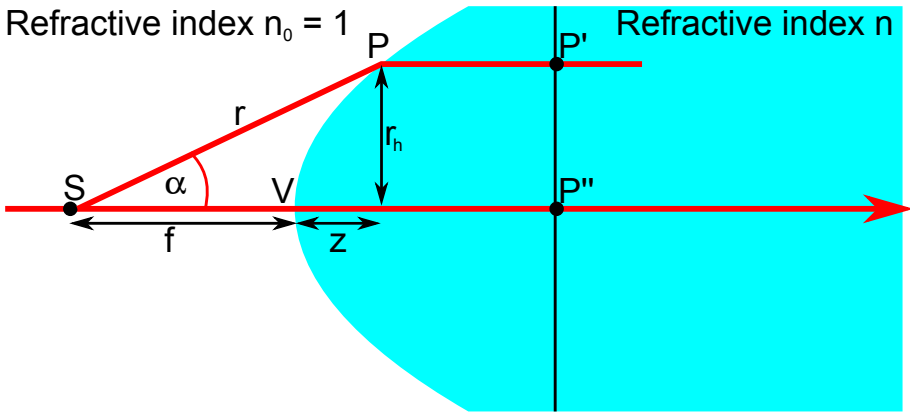

Figure 7.3.: Sketch of rays from a point source passing through a hyperbolic interface. The interface's shape is such that the optical path lengths $\overline{SPP'}$ and $\overline{SVP''}$ are equal.

beam waist will decrease with increasing frequency (see equation 2.47). The figure also shows that decreasing the focal length further from 10 cm to 7.5 cm does not significantly decrease the beam waist so that the chosen focal lengths seem to be a good compromise between a small beam waist and low losses.

7.1.2. Lens material

In the next step an appropriate material for the lenses have to be found. The refractive index has to be nearly constant over the desired frequency range and the absorption has to be as low as possible. Mainly polymers are promising for THz optics and many have been investigated related to that purpose but also silicate glasses have been studied [115–118]. So far high-density polyethylene (HDPE) seems to be the best material for THz optics. It has a constant refractive index n of 1.54 over the whole THz range. The absorption coefficient α is about 2 cm^{-1} which is quite small [115]. Additionally, this material has the advantage of being inexpensive hence it is the best choice for lens fabrication.

7.1.3. Lens design

After deciding about the focal length and material, i. e. setting f and n, the shape of the lens surface can be calculated. Simple spherical lenses are not appropriate in the case of Gaussian optics. Here, hyperbolic lenses have to be implemented.

The shape of this hyperbolic surface can be calculated from Fermat's Principle of least time[1]. Divergent rays from a point source S should be parallel after passing the interface like depicted in figure 7.3. This means that the optical path lengths

[1]Derivation according to [119]

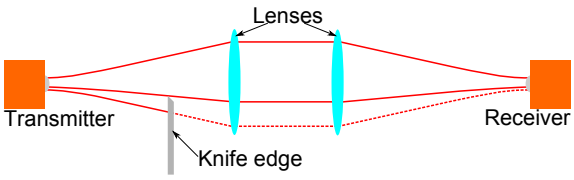

Figure 7.4: Schematic drawing of the lens setup used for beam profiling. The knife edge was gradually moved into the beam so that it blocked part of it.

$\overline{SPP'}$ and $\overline{SVP''}$ have to be equal. Assuming the first medium to be air with $n_0 = 1$ and the second medium to have a refractive index n,

$$\overline{SP} + n\overline{PP'} = \overline{SV} + n\overline{VP''} \tag{7.1}$$

Substituting the optical path lengths as given in figure 7.3 and setting $\overline{VP''} = n([r\cos\alpha - f] + \overline{PP'})$ one gets:

$$r = \frac{(n-1)f}{n\cos\alpha - 1} \quad . \tag{7.2}$$

Transforming this into cylindrical coordinates with the z axis being the axis of symmetry and the vertex of the interface defined as origin of the coordinate system, the distance r_h from the z axis as a function of z is given by:

$$r_h^2 = 2fz(n-1) + z^2(n^2-1) \quad . \tag{7.3}$$

With this equation, the hyperbolic curvature of a plane-convex lens with focal length f can be calculated. For a biconvex lens with two equal curvatures, the actual focal length will be half the focal length used for the calculation.

To avoid plane surfaces that might give rise to standing waves, biconvex lenses were fabricated. The lens radius was set to 5 cm to minimize diffraction. The lenses were fabricated by lathing them from a HDPE cylinder with a CNC lathe. Therefore the r_h-z coordinates were calculated in steps of 10 μm and given to the machine. To be able to fix the lenses to conventional posts in the THz beam path, the lenses were mounted on a circular frame made out of polyvinyl chloride (PVC) which has a higher absorption coefficient than HDPE and should absorb remnant THz radiation [120, 121]. Besides for the use in the actual experiments the lenses were also needed for measuring the beam profile which will be discussed in the following section.

7.2. Beam profile

The beam profile can be measured with different methods. A highly resolved beam profile can be obtained using the pinhole method. This method allows for the detection of hot spots and other local variations of the beam profile. However, this is very time consuming since the whole area of the beam has to be scanned and it is resolution limited due to diffraction. Nevertheless, the pinhole method has been

applied successfully in the THz range [122] and also some variations of the pinhole method were proven to show good results [123].

If one is only interested in dimensions of the beam, i. e. the beam radius, less time-consuming methods can be used. Here, the knife-edge method was employed which is commonly applied for lasers [124] to get a reasonable value for the beam radius although diffraction effects are neglected[2]. To minimize the diffraction a sharp edge is needed. For laterally small laser beams a razor blade is therefore usually utilized. In case of the THz beam this is not possible since a razor blade is too small to block the whole beam, thus we employed a 1 mm thick metal plate that was sharpened at one edge. The collimating lenses were used to collect all the radiation emitted from the photomixer. They were set with a distance of 30 cm to each other so that also the beam profile between the lenses could be determined. In a second step, the focusing lenses were also implemented to determine the beam radius at the focal spot. The beam profile was measured by moving the metal plate with the sharp edge into the beam and recording the photocurrent I_{ph} as a function of the edge position as shown in figure 7.4. This was repeated for several distances between emitter and knife edge. From the change in the measured total intensity ($I \propto I_{ph}^2$) the beam profile is derived by

$$\frac{dI}{dx} = \frac{1}{2}\left(\frac{y_{i+1} - y_i}{x_{i+1} - x_i} + \frac{y_i - y_{i-1}}{x_i - x_{i-1}}\right) \tag{7.4}$$

The derivative of the measured total intensity yields the beam profile. To finally determine the beam radius, a Gaussian function was fitted to the data and the half width at $1/e^2$ of the peak value was extracted. An example of the intensity and the calculated beam profile together with the Gaussian fit for 450 GHz is shown in figure 7.5. Note that the offset of the fitted function was fixed to zero. The Gaussian shape is nicely reproduced by the data. At low frequencies, the photocurrent and thus its derivative exhibit stronger disturbances that are most probably due to diffraction, when only a small part of the beam is blocked. Nevertheless, the slope obtained when more than half the beam was blocked, was always reasonable for fitting. Figure 7.6 shows the development of the beam profile for a constant frequency as a function of the distance from the emitter. As expected for a Gaussian beam, the amplitude decreases and the beam gets broader, i. e. the energy of the beam distributes.

The beam profile was determined for two perpendicular directions, i. e. the x axis and the y axis in steps of 50 GHz. To measure the second beam profile both photomixers were turned by 90 degrees. For the y axis only a few distances were measured since the beam radius came out to be similar to that of the x direction. Figure 7.7 shows the beam radius as a function of distance from the emitter for some selected frequencies. Closed and open symbols denote the beam radius along the x axis and the y axis, respectively. As expected, the opening angle decreases with increasing frequency. It is about 7.2° at 150 GHz (which is close to the assumed

[2]The beam profile was measured in cooperation with Jennifer Marx (see [125])

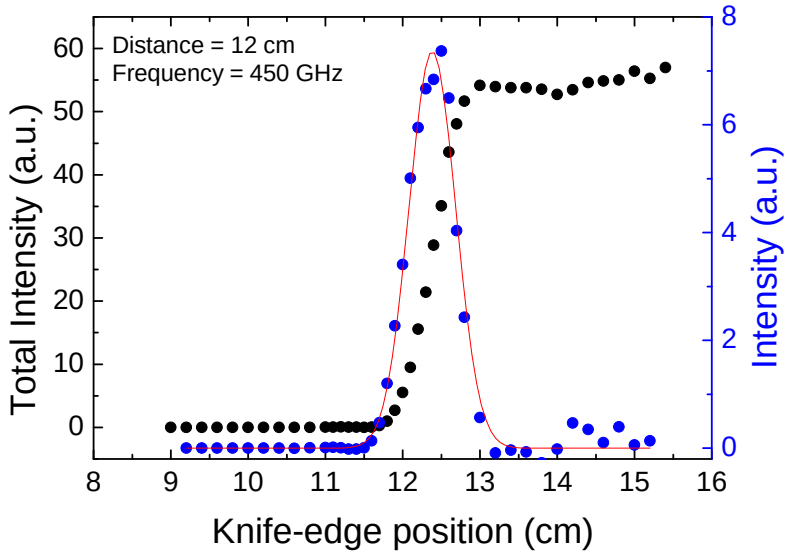

Figure 7.5.: The intensity and its derivative as a function of the knife-edge position. Black dots denote the recorded total intensity while the blue dots denote the calculated derivative. The agreement between the measurement and the corresponding Gaussian fit (red) is very good.

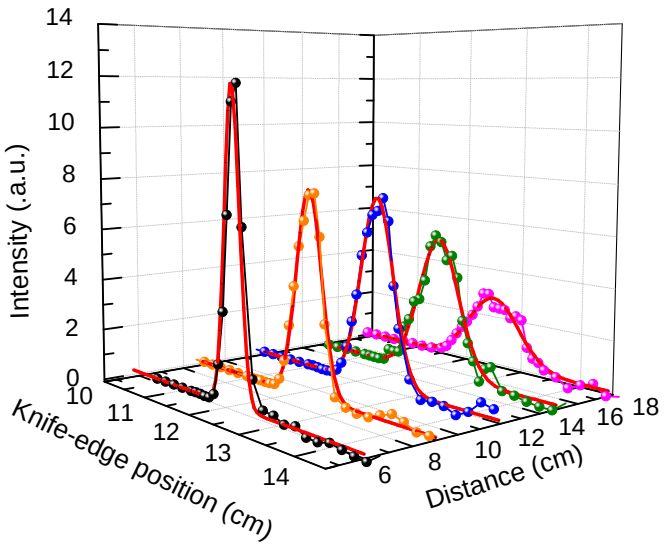

Figure 7.6.: Beam profile at 450 GHz for different distances from the transmitter. The amplitude of the profile decreases and the distribution broadens with increasing distance as expected for a Gaussian beam.

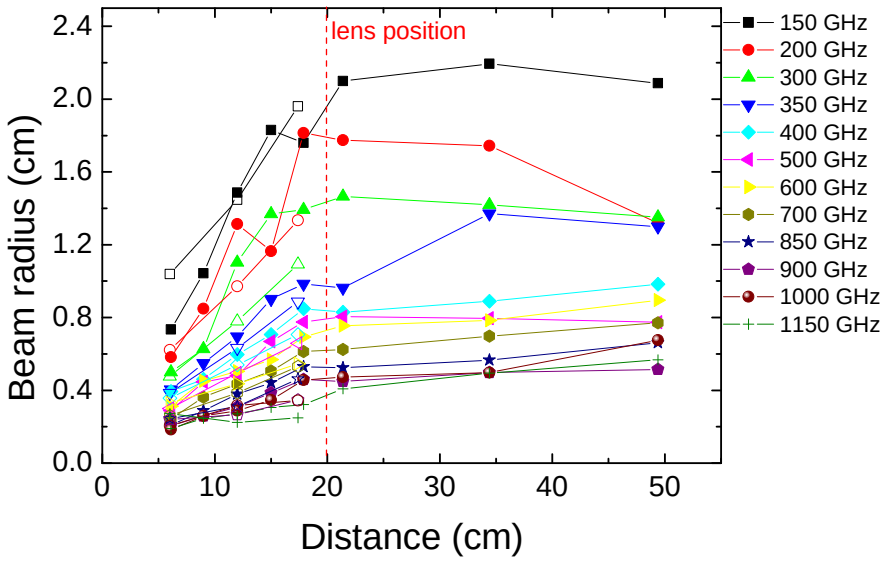

Figure 7.7.: Beam radius as a function of distance from the source for different frequencies. The closed symbols denote the beam radius along the x axis and the open symbols along the y axis. At a distance of 20 cm the collimating lens is sitting and after passing the lens the beam radius stays almost constant, at least below 1 THz.

angle of 7.5° in section 7.1.1) and around 2° for 1 THz. The opening angle as a function of frequency for both axes is given in figure 7.8. It seems to be a bit smaller for the y axis than for the x axis. However, both axes show a similar behavior which indicates that there are no hot spots or other local variations disturbing the beam and that a TEM_{00} mode is present or at least dominant. For distances larger than 20 cm, i. e. behind the collimating lens, the beam is almost parallel over the whole length of 30 cm illustrating the high performance of the lenses (see figure 7.7). The variation of the beam radius observed for 200 GHz and 350 GHz is attributed to the poorer data quality at large distances and low frequencies (see Appendix A.3).

Figure 7.9 finally shows the beam waist at the focal spot as a function of frequency. At 100 GHz, a value of $w_0 \approx 2.6$ mm is determined and w_0 decreases with increasing frequency. For frequencies above 500 GHz the beam waist $w_0 \approx 2$ mm remains nearly constant. To show the consistency with theory, the beam waist was calculated by equation 2.47 from the beam radius measured at a distance of 15 cm behind the collimating lens (red symbols in figure 7.9). The deviation of about 0.5 mm below 300 GHz is assigned to the uncertainty of the knife-edge method at low frequencies due to diffraction. Nevertheless, the measured beam waist is reasonable to investigate single crystal samples. To minimize losses when guiding the beam into an optical cryostat, the divergence angle behind the focusing lens has to

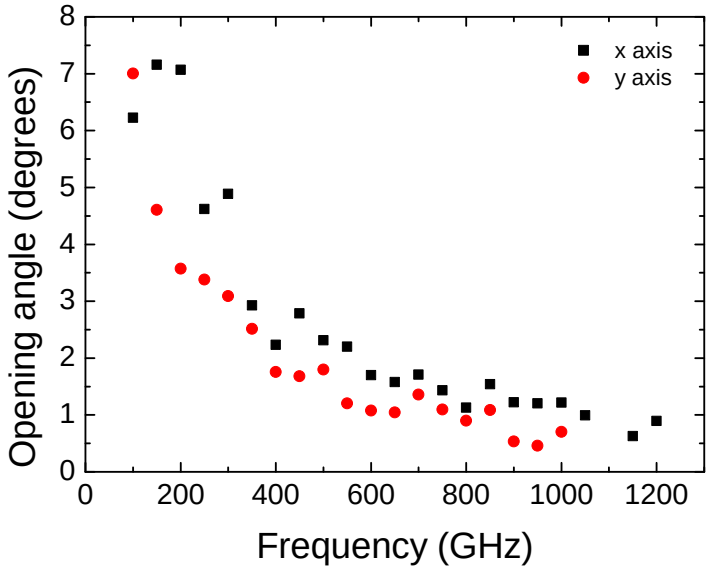

Figure 7.8.: The opening angle as a function of frequency for both axes. The opening angle is smaller for the y axis, nevertheless the behavior for both axes is very similar.

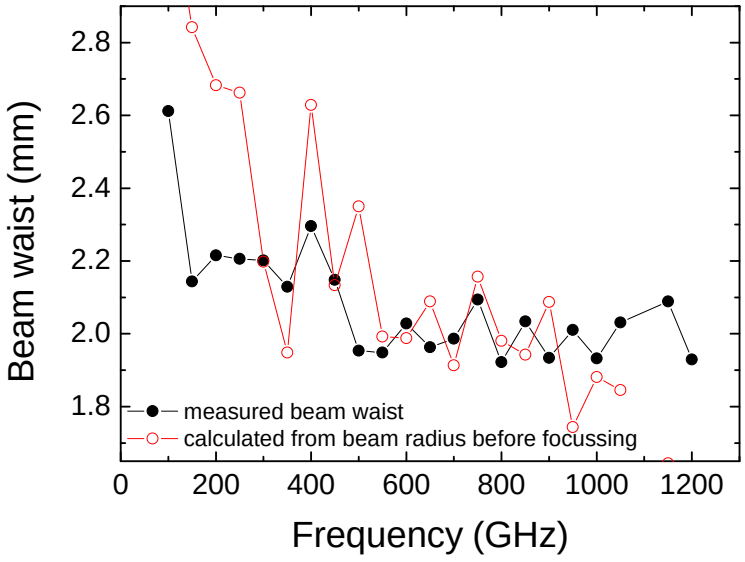

Figure 7.9.: At low frequencies, the beam waist at the focal point decreases with increasing frequency, whereas it is almost constant above 500 GHz.

be considered. The divergence angle can be estimated from the beam radius r_C after the collimation and the size of the beam waist w_0 by $\tan\alpha = (r_C - w_0)/f$ when considering the focal length f of 10 cm. The angle can be calculated to $\sim 11\,^\circ$ for 100 GHz and $\sim 1.6\,^\circ$ for 1200 GHz.

Altogether the lens setup shows a very good performance. The measured total intensity is increased considerably compared to a measurement without using the lenses since all the radiation is collected and guided to the receiver. Effects of standing waves are minimized due to the small absorption of the HDPE. Especially the small beam waist and the divergence angle of the focal spot enable measurements in the cryostat which is desirable for spectroscopy as shown in chapter 9.

7.3. Polarization

A lot of solid-state materials show optical anisotropy which originates from the non-cubic unit cell. An important effect arising from the anisotropy is birefringence which has been extensively studied at visible wavelength [126] but recently also in the THz regime [127–129]. Crystallographic anisotropy leads to anisotropy in optical as well as other physical properties. Some materials exhibit unique properties only in planes or along a certain direction. For example, the superconductivity in doped cuprates takes place in the CuO_2 planes. To investigate the optical anisotropic properties, linearly polarized light is needed.

7.3.1. Polarization dependence of cw THz sources

A certain crystallographic plane can be selected by means of Laue scattering. However, the sample is mounted at a fixed orientation in a cryostat which cannot be changed during a measurement. Therefore the crystallographic direction is usually selected employing a linear polarizer. In order to obtain a high intensity at the sample independent of the orientation of the polarizer, a source which emits either unpolarized or circularly polarized light is desired. The same argument is valid for the detector. For spectroscopy in the infrared regime this is no problem since the black-body sources as well as the used detectors, for example bolometers, have no polarization dependence. However, in the THz regime this is an issue. Many table-top continuous-wave sources such as Gunn diodes or BWOs are linearly polarized [53]. Here either the sample has to be mounted in precise direction or the source has to be oriented which is both quite cumbersome. For the laser based cw THz spectroscopy, it is even more complicated. The polarization of the emitted light depends on the geometry of the antenna. Employing a homodyne-detection scheme which uses a second photomixer for detection implies that the detection is also polarization dependent. For a logarithmic spiral antenna the emitted radiation was reported to be elliptically polarized below 800 GHz [36, 76]. Above 800 GHz the interdigitated finger structure starts to radiate which leads to an increasing linearly polarized

contribution to the elliptically polarized light. A circular polarization of the THz radiation would be very advantageous for polarization-dependent spectroscopy. To check whether the radiation is circularly or elliptically polarized, the polarization was investigated including its frequency dependence.

7.3.2. Measurement of the polarization dependence

In case of the spectrometer used in this work, both the polarization dependence of transmitter and receiver are not exactly known. Nevertheless, transmitter and receiver are identically constructed, which means that it is sufficient to investigate the polarization dependence of one of them. It is prudent to investigate the polarization dependence of the receiver. To do so, first the polarization dependence of the transmitter has to be eliminated. Therefore a linear polarizer is employed so that linearly polarized light with a fixed amplitude radiates on the receiver. The best way to analyze the polarization dependence of the receiver would be to rotate the receiver. In this configuration the intensity radiated on the receiver is always the same and the detected signal is only depending on the orientation of the detector. However, mechanical stress on the optical fiber due to the rotation can change the laser power at the photo-active area and hence the detected amplitude. Since this effect cannot be disentangled from the amplitude change due to the polarization dependence, a rotation of the receiver is unfavorable. Therefore a second polarizer which acts as analyzer is employed. The intensity at the receiver is measured as a function of the analyzer angle φ. If the photomixer exhibits no polarization dependence, the measured intensity is in fact independent of polarization. In this case the measured intensity should only reflect the influence of the two linear polarizers. Since linear polarized light from the polarizer is radiated on the analyzer, the intensity as function of analyzer angle should follow a cosine-squared curve. However, if the receiver exhibits a non-circular polarization dependence deviations from the simple cosine squared are expected. In this case a model which includes a polarization dependence of the receiver has to be used and fitted to the angle-dependent intensity. Therefore a function resembling the polarization dependence of the receiver is multiplied with the cosine-squared behavior expected from the linear polarizers. The exact model is explained in detail below in the course of the analysis. However, at analyzer angles where both polarizers are almost perpendicular, the intensity at the receiver is very low. At those angles the polarization dependence of the receiver cannot be determined accurately. For that reason, the intensity as function of the analyzer angle has to be measured for different polarizer angles.

For the measurement two wire-grid polarizers G50 x 20-S from Microtech have been employed. The polarizers were tilted with respect to beam propagation to minimize standing waves. The intensity as a function of analyzer angle was measured for three polarizer angles, namely 0°, 45°, and 90°. In the measurements the analyzer angle was varied between 0° and 180° in steps of 10°. For each set of angles the frequency ranges between 499 GHz and 502 GHz as well as between

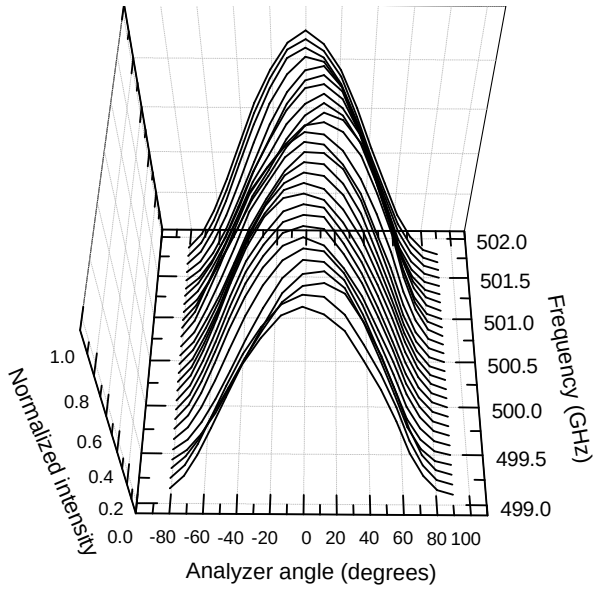

Figure 7.10.: Normalized intensity as a function of analyzer angle between 499 GHz and 502 GHz for a polarizer angle of 0 °.

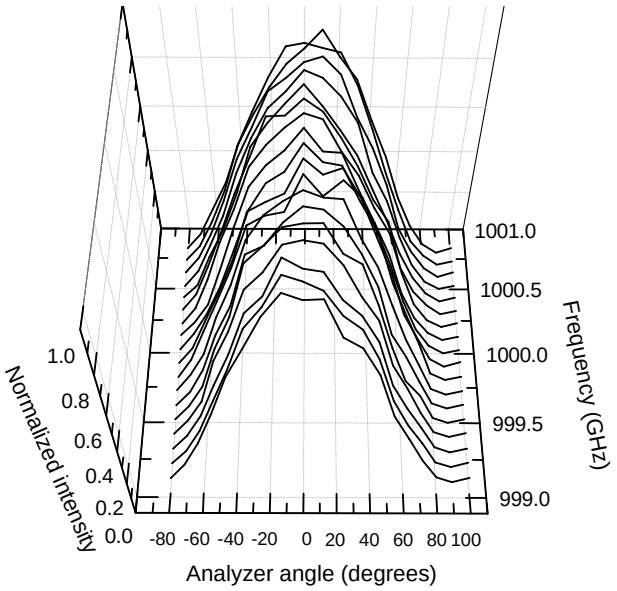

Figure 7.11.: Normalized intensity as a function of analyzer angle between 999 GHz and 1001 GHz for a polarizer angle of 0 °.

999 GHz and 1001 GHz have been measured in steps of 100 MHz. Each frequency range was measured four times in a row and the results were averaged.

Figure 7.10 shows the measured normalized intensity as a function of the analyzer angle between 499 GHz and 502 GHz for a polarizer angle of 0°. It can be seen that the shape of the curves nearly represents a cosine-squared function but exhibits a slight asymmetry. The shift of the position of the maxima shows that the polarization dependence changes rather strongly with frequency. The asymmetry of the curves can be described by assuming an elliptic polarization dependence for the receiver. If the angle between the large half-axis and the polarization vector of the first polarizer is different from 0°, the polarization angle of maximum intensity is different from that of maximum signal. Consequently a side of the peak increases while the other decreases and as a result the maximum is shifted slightly off-center. Figure 7.11 shows the normalized intensity between 999 GHz and 1001 GHz for a polarizer angle of 0°. Due to the lower signal-to-noise ratio, the variation of the polarization dependence with frequency cannot be easily observed. For a quantitative analysis the polarization curves were fitted by a function assuming elliptical polarization dependence of the receiver. The fitted function reads as follows:

$$I = I_0 \cos^2\left(\frac{\varphi + \varphi_0}{\pi}\right) \frac{ab}{\sqrt{(b\cos(\varphi+\theta))^2 + (a\sin(\varphi+\theta))^2}} \tag{7.5}$$

The first term describes the dependence of the intensity on the analyzer angle φ and the second term the elliptic polarization dependence of the detector. The offset φ_0 accounts for a small error in the alignment of the analyzer with respect to the polarizer. The amplitudes of the two half-axes are denoted as a and b. The analyzer angle is denoted as φ and the orientation of the ellipse is given by θ. Note that the curves were normalized and I_0 was set to unity and all other parameters were fitted. In figures 7.12 and 7.13 some exemplary data sets taken from the measurements presented in figures 7.10 and 7.11 are shown together with the corresponding fits (red). The good agreement between data and fits shows that the model represented by equation 7.5 is valid which indicates that the assumption of an elliptical polarization state for the receiver is reasonable and justified.

From the fit the orientation θ of the ellipse as well as the amplitudes of the half-axes a and b are extracted. The angle θ is plotted as a function of frequency in figure 7.14 (c) and (d). It can be seen that the orientation of the ellipse changes strongly with frequency. In the frequency range around 500 GHz a rotation of more than 100° is observed within a few hundred MHz. Simultaneously the ratio of the half-axes is changing (see figure 7.14 (a) and (b)). Between 499.8 GHz and 500.5 GHz the ratio of the half-axes is relatively close to unity. Here, the precise determination of the orientation is difficult. This might indicate that the large change of the orientation of ellipse around 499.2 GHz, 499.6 GHz, and 500.7 GHz is due to the change of the eccentricity. Around 1 THz, the ratio of the half-axes is lower on average as around 500 GHz and thus the orientation of the ellipse is not determined as precisely.

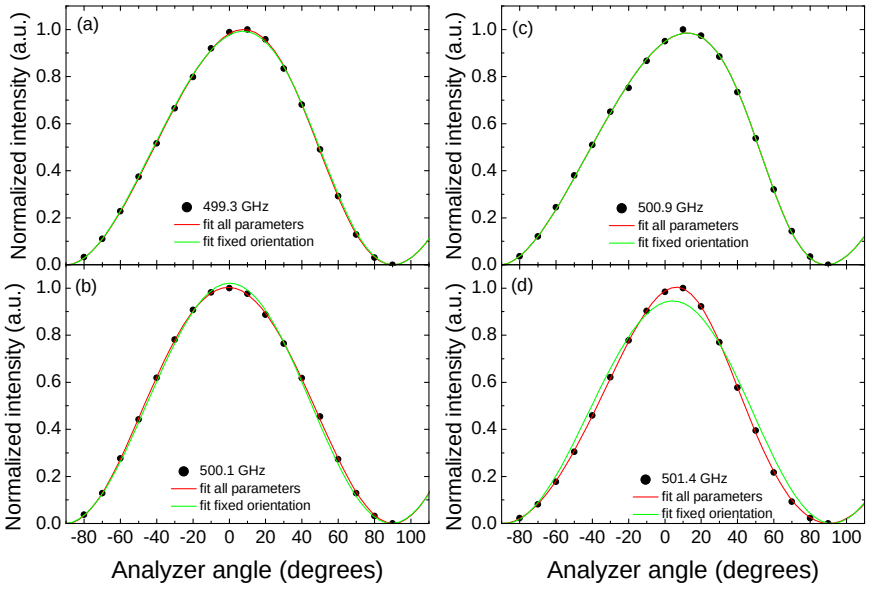

Figure 7.12.: Some of the polarization curves measured with a polarizer angle of 0 ° are shown together with the corresponding fits. For the fit shown in red the orientation of the ellipse was fitted while for the fit shown in green θ was fixed at 40 °.

Therefore a tentative fit was performed, keeping θ at a fixed value. Around 500 GHz the supposed orientation of the ellipse can be extracted at frequencies where the eccentricity is large. Here, the orientation was read off at 499.4 GHz where both the half-axes ratio and the orientation show a peak. At this frequency θ is about 60 ° considering the measurement with a polarizer angle of 0 °. However, the best fitting result for the frequency range was obtained for an intermediate angle of $\theta = 40$ ° (see green curves in figure 7.12). Note that independent of the chosen θ not all curves could be well fitted at the same time, which can be seen in figure 7.14 (d). This indicates that the orientation of the ellipse is changing with frequency. The fast change of both orientation and eccentricity of the ellipse is most probably due to resonances in the logarithmic-spiral antenna [130]. For a perfect logarithmic-spiral antenna the impedance is independent of frequency. However, due to the production tolerance this is not the case. At some distinct frequencies the antenna impedance changes involving a change of the current distribution which directly affects the polarization state, i. e. orientation and eccentricity of the ellipse.

At high frequencies the measured results can be described reasonably by assuming a fixed orientation of the ellipse (see green curves in figure 7.13). Here, θ was set to the average value of about 80 ° in this frequency range. The smaller eccentricity at high frequencies might be a possible reason why the measured data can be described by an ellipse with fixed orientation. Still, the small eccentricity at high frequencies

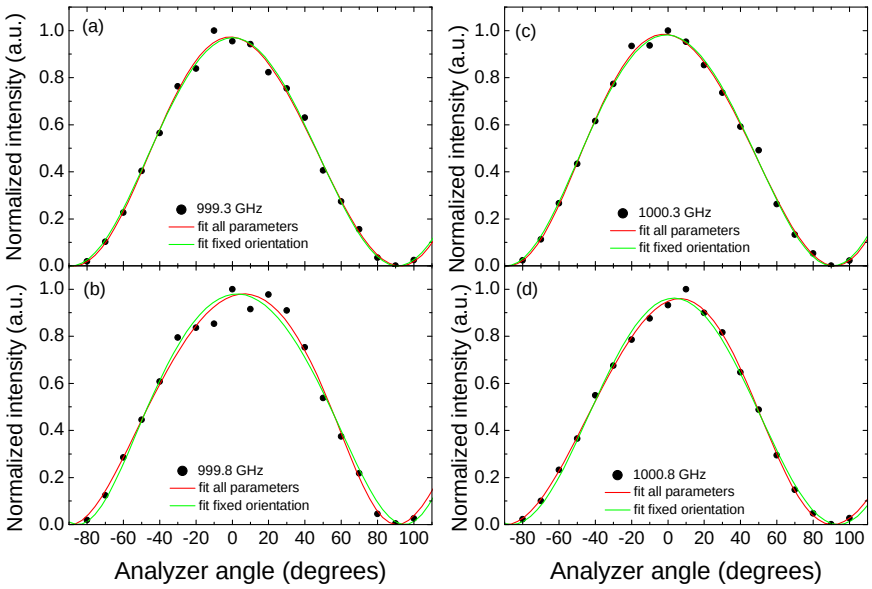

Figure 7.13.: Some of the polarization curves measured with a polarizer angle of 0° are shown together with the corresponding fits. For the fit shown in red the orientation of the ellipse was fitted while for the fit shown in green θ was fixed at 80°.

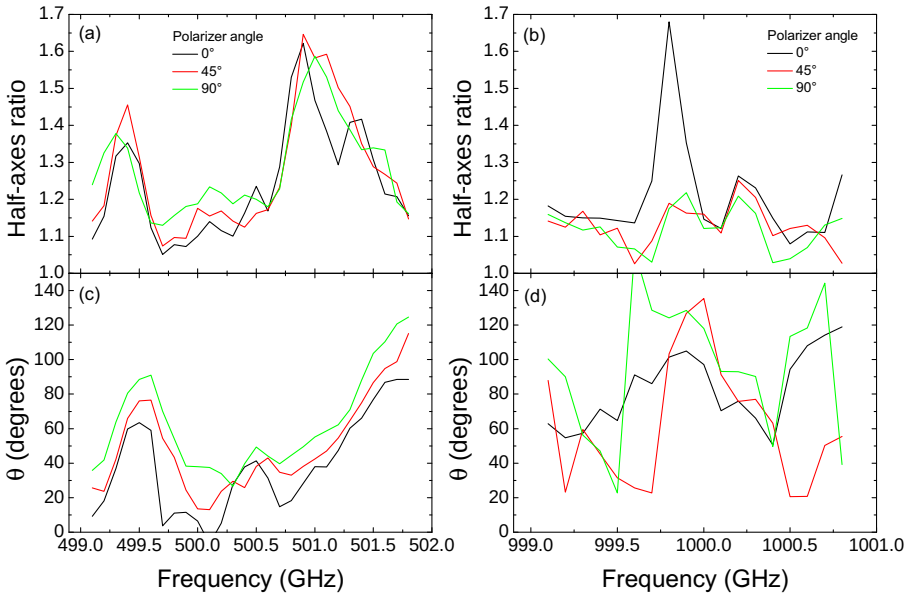

Figure 7.14.: The frequency dependence of the half-axes ratio and the ellipse orientation θ. The left side shows the data around 500 GHz and the right panel the data around 1 THz.

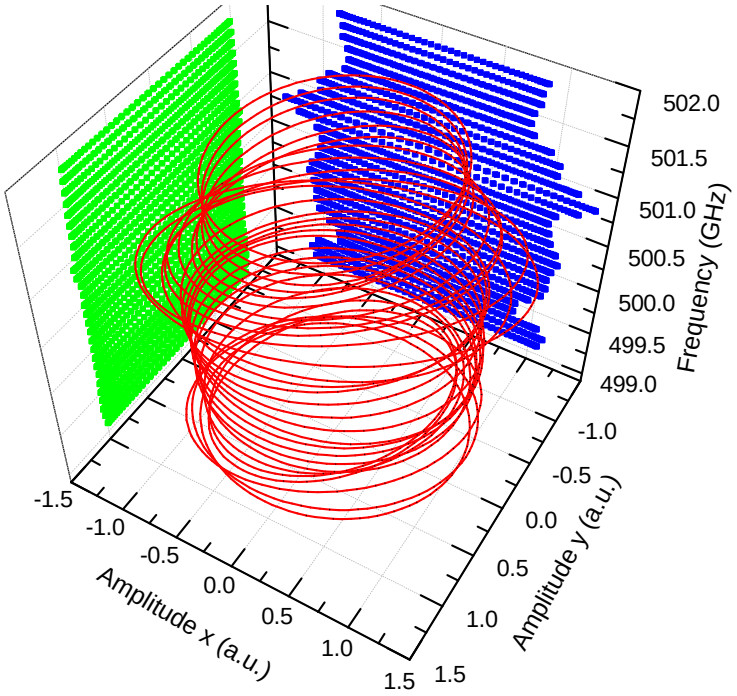

Figure 7.15.: Form and orientation of the ellipse as a function of frequency around 500 GHz extracted from the analysis with θ being a fit parameter. The projections on the x axis and y axis are shown in blue and green, respectively.

is unexpected since the polarization dependence of logarithmic-spiral antennas was found to become more linear with increasing frequency [36, 76]. Figures 7.15 and 7.16 show the form and orientation of the ellipses as a function of frequency extracted from the analysis with θ being a fit parameter. The plot is given in Cartesian coordinates:

$$x = a \cdot \cos(\psi)\cos(\theta) - b \cdot \sin(\psi)\sin(\theta) \tag{7.6}$$

$$y = a \cdot \cos(\psi)\sin(\theta) + b \cdot \sin(\psi)\cos(\theta) \qquad \text{with } 0 \leq \psi \leq 2\pi \tag{7.7}$$

In the frequency range around 500 GHz a very pronounced change of the elliptical shape is observed at 500.8 GHz. For all other frequencies in this range, the ellipse shows smaller changes. Remarkably, the projection on the y axis (green) is almost constant at unity for both frequency ranges. Only the projection on the x axis (blue) shows changes. At 499.4 GHz and above 500.8 GHz it is smaller than unity due to the strong change of the orientation of the ellipse. Except for the value of 999.8 GHz, the changes of the projection on the x axis are quite small in the frequency range around 1000 GHz which was already indicated by the nearly constant ratio of the half-axes (see figure 7.14 (b)). In this range the receiver still exhibits an almost circular polarization dependence.

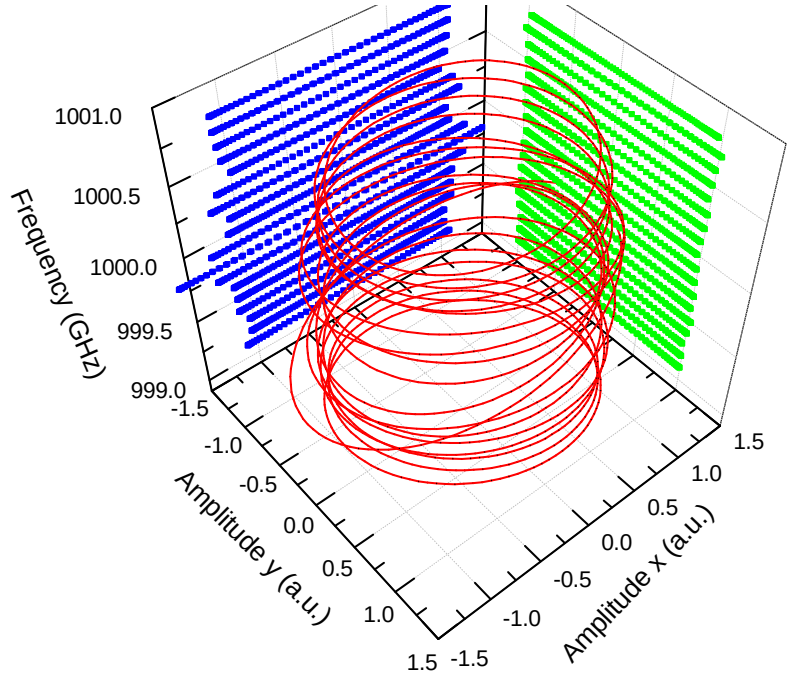

Figure 7.16.: Form and orientation of the ellipse as a function of frequency around 1000 GHz extracted from the analysis with θ being a fit parameter. The projections on the x axis and y axis are shown in blue and green, respectively.

In summary the results show that the photomixers exhibit an elliptical polarization dependence which has a relatively small eccentricity even at high frequencies. Consequently the orientation of a single polarizer can be chosen freely without changing the intensity significantly. This is advantageous for polarization dependent measurements since the polarization vector of linearly polarized light can be adjusted to any crystallographic direction.

8. Measurements on MgO

Magnesium oxide (MgO) is almost non absorbing in the THz spectral range. Only the tail of phonons at higher frequencies influences the optical functions [109]. Due to the weak absorption, Fabry-Perot fringes are very pronounced. Additionally the static dielectric constant is relatively low so that MgO is considered as substrate for high-T_C superconducting materials [131, 132]. Measurements on MgO were performed using all three different methods discussed in chapter 5. In the first part of this chapter the results of the frequency-scan method and the fiber-stretcher method are compared. To show the improvement of the phase stability by the three-laser method, in the second part of this chapter the results of the three-laser method are discussed.

8.1. Comparison between frequency-scan method and fiber-stretcher method

For all measurements shown in this chapter a 1 mm thick and 3 mm × 3 mm large piece of MgO was used. In the frequency-scan method small spectral ranges with an overlap of 40 GHz were measured as described in section 5.1.3. For each spectral range the spectrum was measured five times by switching between sample and reference after every frequency sweep. The different results were averaged. Finally the different spectral ranges were merged. The effective resolution, i.e. the photocurrent period in this measurement is about 500 MHz. Hence, to resolve the oscillations of the photocurrent, the actual frequency step size was 30 MHz. Due to the effective resolution of 1 GHz used in the fiber-stretcher method, the time per frequency sweep decreases considerably and the whole frequency range was measured in one go. Three spectra were measured by switching between sample and reference after every frequency sweep and the results were averaged. Note that 1 GHz is still a very good resolution for solid-state spectroscopy where linewidths are usually larger than several ten GHz. Here, the period of the Fabry-Perot fringes is about 50 GHz. Figure 8.1 shows the transmittance and the effective sample thickness obtained by both methods. Note that the frequency-scan measurement was performed using the 850 nm laser diodes whereas for the fiber-stretcher measurement the 780 nm diodes were implemented. Hence, for the frequency-scan method the spectrum is measured over a broader frequency range (see section 4.1.1). The data shown here is smoothed by adjacent averaging over 5 GHz to reduce the standing-wave pattern (see section 6.2). As a result of the correction of the absolute value of L_{eff}, a constant offset

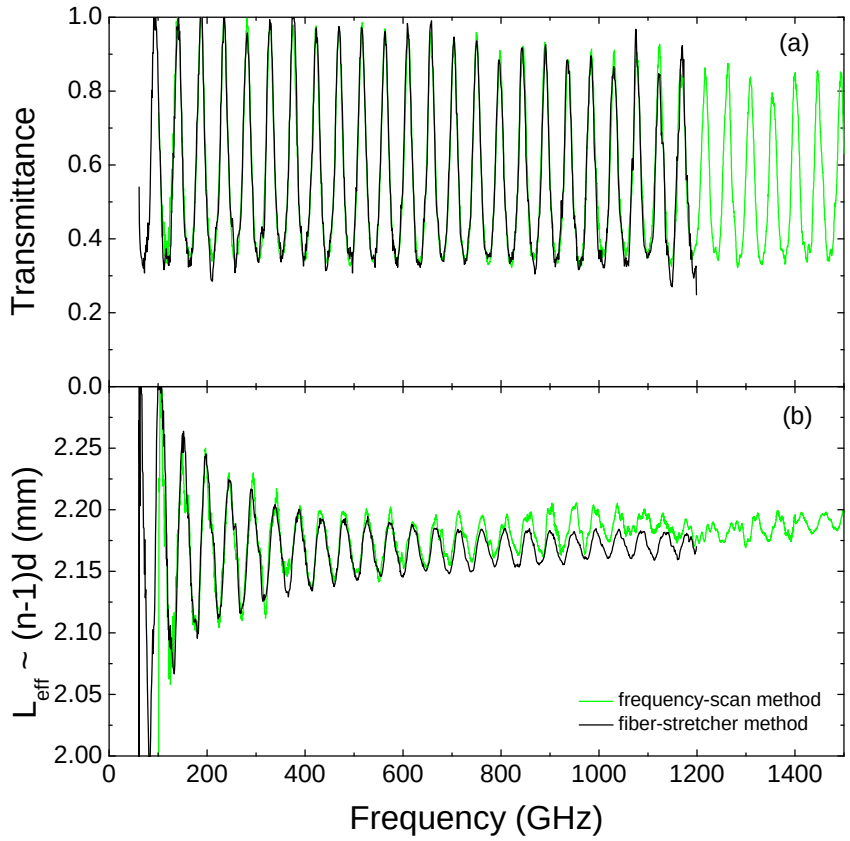

Figure 8.1.: (a) Transmittance of MgO measured by the frequency-scan method (green) and the fiber-stretcher method (black). (b) The corresponding effective sample thicknesses.

of 3 μm was added for fiber-stretcher data (section 5.4). Both transmittances are comparable. However, to obtain such quality by the frequency-scan method about one week of measurement was necessary whereas the data of the fiber-stretcher method was obtained in half a day. The effective sample thickness is comparable for frequencies below 600 GHz, but the envelope of the fiber-stretcher data shows a more continuous behavior. Above 700 GHz the envelope of the frequency-scan data shows large discontinuities. The effective sample thickness first increases up to about 950 GHz and then drops again. Due to the long measurement time of about 30 minutes per frequency sweep and the fact that ΔL cannot be set to almost zero in the frequency-scan method, rather large fluctuations in ΔL can be induced by fluctuations in the environmental conditions. This has a large effect on L_{eff}. Here, the deviation between the two values of L_{eff} amounts to up to 30 μm. Such fluctuations prevent the precise determination of the complex optical functions.

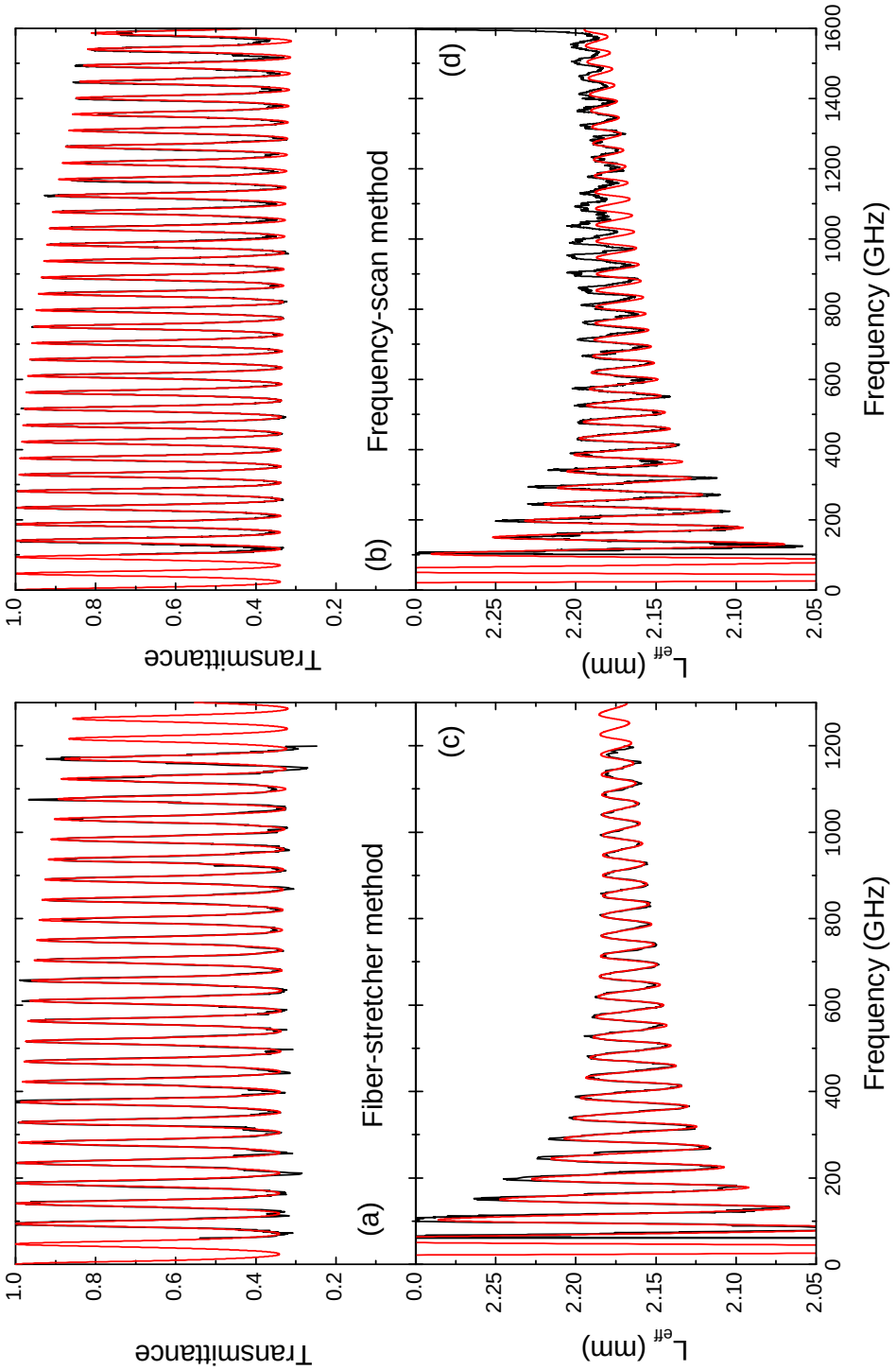

Figure 8.2.: Panel (a) and (c) show the transmittance and effective sample thickness of MgO measured with the fiber-stretcher method. The Drude-Lorentz fit is depicted in red. The results obtained with the frequency-scan method together with the corresponding fit are shown in panel (b) and (d).

For both measurements the data was fitted by a model containing a single Lorentz oscillator at $\nu_0 = 11.87$ THz [109]. Following reference [109], $\varepsilon_\infty = 2.85$ and $\nu_0 = 11.87$ THz were considered as fixed parameters in the fit. Note that the phase data of the frequency-scan measurement was only fitted below 600 GHz due to the large fluctuations. Figure 8.2 shows the data and the corresponding fits. The extracted parameters are given in table 8.1.

Table 8.1.: Extracted plasma frequency ν_p, damping constant $\gamma/2\pi$, and sample thickness d of the Drude-Lorentz model

Method	ν_p (GHz)	$\gamma/2\pi$ (GHz)	d (mm)
Fiber stretcher	31.02 ± 0.13	165 ± 9	1.026 ± 3
Frequency scan	31.12 ± 0.14	144 ± 27	1.025 ± 3

The agreement between fiber-stretcher data and the fit is very good for both transmittance and L_{eff}. Concerning the data obtained by the frequency-scan method, the transmittance is well described by the fit. For L_{eff} there is good agreement between data and fit within the fitted range. Around 900 GHz the deviation between data and fit is about 15 μm. Note again, that for the frequency-scan method ΔL cannot be set to zero and hence drifts δL of ΔL larger than 20 μm can occur. Reducing the time span between sample and reference measurement decreases fluctuations of ΔL, still they cannot be completely suppressed. The parameters obtained by the two methods agree within the errorbars. Due to the larger frequency range measured by the frequency-scan method, the decrease in the transmittance can in principle be fitted more accurately. However, the envelope of the transmittance is not continuously falling which leads to a larger uncertainty in the extracted γ. Note that the thickness obtained by the fit agrees well with the mechanically measured thickness of (1.026 ± 0.002) mm.

Figure 8.3 shows the refractive index n and the extinction coefficient κ obtained by the inversion method and the PDL fit (see section 5.5) together with the ones extracted from the Drude-Lorentz fit of the entire frequency range. For both, the inversion method and the PDL fit, the fitted range was chosen to be 50 GHz which corresponds to one period of the Fabry-Perot oscillations. The sample thickness used for analysis was the one obtained by the fit of the entire data. Note that for the PDL fit ν_0 as well as d were fixed parameters (see section 5.5). For the fiber-stretcher data as well as for the frequency-scan data, the results of both methods are similar, as seen in section 5.5. Due to the low absorption, the exact values of κ are difficult to determine (see chapter 5.5). Still both results are in good agreement with n and κ extracted from the fit of the entire data. The anomalous increase of L_{eff} observed in the frequency-scan data around 900 GHz influences the result of both analyses in the same way. Here, also n shows an anomalous increase.

The refractive indices n obtained from the fiber-stretcher data as well as the frequency-scan data show the same general behavior but the fluctuations are much

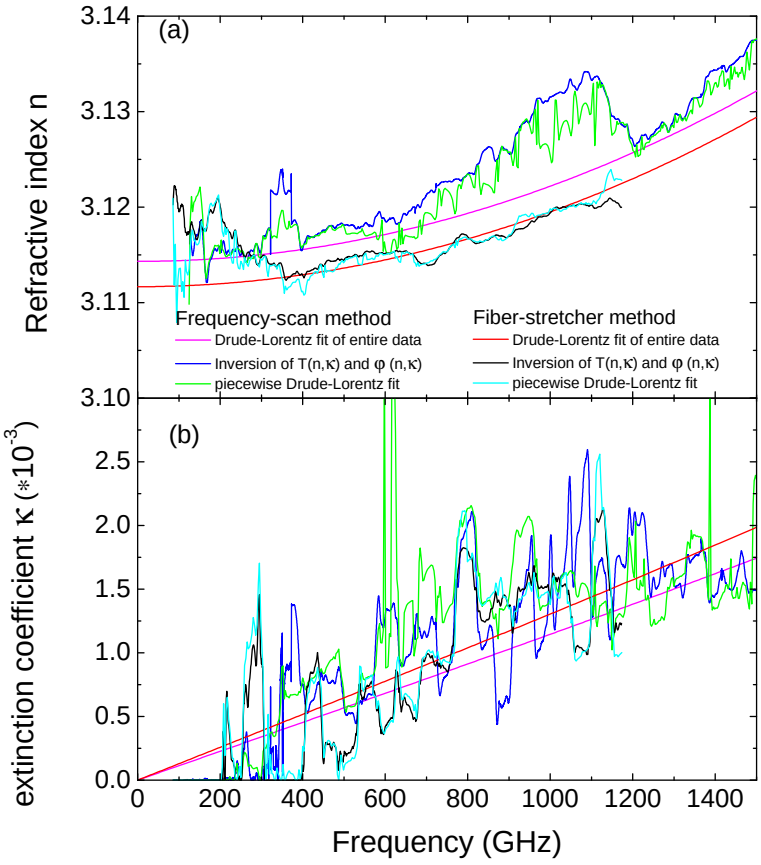

Figure 8.3.: Refractive index and extinction coefficient obtained from frequency-scan and the fiber-stretcher data by the inversion method as well as the PDL fit. The values extracted from the Drude-Lorentz fit of the entire frequency range are shown in red and magenta.

larger for the frequency-scan data. Due to the longer measurement time, the frequency-scan method is more prone to drifts. The values obtained for $n_{\nu\to 0}$ are 3.112 and 3.114 for the fiber-stretcher and the frequency-scan method, respectively. The small offset is due to the uncertainty in the absolute value of L_{eff}. Both values are in good agreement with $n_{\nu\to 0} = 3.11$ which was reported by Pimenov *et al.* [133]. However, as mentioned above the phase data of the frequency-scan measurement was only fitted below 600 GHz neglecting pronounced drift above 700 GHz whereas for the fiber-stretcher data the whole frequency range was used. Especially the results obtained by the frequency-scan method show that it is mandatory to correct for the fluctuations in ΔL to extract the precise frequency dependence of n and κ. In the next section it is shown that the correction of the relative phase fluctuations results in a very precise determination of n and κ.

Table 8.2.: Extracted fit parameters

Fixed frequency ω_{ref} (GHz)	sweep range ω_{tb1} (GHz)	sweep range ω_{tb2} (GHz)
371	60 - 750	431 - 1121
272	60 - 700	332 - 972
170	60 - 1000	230 - 1170
-178	700 - 1300	522 - 1122

8.2. Comparison of 3-laser setup and 2-laser setup

The same 1 mm thick MgO crystal as in the previous section was measured with the 3-laser setup using different values of ω_{ref} listed in table 8.2. The frequency ω_0 was calculated from the first few frequencies of the corresponding reference measurements as described in 5.3.2. The measurements were performed with and without absorber to take standing-wave effects into account. Still, for the measurements with absorber, the noise in the range where ω_{tb1} and ω_{tb2} overlap is high due to lower intensity. Since this range is important for the following discussion, the data measured without absorber is shown. The data measured with absorber is given in Appendix A.5.

Figure 8.4 shows the transmittance and the effective sample thickness for two different values of ω_{ref}, namely 371 GHz and 170 GHz, together with data from a fiber-stretcher measurement discussed in section 8.1. Note that the transmittance was smoothed by adjacent averaging over 5 GHz for better comparison. Agreement between the transmittance of MgO measured by the three-laser method and the two-laser method is very good. The inset of figure 8.4 (c) shows a section of the transmittance for $\omega_{\mathrm{ref}} = 371$ GHz. It can be seen that the Fabry-Perot patterns really lie on top of each other demonstrating that the determination of ω_0 is very precise. When two frequencies are comparable the fit routine cannot differentiate anymore which amplitude and phase to assign to which frequency. Hence amplitude and phase of two similar frequencies can be interchanged for some frequencies which then results in jumps of transmittance and phase in the evaluated data [105]. This effect can be seen in the transmittance data for $\omega_{\mathrm{ref}} = 170$ GHz in figure 8.4 (b) around 170 GHz. Here ω_{tb1} is comparable to the stable frequency ω_{ref}.

In principle the covered range increases with decreasing ω_{ref} since the maximum reachable frequency of ω_{tb1} increases. However, since the starting frequencies of all three lasers are roughly the same, ω_{if} has to be set close to its minimum value to measure the whole frequency range with one choice of ω_{ref}. To measure the highest reachable frequencies both iScan-controlled lasers have to be operated close to their temperature and current limits which is unfavorable for lifetime of the laser diodes. Therefore, the whole spectral range is measured with two choices of ω_{ref} to keep the time at which the laser diodes are operated at extreme conditions as short as possible.

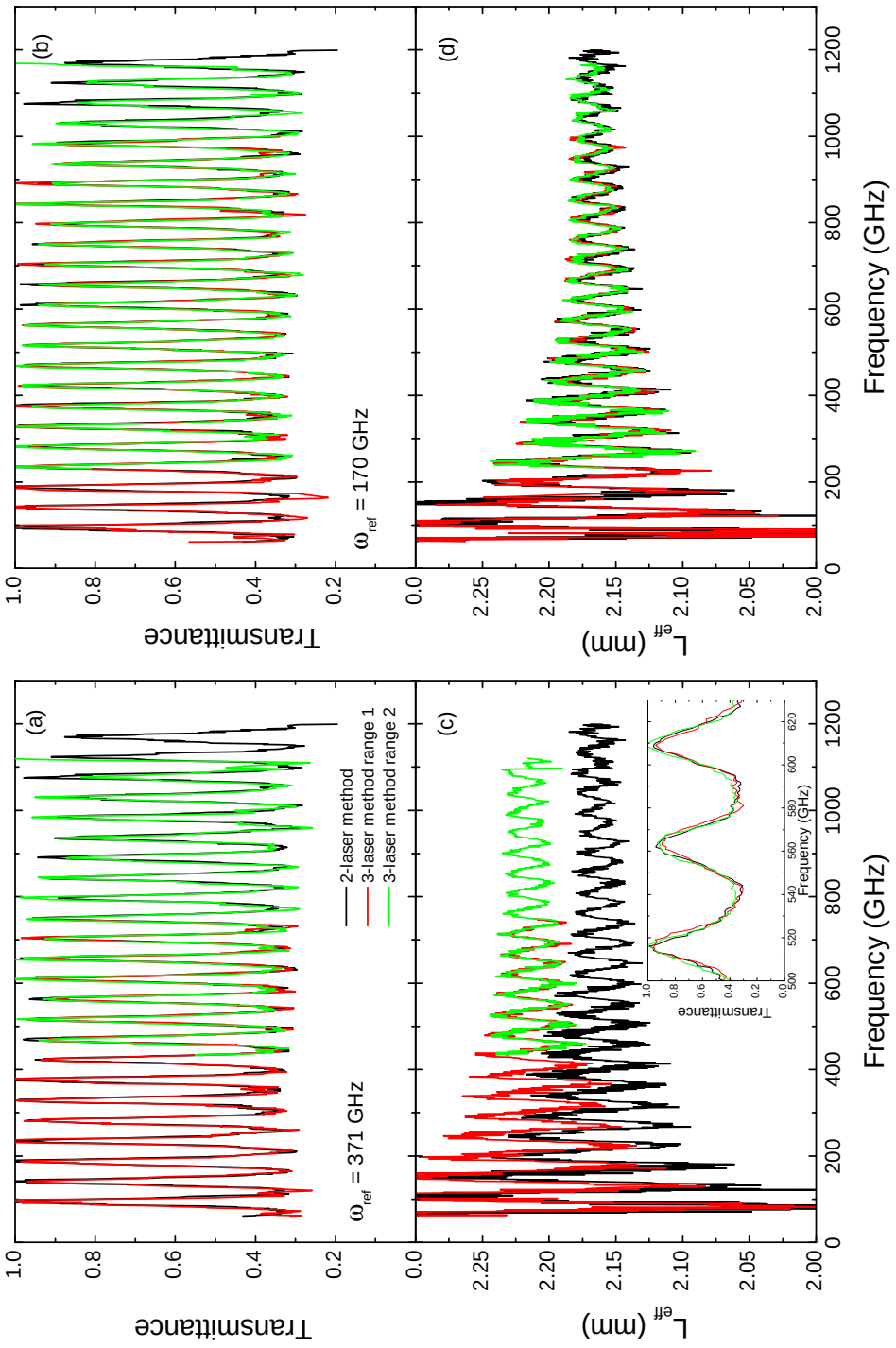

Figure 8.4.: Panel (a) and (b): Comparison between the transmittance of MgO obtained with the 2-laser setup and 3-laser setup for $\omega_2 = 371$ GHz (panel (a)) and $\omega_2 = 170$ GHz (panel (b)). The corresponding effective sample thicknesses $(n-1)d$ are shown in panel (c) and (d). The inset shows a section of the transmittance shown in panel (a).

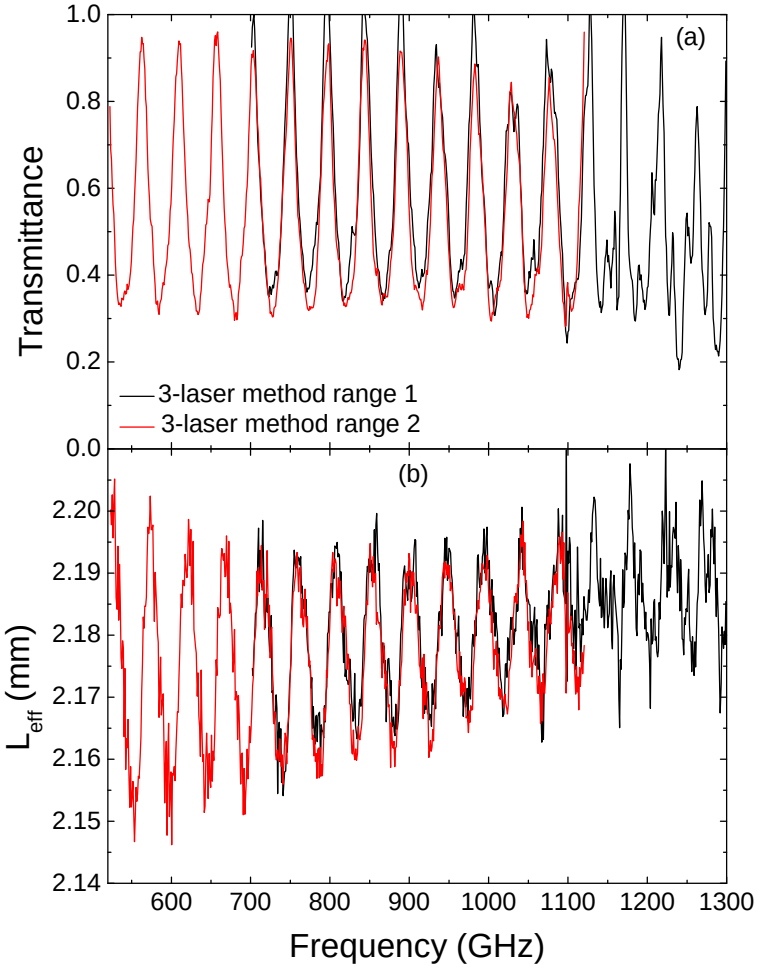

Figure 8.5.: (a) Transmittance of MgO measured with the 3-laser method for $\omega_{\mathrm{ref}} = -178$ GHz. (b) Corresponding effective sample thickness $(n-1)d$.

However, it is also possible to take advantage of the different laser powers. Since the efficiency of the photomixers is decreasing with increasing frequency, it is favorable to have higher laser power at higher frequencies. For $\omega_{\mathrm{ref}} > 0$, the high frequency range is covered by ω_{tb2} which is the beat signal between ω_{it} and ω_{Rb}. The latter has the highest output power as discussed in section 5.3.2. For $\omega_{\mathrm{ref}} < 0$ the lower frequency range is covered by ω_{tb2}. Nevertheless, for the minimum of $\omega_{\mathrm{ref}} = -178$ GHz chosen here, ω_{tb2} still covers frequencies up to 1.1 THz. In figure 8.5, the transmittance and the effective sample thickness L_{eff} for the measurement with $\omega_{\mathrm{ref}} = -178$ GHz are shown. The higher quality of the data in the high frequency range offered by ω_{tb2} (shown in red) can be clearly observed.

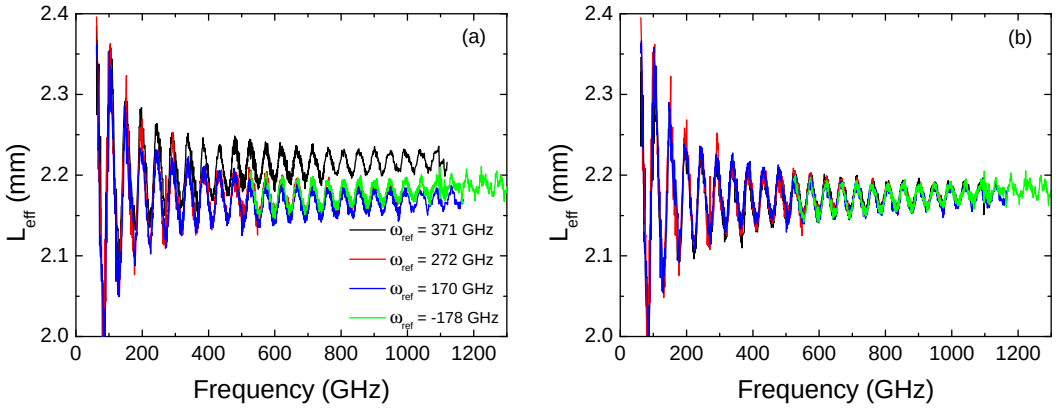

Figure 8.6.: (a) Effective sample thickness measured for different ω_{ref} before correction of the absolute value. (b) Effective sample thickness after the correction.

Table 8.3.: Extracted fit parameters

Parameter	Result
ε_∞	2.85 (fixed)
ν_0	11.87 THz (fixed)
ν_p	30.98 THz
$\frac{\gamma}{2\pi}$	196 GHz
d	1.026 mm

The deviation between the effective sample thickness obtained by the two-laser measurement and the three-laser measurement for $\omega_{\mathrm{ref}} = 371$ GHz shown in figure 8.4 (c) is due to the limited precision concerning the absolute value of ΔL. To have a closer look on the phase data, the performance of the correction of the absolute value of L_{eff} will be demonstrated. Figure 8.6 (a) shows L_{eff} which is already corrected for the relative changes for all sets of ω_{ref} as described in section 5.3.1. Note that the different frequency regions measured by ω_{tb1} and ω_{tb2} are merged for the following analysis. Deviations in the absolute value of L_{eff} amount to up to 25 μm. The correction was carried out like described in section 5.4. To determine the frequencies of the interference maxima a simple peak search was done. For frequencies above 200 GHz a range of 5 GHz around the found peaks was fitted with a parabola to determine the frequencies of the extrema accurately. The mechanically determined thickness of 1.026 mm was used to calculate the refractive index $n_{T,i}$ at each extremum and all $n_{T,i}$ were averaged. For the correction, the refractive index calculated from the phase data $n(\omega)_\varphi$ was shifted by a constant offset such that the mean of $n(\omega)_\varphi$ coincides with the average of $n_{T,i}$. Note that for correction in case MgO the frequency dependence of n was neglected. The result of this correction is shown in figure 8.6 (b). It can be seen that all curves are lying on top of each other.

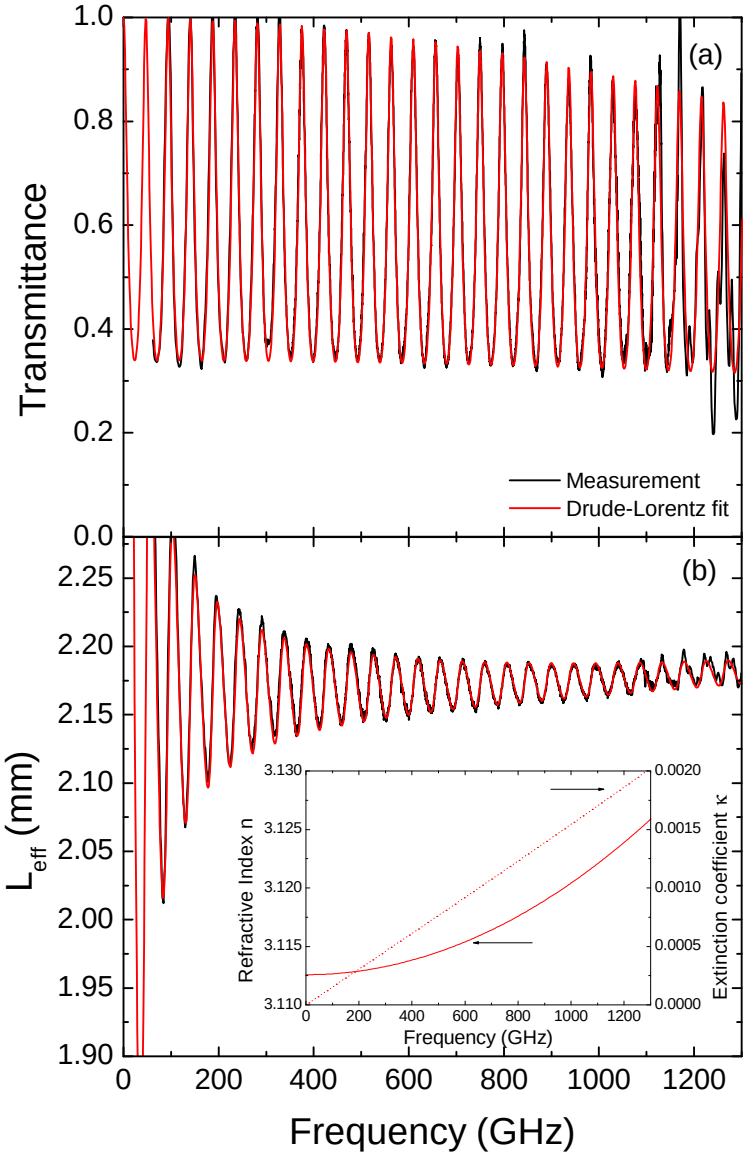

Figure 8.7.: (a) Averaged transmittance of all measurements with different ω_{ref}. (b) Corresponding averaged effective sample thickness $L_{\mathrm{eff}} \approx (n-1)d$. The Drude-Lorentz fit is shown in red. The inset shows the refractive index and the extinction coefficient extracted from the Drude-Lorentz fit.

To fit a model to the data, the data for the different frequencies ω_{ref} were averaged and smoothed. Like in the previous section, a simple model with one oscillator at $\nu_0 = 11.87$ THz to account for the phonon excitation at higher frequencies was

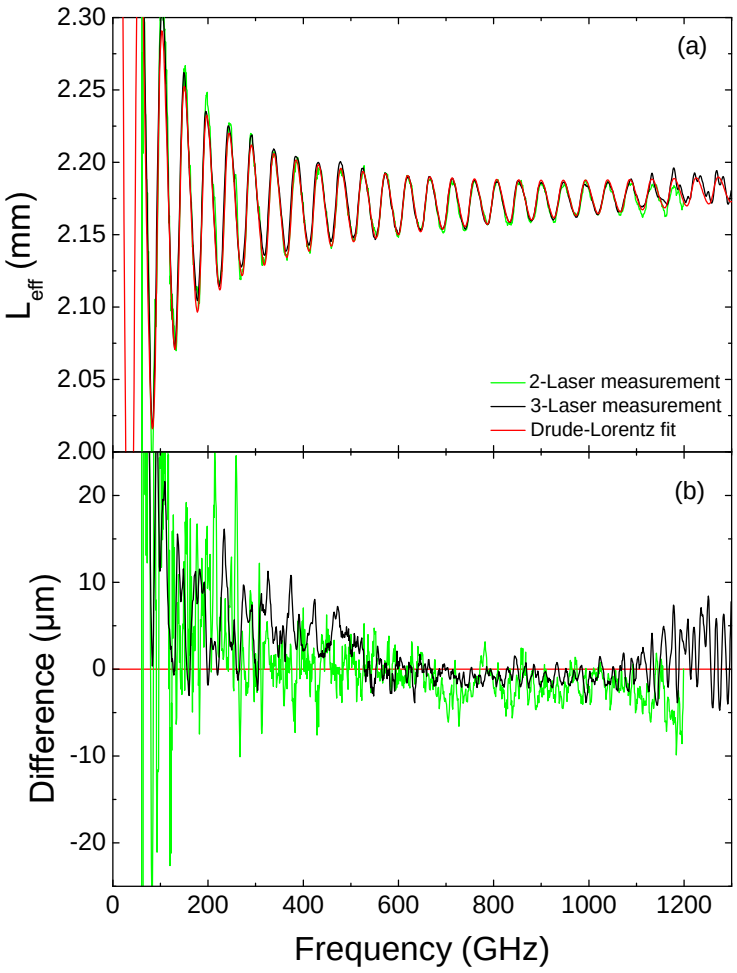

Figure 8.8.: (a) Effective sample thickness of MgO measured with the 2-laser setup and 3-laser method together with the fit of the 3-laser data. (b) Difference between the measured L_{eff} and the Drude-Lorentz fit.

fitted to the data. Thereby, the resonance frequency ν_0 and ε_∞ were kept constant like given in reference [109]. The result of the fit is shown in figure 8.7 and the corresponding values are given in table 8.3. The agreement between the data and the fit is very good. Especially in the phase only very small deviations between fit and data can be seen. The refractive index and extinction coefficient extracted from the model are shown in the inset of figure 8.7. For $\nu \to 0$ the refractive index n approaches 3.113 which is in excellent agreement with the literature [133].

To prove the superior quality of the phase measurement with the three-laser system, both L_{eff} measured with the two-laser setup and three-laser system are plotted

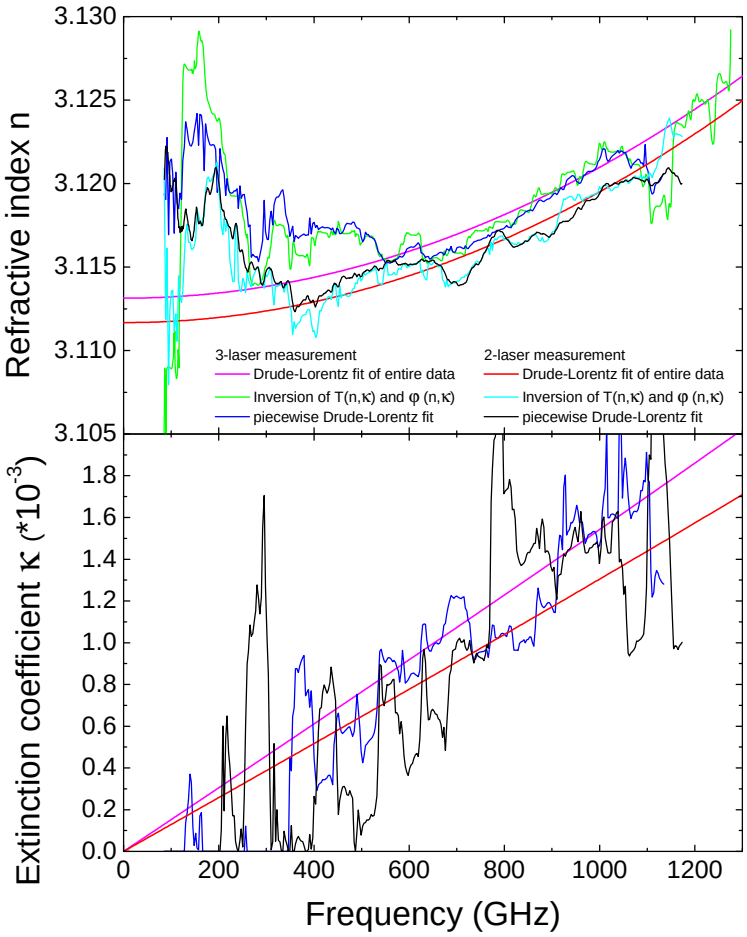

Figure 8.9.: Comparison of the refractive index and extinction coefficient of MgO measured with the 3-laser setup and the 2-laser setup. Shown are the results obtained by the inversion method, the PDL fit, and the Drude-Lorentz fit of the entire frequency range.

together with the fit in figure 8.8 (a). For the two-laser method the L_{eff} obtained by the fiber-stretcher method in section 8.1 is shown. For a more detailed analysis the fit was subtracted from both measured curves. The result is shown in figure 8.8 (b). Below 500 GHz, both curves show deviations from the fit. However, the fluctuations in the two-laser data are larger than for the three-laser data. For frequencies above 500 GHz the data of both methods agree well with the fit. Still, fluctuations in the two-laser data are more than a factor of two larger compared to the three-laser data. The deviations are about 7 μm and 3 μm for the two-laser measurement and the three-laser measurement, respectively.

The refractive indices and extinction coefficients obtained from the different data sets are shown in figure 8.9. It can be seen, that the higher data quality of the measurement with the three-laser setup results in a higher precision of the extracted n and κ. For frequencies above 500 GHz, the n obtained by the two analysis methods show a very smooth behavior and less deviations from the refractive index extracted from the fit of the entire data than for the two-laser measurement (see figure 8.9 (a)). The influence of the data quality is seen clearly in the results of the extinction coefficient. The discontinuities are much smaller in κ determined from the three-laser data (see figure 8.9 (b)). Since the analysis of n and κ by the inversion method and the PDL fit show very similar results (see section 5.5), for κ only the results of the latter method are shown.

Overall the performance of the phase correction is very powerful. It has been shown that temporal fluctuations of the path-length difference can be corrected with this method. Also the uncertainty between L_{eff} of different measurements could be minimized by the correction of the absolute value. Thus the accuracy of the determination of the refractive index was improved considerably.

9. Measurements on silicon

Investigation of the dynamics of carriers in semiconductors is very important in scientific research. Interesting phenomena occur mostly at frequencies comparable to the plasma frequency or the damping rate which for many materials lie in the THz range (see [134] and references therein). Also for industry, THz spectroscopy can be very interesting, for example as contactless method for testing the doping concentration and conductivity of wafers. Silicon is a widely investigated material. In THz spectroscopy extensive studies with time-domain spectroscopy have been performed by Grischkowsky *et al.* [134–137] and Hangyo *et al.* [138–142] but also THz imaging on Si wafers has been performed [143].

In this section cw THz spectroscopy of silicon is presented. A 0.5 mm thick piece of a high-resistivity silicon wafer was investigated. In the first part room-temperature measurements are presented. In the second part of the chapter temperature dependent measurements are shown. To keep the measurement time at low temperatures short, in this chapter the fiber-stretcher method was used for all presented measurements (see section 5.2).

9.1. Room-temperature measurements of silicon

For the room-temperature measurements the silicon wafer was mounted on a holder with an aperture of 16 mm in diameter. The frequency range from 60 GHz to 800 GHz was measured with absorbers in the THz path. As absorbers 2.5 mm thick pieces of cardboard were used, one between sample and transmitter and the other between sample and receiver. In the range from 700 GHz to 1.2 THz, the signal was too low so that it had to be measured without absorbers. The measurement was not performed by alternatively switching between sample and reference. Because of the possibility to correct amplitude drifts by the photocurrent correction, several sample runs were measured before switching to the reference where again several runs were measured in direct succession. This method saves the time of switching between sample and reference after every frequency sweep. For the analysis of the data the single sample and reference measurements were photocurrent corrected as described in section 4.1.7. Before averaging, all single runs were plotted together to eliminate those that despite photocurrent correction display a relatively strong deviation from the others. The final transmittance was calculated from the averaged amplitudes.

However, the averaging of the phase data is more complicated. To average the phase data, the drifts of ΔL between the single measurements have to be taken

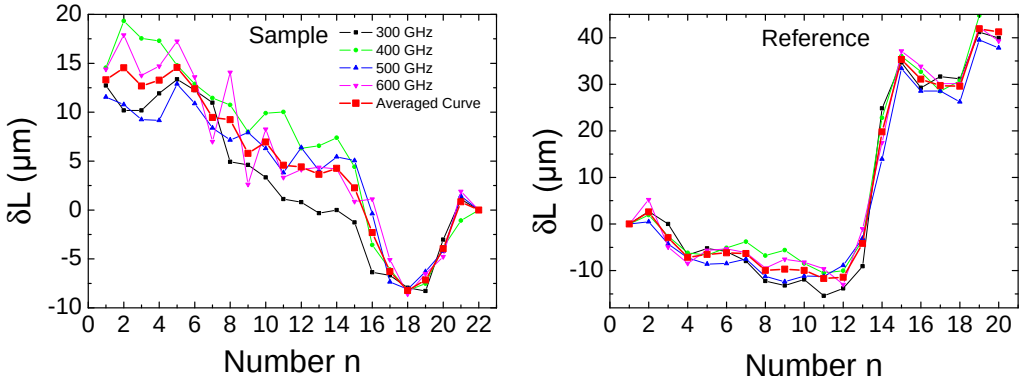

Figure 9.1.: Left: Deviation of ΔL of the sample measurements with respect to the last measurement for different frequencies. Right: Deviation of ΔL of the reference measurements with respect to the first measurement for different frequencies. The red curve is the average.

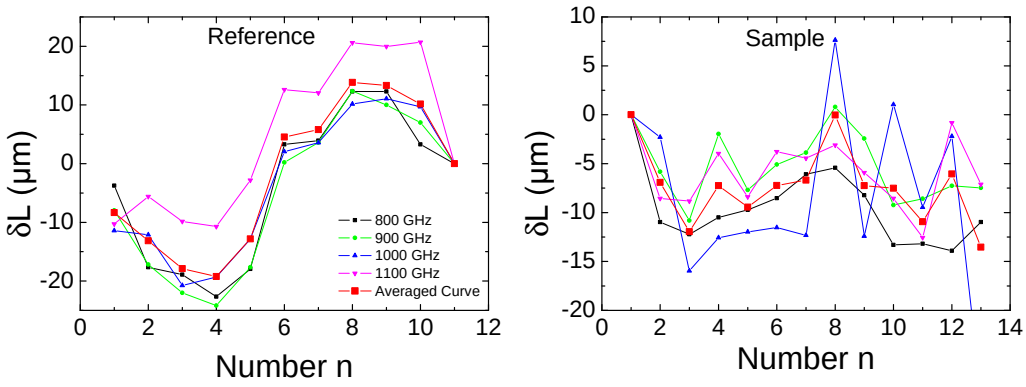

Figure 9.2.: Left: Deviation of ΔL of the reference measurements with respect to the last measurement for different frequencies. Right: Deviation of ΔL of the sample measurements with respect to the first measurement for different frequencies. The red curve is the average.

into account. Therefore the time-dependent drift δL of ΔL was determined experimentally for the sample and reference measurements. First the frequency range between 60 GHz and 800 GHz is considered. For the different reference (sample) measurements the deviation of ΔL with respect to the first (last) measurement was determined for some distinct frequencies, which is shown in the right (left) part of figure 9.1. Since the δL obtained for different frequencies show the same temporal evolution they were averaged. To correct the ΔL of the different measurements, they are shifted by the averaged value of δL_n obtained for the particular measurement n:

$$\Delta L_{corr,n} = \Delta L_n + \delta L_n \tag{9.1}$$

Finally the corrected values of ΔL can be averaged. The same procedure is also applied to the sample measurements (see left part of figure 9.1). To get a precise result for $L_{\text{eff}} = \Delta L_{\text{sample}} - \Delta L_{\text{reference}}$ the time difference between sample and reference measurement has to be small. Since the last sample measurement and the first reference measurement had the smallest temporal gap, the sample measurements were corrected with respect to the last measurement. It can be seen that the drift during the sample measurements is within precision of the spectrometer (see section 6.5.1). However, in the data set of the reference measurements a large drift of ΔL of about 50 μm occurs over a short period of time of which the origin is not clear. It is important to note that drift between sample and reference measurements cannot be corrected within this method. To do so, sample and reference have to be measured in an alternating fashion. In this case a drift between sample and reference is measured in every spectrum but can be minimized by averaging over many spectra. However, it is time consuming to change between sample and reference after every frequency sweep and the longer a measurement takes the more it is liable to drifts. Still, the following analysis shows that this correction gives a precise value of L_{eff}, showing that the drift of ΔL between the last sample and the first reference measurement was small. The drift δL as a function of measurement number for frequency range between 700 GHz and 1200 GHz is shown in figure 9.2.

Figure 9.3 shows the results of the measurement in comparison to a measurement without absorbers. The standing-wave pattern is decreased by one order of magnitude. Also the effect of the phase correction can be seen for the range between 60 GHz and 800 GHz in figure 9.3. Without the correction, L_{eff} is shifted about 15 μm with respect to the measurement without absorbers where sample and reference were measured in direct succession. After the correction both curves of L_{eff} are lying directly on top of each other. After the correction of frequency range measured without absorber the shift of L_{eff} is still about 25 μm as can be seen by the dark yellow curve in figure 9.3. Figure 9.2 shows that for the sample measurements the deviation between the values of δL obtained for the different frequencies is quite large but in same order as for the other frequency range (see figure 9.1). Here, a phase drift in the period of changing between sample and reference might be responsible for the insufficient performance of the correction. However, the absolute uncertainty of 25 μm is within the precision of the spectrometer so that for further analysis L_{eff} was shifted so that it agrees with the low-frequency range (see black curve in figure 9.3).

For the analysis, a Drude model with a single oscillator at zero frequency to describe the free-carrier contribution was fitted simultaneously to transmittance and phase. The parameters extracted from the fit were $\nu_p \approx 292$ GHz, $\gamma/2\pi \approx 1.08$ THz, and a sample thickness of $d = 0.506$ mm which is consistent with the mechanically measured thickness of $d = 505\ \mu\text{m} \pm 3\ \mu\text{m}$. From these values the carrier density $N_c = \varepsilon_0 \cdot (2\pi\nu_p)^2 m^*/e^2 \approx 3.9 \times 10^{14}$ cm^{-3} and the mobility $\mu = e/\gamma m^* \approx 0.79 \times 10^3$ cm^2/Vs were calculated. Here, ε_0 is the permittivity of free space and e is the electric charge of the electron. Both values are reasonable for high-resistivity

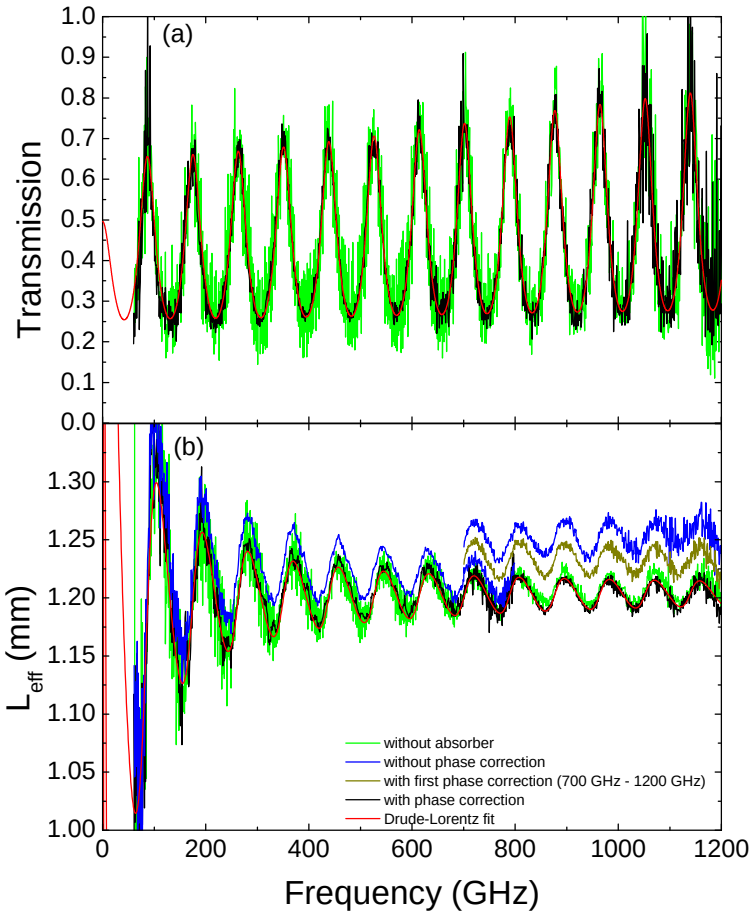

Figure 9.3.: Upper panel: Transmittance of silicon measured with and without absorbers. Lower panel: Effective sample thickness measured with and without absorbers. The usage of the absorbers reduce the effect of standing waves by one order of magnitude. The red curve shows the corresponding Drude-Lorentz fit.

silicon [136]. In the calculation the effective hole mass was assumed to be $m^* = 0.37m_0$, where m_0 is the free-electron mass [136]. The extracted DC conductivity of $\sigma_{DC} = eN_c\mu \approx 0.044\ (\Omega\text{cm})^{-1}$ is in good agreement with the value of $0.047\ (\Omega\text{cm})^{-1}$ obtained by a room-temperature resistivity measurement.

From the fit, the frequency-dependent refractive index n and extinction coefficient κ were extracted. Figure 9.4 depicts the refractive index and the extinction coefficient obtained by the inversion method and the PDL fit as described in section 5.5 together with the result of the Drude-Lorentz fit of the entire frequency range. For

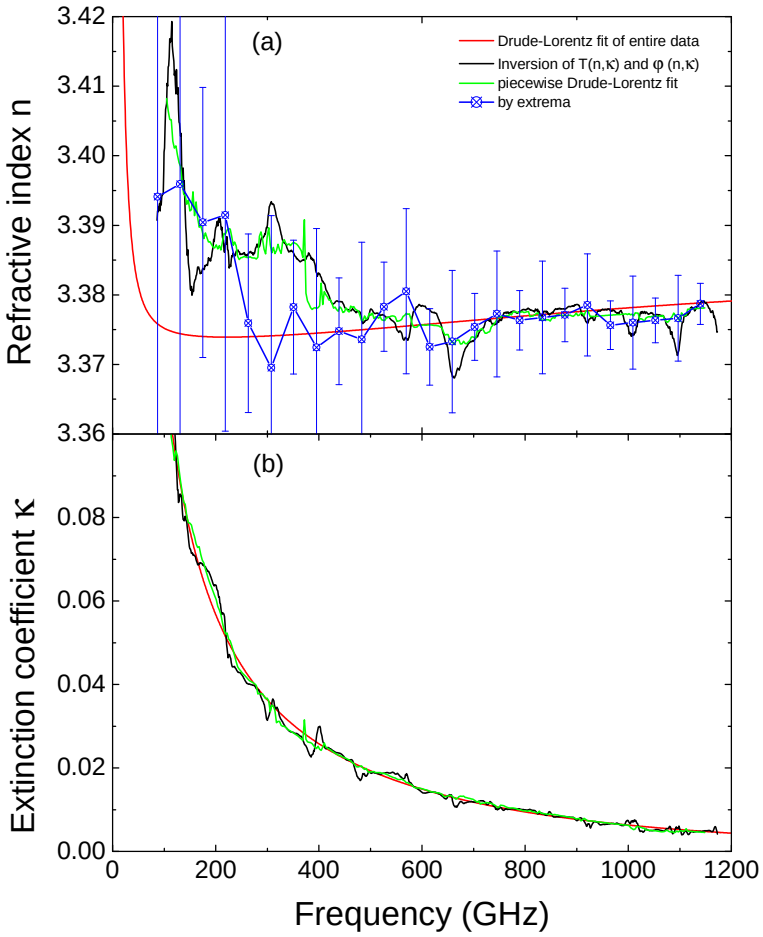

Figure 9.4.: The upper part shows the refractive index and the lower part the extinction coefficient of silicon. For the measurements with absorber, n and κ were analyzed by the inversion method and the PDL fit. In both cases the fitted range was set to one period of the Fabry-Perot fringes. For a consistency check n was also calculated from the extreme of the interference fringes.

the inversion method as well as for the PDL fit, the fitted range was chosen to be one period of the Fabry-Perot oscillations. Note that for the PDL fit a Drude-Lorentz model containing three oscillators was applied to have more freedom reproducing the exact shape of the data. Agreement between the n and κ determined by numerical inversion respectively the PDL fit and the ones extracted from the Drude-Lorentz fit of the entire frequency range is very good. The extinction coefficient κ changes strongly with frequency and thus κ is well determined. In contrast the change of n with frequency is small. Since n and κ are connected via Kramers-Kronig transfor-

mation, also the slight increase of the refractive index with frequency is determined very nicely. For low frequencies stronger deviations occur for every method. Here n and κ are changing more strongly due the Drude absorption. Since in the inversion method both n and κ are assumed to be constant over the fitted range, a strong change leads to deviations. However, also the n obtained from the PDL fit shows deviations of the same order for frequencies below 400 GHz. Here, remaining contributions of standing waves are present which influence the fit as discussed in section 6.5.1. Still, the deviations appear large since the total change of n is small. The increase of κ with decreasing frequency is very well described which means that these methods are very effective to determine the behavior of the complex optical functions reasonably even when n and κ are changing more strongly.

For a consistency check the refractive index can also be calculated from the extrema of the interference fringes in the transmittance. At the maxima (minima) the condition of constructive (destructive) interference $m\lambda = 2nd$ ($(m + 1/2)\lambda = 2nd$) is fulfilled. The position of the extrema was determined by fitting the transmittance only in the vicinity of each extremum. For the calculation the mechanically measured thickness was employed. The result is also shown in figure 9.4 (a). It can be seen that especially for high frequencies the refractive index calculated from the extrema is lying on top of the numerically determined ones showing the good performance of these methods. The error bars are defined by the reading error of the extrema positions which was roughly 1 GHz for the maxima and 2 GHz for the minima. Hence the optical properties of silicon can be determined very precisely at room-temperature outside a cryostat.

However, a lot of physical phenomena that are of interest can only be investigated at low temperatures or high magnetic fields. The transition temperature of many multiferroic materials are located for instance below 20 K. These temperatures can only be reached with a liquid-He cryostat. Therefore in the next section the implementation of a cryostat into the THz setup and first results on silicon are shown.

9.2. Low-temperature measurements on silicon

Although liquid-He cryostats are a very common technology in low-temperature physics, in the case of THz spectroscopy some special criteria have to be considered. The cryostat used in this work was specially designed for THz frequencies[1]. In the first part of this section the layout of the cryostat will be briefly described with emphasis on the design of the optical tail. To demonstrate that this design significantly increases the quality of the measured data, in the second part of this section low-temperature measurements of silicon obtained with two different cryostats are compared.

[1]The cryostat was implemented into the setup within the framework of the master thesis of Jennifer Marx (see [125]).

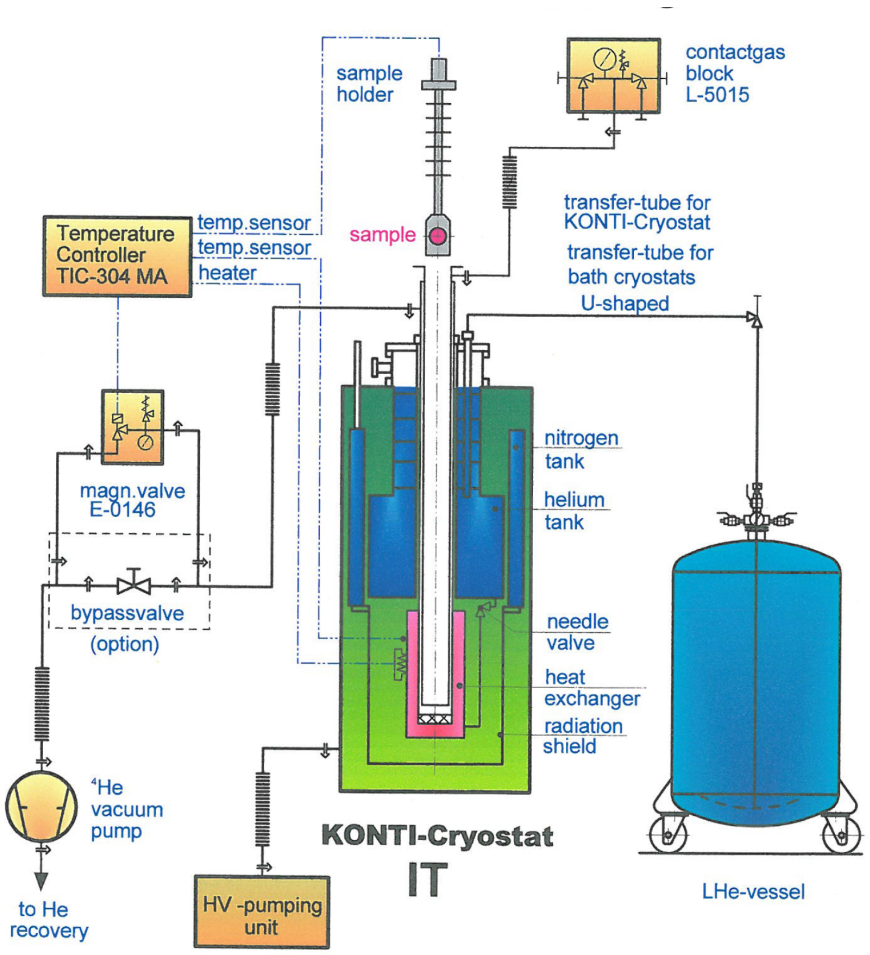

Figure 9.5.: Schematic sketch of the cryostat and the control units. Picture taken from [144]

9.2.1. Cryostat layout

The cryostat (CryoVac KONTI-Kryostat IT) implemented into the setup is a combination of a bath cryostat and a continuous-flow cryostat with a top-loading scheme. In the following it is denoted as bath cryostat. A schematic view of the cryostat is shown in figure 9.5. The main parts are the helium storage tank and the heat exchanger which are connected by a needle valve. In addition to the isolation vacuum the helium tank is surrounded by a liquid-nitrogen bath. Thermal contact between heat exchanger and sample chamber is realized by a thin metal plate. Filling the heat exchanger is accomplished by transferring liquid helium from the storage tank via the needle valve by sucking on the exhaust gas stub with a pump. To reach temperatures below 4.2 K, the heat exchanger filled with enough helium can be pumped. Temperatures above 4.2 K are reached by heating the heat exchanger while applying a continuous flow of helium. The overall accessible temperature ranges from

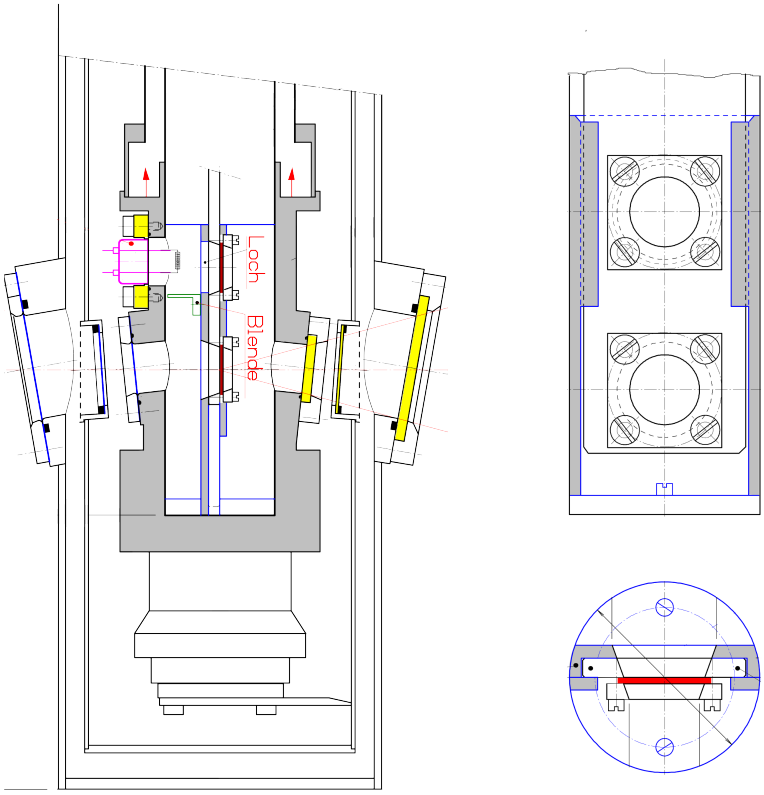

Figure 9.6.: Left: Side view of the optical tail of the cryostat. Right: Sketch of the sample holder and the slot in the sample chamber. Picture taken from [144]

2 K to 350 K. The temperature is measured at the heat exchanger as well as at the sample position. For a better temperature coupling between sample and the heat exchanger, helium gas can be injected into the sample chamber. Sample and reference are exchanged in a fast way with a stepper motor inside the sample rod. A detailed description of the cryostat can be found in [125].

Optical design

As mentioned already, the design of the optical path inside the cryostat has to be considered due to the long wavelengths. In total the cryostat contains six windows. One pair between the sample chamber and the isolation vacuum, one pair in the radiation shield, and the third pair between the isolation vacuum and the environment as shown in the left part of figure 9.6. Note that the windows at the radiation shield can in principle be left out with a compromise on the base temperature. To avoid standing waves between the windows, they are tilted with different angles to the

optical axis. Nevertheless, standing waves especially within the windows can never be totally suppressed. Usually thin Mylar foil is used as window material in the far infrared and THz range. However, the windows between the sample chamber and the isolation vacuum get cold due to the exchange gas and thermal expansion affects the stability of the windows. Therefore, it is preferable to make this window thick and hence Mylar foil was not appropriate as window material. Here, HDPE foil turned out to be the best choice for the window material since it has low absorption and a constant refractive index in the THz range as described in section 7.1.2. It is favorable to choose the window thicknesses such that constructive interference of the standing waves is achieved at high frequencies, where the overall THz signal is low. The best result was obtained using 200 μm thick HDPE for the windows between sample chamber and isolation vacuum and 100 μm for the windows between isolation vacuum and environment [125]. The transmittance spectra of this window combination for the evacuated as well as for the non-evacuated cryostat are shown in figure 9.7. As reference a measurement without cryostat in the optical path was used. The lowest transmittance is about 50% around 700 GHz where the overall THz amplitude is still reasonable. In return, the transmittance is nearly 100% around 1 THz where the output power of the photomixers is low and enhanced absorption due to water vapor is present.

Also it is very important to consider reflections in other parts of the cryostat. In order to supply optimal thermal coupling within the cryostat and to guarantee optimal stability, the cryostat and the sample rod are mostly composed of metal. Since metal surfaces are reflective for THz radiation, it has to be avoided that light reflected from the walls of the sample chamber enters the detector. To guarantee this, a slot is incorporated into the walls of the sample chamber that lines up precisely with the sample holder as illustrated in the right part of figure 9.6. This construction makes sure that all rays not passing through the sample or reference aperture are blocked.

Since the apertures are also made of metal, a cylindrical hole might act as a waveguide and affect the phase measurement. To prevent this, the apertures have a conical shape where the smaller end faces the incoming beam (see right part of figure 9.6).

In the following, silicon was used as a sample to compare the spectra obtained with this cryostat to spectra obtained (i) without a cryostat and (ii) using an older cryostat which lacks the modifications discussed above.

9.2.2. Comparison of data obtained with and without the cryostat

In this section a room-temperature measurement with the Si sample mounted inside the bath cryostat is compared to a single run of the measurement discussed in section 9.1 where the same sample was mounted on a simple aperture. Note that for the

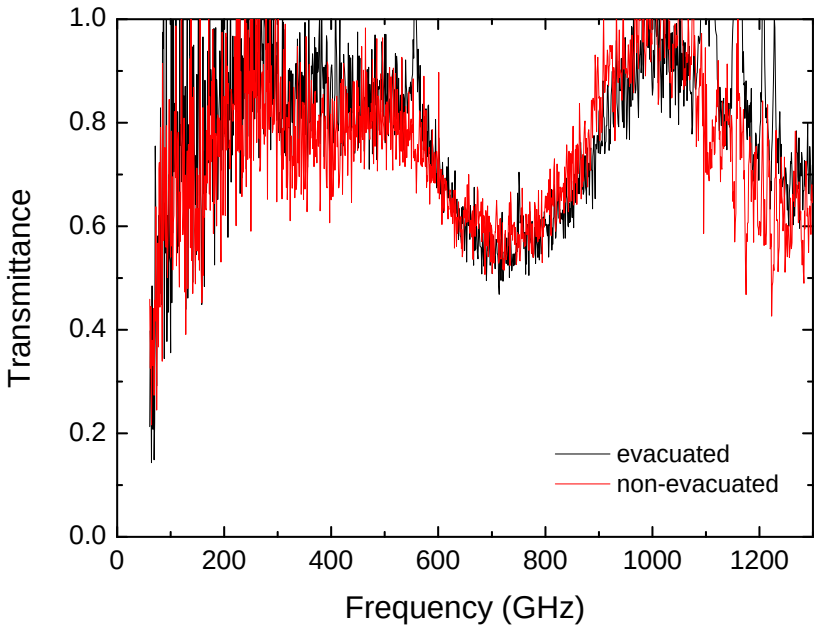

Figure 9.7.: Transmittance of the empty cryostat for evacuated as well as for non-evacuated case. The fringes are due to standing waves within the HDPE windows.

measurement without the cryostat the aperture is 16 mm whereas the maximum aperture when using the bath cryostat is 11 mm. Due to the relative thick HDPE windows, for the measurements with cryostat no absorbers were used in contrast to the room-temperature measurement (see section 9.1).

Figure 9.8 shows the obtained transmittances and effective sample thicknesses. The agreement between both transmittances is very good. In the phase data deviations are present which are very pronounced around 400 GHz and 600 GHz. This might be due to the fact that the environmental conditions for the setup are not as stable as for a simple room temperature measurement since the different pumps needed to operate the cryostat crucially influence the environment. Nevertheless, these deviations are about 20 μm which is within the range of the precision of the setup (see section 6.5.1). Below 300 GHz the noise-like fluctuations caused by standing waves (see section 6.2) are much smaller for the measurement without cryostat due to the use of absorbers. Since for low frequencies the beam radius exceeds the dimensions of the apertures, the influence of standing waves on the measured data increases with decreasing aperture size. At the same time the noise increases due to the decreasing THz power at the receiver. For frequencies above 300 GHz the short-term fluctuations in both measurements are comparable. This shows that the low but finite absorption of the windows helps to suppress standing waves similar to

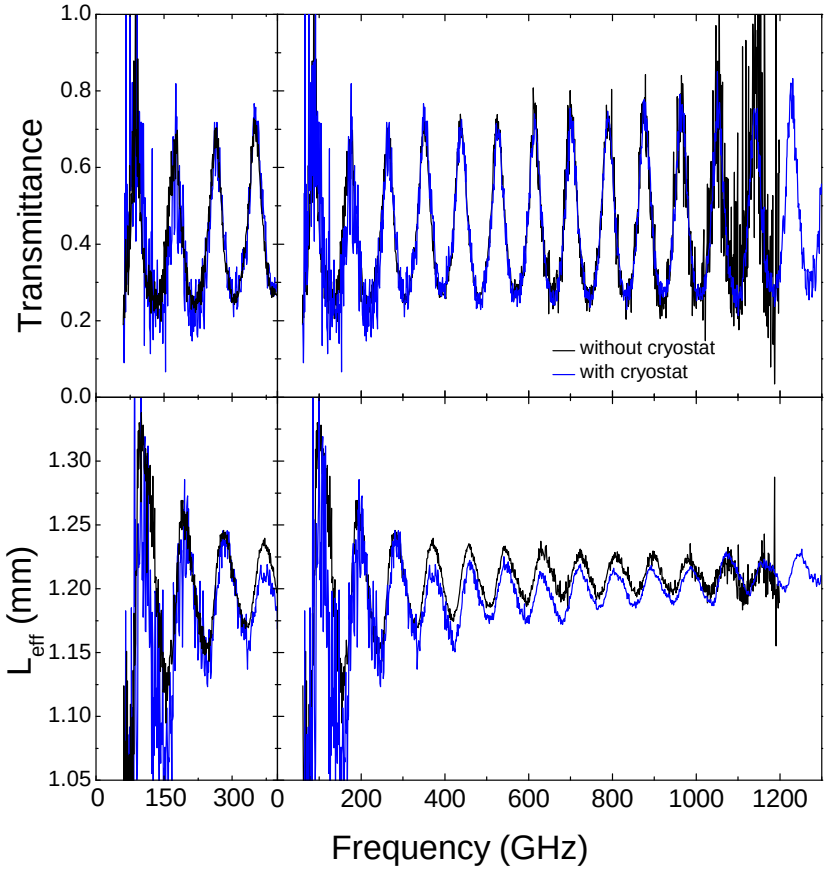

Figure 9.8.: Comparison of two measurements where the sample was mounted on a simple aperture of 16 mm in diameter (black) and inside the bath cryostat (blue). The aperture within the cryostat has a diameter of 11 mm. On the left-hand side the low-frequency region is shown with the results from the measurement without cryostat in the foreground.

the absorbers used for the measurement without cryostat (see section 9.1). However, the standing-wave effects are still very pronounced. Here, the use of absorbers is necessary to improve the data quality. At frequencies above 1 THz, the quality of the cryostat data is better due to the higher THz power in this measurement. Note that the THz power depends on the quality of fiber coupling which diminishes due to long-time drifts and has to be checked at regular intervals.

9.2.3. Comparison of the different cryostats

Low-temperature measurements of silicon were performed using two different cryostats. On the one hand the bath cryostat described in section 9.2.1 and on the other hand a cold-finger cryostat which is used for the Fourier spectrometer of this group were employed. In a cold-finger cryostat the sample holder is in direct thermal contact with a copper block which is cooled by a continuous flow of liquid helium. Since no helium tank is present to pump on, the lowest reachable temperature is about 4 K. For this type of cryostat no exchange gas is used, thus only one pair of windows is needed to seal the isolation vacuum inside from the environment. Since the windows do not experience strong thermal expansion, here Mylar foil with a thickness of 75 μm is used as window material. Note that only one of the two windows is tilted. To obtain the best possible results for both measurements the available maximum aperture was used which is 11 mm for the bath cryostat and 8 mm for the cold-finger cryostat.

A comparison of exemplary transmittance and L_{eff} is shown in figure 9.9 for a measurement at 200 K. The transmittance data is smoothed by an adjacent averaging over 5 GHz. The data measured with the cold-finger cryostat can only be used for fitting above 200 GHz which can be seen especially in L_{eff}. In contrary, the Fabry-Perot fringes in the bath-cryostat measurement can be observed down to lowest frequencies. Having a close look at the transmittance data at 200 GHz, it can be seen that there is a deviation in the apparent position of the Fabry-Perot fringes. Hence at low frequencies the data of the cold-finger cryostat is more influenced by standing-wave effects. At frequencies between 300 GHz and 700 GHz the smoothed transmittance data are comparable. However, considering L_{eff} the fluctuations in the cold-finger cryostat measurement are more than twice as large as for the bath cryostat measurement which shows that the special design of the bath cryostat minimizes effects of standing waves. The deviations at high frequencies are assigned to the lower signal in case of the cold-finger cryostat. These large fluctuations lead to large uncertainties in the determination of n and κ as well as in the fit of the data and thus in the extracted values such as for example plasma frequency or damping constant. A detailed comparison of the two cryostats is given in [125]. Considering the envelope of L_{eff} of the measurements using the bath cryostat in figure 9.8 and figure 9.9, the envelope of L_{eff} is not continuously falling as for other measurements but exhibits some local disturbances. This can be clearly seen at 400 GHz and 600 GHz in the room-temperature measurement and at 700 GHz in the measurement at 200 K. This kind of deviations is mainly observed in the measurements where the bath cryostat is used. For the operation of both the cold-finger cryostat and bath cryostat various pumps are needed. However, the helium pump used for the bath cryostat is more voluminous and stronger than the one used for the cold-finger cryostat. The influence of this pump on the environmental conditions might be stronger than for the cold-finger cryostat setup.

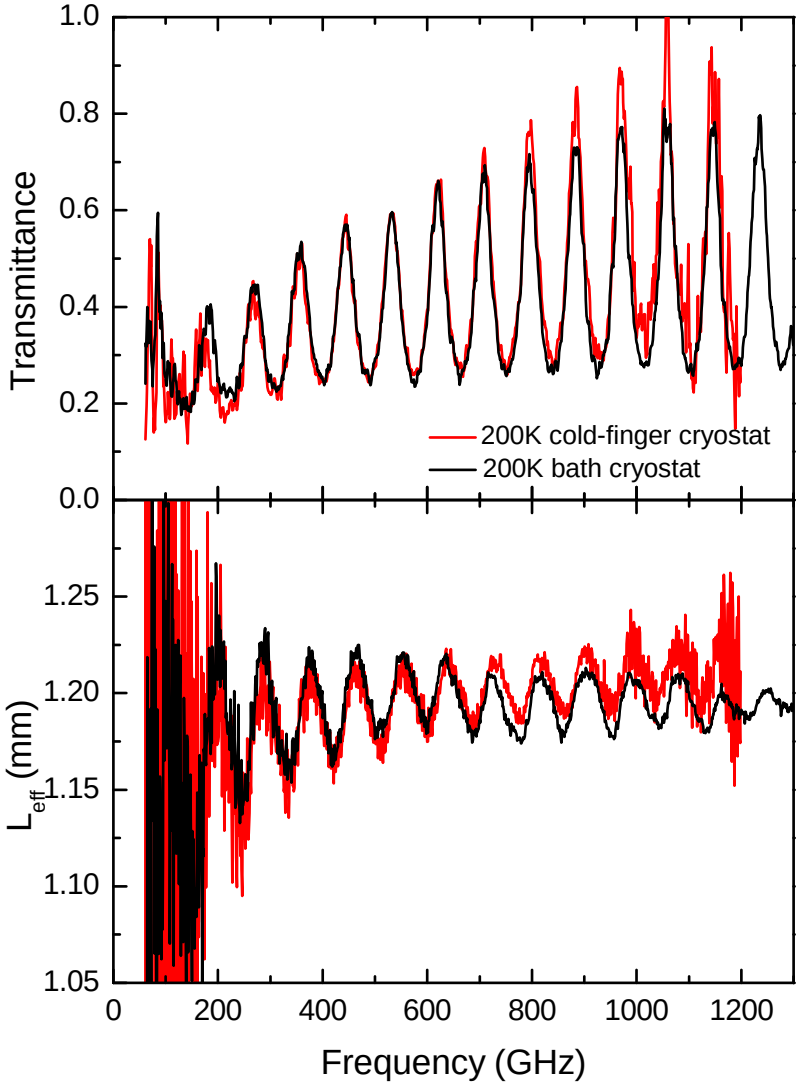

Figure 9.9.: Comparison between the data obtained by the bath cryostat and the cold-finger cryostat. Both measurements were performed at 200 K.

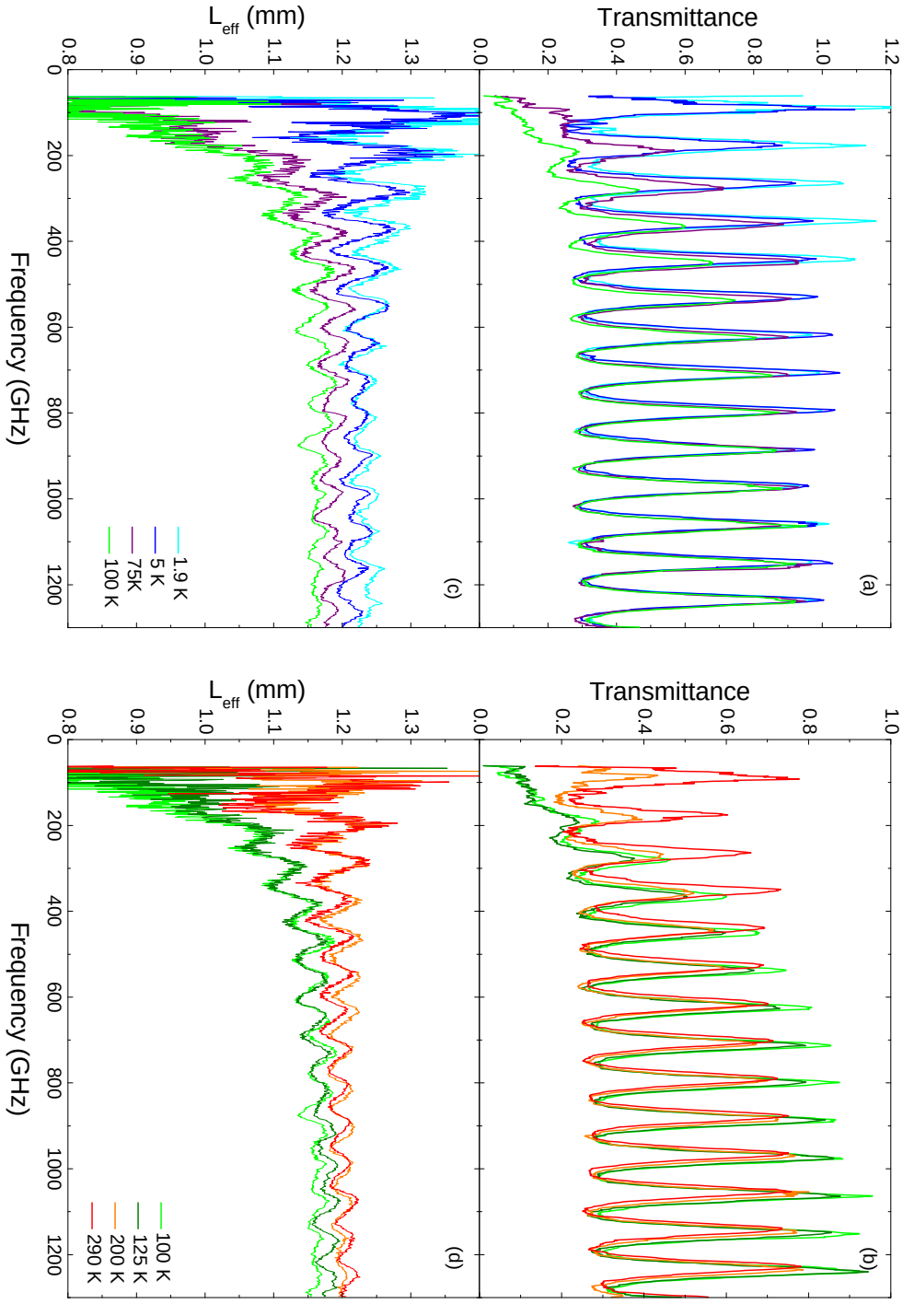

Figure 9.10.: (a) Smoothed transmittance from 2 K to 100 K. (b) Smoothed transmittance from 100 K to 290 K. (c) Effective sample thickness from 2 K to 100 K. (d) Effective sample thickness from 100 K to 290 K.

9.2.4. Results of the low-temperature measurements

Bath cryostat

A piece of the same silicon wafer, investigated at room-temperature in chapter 9.1 was mounted on a sample holder with an aperture of 11 mm diameter using silver paint. The windows of the radiation shield were not used (see section 9.2.1). In order to set ΔL roughly to zero and hence obtain a high phase stability as described in section 6.5.1, the photomixers were set face-to-face and no additional optics were used. The transmittance and phase were measured for temperatures between 2 K and 300 K. Except for 2 K, where temperature stabilization was difficult, the transmittance was measured twice for each temperature. The averaged transmittance spectra from 2 K up to 100 K are shown in figure 9.10 (a) and the transmittance spectra for temperatures from 100 K up to room temperature are shown in figure 9.10 (b). The corresponding data of L_{eff} are shown in figures 9.10 (c) and (d). Note that the transmittance data were smoothed by adjacent-averaging over 5 GHz to better distinguish between the different curves. The transmittance data at 2 K and 50 K exceed unity. This is due to a wrong alignment in the reference position at these temperatures that has only been noticed after the measurement. Therefore the spectrum at 50 K is not shown here.

From figure 9.10 (b), it can be seen that the width of the low-frequency absorption narrows with decreasing temperature down to 125 K. In the temperature range from 100 K down to 2 K shown in figure 9.10 (a), the absorption weakens until it cannot be observed at 5 K anymore. To analyze the data quantitatively, a model containing a single oscillator at zero frequency to model the free-carrier response (Drude peak) was fitted to the data. At 5 K the data was fitted without any oscillator term since the Drude absorption is too weak to be observed. Note that the averaged data without smoothing was used for fitting.

As described in section 6.5.1, the absolute value of ΔL can be determined with a precision of about 20 μm due to thermal drifts. To obtain more precise fit results, the absolute value of L_{eff} was corrected as described in section 5.4 by a frequency independent shift. In the correction the sample thickness of 506 μm was used for all temperatures. The value was obtained very precisely for the room-temperature measurement outside the cryostat by repeating the experiment several times and averaging over the results (see section 9.1). This is valid since the thermal expansion coefficient α is in the range of 10^{-6} K^{-1} [145] and hence no observable change of the sample thickness is expected. The transmittance and the corrected L_{eff} were fitted simultaneously while varying all parameters. The values δL_{eff} used to correct the different data sets are summarized in table 9.1. It can be seen that δL_{eff} is within the determined precision of 20 μm. Table 9.1 shows that the determined sample thickness d lies within ± 3 μm of the value determined in section 9.1 which is expected since the thickness of 506 μm was given for the correction of L_{eff}. In figure 9.11, the data and the corresponding Drude fits are shown exemplary for 75 K and

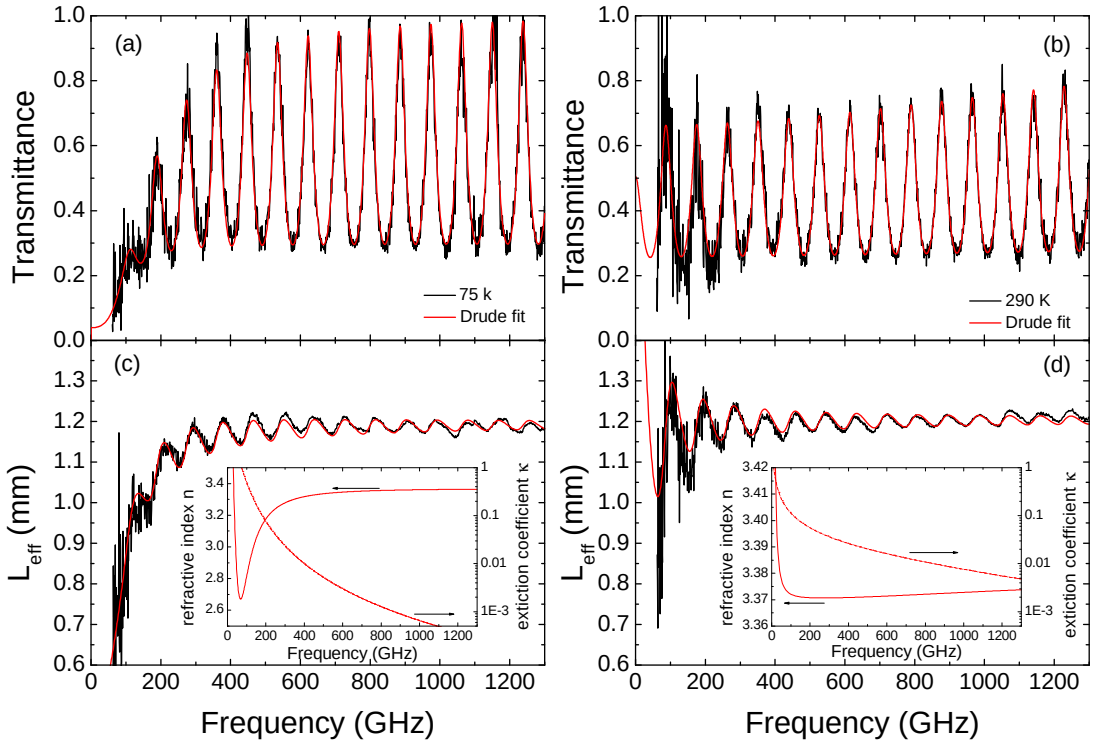

Figure 9.11.: Transmittance (black) and the corresponding Drude fit for 75 K (panel (a)) and 290 K (panel (b)). The effective sample thicknesses L_{eff} (black) and the corresponding Drude fit for 75 K and 290 K are shown in panels (c) and (d), respectively. In the insets the frequency-dependent refractive index and extinction coefficient are shown.

Table 9.1.: Extracted fit parameters for silicon

Temperature	ν_p (GHz)	$\gamma/2\pi$ (GHz)	d (μm)	δL_{eff} (μm)
75 K	241 ± 9	76 ± 6	504	3
100 K	319 ± 6	141 ± 12	506	22
125 K	340 ± 6	192 ± 9	506	13
200 K	328 ± 6	563 ± 90	504	-5
290 K	331 ± 15	1427 ± 240	507	5

room temperature. The insets show the frequency dependent refractive index and extinction coefficient extracted from the fit. The data and the corresponding fits of the other temperatures are given in Appendix A.6. The agreement between the data and the fits is good, especially for the transmittance. Although the influence of standing waves increases with decreasing frequency, the data quality is good and allows fitting the data over the whole frequency range. However, deviations between

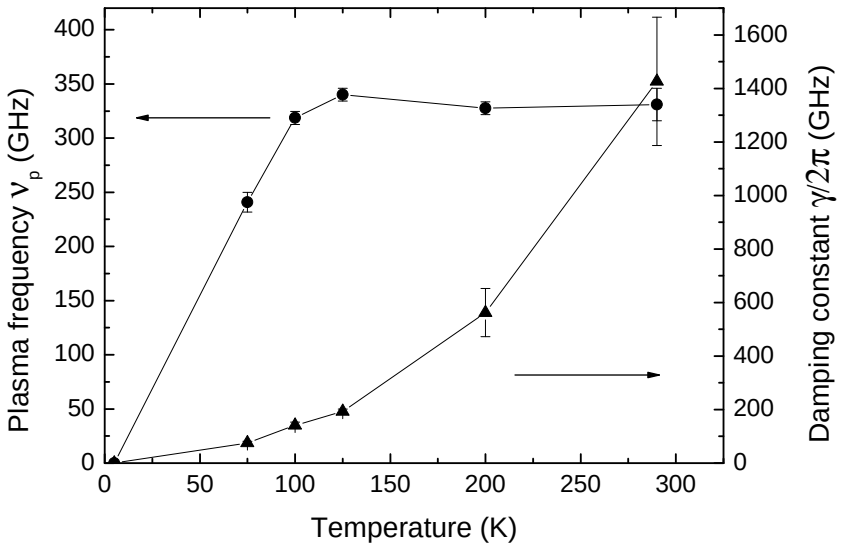

Figure 9.12.: Temperature-dependent plasma frequency ν_p and damping constant γ of silicon obtained using the bath cryostat.

data and fit are observed for L_{eff}. Clear deviations can be seen between 400 GHz and 600 GHz in data obtained at 75 K (figure 9.11 (c)) and between 300 GHz and 800 GHz in the room-temperature data (figure 9.11 (d)). At these frequencies the deviations amount to up to 10 μm. These relative fluctuations are within the precision of the spectrometer. However, such pronounced relative fluctuations have not been observed in the measurements without cryostat. Note that for all different measurements ΔL was set roughly to zero so that the phase stability in all measurements should be comparable. As discussed in section 9.2.2, the environmental conditions might not be as stable as for room-temperature measurements due to the different vacuum and helium pumps and the icing of the cryostat. All this might cause fluctuations of the temperature which affects the value of ΔL and hence induces fluctuation in the phase data.

From each fit, the plasma frequency ν_p and the damping constant $\gamma/2\pi$ of the Drude absorption were extracted (see table 9.1). Figure 9.12 shows the temperature dependence of ν_p and $\gamma/2\pi$. Between 5 K and 125 K the plasma frequency ν_p increases with temperature. For higher temperatures, ν_p is constant within the error bars. With increasing temperature the excitation of charge carriers from the donor level into the conduction band becomes stronger. This leads to a larger photon absorption in the THz range. The damping constant $\gamma/2\pi$ increases strongly with temperature due to the increasing number of excited phonons by which the free electrons are scattered.

Figure 9.13 shows the frequency-dependent refractive index and extinction coeffi-

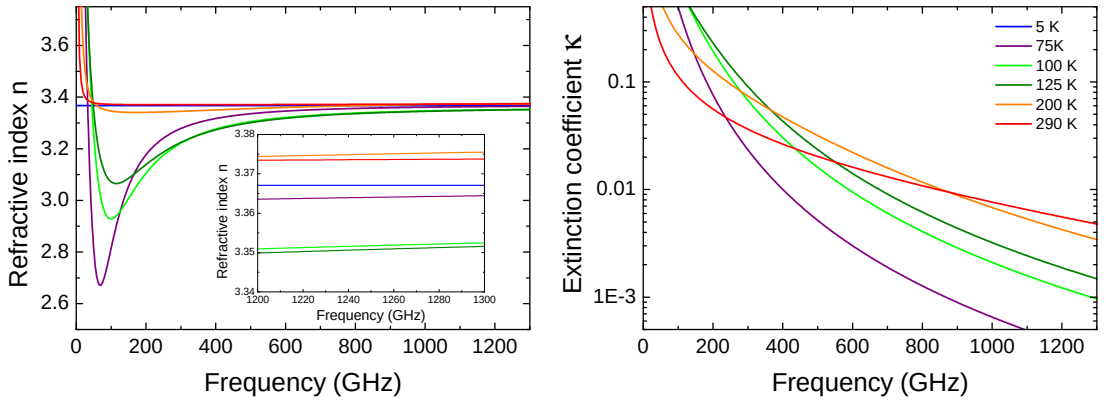

Figure 9.13.: Frequency-dependent refractive index n and extinction coefficient κ of silicon obtained for different temperatures using the bath cryostat. The inset shows n for high frequencies.

Table 9.2.: Obtained carrier density N_c and mobility μ of silicon.

Temperature	N_c (10^{14} cm^{-3})	μ (10^3 cm^2/Vs)
75 K	2.66 ± 0.2	9.956 ± 0.786
100 K	4.66 ± 0.18	5.355 ± 0.454
125 K	5.31 ± 0.19	3.928 ± 0.183
200 K	4.93 ± 0.18	1.345 ± 0.251
290 K	5.03 ± 0.46	0.530 ± 0.089

cient for the different temperatures. For reasons of clarity only the n and κ extracted from the Drude-Lorentz fit of the entire frequency range are shown. The peak of κ gets more pronounced with increasing temperature since the number of free carriers increases which absorb the electromagnetic radiation. At the same time the peak broadens due to the stronger damping. Between 75 K and room temperature, the dispersion of n decreases with increasing temperature due the increasing damping. At the high frequency end of the measured range, n decreases when the temperature is increased from 5 K to 100 K and then increases between 100 K and 290 K as depicted in the inset of figure 9.13.

From the extracted parameters, the carrier density N_c and mobility μ are determined as described in section 9.1. The result is shown in figure 9.14 and the calculated values are also listed in table 9.2. The free-carrier density N_c is constant for temperatures between 300 K and 100 K. Further decreasing of the temperature leads to a decrease of the carrier density. For the temperature dependence of the mobility μ a power law behavior is observed. This behavior is expected for semiconductors. Due to the freezing out of phonons at low temperatures, the mean free path of the carriers increases and hence the damping decreases. At the same time

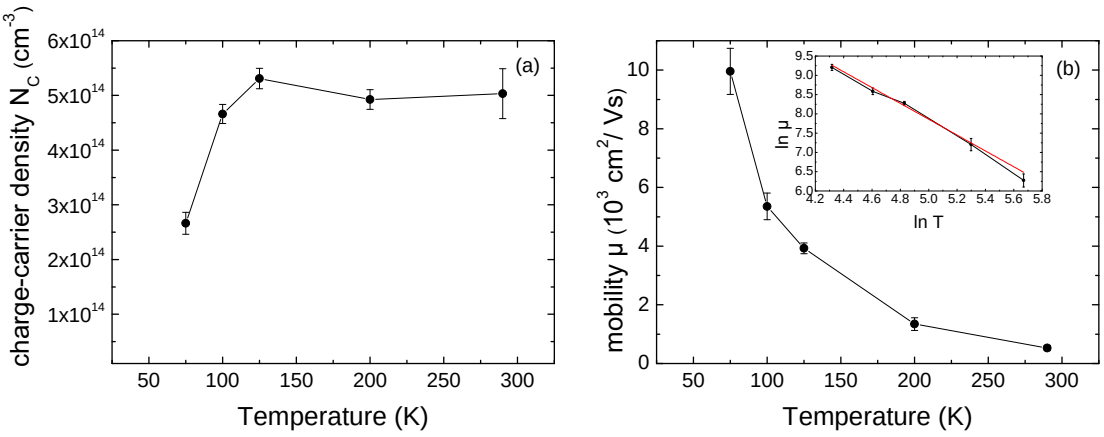

Figure 9.14.: (a) Temperature dependence of the free-carrier density N_c. (b) Temperature dependence of the free-carrier mobility μ. The inset shows $\ln \mu$ as a function of $\ln T$. The expected power law behavior can be observed and an exponent of -2.1 was found.

the number of free charge carriers decreases since the thermal energy is not sufficient to excite the carriers from the donor level to the conduction band. The inset of figure 9.14 (b) shows the temperature dependence of the mobility, plotted on a double logarithmic scale. The slope of the double logarithmic plot was determined to $\sim -2.1 \pm 0.1$. A deviation of the temperature dependence of the hole mobility in silicon from the $T^{-3/2}$ law was reported by several groups [146–148]. The exponents of the T^n law determined by the different groups are between -2 and -2,7. It has been shown that the non-parabolicity of the valence band as well as sub-band interaction and optical phonon scattering give rise to a complicated temperature dependence of the hole mobility [149, 150].

Cold-finger cryostat

The temperature dependence of the optical properties of silicon was also investigated using the cold-finger cryostat. The measurement was performed analogous to the one in the bath cryostat, i.e. two spectra at each temperature were measured and averaged. As already mentioned, the cold-finger cryostat has only one pair of windows of which one is tilted and the maximum aperture is only 8 mm. The averaged transmittance spectra for temperatures between 5 K and 100 K are shown in figure 9.15 (a) and between 100 K and room temperature in figure 9.15 (b). The corresponding data of L_{eff} are shown in figure 9.15 (c) and (d). For comparison the transmittance is smoothed by adjacent averaging over 5 points, like the bath-cryostat data, shown in figure 9.10 (a) and (b). As expected, the data shows the same behavior as data obtained with the bath cryostat. However, the influence of standing waves on the data is much larger for the cold-finger cryostat. Below 200 GHz the

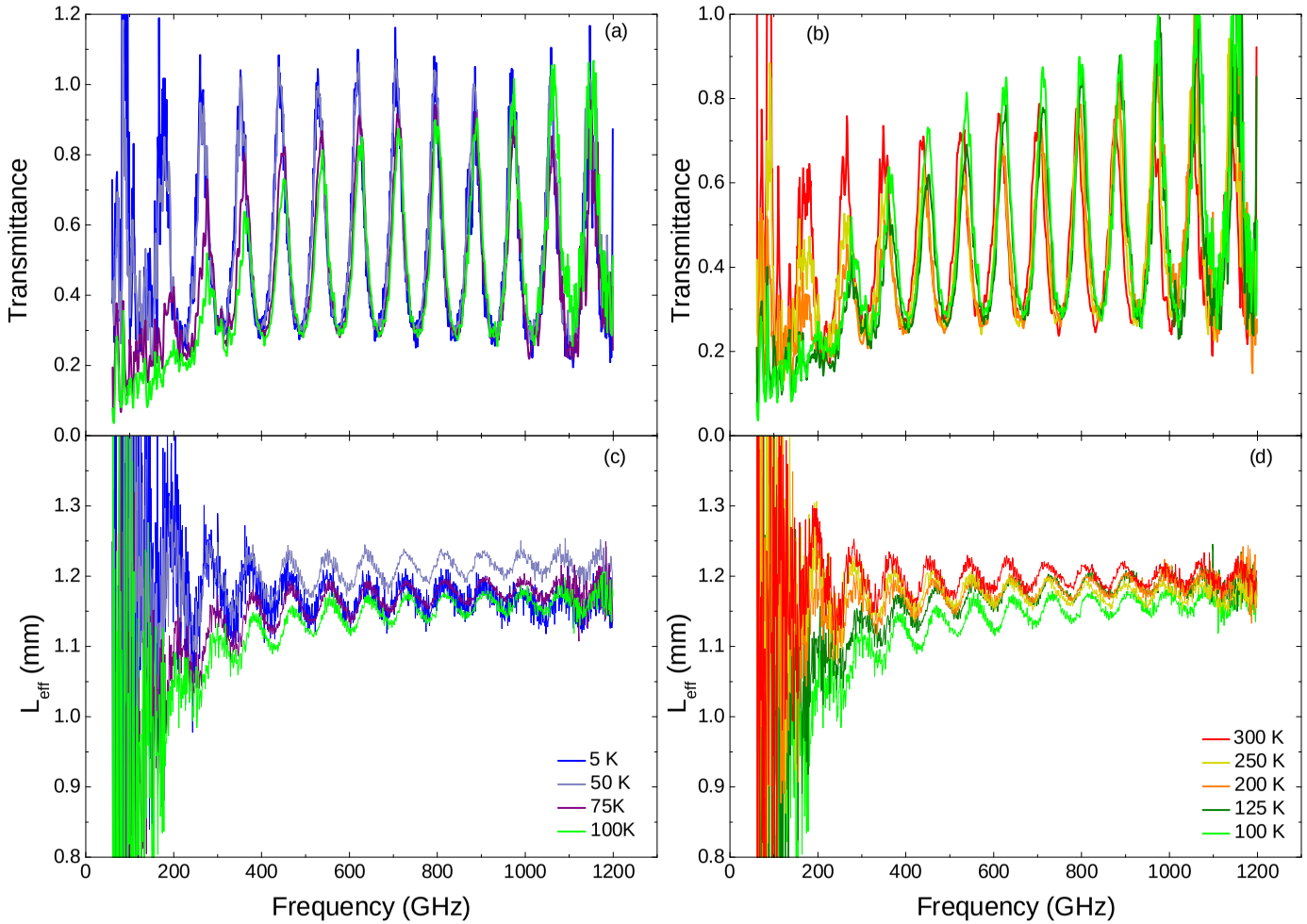

Figure 9.15.: Transmittance and phase data of silicon obtained with the cold-finger cryostat. (a) Smoothed transmittance from 5 K to 100 K. (b) Smoothed transmittance from 100 K to 300 K. (c) Effective sample thickness from 5 K to 100 K. (d) Effective sample thickness from 100 K to 300 K.

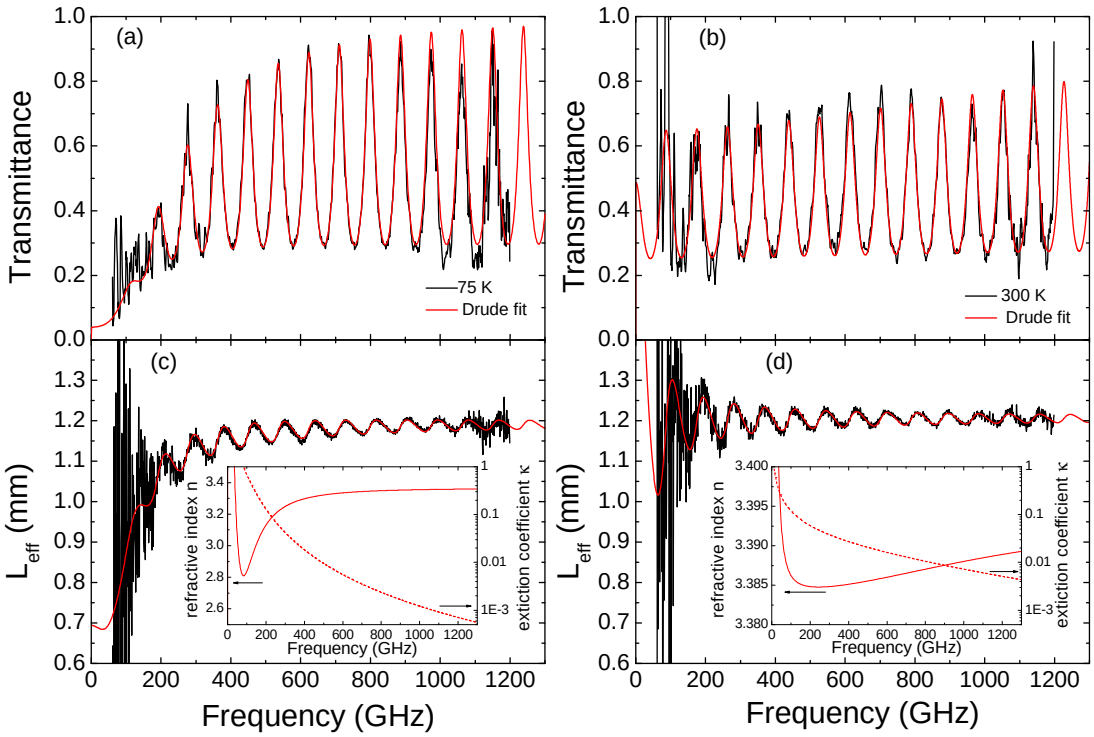

Figure 9.16.: Examples for the fits to the Si data obtained with the cold-finger cryostat. The transmittance (black) and the corresponding Drude fit for 75 K and 300 K are shown in panel (a) and (b), respectively. The corresponding effective sample thicknesses L_{eff} (black) together with the Drude fit are given in panels (c) and (d). In the insets the frequency-dependent refractive index and extinction coefficient are shown.

behavior of transmittance and phase data is not clear. Considering L_{eff} at frequencies above 1 THz, despite the larger short term fluctuations, the Fabry-Perot fringes are better resolved in the data obtained by the cold-finger cryostat.

The correction of the phase data and the further analysis were done in the same way as for the measurement with the bath cryostat described above. Note that in case of the cold-finger cryostat the smoothed transmittance data had to be used for the analysis. Otherwise the standing-wave effects are too strong to obtain reasonable fit results. Figure 9.16 shows the transmittance and phase data together with the corresponding Drude fits for the measurements at 75 K and room temperature. To determine the temperature dependence of the carrier density and mobility most precisely it is crucial to have a high data quality at low frequencies, particularly at low temperatures where the Drude absorption is narrow. Deviations of 10 μm between the measured L_{eff} and the fit are not present in the measurements using the cold-finger cryostat in contrast to the measurement with the bath cryostat. Still, the

Table 9.3.: Comparison of the extracted fit parameters obtained from the cold-finger cryostat and bath-cryostat data

Temperature	plasma frequency ν_p (GHz)		$\gamma/2\pi$ (GHz)		d (μm)		δL_{eff} (μm)	
	cold-finger cryostat	bath cryostat	cold-finger	bath	cold-finger	bath	cold-finger	bath
50 K	117 ± 10	-	71 ± 55	-	503	-	20	-
75 K	281 ± 21	241 ± 9	105 ± 37	76 ± 6	505	504	9	3
100 K	319 ± 27	319 ± 6	144 ± 24	141 ± 12	508	506	24	22
125 K	331 ± 21	340 ± 6	185 ± 15	192 ± 9	501	506	4	13
200 K	311 ± 9	328 ± 6	347 ± 150	563 ± 90	491	504	20	-5
250 K	287 ± 21	-	573 ± 90	-	507	-	20	-
300 K	316 ± 12	331 ± 15	1222 ± 180	1427 ± 240	505	507	6	5

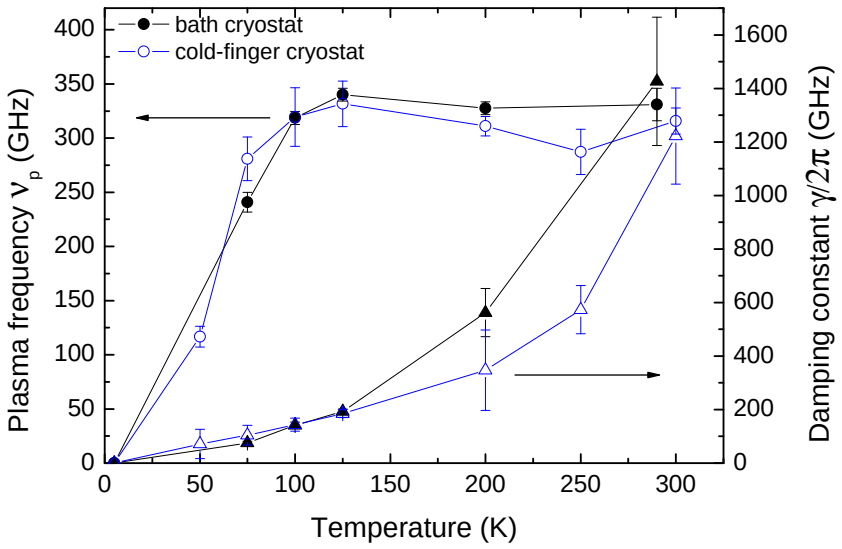

Figure 9.17.: Comparison of the temperature dependence of the plasma frequency ν_p and the damping constant γ of silicon obtained using the different cryostat.

data quality is inferior compared to the one of the bath cryostat. Below 200 GHz the data cannot be used for the fitting procedure which implies a large uncertainty of the extracted values of ν_p and γ of the Drude absorption as can be seen in figure 9.16. The values extracted from the fit are summarized in table 9.3. The applied shift δL_{eff}, to correct the phase data, is in the same range as in case of the measurements with the bath cryostat. However, the values of the sample thickness obtained by the simultaneous fitting of the transmittance and the corrected L_{eff} show larger deviations than for the measurement using the bath cryostat. For the measurement at 200 K this deviation is about 14 μm which is much larger than the uncertainty of the mechanical thickness determination.

Figure 9.17 shows the temperature dependence of the plasma frequency and the damping constant extracted from both measurements. For ν_p the same behavior is found. Nevertheless, the uncertainty of the values obtained by the cold-finger cryostat is larger. Concerning the damping constant, below 125 K the extracted values agree within the error bars. Above 125 K the γ extracted from the bath-cryostat data shows a stronger increase with decreasing temperature. The frequency-dependent refractive index and extinction coefficient extracted for the different temperatures are depicted in figure 9.18. Both show approximately the same behavior as obtained from the measurement using the bath cryostat. However, two distinct differences are seen in the refractive index. At 75 K the dispersion found for the data obtained with the cold-finger cryostat is less than for the data obtained with the bath cryostat. Also the high-frequency value of n at 200 K is much larger than the one extracted

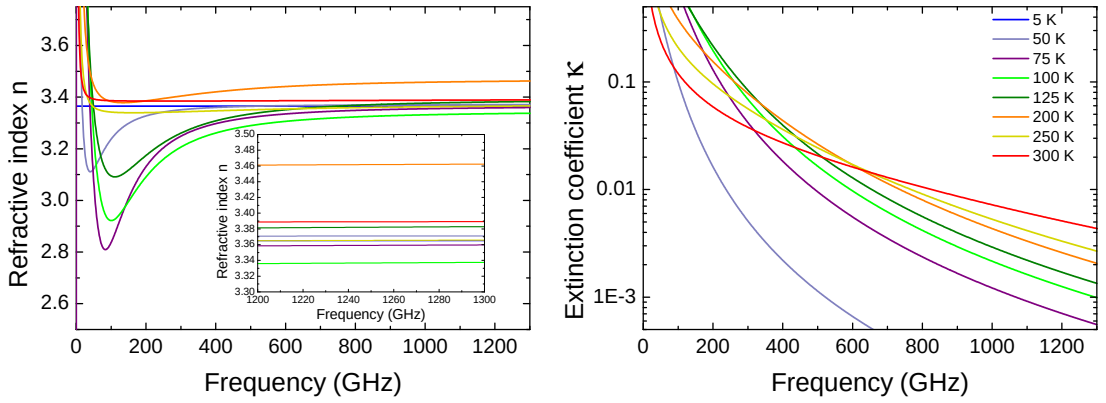

Figure 9.18.: Frequency-dependent refractive index n and extinction coefficient κ of silicon obtained for different temperatures using the cold-finger cryostat. The inset shows n for high frequencies.

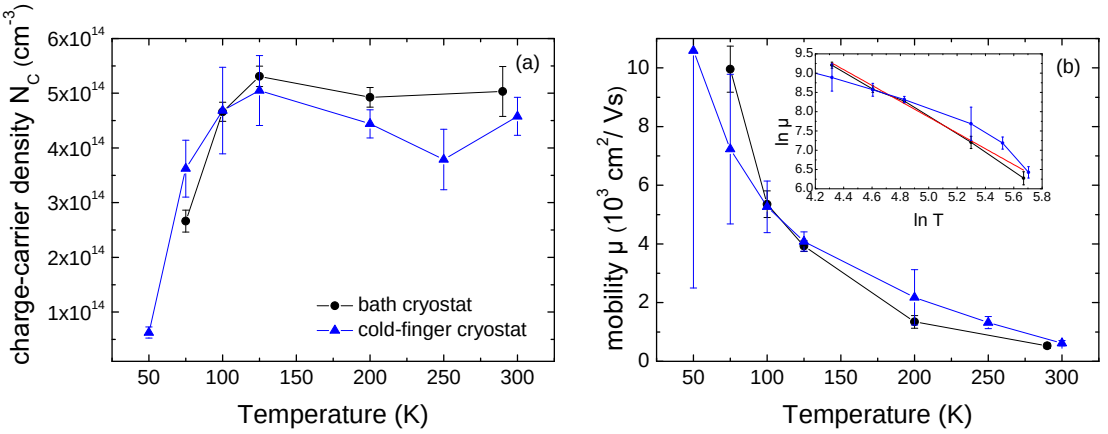

Figure 9.19.: (a) Comparison between the temperature dependence of the free-carrier density N_c obtained from the measurements with cold-finger cryostat and the bath cryostat. (b) Comparison between the temperature dependence of the free-carrier mobility μ obtained from the measurements with cold-finger cryostat and the bath cryostat. The inset shows $\ln \mu$ as a function of $\ln T$. For the data obtained with the cold-finger cryostat the exponent of the power law is -1.5.

from the bath-cryostat data which is attributed to the inferior data quality of the measurements using the cold-finger cryostat.

Figure 9.19 shows N_c and μ for both the cold-finger cryostat and the bath-cryostat measurement. The values recorded using the cold-finger cryostat are summarized in table 9.4. Below 100 K the values of N_c obtained from the cold-finger cryostat measurement are higher than the ones found by the bath cryostat measurement,

Table 9.4.: Carrier density N_c and mobility μ of silicon obtained from the cold-finger cryostat and bath cryostat data.

Temperature	N_c (10^{14} cm^{-3})		μ (10^3 cm^2/Vs)	
	cold-finger cryostat	bath cryostat	cold-finger cryostat	bath cryostat
50 K	0.63 ± 0.1	-	10.59 ± 8	-
75 K	3.62 ± 0.52	2.66 ± 0.2	7.23 ± 2.55	9.96 ± 0.79
100 K	4.68 ± 0.79	4.66 ± 0.18	5.27 ± 0.88	5.36 ± 0.45
125 K	5.05 ± 0.64	5.31 ± 0.19	4.08 ± 0.33	3.93 ± 0.18
200 K	4.44 ± 0.26	4.93 ± 0.18	2.18 ± 0.94	1.35 ± 0.25
250 K	3.79 ± 0.55	-	1.32 ± 0.21	-
300 K	4.58 ± 0.35	5.03 ± 0.46	0.62 ± 0.09	0.53 ± 0.09

whereas above 100 K they are lower. For the mobility μ, the opposite behavior is observed. Below 125 K the drop of N_c is not as large for the cold-finger cryostat measurement as for the bath cryostat. At 250 K a kink is observed in the data of the cold-finger cryostat. Nevertheless, considering the errors, N_c is constant above 125 K. The results extracted from the measurements with the cold-finger cryostat and the bath cryostat agree within their errors. However, due to the inferior data quality achieved using the cold-finger cryostat, the uncertainty in this analysis is quite large. It can amount to up to 15% of the determined value.

The temperature dependence of μ obtained with the cold-finger cryostat shows a strong increase when the temperature decreased from room temperature to 125 K which can be described by a power law. Further decrease of the temperature leads to a stronger increase of μ. In the inset of figure 9.19 (b) a double logarithmic plot for both the obtained mobilities is shown. The mobility recorded with the cold-finger cryostat shows a power law behavior between 5 K and 200 K. However, above 200 K the behavior deviates from that of straight line. Also the slope between 5 K and 200 K is not as steep as the one obtained using the bath cryostat. Here the slope is about -1.5. In section 9.2.4 it is discussed, that for the hole mobility in silicon a larger value is observed. This shows that the quality of the bath-cryostat data is much higher than quality of the data obtained with the cold-finger cryostat. Figure 9.20 shows the DC conductivity calculated from the charge-carrier density and mobility. The results obtained from both measurements are in very good agreement with each other. The conductivity increases between 50 K and 75 K due to the increase of N_c. For further increase of T, σ_{DC} decreases due to the enhanced damping. The values found at room temperature are in good agreement with the value of 0.047 $(\Omega\text{cm})^{-1}$ obtained by a room-temperature resistivity measurement.

In summary it has been shown that the modifications to the optical tail of the cryostat help to increase the data quality significantly compared to a cryostat without these improvements. The data could be used for fitting the entire measured range. This has been shown determining the temperature dependence of the charge-

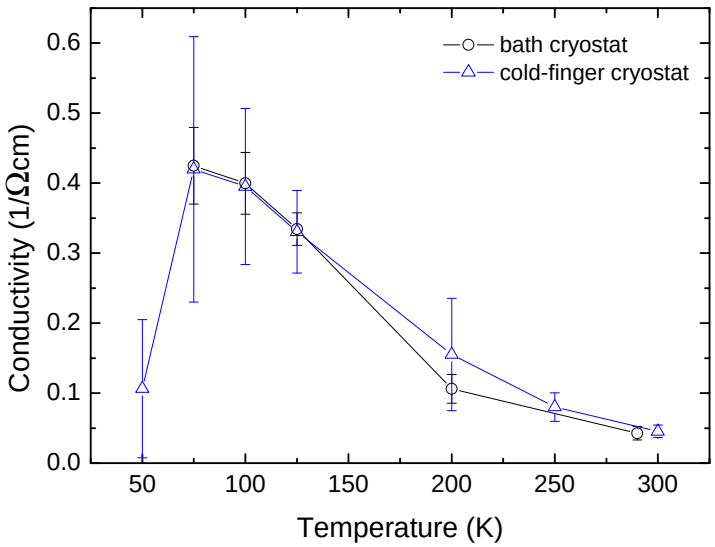

Figure 9.20.: Temperature-dependent conductivity $\sigma_1(\omega = 0)$ calculated from N_c and μ.

carrier density and mobility of high-resistivity silicon. Here, the data quality at frequencies below 400 GHz is crucial to determine the carrier density and the mobility accurately. The extracted temperature dependence shows the expected behavior for semiconductors. Especially the double logarithmic plot of the mobility shows the predicted T^n law with $n < -1.5$ for p-doped silicon. These results show that precise measurements over the whole temperature range between 2 K and room temperature can be performed with the modified cryostat.

10. Results on α-lactose monohydrate

α-lactose monohydrate ($C_{12}H_{22}O_{11}$) has one of the narrowest absorption lines in the THz spectral range among solids. It is therefore often studied in both THz TDS and CW TS, and used for calibration of various kinds of THz spectrometers [2, 22, 43, 151–155].

10.1. Sample preparation and measurement

Powder of α-lactose monohydrate is readily available commercially. For the measurement it was pressed into pellets by applying roughly 5 kbar pressure for 1 minute. The pellets have a diameter of 1.3 cm and a thickness of about 1 mm. For the transmittance measurement the pellets were mounted on an aperture with a diameter of 1 cm and an empty aperture was used as reference.

The measurement was performed using the frequency-scan method discussed in section 5.1. An effective resolution of about 1.5 GHz was adjusted. In order to resolve the oscillation of the photocurrent accurately, the actual frequency-step size was chosen to be 40 MHz. Both sample and reference were measured 17 times and the results were averaged[1]. The envelope and the phase information of the photocurrent were analyzed as described in section 5.1.

The transmittance of α-lactose monohydrate is shown in figure 10.1. Three absorption lines can be observed up to 1.8 THz. A detailed description of the origin of these absorption lines can be taken from references [156, 157]. Additionally, Fabry-Perot oscillations due to multiple reflections in the sample are present. The noisy appearance of the low-frequency part of the spectrum is due to the contributions from standing waves. Owing to the large wavelength of about 3 mm around 100 GHz, the standing waves are very pronounced in this frequency range.

The Fabry-Perot fringes allow for an independent determination of the sample thickness d as follows: The frequency of the m^{th} maximum of the Fabry-Perot oscillations is given by

$$\nu_m = m\frac{c}{2nd} \quad . \tag{10.1}$$

[1]The measurement was carried out by Axel Roggenbuck and Anselm Deninger at Toptica Photonics. The data was analyzed at the University of Cologne.

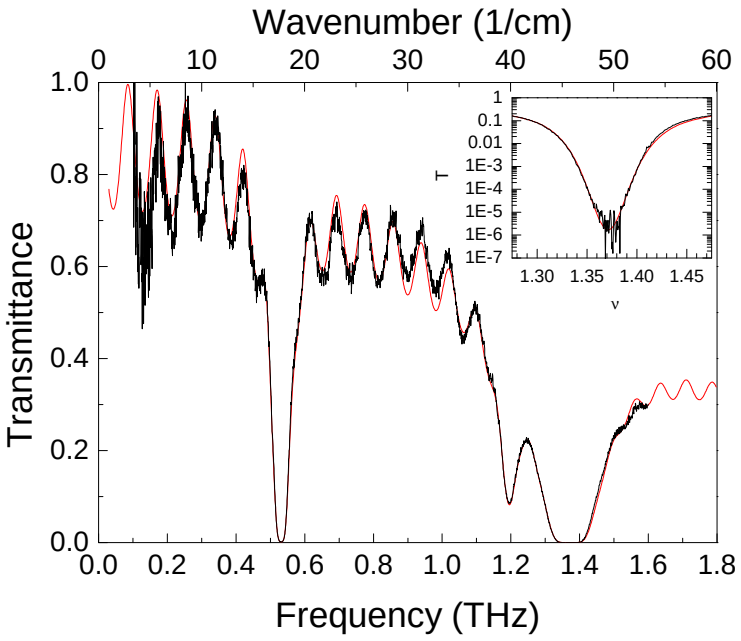

Figure 10.1.: Transmittance of α-lactose monohydrate measured on a pellet of 0.98 mm thickness. Fabry-Perot oscillations due to multiple reflections within the sample can be observed. The red line depicts a fit according to the Drude-Lorentz model. The inset shows the strong absorption line at 1.37 GHz on a logarithmic scale.

By knowing ν_m with an accuracy of a few GHz, the optical thickness nd can be determined with a precision of 0.5%. From the frequencies of the Fabry-Perot maxima and the measured phase data, the sample thickness can be obtained using equation 5.6. The thickness of the sample investigated is $d = 0.98$ mm $\pm$ 0.01 mm.

The absorption line at around 0.53 THz is the narrowest of the three observed. Although it is a very strong absorption with $T \to 0$, the minimum can be reliably determined as shown in the logarithmic plot in figure 10.2. The absorption line at 1.37 THz is even stronger. It is shown on a logarithmic scale in the inset of figure 10.1. This demonstrates the advantage of the homodyne detection and the high SNR of the spectrometer. The transmittance can be measured down to values of $T \approx 10^{-5}$.

The frequencies of the absorption lines were determined by fitting a model of three Lorentz oscillators to the transmittance. Contributions from phonons at higher frequencies that cause a steady decrease of the transmittance with increasing frequency were taken into account by adding two Lorentz oscillators located above 2.5 THz to the model which have been observed by THz TDS [22]. Figure 10.2 shows that the line shape of the absorption feature is very well reproduced by the model. The parameters of the three absorption lines obtained from the fit are as in table 10.1.

The agreement between measurement and fit is very good. The resonance fre-

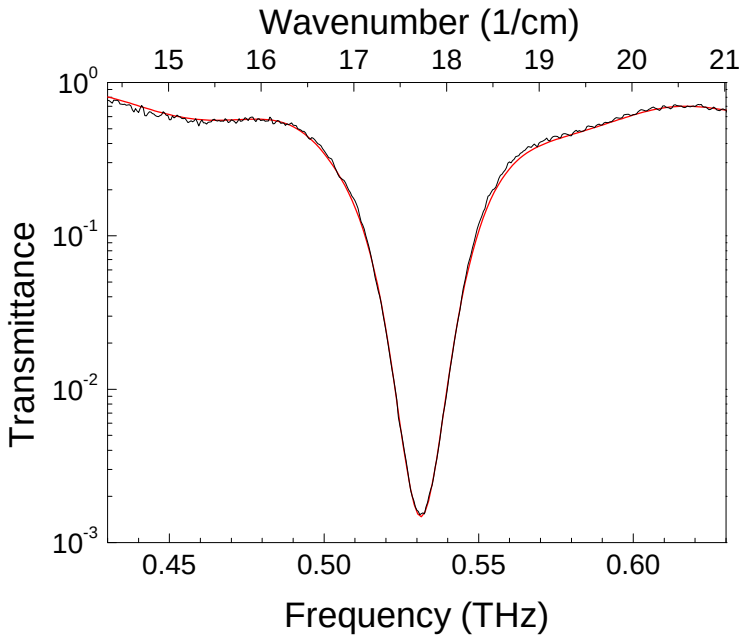

Figure 10.2.: Transmittance of α-lactose monohydrate in the vicinity of the absorption line at 0.53 THz. The fit according to the Drude-Lorentz model is depicted as red line.

Table 10.1.: Resonance frequencies $\nu_{0,i}$ and linewidths γ_i extracted from the Drude-Lorentz fit.

i	resonance frequency (GHz)	linewidth (GHz)
1	530.4 GHz ± 0.5 GHz	25 GHz ± 1 GHz
2	1195 GHz ± 1 GHz	44 GHz ± 3 GHz
3	1369 GHz ± 2 GHz	58 GHz ± 4 GHz

quency of the lowest absorption feature is in good agreement with results of other groups obtained by THz TDS [2, 22, 152–155]. However, the linewidth of this feature was mostly not considered. Resonance frequency and linewidth of the absorption around 530 GHz were studied by Brown *et al.* using THZ TDS, CW TS, and a frequency multiplier chain [43]. The results obtained by the various techniques are shown in figure 10.3. For the THz TDS measurement it can be seen that the resolution (∼45 GHz) is too low to extract the shape of the absorption line accurately. Thus the extracted FWHM of about 69 GHz is much higher than the value obtained by CW TS shown in figure 10.3 (b). In this measurement the resolution is 300 MHz which is much higher than for THz TDS. The extracted linewidth of 23 GHz is in agreement with the results obtained in this work (compare table 10.1). Nevertheless, the data obtained by CW TS is noisy and the exact shape of the absorption line is still not clear. In figure 10.3 (b) it can also be seen that a contribution of the water

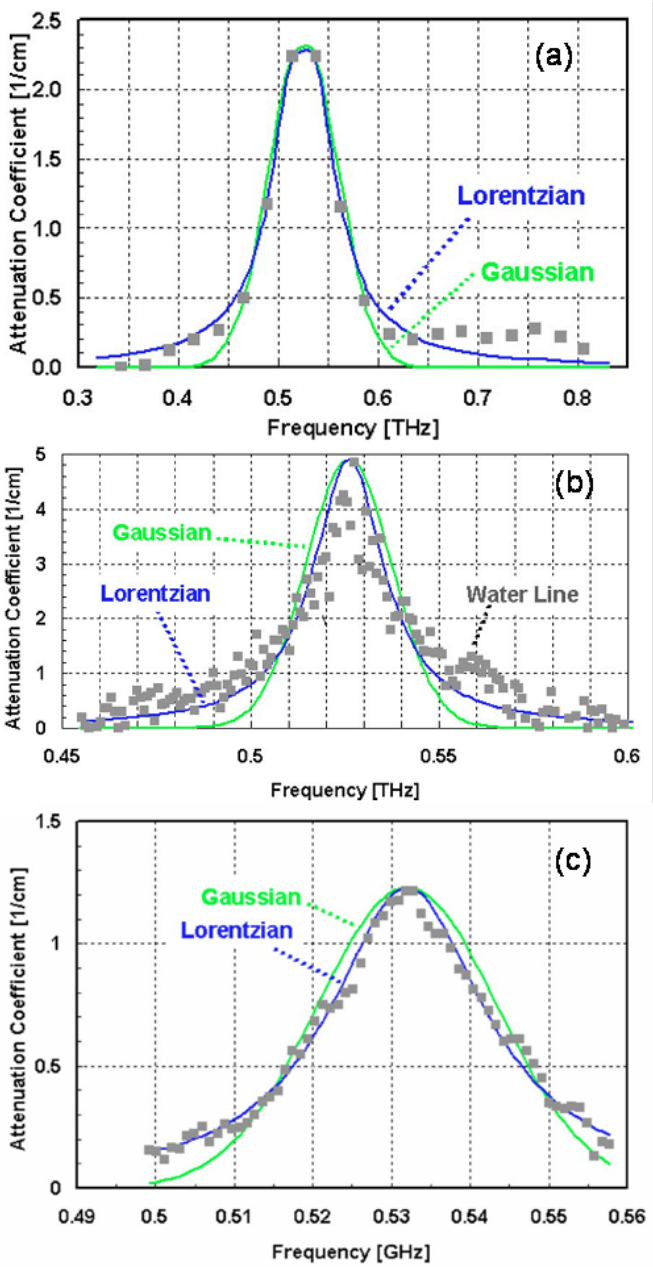

Figure 10.3.: Attenuation coefficient measured with three different methods, namely (a) THz TDS, (b) cw terahertz spectroscopy, and (c) frequency multiplier chain. The figures are taken from [43].

absorption around 560 GHz is still present in the attenuation coefficient. This might be due to moisture in the powder sample. The extracted resonance frequencies extracted from the THz TDS and CW TS data are 525 GHz and 526 GHz, respectively, which is in contradiction with the results of this work and results of other THz TDS

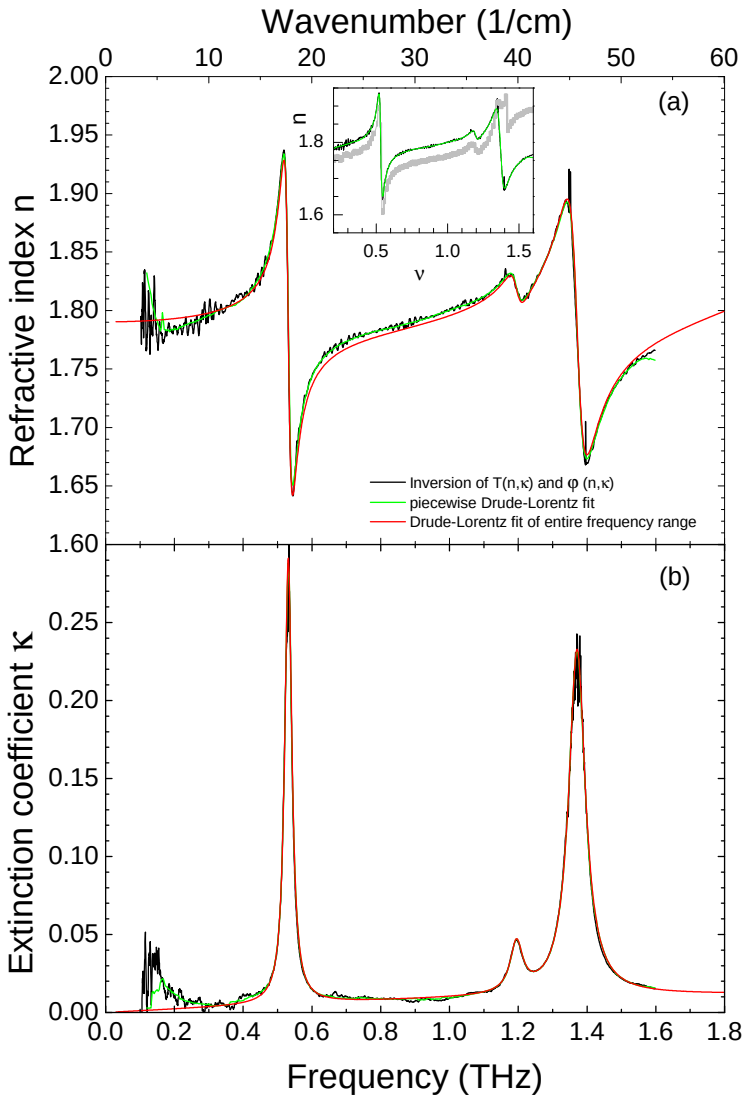

Figure 10.4.: Refractive index and extinction coefficient of α-lactose monohydrate. The data obtained by the inversion method and the PDL fit are shown in black and green, respectively. The refractive index extracted from the Drude-Lorentz model fitted to the entire frequency range is depicted as red line. Inset: Comparison between the data measured in this work (black and green) and the data from Fischer (gray) [22].

measurements [2, 22, 152–155]. The deviation from the results of the other groups was attributed to the dilution of the lactose power [43]. Figure 10.3 (c) shows the result for the frequency multiplier technique. Due to the high resolution of this method, which was reported to be 0.5 MHz, the line shape could be measured more accurately. Thanks to higher output power of the multiplier chain, the SNR of the measurement was about three times higher than for the CW TS measurement [43].

However, the tuning range of the frequency multiplier chain is only about 50 GHz. The extracted resonance frequency and linewidth are 532 ± 1 GHz and 24 ± 1 GHz, respectively, which is in good agreement with the results presented in table 10.1 which demonstrates the high quality of the data obtained by the THz spectrometer optimized in the scope of this thesis.

Figure 10.4 shows the frequency-dependent refractive index and extinction coefficient derived from the transmittance and phase data. Both n and κ were on the one hand obtained by PDL fit (green) and on the other hand obtained by the inversion method (black). The frequency-dependent n and κ extracted from the Drude-Lorentz fit of the entire frequency range are shown in red. Due to the strong variation of n in the vicinity of the absorption lines, the numerical inversion has to be performed using a very small frequency range. Note that the numerical inversion is performed by fitting equation 5.18 (which is a combination of equations 2.17 and 2.18) to a small data range as described in section 5.5. For α-lactose monohydrate a size of the fitted range of about 3 GHz was used. Due to this small range, the accurate determination of κ at the absorption feature at 1.37 THz is difficult. Here, the transmittance is almost zero and the exact behavior of T is not clear within the small fitted frequency range applied for the inversion method. For the PDL fit the fitted range was again chosen to be one period of the Fabry-Perot fringes and thus much larger than for the inversion method. Therefore κ is better determined by the PDL fit at 1.37 GHz. Note that for the PDL fit the thickness as well as the resonance frequencies and damping constants of the three oscillators below 1.8 THz were kept constant at the values obtained from the Drude-Lorentz fit of the entire frequency range.

Both methods give very good results. The dispersion caused by the absorption features is well resolved even for the weak absorption feature at 1195 GHz. Also the consistency with the n and κ obtained from the fit of the entire frequency range is very good. The evaluated refractive index agrees with results from Fischer [22] measured with THz TDS which is shown in the inset of figure 10.4. The overall behavior in both measurements is the same. Deviations in the range of 2% at low frequencies are most probably due to uncertainties in the thickness determination. The discrepancy at frequencies above the absorption line at 1.369 THz is due to a phase jump which has not be resolved in the time-domain data. Note that results obtained on α-lactose monohydrate diluted by polyethylene yield a smaller value of the refractive index and a reduced dispersion [155].

It is important to note that the model shown in red is derived from the Drude-Lorentz fit of the transmittance only. As can be seen, the agreement between both n and κ determined by the numerical inversion as well as PDL fit and the ones obtained from the Drude-Lorentz fit of the entire frequency range is very good. This very impressively shows that with the frequency-scan method transmittance and refractive index in particular or the real and imaginary part of the optical functions in general can be determined independent of each other and that the measured data is Kramers-Kronig consistent.

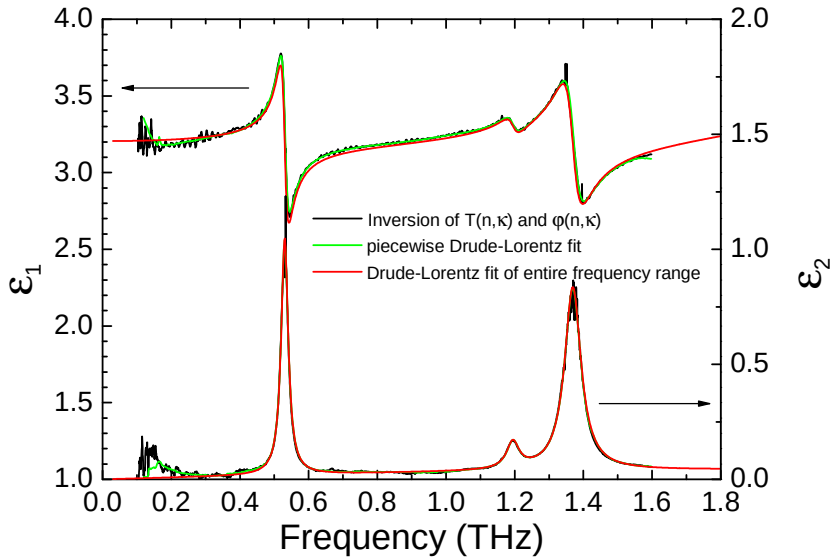

Figure 10.5.: Real part ε_1 and imaginary part ε_2 of the complex dielectric function of α-lactose monohydrate. The functions were calculated from the refractive index and the extinction coefficient as described in the text. The red line depicts ε_1 and ε_2 extracted from the fit of a Drude-Lorentz model to the transmittance.

All other optical functions can be calculated from the measured transmittance and refractive index. Figure 10.5 shows the real and imaginary part of the dielectric function calculated from the complex refractive index using equations 2.9 and 2.10. Also here the agreement between the calculated data and behavior extracted from the fit of the transmittance is very good. This again shows the Krames-Kronig consistency of the data.

11. Conclusion

This work reports on the realization and improvement of a novel THz spectrometer. Various performance checks and optimizations for solid-state spectroscopy have been carried out. Different measurement methods have been developed: The frequency-scan method tunes the frequency in small steps for a constant ΔL. In this method, no moving parts are present. The photocurrent oscillates as a function of frequency, and amplitude and phase are gained from the envelope and the positions of the extrema. In the fiber-stretcher method, ΔL is varied at a constant frequency. For the variation of ΔL a fiber stretcher is implemented in the setup. It guarantees a fast modulation while having the advantage of a compact, all fiber based setup. Here, amplitude and phase are extracted by a sinusoidal fit to the photocurrent. Both methods are proven to show very precise results. Still, to obtain the same data quality with both methods, the time required when employing the frequency-scan method is much larger than for the fiber-stretcher method.

To obtain such precise results, drifts in amplitude and phase have been minimized. The amplitude stability strongly depends on the amount of light reaching the photo-active region of the photomixers. Mechanical stress induced by temperature fluctuations can either cause mechanical displacement between the fiber and the photo-active region or change the polarization in the fiber. Taking advantage of the fact that the photomixers can act as photo diodes, the amount of light radiating on the photo-active regions can be measured by DC currents. The fluctuations of the DC currents are used to correct the photocurrent amplitude, achieving an amplitude stability of $\pm$ 2% within the fiber-stretcher method. A good 100% line is also obtained in the frequency-scan method, but because of the need for interpolation of the envelope, the noise is much larger than for the fiber-stretcher method.

Temperature fluctuations also influence the phase stability since they can change the value of ΔL. The other crucial factor for the phase stability is the frequency stability of the laser beat. The influence of the temperature fluctuations can be minimized by equalizing the length of both the fiber arms to the transmitter and to the receiver. The influence of the frequency instabilities is minimized by adjusting ΔL to almost zero. Since it is shown that the frequency drifts have a stronger influence on the phase stability, ΔL was adjusted to zero resulting in a stability of ΔL of about 20 μm. For a further reduction of the uncertainty of the phase a new method to correct for the remaining phase drifts has been invented in this group: For this purpose a third laser was implemented into the setup. Two lasers are kept at constant frequency and the third one is tuned resulting in one fixed and two tunable beat frequencies. Although three beat signals are present, the amplitude and phase

information of all frequencies can be precisely extracted by a fit of superpositions of cosine functions. Still, in the fit, uncertainties in the frequencies add up to the uncertainties in amplitude and phase. Therefore the three beat frequencies are determined and given as fixed parameters to the fit. The fixed frequency serves as reference frequency for which, in the ideal case also the phase φ_{ref} should be constant. In the experiment φ_{ref} is recorded simultaneously with phases of the tunable beat signals. Since the fluctuations of ΔL are assumed to be the same for all frequencies, the fluctuations of φ_{ref} can be used to correct the fluctuations in the other phases via the fluctuations in ΔL. By this correction the uncertainty in ΔL is reduced to $\pm$ 3 μm.

It has been shown that the complex optical functions can be determined accurately and reliably from the measured transmittance and phase. One model-free method has been demonstrated by numerically inverting the equations $T(n, \kappa)$ and $\varphi(n, \kappa)$. Due to noise it is not enough to invert T and φ at every frequency point but the behavior in a certain frequency range has to be taken into account. Very good results are obtained when this frequency range is in the order of one period of the Fabry-Perot fringes. Although this method assumes n and κ to be constant within the fitted range it is shown that good results can also be obtained at absorption features. Another method that overcomes the disadvantage of assuming n and κ to be constant within the fitted range is the fit of a Drude-Lorentz model. When the Drude-Lorentz model is fitted to a small frequency range, the data is very well described by the fit. In this case the obtained parameters ν_0, ν_p, and γ do not have to resemble the real properties of the material, but the complex optical functions calculated from these parameters resemble the actual properties of this frequency range very well. With both methods very small changes in n can be resolved and κ can be determined reliably down to the order of 10^{-3}.

The beam profile has been investigated using the knife-edge method. The half-opening angle of the source has been determined to be about 7.5° at 100 GHz and about 1° at 1 THz. Lenses made of high-density polyethylene have been designed and manufactured to focus the beam. The beam waist at the focal spot achieved with the designed optics is about 2 mm which is adequate for the investigation of single crystals. The photomixers show an elliptical polarization dependence of which the form and the orientation of the ellipse can change rather strongly with frequency due to changes in the antenna impedance.

Magnesium oxide has been investigated using all three measurement techniques. Both the frequency-scan method and the fiber-stretcher method show good results. Due to the long measurement time and the fact that ΔL cannot be adjusted to zero in the frequency-scan method, fluctuations in the phase data are larger than for the fiber-stretcher method. Also the time required to measure the whole frequency range is larger for the frequency-scan method. Using the three-laser setup, the phase and hence the complex optical function can be determined very precisely in good agreement with literature.

For measurements at low temperatures a bath cryostat which is especially de-

signed for THz frequencies has been implemented into the setup. The temperature-dependent properties of Si have been investigated and compared to a measurement using a cold-finger cryostat which lacks the special design of the bath cryostat. To resolve the Drude absorption accurately the suppression of standing waves is crucial. Because of the special design of the bath cryostat, standing waves are considerably reduced and thus the temperature-dependent properties are determined more precisely than by using the cold-finger cryostat.

As third sample α-lactose monohydrate has been investigated which has the narrowest absorption line known for solid-state samples. The line shape of all absorption features up to 1.8 THz was resolved very well and the resonance frequency and linewidth were determined very precisely, clarifying contradictory results of a previous publication [43].

A. Appendix

A.1. Scripts

A.1.1. Frequency-scan analysis

The following script was used to analyze the frequency-scan data. It contains the frequency correction as well as the extraction of the envelope and the extrema and zero crossing frequencies. The script was written for *GNU Octave* [158]. The calculation of the phase was done manually. The procedure is described in section 5.1.

```
clear all;

format long;
DataRef=[];
DataSample=[];

DataRefIn=load('C:\...');
%DataSampleIn=load('C:\...');

zaehl1=1;
zaehl2=1;
zaehl3=1;
zaehl4=1;
zaehl5=1;
zaehl6=1;
zaehl7=1;

runlength=2700;

for iref=1:(2*runlength):length(DataRefIn)
    %DataRef=[];
    %DataSample=[];
    q=1;
    for j=iref:1:iref+runlength-1
        DataRef(q,1)=DataRefIn(j,1);
        DataRef(q,2)=DataRefIn(j,2);
        q=q+1;
    endfor
    p=1;
    for k=iref+runlength:1:iref+(2*runlength)-1
        DataSample(p,1)=DataRefIn(k,1);
        DataSample(p,2)=DataRefIn(k,2);
```

```
33          p=p+1;
    endfor
35
    MaxRef=[];
37  c1=1;
    n=1;
39  pi=3.141592654;
    c=3e8;
41  thickness=0.001;

43  for i=3:1:(length(DataRef)-2)
        if DataRef(i,2)==0                          %% Ist ein Wert 0,
            so ist die Nullstelle direkt gefunden
45          NullRef(n,1)=n;                         %% Index an der die
                Nullstelle gefunden wurde
            NullRef(n,2)=DataRef(i,1);              %% x-Wert der
                Nullstelle
47          n=n+1;
        elseif DataRef(i-1,2)*DataRef(i,2)<0    %% Anderenfalls wird
            über das Produkt zweier benachbarter Punkte festgestellt,
            ob eine Nulldurchgang stattfindet
49          a=((DataRef(i,2)-DataRef(i-1,2))/(DataRef(i,1)-DataRef(i
                -1,1)));    %Steigung, der durch die zwei Punkte
                definierten Geraden.
            NullRef(n,1)=n;
51          NullRef(n,2)=DataRef(i-1,1)-(DataRef(i-1,2)/a);
                                    %Berechnung von x0 mittels
                linearer Approximation
            a=0;
53          n=n+1;
        endif
55
        %% Bestimmung der Extrema der Rohdaten
57
        u=1;
59      if DataRef(i,2)==DataRef(i+1,2)
                                        %%Haben zwei Datenpunkte
            denselben Wert, wird der übernächste genommen.
            u=2;
61      else
            u=1;
63      endif
        if (DataRef(i-1,2)-DataRef(i,2))*(DataRef(i,2)-DataRef(i+u,2))
            <0 & (DataRef(i-1,2)-DataRef(i-2,2))*(DataRef(i+u+1,2)-
            DataRef(i+u,2))<0
65          alpha=DataRef(i-1,1)-DataRef(i,1); beta=DataRef(i-1,1)+
                DataRef(i,1); gamma=DataRef(i-1,1)-DataRef(i+1,1);
                delta=DataRef(i-1,1)+DataRef(i+1,1);
            if DataRef(i-1,2)==DataRef(i+1,2)               %% In
                diesem Fall ist die Kurve Symmetrisch. Mittlerer der
                drei Punkte wird als Extremum genommen
```

```
67                  MaxRef(c1,1)=c1;
                    MaxRef(c1,2)=DataRef(i,1);
69                  MaxRef(c1,3)=DataRef(i,2);
                    c1=c1+1;
71              else
                    epsilon=(DataRef(i-1,2)-DataRef(i,2))/(DataRef(i-1,2)-
                        DataRef(i+1,2)); %% An drei Punkten am Extremum
                        wird eine Parabel angepasst um den Wert des
                        Extremums zu bestimen
73                  MaxRef(c1,1)=c1;
                    MaxRef(c1,2)=(delta*epsilon*gamma-alpha*beta)/(2*
                        epsilon*gamma-2*alpha);
75                  if beta-2*MaxRef(c1,2)~=0
                        b=(DataRef(i-1,2)-DataRef(i,2))/(alpha*beta-2*alpha
                            *MaxRef(c1,2));
77                  end
                    MaxRef(c1,3)=abs(DataRef(i-1,2)-b*(DataRef(i-1,1)-
                        MaxRef(c1,2))^2);
79                  c1=c1+1;
                endif
81              if c1>2
                    if MaxRef(c1-1,2)-MaxRef(c1-2,2)<0.72 | MaxRef(c1-1,2)
                        -MaxRef(c1-2,2)>0.78
83                      c1-1; MaxRef(c1-1,2)-MaxRef(c1-2,2);
                    endif
85              endif
            endif
87      endfor

89      %%Differenz zwischen Nullstellen und Maxima vor der
            Freuqunzkorrektur
        i=1;
91      for i=1:1:length(NullRef)-1
            NullRefDiff(i,1)=i;
93          NullRefDiff(i,2)=NullRef(i+1,2)-NullRef(i,2);
        endfor
95      i=1;
        for i=1:1:length(MaxRef)-1
97          MaxRefDiff(i,1)=i;
            MaxRefDiff(i,2)=MaxRef(i+1,2)-MaxRef(i,2);
99      endfor

101     %%%%%%%%%%%%%%%%%%%%%%%%%%%%%%%%%%%%%%%%%%%%%%%%%%%%%%%%%%%%%%%%%%%%%%%
        %% Frequenzkorrektur
103
        %% Bestimmung des Frequenzfehlers: Hierzu wird die Nummer das
            Maximums gegen
105     %% die Frequenz, an der das Maximum liegt, aufgetragen und eine
            Gerade an die
        %%Funktion angepasst. Der Fit wird anschlieSSend von der Gerade
            abgezogen.
```

```
%%%%%%%%%%%%%%%%%%%%%%%%%%%%%%%%%%%%%%%%%%%%%%%%%%%%%%%%%%%%

Fit1Ref=[];
Para1 = polyfit(MaxRef(:,1),MaxRef(:,2),1);                 %Es wird die Ordnung gegen die Position der Maxima aufgetragen und eine Gerade angepasst
Fit1Ref(:,1)=MaxRef(:,1);                                   %Ordnung
for d=1:1:length(MaxRef)
    Fit1Ref(d,2)=MaxRef(d,2);                               %Frequenzen der Rohdaten
    Fit1Ref(d,3)=Fit1Ref(d,1)*Para1(1,1)+Para1(1,2);        %Frequenzen des linearen Fits (Frequenz, die das Maximum nach dem Fit haben müsste)
    Fit1Ref(d,4)=MaxRef(d,2)-Fit1Ref(d,3);                  %Differenz zwischen Rohdaten und Fit (Abweichung vom Soll)
endfor

%% Für den Fall, dass der Brechungsindex während der Messung ändert (möglich
%% da die THz Strahlen auch ohne Probe durch Antenne und Linsenen müssen),
%% liegen die Extrema nicht mehr auf einer Geraden (Dispersion). Im
%% folgenden wird die daher die Differenz zwischen Rohdaten und Fit
%% geglättet und die gelättete Kurve nochmals von der schon gebildeten
%% Differenz abgezogen, um die die dispersion aus der Korrektur
%% herauszurechnen. (Untergrund der zu erwartenden Kosinusschwingung wird berechnet und abgezogen)

%% Glättung über Savitzky Golay Algorithmus

clear test;
test(:,1)=Fit1Ref(:,2);
test(:,2)=Fit1Ref(:,4);

F=sgolay(3,351);                                                            %Finden der optimalen Parameter
test2=sgolayfilt(test,F);

Fit1Ref(:,5)=test2(:,2);                                              %Geglättete Kurve mit Savitzky Golay Algorithmus
i=1;

for i=1:length(Fit1Ref)
    Fit1Ref(i,6)=Fit1Ref(i,4)-Fit1Ref(i,5);                 %Untergrund wird von der Korrekturkurve abgezogen
endfor

```

```
%% Zur Bestimmung der Frequenzfehlers der Probe werden in der Kurve
%% #-gegen-delta_w die # wieder durch die zugehörigen gemessenen Frequenzen
%% substituiert (nicht die des Fits !!!). AnschlieSSend wird die Kurve omega
%% gegen delta-omega für alle Frequenzen der Messung interpoliert.

IntpErr=[];
freqErrSample=interp1(MaxRef(:,2),Fit1Ref(:,6),DataSample(:,1), 'spline'); %%(FreqCorrExtern(:,1),FreqCorrExtern(:,2), DataSample(:,1), 'spline');
freqErrRef=interp1(MaxRef(:,2),Fit1Ref(:,6),DataRef(:,1), 'spline'); %%(FreqCorrExtern(:,1),FreqCorrExtern(:,2),DataRef(:,1), 'spline');

IntpErr(:,1)=DataSample(:,1);                                          %% Frequenzfehler für alle gemessenen Frequenzen durch obige Interpolation.
IntpErr(:,2)=freqErrSample;

dlmwrite('Geradenfit', Fit1Ref, 'delimiter', '\t');
%dlmwrite('InterpolationFreqErr', IntpErr, 'delimiter', '\t');

%%%%%%%%%%%%%%%%%%%%%%%%%%%%%%%%%%%%%%%%%%%%%%%%%%%%%%%%%%%%%%%%%%%%%%%%%%%%
%% Korrektur der Daten. Von den "gemessenen" Frequnzen wird der
%% Differenzwert des Fits abgezogen.
%%%%%%%%%%%%%%%%%%%%%%%%%%%%%%%%%%%%%%%%%%%%%%%%%%%%%%%%%%%%%%%%%%%%%%%%%%%%

FreqCorrRef=[];
FreqCorrSample=[];
for f=1:1:length(freqErrSample)
    if (DataSample(f,1)>0 & DataSample(f,1)<1533) %freqErrRef(f,1)<2.7 %% Es wird nur an den Stellen korrigiert, an denen der Kosinus sauber ist
        FreqCorrRef(f,1)=DataRef(f,1)-freqErrRef(f,1);
        FreqCorrSample(f,1)=DataSample(f,1)-freqErrSample(f,1);
    else
        FreqCorrRef(f,1)=DataRef(f,1);
        FreqCorrSample(f,1)=DataSample(f,1);
    endif
endfor

%%%%%%%%%%%%%%%%%%%%%%%%%%%%%%%%%%%%%%%%%%%%%%%%%%%%%%%%%%%%%%%%%%%%%%%%%%%%
%% Übergeben der korrigierten Daten
%%%%%%%%%%%%%%%%%%%%%%%%%%%%%%%%%%%%%%%%%%%%%%%%%%%%%%%%%%%%%%%%%%%%%%%%%%%%

DataCorrRef=[];
DataCorrSample=[];

DataCorrRef(:,1)=FreqCorrRef(:,1);  %DataRef(:,1);
DataCorrRef(:,2)=DataRef(:,2);
```

```
183     DataCorrSample(:,1)=FreqCorrSample(:,1);      %DataSample(:,1);
        DataCorrSample(:,2)=DataSample(:,2);
185
        %%%%%%%%%%%%%%%%%%%%%%%%%%%%%%%%%%%%
187     %%Auswertung der korrigierten Daten
        %%%%%%%%%%%%%%%%%%%%%%%%%%%%%%%%%%%%
189
        NullCorrRef=[];
191     MaxCorrRef=[];
        n=1;
193     m=1;
        a=0;
195     b=0;
        alpha=0; beta=0; gamma=0; delta=0; epsilon=0;
197     c2=1;
        %% In dieser Schleifen werden die Nullstellen über den
            Vorzeichenwechsel
199     %% identifiziert. Zwischen den Punkten, die zwischen einer
            Nullstelle
        %% liegen, wird dabei eine lineare Interpolation angenommen.
201     for i=3:1:(length(DataCorrRef)-2)
            if DataCorrRef(i,2)==0                              %% Ist ein Wert
                0, so ist die Nullstelle direkt gefunden
203             NullCorrRef(n,1)=n;
                NullCorrRef(n,2)=DataCorrRef(i,1);
205             NullCorrRef(n,3)=i;
                n=n+1;
207         elseif DataCorrRef(i-1,2)*DataCorrRef(i,2)<0    %% Anderenfalls
                wird über das Produkt zweier benachbarter Punkte
               festgestellt, ob eine Nulldurchgang stattfindet
                a=((DataCorrRef(i,2)-DataCorrRef(i-1,2))/(DataCorrRef(i,1)-
                    DataCorrRef(i-1,1)));     %Steigung, der durch die zwei
                    Punkte definierten Geraden.
209             NullCorrRef(n,1)=n;
                NullCorrRef(n,2)=DataCorrRef(i-1,1)-(DataCorrRef(i-1,2)/a);
                                              %Berechnung von x0
211             NullCorrRef(n,3)=i;
                a=0;
213             n=n+1;
            endif
215     %% Hier werden die Maxima gesucht, indem aus drei Punkten am
            Maximum eine
        %% Parabelform berechnet wird.
217         u2=1;
            if DataCorrRef(i,2)==DataCorrRef(i+1,2)          %%Haben zwei
                benachbarte Punkte den gleichen y-Wert soll für die
                Berechnung der übernächste genommen werden
219             u2=2;
            else
221             u2=1;
            endif
```

```
223         %%Für die Bestimmung ob ein Extremum vorliegt, wird die
                Differenz (d.h. Steigung) von 5 aufeinanderfolgenden
                Punkten verglichen.
            if (DataCorrRef(i-1,2)-DataCorrRef(i,2))*(DataCorrRef(i,2)-
                DataCorrRef(i+u2,2))<0 & (DataCorrRef(i-1,2)-DataCorrRef(i
                -2,2))*(DataCorrRef(i+u+1,2)-DataCorrRef(i+u,2))<0
225             alpha=DataCorrRef(i-1,1)-DataCorrRef(i,1); beta=DataCorrRef
                    (i-1,1)+DataCorrRef(i,1); gamma=DataCorrRef(i-1,1)-
                    DataCorrRef(i+1,1); delta=DataCorrRef(i-1,1)+
                    DataCorrRef(i+1,1);
                if DataCorrRef(i-1,2)==DataCorrRef(i+1,2)
227                 MaxCorrRef(m,1)=m;
                    MaxCorrRef(m,2)=DataCorrRef(i,1);
229                 MaxCorrRef(m,3)=DataCorrRef(i,2);
                    m=m+1;
231             else
                    epsilon=(DataCorrRef(i-1,2)-DataCorrRef(i,2))/(
                        DataCorrRef(i-1,2)-DataCorrRef(i+1,2));
233                 MaxCorrRef(m,1)=m;
                    MaxCorrRef(m,2)=(delta*epsilon*gamma-alpha*beta)/(2*
                        epsilon*gamma-2*alpha);
235                 if beta-2*MaxCorrRef(m,2)~=0
                        b=(DataCorrRef(i-1,2)-DataCorrRef(i,2))/(alpha*beta
                            -2*alpha*MaxCorrRef(m,2));
237                 endif
                    MaxCorrRef(m,3)=abs(DataCorrRef(i-1,2)-b*(DataCorrRef(i
                        -1,1)-MaxCorrRef(m,2))^2);
239                 MaxCorrRef(m,4)=(DataCorrRef(i-1,2)-b*(DataCorrRef(i
                        -1,1)-MaxCorrRef(m,2))^2);
                    m=m+1;
241             endif
                if m>2
243                 if (MaxCorrRef(m-1,2)-MaxCorrRef(m-2,2)<0.13) | (
                        MaxCorrRef(m-1,2)-MaxCorrRef(m-2,2)>0.2)
                        logmaxRef(c2,1)=m-1;
245                     logmaxRef(c2,2)=MaxCorrRef(m-1,2)-MaxCorrRef(m-2,2)
                            ;
                        logmaxRef(c2,3)=MaxCorrRef(m-1,2);
247                     c2=c2+1;
                    endif
249             endif
        endif
251 endfor

253 %%%%%%%%%%%%%%%%%%%%%%%%%%%%%%%%%%%%%%%%%%%%%%%%%%%%%%%%%%%%%%%%%%%%%%%%
    %% Korrektur der Nullstellen
255 %% Durch Rauschen in der Nähe der Nulstellen kann es durch mehrere
    %% benachbarte "falsche" Nullstellen kommmen
257 %%%%%%%%%%%%%%%%%%%%%%%%%%%%%%%%%%%%%%%%%%%%%%%%%%%%%%%%%%%%%%%%%%%%%%%%
    i=3;
259 j=1;
```

```
N=1;
T=Para1(1);
while i<length(NullCorrRef)
    clear nc;
    clear ic;
    for j=i:1:length(NullCorrRef)
        if(NullCorrRef(j,2)-NullCorrRef(i,2))<0.25*T %%Kontrolle ob der Abstand von einer Nullstelle zur Nächsten kleiner als 0,25*Periode ist
            nc(j-i+1,1)=NullCorrRef(j,2);   %Position der Nullstelle
            ic(j-i+1,1) = NullCorrRef(j,3); %Index der Nullstelle
        endif
    endfor

    if length(nc)==1                        %Wenn nur eine Nullstelle aufgelistet wurde (d.h. keine andere liegt in der Umgebung von 0,25*T)
        NullCorrFinalRef(N,1)=N;            %wird diese Nullstelle übernommen
        NullCorrFinalRef(N,2)=NullCorrRef(i,2);
        NullCorrFinalRef(N,3)=NullCorrRef(i,3);
        N=N+1;
        i=i+1;
    else
        xmRef = mean(nc(:,1));              % Anderenfalls wird an die Punkte, die um den Mittelwert der gefundenen Nullstellen liegen,
        unten=11;                           % eine Gerade angepasst und deren Nullstelle als "echte" Nullstelle genommen.
        while DataCorrRef(unten,1) < xmRef-0.35*T
            unten=unten+1;
        endwhile
        oben = length(DataCorrRef)-11;
        while DataCorrRef(oben,1) > xmRef+0.35*T
            oben = oben -1;
        endwhile

        gerade = polyfit(DataCorrRef(unten:oben,1), DataCorrRef(unten:oben,2),1);
        NullCorrFinalRef(N,1)=N;
        NullCorrFinalRef(N,2)=-gerade(2)/gerade(1);
        NullCorrFinalRef(N,3)=round(mean(ic(:,1)));
        N=N+1;
        i=i+length(nc);
    endif
endwhile

%%%%%%%%%%%%%%%%%%%%%%%%%%%%%%%%%%%%%%%%%%%%%%%%%%%%%%%%%%%%%%%%%%%%%%%%%%%%%%%
%% Extrema werden in Minima und Maxima aufgespalten
```

```
%%%%%%%%%%%%%%%%%%%%%%%%%%%%%%%%%%%%%%%%%%%%%%%%%%%%%%%

MaximaRef=[];
MinimaRef=[];
i=1;
r=1;
s=1;

for i=2:1:length(MaxCorrRef)
    if MaxCorrRef(i,4)>0
        MaximaRef(r,1)=r;
        MaximaRef(r,2)=MaxCorrRef(i,2);
        MaximaRef(r,3)=MaxCorrRef(i,4);
        r=r+1;
    else
        MinimaRef(s,1)=s;
        MinimaRef(s,2)=MaxCorrRef(i,2);
        MinimaRef(s,3)=MaxCorrRef(i,4);
        s=s+1;
    endif
endfor

%%%%%%%%%%%%%%%%%%%%%%%%%%%%%%%%%%%%%%%%%%%%%%%%%%%%%%%%%%%%%%%%%%%%
%%Differenz zwischen Nullstellen und Maxima nach der
    Frequenzkorrektur
%%%%%%%%%%%%%%%%%%%%%%%%%%%%%%%%%%%%%%%%%%%%%%%%%%%%%%%%%%%%%%%%%%%%

F=sgolay(3,51);
                                                                            %Finden
    der optimalen Parameter
i=1;
for i=1:1:length(NullCorrFinalRef)-1
    NullCorrFinalRefDiff(i,1)=i;
    NullCorrFinalRefDiff(i,2)=NullCorrFinalRef(i+1,2)-
        NullCorrFinalRef(i,2);
endfor
NullCorrFinalRefDiff(:,3)=sgolayfilt(NullCorrFinalRefDiff(:,2),F);
i=1;
for i=1:1:length(MaxCorrRef)-1
    MaxCorrRefDiff(i,1)=i;
    MaxCorrRefDiff(i,2)=MaxCorrRef(i+1,2)-MaxCorrRef(i,2);
endfor
MaxCorrRefDiff(2:(end-1),3)=sgolayfilt(MaxCorrRefDiff(2:(end-1),2),
    F);
MaxCorrRefDiff(1,3)=MaxCorrRefDiff(2,3);
                                            %Auffüllen des ersten und
    letzten Wertes mit dem zweiten bzw. vorletzten
MaxCorrRefDiff(end,3)=MaxCorrRefDiff(end-1,3);

%dlmwrite('DataCorrRef', DataCorrRef, 'delimiter', '\t');
%dlmwrite('ExtremaRef', MaxCorrRef, 'delimiter', '\t');
```

```
    %dlmwrite('NullstellenRef', NullCorrRef, 'delimiter', '\t');
345 %dlmwrite('MaximaRef', MaximaRef, 'delimiter', '\t');
    %dlmwrite('MinimaRef', MinimaRef, 'delimiter', '\t');
347 %dlmwrite('NullCorrFinalRefDiff', NullCorrFinalRefDiff, 'delimiter
        ', '\t');
    %dlmwrite('MaxCorrRefDiff', MaxCorrRefDiff, 'delimiter', '\t');
349
    for i=1:1:length(DataCorrRef)
351     DataCorrRefGes(zaehl1,1)=DataCorrRef(i,1);
        DataCorrRefGes(zaehl1,2)=DataCorrRef(i,2);
353     zaehl1=zaehl1+1;
    endfor
355 for i=1:1:length(MaxCorrRef)
        MaxCorrRefGes(zaehl2,1)=MaxCorrRef(i,1);
357     MaxCorrRefGes(zaehl2,2)=MaxCorrRef(i,2);
        zaehl2=zaehl2+1;
359 endfor
    for i=1:1:length(NullCorrRef)
361     NullCorrRefGes(zaehl3,1)=NullCorrRef(i,1);
        NullCorrRefGes(zaehl3,2)=NullCorrRef(i,2);
363     zaehl3=zaehl3+1;
    endfor
365 dlmwrite('DataCorrRefGes', DataCorrRefGes, 'delimiter', '\t');
    dlmwrite('ExtremaRefGes', MaxCorrRefGes, 'delimiter', '\t');
367 dlmwrite('NullstellenRefGes', NullCorrRefGes, 'delimiter', '\t');

369 NullCorrSample=[];
    MaxCorrSample=[];
371 n=1;
    m=1;
373 a=0;
    b=0;
375 alpha=0; beta=0; gamma=0; delta=0; epsilon=0;
    c3=1;
377 %% In dieser Schleifen werden die Nullstellen über den
        Vorzeichenwechsel
    %% identifiziert
379 for i=3:1:(length(DataCorrSample)-2)
        if DataCorrSample(i,2)==0
381         NullCorrSample(n,1)=n;
            NullCorrSample(n,2)=DataCorrSample(i,1);
383         NullCorrSample(n,3)=i;
            n=n+1;
385     elseif DataCorrSample(i-1,2)*DataCorrSample(i,2)<0
            a=((DataCorrSample(i,2)-DataCorrSample(i-1,2))/(
                DataCorrSample(i,1)-DataCorrSample(i-1,1)));
387         NullCorrSample(n,1)=n;
            NullCorrSample(n,2)=DataCorrSample(i-1,1)-(DataCorrSample(i
                -1,2)/a);
389         NullCorrSample(n,3)=i;
            a=0;
```

```
391             n=n+1;
        endif
393     %% Hier werden die Maxima gesucht, indem aus drei Punkten am
            Maximum eine
        %% Parabelform berechnet wird.
395         u3=1;
        if DataCorrSample(i,2)==DataCorrSample(i+1,2)
397             u3=2;
        else
399             u3=1;
        endif
401     if (DataCorrSample(i-1,2)-DataCorrSample(i,2))*(DataCorrSample(
            i,2)-DataCorrSample(i+u3,2))<0 & (DataCorrSample(i-1,2)-
            DataCorrSample(i-2,2))*(DataCorrSample(i+u+1,2)-
            DataCorrSample(i+u,2))<0
            alpha=DataCorrSample(i-1,1)-DataCorrSample(i,1); beta=
                DataCorrSample(i-1,1)+DataCorrSample(i,1); gamma=
                DataCorrSample(i-1,1)-DataCorrSample(i+1,1); delta=
                DataCorrSample(i-1,1)+DataCorrSample(i+1,1);
403         if DataCorrSample(i-1,2)==DataCorrSample(i+1,2)
                MaxCorrSample(m,1)=m;
405             MaxCorrSample(m,2)=DataCorrSample(i,1);
                MaxCorrSample(m,3)=DataCorrSample(i,2);
407             m=m+1;
            else
409                 epsilon=(DataCorrSample(i-1,2)-DataCorrSample(i,2))/(
                        DataCorrSample(i-1,2)-DataCorrSample(i+1,2));
                    MaxCorrSample(m,1)=m;
411                 MaxCorrSample(m,2)=(delta*epsilon*gamma-alpha*beta)/(2*
                        epsilon*gamma-2*alpha);
                    if beta-2*MaxCorrSample(m,2)~=0
413                     b=(DataCorrSample(i-1,2)-DataCorrSample(i,2))/(
                            alpha*beta-(2*alpha*MaxCorrSample(m,2)));
                    endif
415                 MaxCorrSample(m,3)=abs(DataCorrSample(i-1,2)-b*(
                        DataCorrSample(i-1,1)-MaxCorrSample(m,2))^2);
                    MaxCorrSample(m,4)=DataCorrSample(i-1,2)-b*(
                        DataCorrSample(i-1,1)-MaxCorrSample(m,2))^2;
417                 m=m+1;
            endif
419         if m>2
                if (MaxCorrSample(m-1,2)-MaxCorrSample(m-2,2)<0.13) | (
                    MaxCorrSample(m-1,2)-MaxCorrSample(m-2,2)>0.2)
421                     logmaxSample(c3,1)=m-1;
                        logmaxSample(c3,2)=MaxCorrSample(m-1,2)-
                            MaxCorrSample(m-2,2);
423                     logmaxSample(c3,3)=MaxCorrSample(m-1,2);
                        c3=c3+1;
425             endif
            endif
427     endif
```

```
    endfor
429
    i=3;
431 j=1;
    N=1;
433 T=Para1(1);
    while i<length(NullCorrSample)-1
435     clear nc;
        clear ic;
437     for j=i:1:length(NullCorrSample)
            if(NullCorrSample(j,2)-NullCorrSample(i,2))<0.25*T
439             nc(j-i+1,1)=NullCorrSample(j,2);
                ic(j-i+1,1) = NullCorrSample(j,3);
441         endif
        endfor
443
        if length(nc)==1
445         NullCorrFinalSample(N,1)=N;
            NullCorrFinalSample(N,2)=NullCorrSample(i,2);
447         NullCorrFinalSample(N,3)=NullCorrSample(i,3);
            N=N+1;
449         i=i+1;
        else
451         xmSample = mean(nc(:,1));
            unten=11;
453         while DataCorrSample(unten,1) < xmSample-0.35*T
                unten=unten+1;
455         endwhile
            oben = length(DataCorrSample)-11;
457         while DataCorrSample(oben,1) > xmSample+0.35*T
                oben = oben -1;
459         endwhile

461         gerade = polyfit(DataCorrSample(unten:oben,1),
                DataCorrSample(unten:oben,2),1);
            NullCorrFinalSample(N,1)=N;
463         NullCorrFinalSample(N,2)=-gerade(2)/gerade(1);
            NullCorrFinalSample(N,3)=round(mean(ic(:,1)));
465         N=N+1;
            i=i+length(nc);
467     endif
    endwhile
469
    MaximaSample=[];
471 MinimaSample=[];
    i=1;
473 r=1;
    s=1;
475
    for i=2:1:length(MaxCorrSample)
477     if MaxCorrSample(i,4)>0
```

```
            MaximaSample(r,1)=r;
            MaximaSample(r,2)=MaxCorrSample(i,2);
            MaximaSample(r,3)=MaxCorrSample(i,4);
            r=r+1;
        else
            MinimaSample(s,1)=s;
            MinimaSample(s,2)=MaxCorrSample(i,2);
            MinimaSample(s,3)=MaxCorrSample(i,4);
            s=s+1;
        endif
    endfor

    %dlmwrite('DataCorrSample', DataCorrSample, 'delimiter', '\t');
    %dlmwrite('ExtremaSample', MaxCorrSample, 'delimiter', '\t');
    %dlmwrite('NullstellenSample', NullCorrSample, 'delimiter', '\t');
    %dlmwrite('MaximaSample', MaximaSample, 'delimiter', '\t');
    %dlmwrite('MinimaSample', MinimaSample, 'delimiter', '\t');

    for i=1:1:length(DataCorrSample)
        DataCorrSampleGes(zaehl4,1)=DataCorrSample(i,1);
        DataCorrSampleGes(zaehl4,2)=DataCorrSample(i,2);
        zaehl4=zaehl4+1;
    endfor
    for i=1:1:length(MaxCorrSample)
        MaxCorrSampleGes(zaehl5,1)=MaxCorrSample(i,1);
        MaxCorrSampleGes(zaehl5,2)=MaxCorrSample(i,2);
        zaehl5=zaehl5+1;
    endfor
    for i=1:1:length(NullCorrSample)
        NullCorrSampleGes(zaehl6,1)=NullCorrSample(i,1);
        NullCorrSampleGes(zaehl6,2)=NullCorrSample(i,2);
        zaehl6=zaehl6+1;
    endfor
    dlmwrite('DataCorrSampleGes', DataCorrSampleGes, 'delimiter', '\t')
        ;
    dlmwrite('ExtremaSampleGes', MaxCorrSampleGes, 'delimiter', '\t');
    dlmwrite('NullstellenSampleGes', NullCorrSampleGes, 'delimiter', '\
        t');

    %%%%%%%%%%%%%%%%%%%%%%%%%%%%%%%%%%%%%%%%%%%%%%%%%%%%%%%%%%%%%%%%%%%
    %% Berechnung der Transmission.
    %% Die Kurve der Extrema von Probe und Referenz werden aud
        denselben Werte
    %% Interpoliert und durcheinder dividiert
    %%%%%%%%%%%%%%%%%%%%%%%%%%%%%%%%%%%%%%%%%%%%%%%%%%%%%%%%%%%%%%%%%%%

    IntpCorr=[];
    freqab=0.2;%abs(round((MaxCorrSample(5,2)-MaxCorrSample(4,2))*100)
        /100);                                          %Abstand zwischen
        Punkten auf der interpolierten Kurve
    freqintp=round(MaxCorrSample(4,2)):freqab:round(MaxCorrSample(
```

```
        length(MaxCorrSample)-1,2));                %Festlegung der Werte
        , auf die interpoliert werden soll
    EintSample=interp1(MaxCorrSample(4:end-1,2),MaxCorrSample(4:end
        -1,3),freqintp,'spline');    %%(2:end-1,3)%Interploation der
        Probendaten
    IntpCorr(:,1)=freqintp.';
    IntpCorr(:,2)=EintSample.';
    EintRef=interp1(MaxCorrRef(4:end-1,2),MaxCorrRef(4:end-1,3),
        freqintp,'spline');
    IntpCorr(:,3)=EintRef.';
    for g=1:1:length(freqintp)
        IntpCorr(g,4)=IntpCorr(g,2)/IntpCorr(g,3);
                                                    %Division der
            Interpolierten Punkte; Probe durch Referenz
    endfor

    %dlmwrite('Transmission', IntpCorr, 'delimiter', '\t');

    for i=1:1:length(IntpCorr)
        TransmissionGes(zaehl7,1)=IntpCorr(i,1);
        TransmissionGes(zaehl7,2)=IntpCorr(i,4);
        zaehl7=zaehl7+1;
    endfor

endfor
dlmwrite('TransmissionGes', TransmissionGes, 'delimiter', '\t');
```

./Scripts/Auswertung_freqscan.m

A.1.2. Inversion of $T(n,\kappa)$ and $\varphi(n,\kappa)$

The script fits equation 5.18 to a short data range with n and κ as the only parameters. After the fit, the fitted frequency range is shifted by one frequency point until the whole data is analyzed. The script was written for *GNU Octave* [158]. The procedure is described in section 5.5.

```
clear -all;

format long;

DataT=load('C:\Doktorarbeit\THz_Messungen\Linsen\090624-Lactose-Toptica
    \aktueller-Lactose-Datensatz\T-Lactose-voll-cm.dat');
Datan=load('C:\Doktorarbeit\THz_Messungen\Linsen\090624-Lactose-Toptica
    \aktueller-Lactose-Datensatz\phase-Lactose-voll-cm.dat');
DataN=load('C:\Doktorarbeit\THz_Messungen\Linsen\090624-Lactose-Toptica
    \aktueller-Lactose-Datensatz\FitResult-Lactose-voll-heavi-3pt.dat')
    ;
DataK=load('C:\Doktorarbeit\THz_Messungen\Linsen\090624-Lactose-Toptica
    \aktueller-Lactose-Datensatz\Data_k_pre_cm.dat');

c=2.99792458e8;
d=0.00098;  %%in m
width=25;

phistart = Datan(:,2);%interp1(Datan(:,1),Datan(:,2),DataT(:,1),'spline
    ');

nstart = interp1(DataN(:,1),DataN(:,2),DataT(:,1),'spline');
kstart = interp1(DataK(:,1),DataK(:,2),DataT(:,1),'spline');

function y=TransPhaseComb(w,p)
  y=(((w.*p(1).*p(3)./p(4)) -...
  atan((abs(p(2)).*(p(1).^2+p(2).^2-1))./(p(1).*(2+p(1)).*(p(1).^2+p(2)
      .^2))) +...
  atan(((((p(1)-1).^2+abs(p(2)).^2)./((p(1)+1).^2+abs(p(2)).^2)).*exp
      (-2.*abs(p(2)).*w.*p(3)./p(4)).*...
  sin(2.*((atan((-2.*abs(p(2)))./(1-(p(1).^2)-abs(p(2)).^2))) +(p(1).*p
      (3).*w./p(4)) ))./...
  (1-((((p(1)-1).^2+abs(p(2)).^2)./((p(1)+1).^2+abs(p(2)).^2)).*exp
      (-2.*abs(p(2)).*w.*p(3)./p(4)).*cos(2.*((atan((-2.*abs(p(2)))
      ./(1-p(1).^2-abs(p(2)).^2)))+(p(1).*w.*p(3)./p(4)))))))).*
      heaviside(w))+...
  (((((((1-(((p(1)-1).^2+abs(p(2)).^2)./((p(1)+1).^2+abs(p(2)).^2))).^2
       + ((4.*((p(1)-1).^2+abs(p(2)).^2)./((p(1)+1).^2+abs(p(2)).^2))
      .*(sin((atan((-2.*abs(p(2)))./(1-p(1).^2-abs(p(2)).^2)))).^2  ))
      ).*exp(-2.*abs(p(2)).*abs(w).*p(3)./p(4))./((1-((((p(1)-1).^2+
      abs(p(2)).^2)./((p(1)+1).^2+abs(p(2)).^2)).*exp(-2.*abs(p(2)).*
      abs(w).*p(3)./p(4)))).^2+(4.*(((p(1)-1).^2+abs(p(2)).^2)./((p(1)
      +1).^2+abs(p(2)).^2)).*exp(-2.*abs(p(2)).*abs(w).*p(3)./p(4)).*(
      sin((atan((2.*abs(p(2)))./(p(1).^2+abs(p(2)).^2-1)))+(p(1).*abs(w
```

```
      ).*p(3)./p(4)))).^2    ))))).*(1-heaviside(w)));
endfunction

clear temp;
for i=width+1:1:length(DataT)-width-1
  for j=1:1:(2*width+1)
    h=i-width+j;
    temp(j,1)=DataT(h,1).*29.9792e9.*2.*pi;
    temp(j,2)=(phistart(h)+(DataT(h,1).*29.9792e9.*2.*pi*d/c));
    temp(j,3)=DataT(h,2);
  endfor

  temp1(:,1)=[-temp(:,1);temp(:,1)];
  temp1(:,2)=[temp(:,3);temp(:,2)];

  pin=[nstart(i);kstart(i);d;c];
  dp=[1e-6;1e-4;0;0];
  wt = ones(length(temp1),1);
  niter=100;
  stol=1e-4;

  [f1, p1, kvg1, iter1, corp1, covp1, covr1, stdresid1, Z1, r21] = ...
  leasqr(temp1(:,1), temp1(:,2), pin, 'TransPhaseComb', stol, niter, wt
      , dp);

  %if i==12
  % plot(temp1(:,1),temp1(:,2),temp1(:,1),TransPhaseComb(temp1(:,1),pin
      ))
  % pause
  %endif
  result(i,1)=DataT(i,1);
  result(i,2)=p1(1);
  result(i,3)=abs(p1(2));

endfor;

dlmwrite('C:\Doktorarbeit\THz_Messungen\Linsen\090624-Lactose-Toptica\
    aktueller-Lactose-Datensatz\FitResult-Lactose-voll-heavi-1pt.dat',
    result, 'delimiter', '\t');
```

./Scripts/Tnk–CombinedFit–Heavi.m

A.1.3. Piecewise Drude-Lorentz fit

The piecewise Drude-Lorentz fit was performed using RefFIT as platform. The script was written by Prof. Dr. Grüninger.

```
# Fit Loop
###################
# this sign indicates a comment
#
MainWindow(XPos = 100, YPos = 50, Width = 800, Height = 600);
#
NewModel(XPos = 100, YPos = 100);
NewModel(XPos = 100, YPos = 300);
# ExpParams;
# SetExpParam(ParamName = "Sample thickness",Value = 0.1027);
# SetExpParam(ParamName = "Thickness spread",Value = 0.0);
#
NewGraph(XPos = 400, YPos = 100, Width = 500, Height = 300);
GraphProperties(GraphNo = 1, Xmin = 0.0, Xmax = 60.0, Xlog = 0, Ymin =
    0.0,
Ymax = 1.0, Ylog = 0, YTitle = "T");
NewGraph(XPos = 400, YPos = 400, Width = 500, Height = 300);
GraphProperties(GraphNo = 2, Xmin = 0.0, Xmax = 60.0, Xlog = 0, Ymin =
    0,
Ymax = 40.0, Ylog = 0, YTitle = "Phase");
#
BeginLoop(LoopFile = "LOOP.DAT");
#
LoadModel(ModelNo = 1,File = "fitloop_model1_special.rfm");
LoadModel(ModelNo = 2,File = "fitloop_model2_eps.rfm");
#
# DatasetManager;
####
#### THE FILENAMES CAN BE CHANGED HERE.
#### THE NUMBER XPts OF FREQUENCY POINTS HAS TO BE ADAPTED IN BOTH (!)
    COMMAND LINES.
####
LoadDataset(DatasetNo = 1, Quantity = "T", MasterFile = "
    T_MgO_fiberstretcher_cm.dat", XMethod = 3, Xmin = %1, Xmax = %2,
XPts = 180, XGrid = 1);
LoadDataset(DatasetNo = 2, Quantity = "Rps", MasterFile = "
    phi_MgO_fiberstretcher-corr_cm.dat", XMethod = 3, Xmin = %1, Xmax =
     %2,
XPts = 180, XGrid = 1);
#
AddDataCurve(GraphNo = 1, DatasetNo = 1, ShowLine = 1, ShowSymbol = 0,
    ShowError = 0, nSymbolSize = 1, nSymbolShape = 0, SymbolOpen = 1);
AddModelCurve(GraphNo = 1, ModelNo = 1, Quantity = "T");
#
AddDataCurve(GraphNo = 2, DatasetNo = 2, ShowLine = 1, ShowSymbol = 0,
    ShowError = 0, nSymbolSize = 1, nSymbolShape = 0, SymbolOpen = 1);
AddModelCurve(GraphNo = 2, ModelNo = 1, Quantity = "Rps");
```

```
#
WindowFit;
AddChiSqTerm(DatasetNo = 1, ModelNo = 1, Weight = 1.0);
AddChiSqTerm(DatasetNo = 2, ModelNo = 1, Weight = 1.0);
Fit(NumIters = 100);
##### Suspend;
#
DeleteDataCurve(GraphNo = 1, DatasetNo = 1);DeleteDataCurve(GraphNo =
    2, DatasetNo = 2);
DeleteModelCurve(GraphNo = 1, ModelNo = 1, Quantity = "T");
    DeleteModelCurve(GraphNo = 2, ModelNo = 1, Quantity = "Rps");
#
# ExportModelCurve(File = "Ret_fit.dat",ModelNo = 1,Quantity = "S1",
    XMin = %1, XMax = %2,XPts = 6);
# ExportModelCurve(File = "Imt_fit.dat",ModelNo = 1,Quantity = "S2",
    XMin = %1, XMax = %2,XPts = 6);
# ExportModelCurve(File = "T_fit.dat",ModelNo = 1,Quantity = "T",XMin =
     %1, XMax = %2,XPts = 6);
#
DeleteChiSqTerm(DatasetNo = 1, ModelNo = 1);
DeleteChiSqTerm(DatasetNo = 2, ModelNo = 1);
#
UnloadDataset(DatasetNo = 1);UnloadDataset(DatasetNo = 2);
#
SaveModel(ModelNo = 2,File = "dump.rfm");
##### flushes parameters to par.dat !!!!!
#
EndLoop();
```

./Scripts/fitloop_T_phase.rfs

A.2. Phase measurements

Here, the phase measurements with varying temperature at constant frequencies of 200 GHz and 800 GHz are shown.

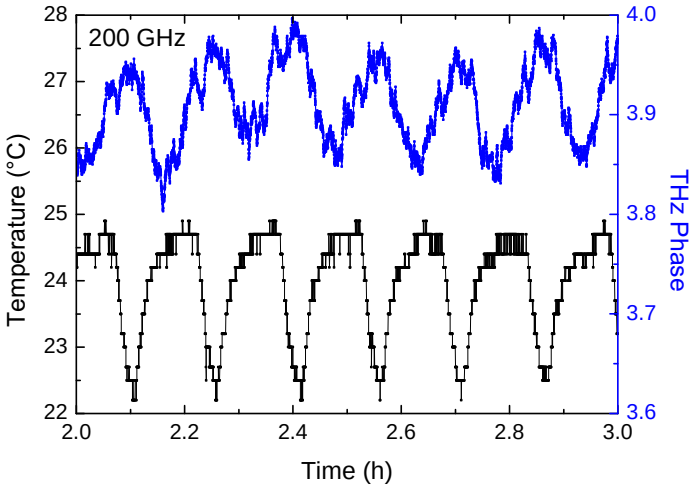

Figure A.1.: Phase measured at a constant frequency of 200 GHz. A temperature variation of about 2.5°C was induced by the air conditioner.

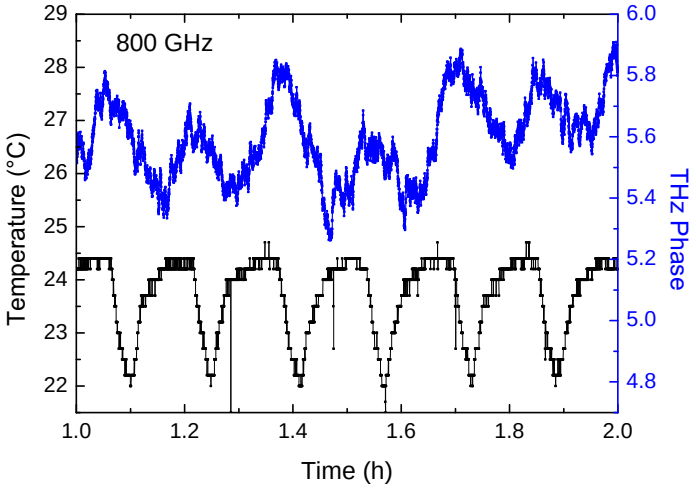

Figure A.2.: Phase measured at a constant frequency of 800 GHz. A temperature variation of about 2.5°C was induced by the air conditioner.

A.3. Beam profile

In this section the measured intensities together with the corresponding derivatives and fits are shown.

A.3.1. x-axis beam profile before collimating

Here, the measured beam profiles along the x axis are shown before collimating the beam. The graphs are sorted by the distance between emitter and knife edge.

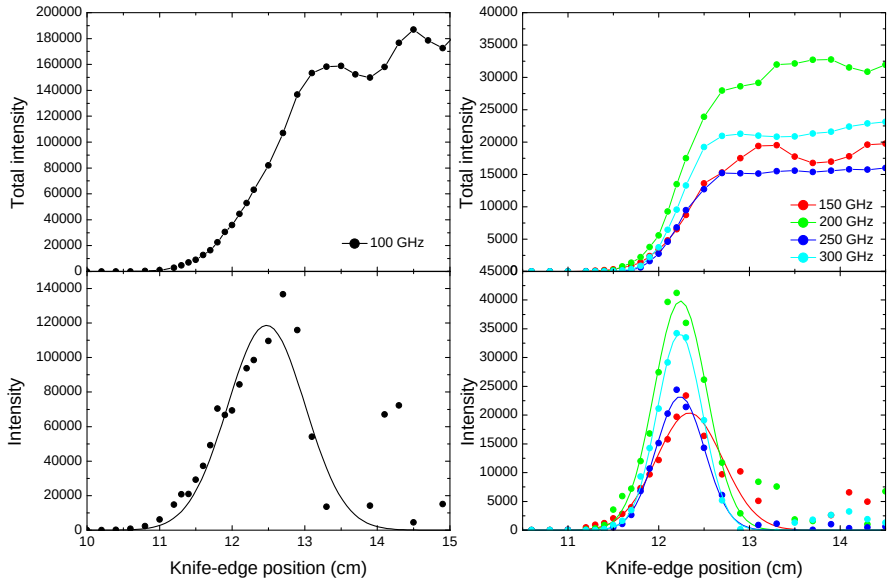

Figure A.3.: Measured intensity and derivative at a distance of 6 cm between photomixer and knife edge.

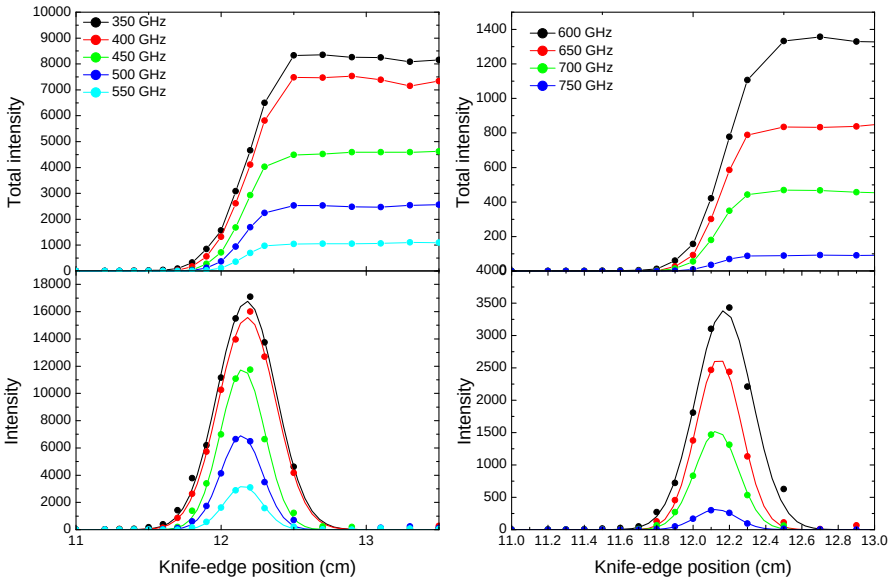

Figure A.4.: Measured intensity and derivative at a distance of 6 cm between photomixer and knife edge.

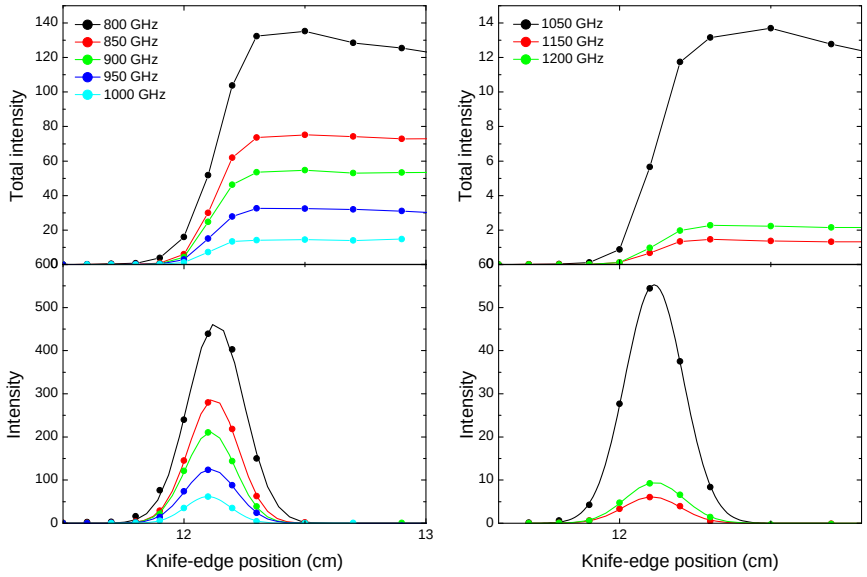

Figure A.5.: Measured intensity and derivative at a distance of 6 cm between photomixer and knife edge.

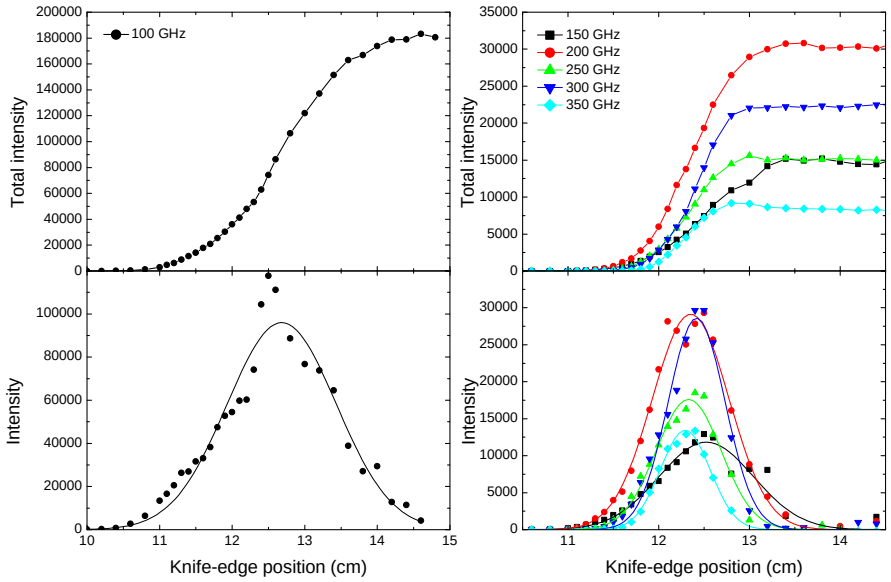

Figure A.6.: Measured intensity and derivative at a distance of 9 cm between photomixer and knife edge.

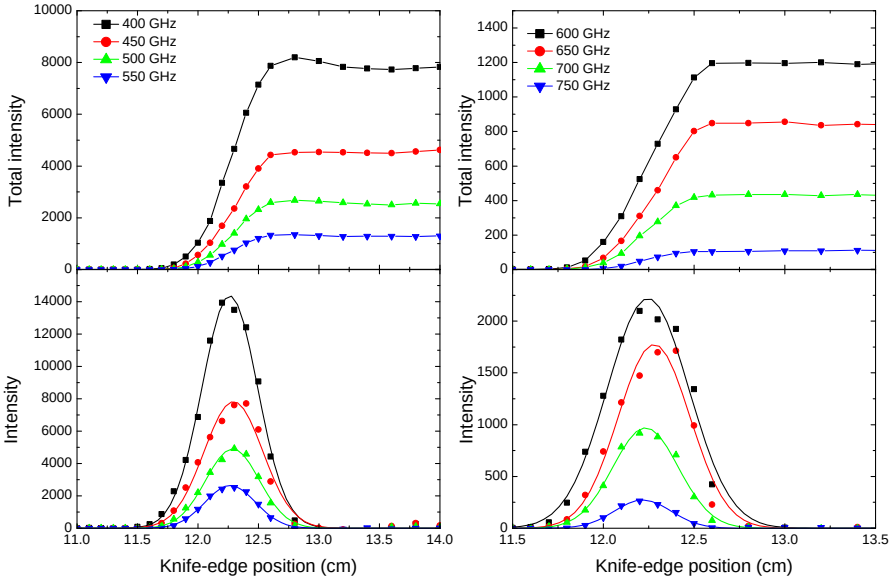

Figure A.7.: Measured intensity and derivative at a distance of 9 cm between photomixer and knife edge.

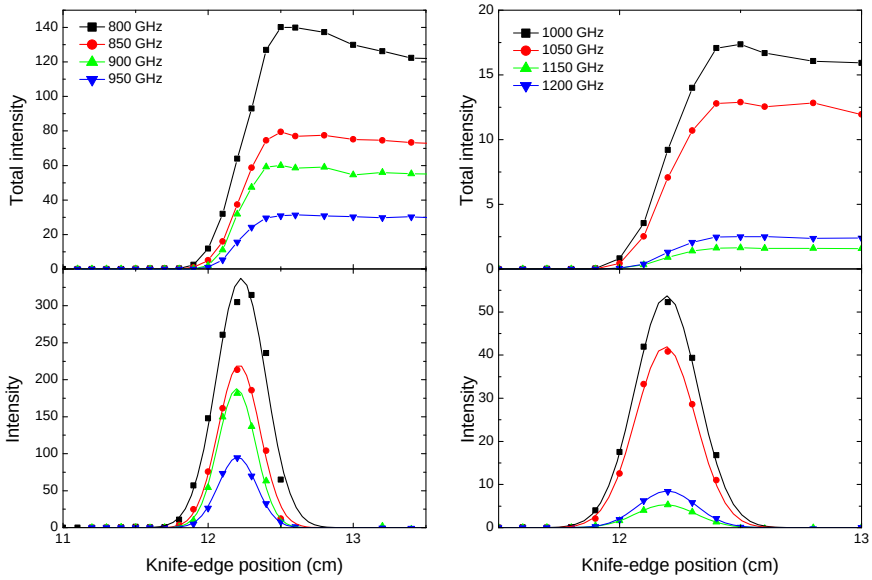

Figure A.8.: Measured intensity and derivative at a distance of 9 cm between photomixer and knife edge.

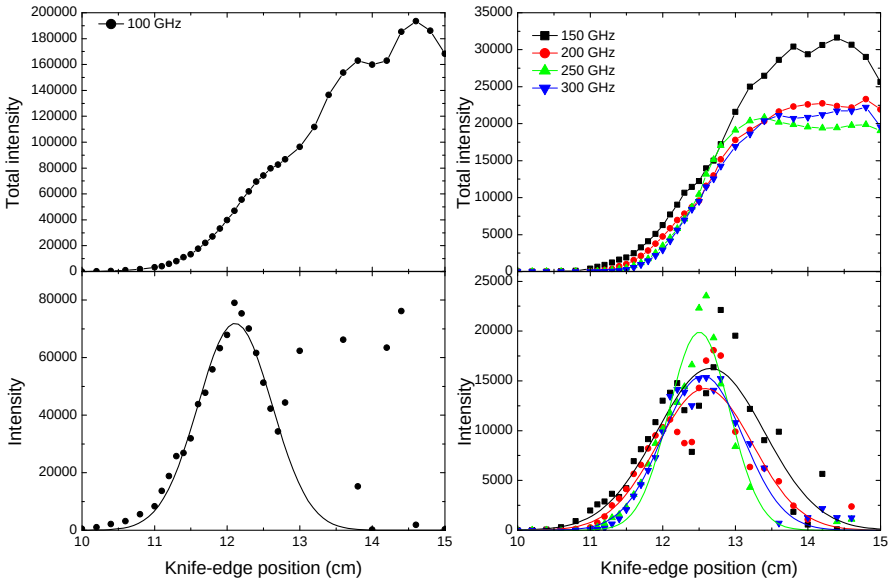

Figure A.9.: Measured intensity and derivative at a distance of 12 cm between photomixer and knife edge.

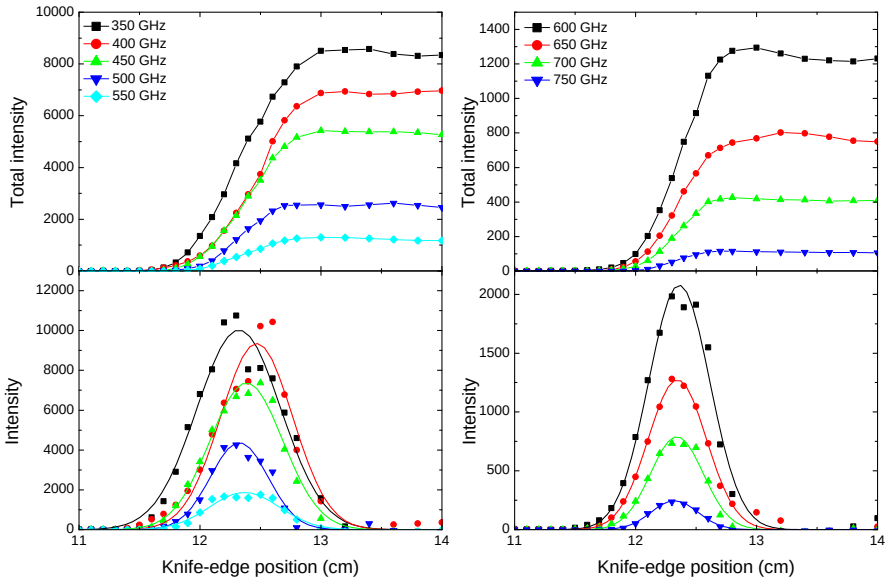

Figure A.10.: Measured intensity and derivative at a distance of 12 cm between photomixer and knife edge.

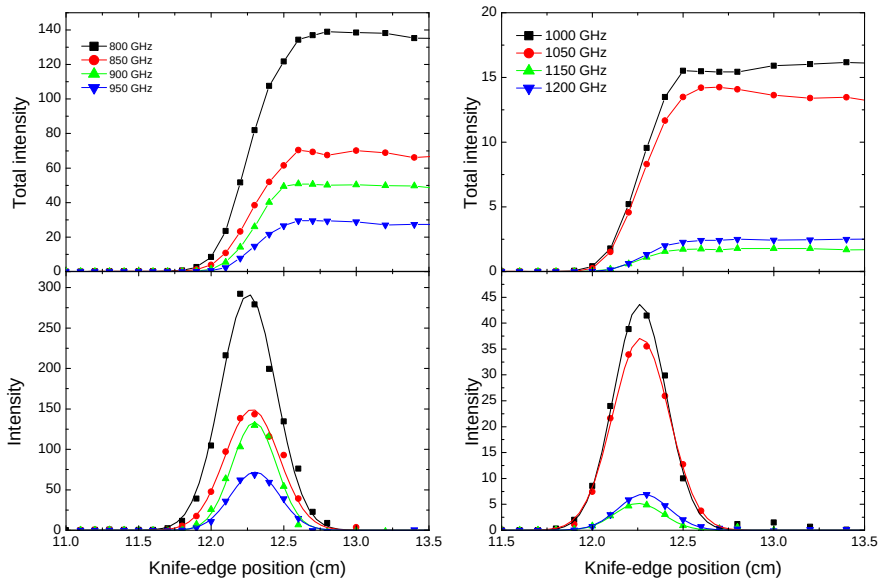

Figure A.11.: Measured intensity and derivative at a distance of 12 cm between photomixer and knife edge.

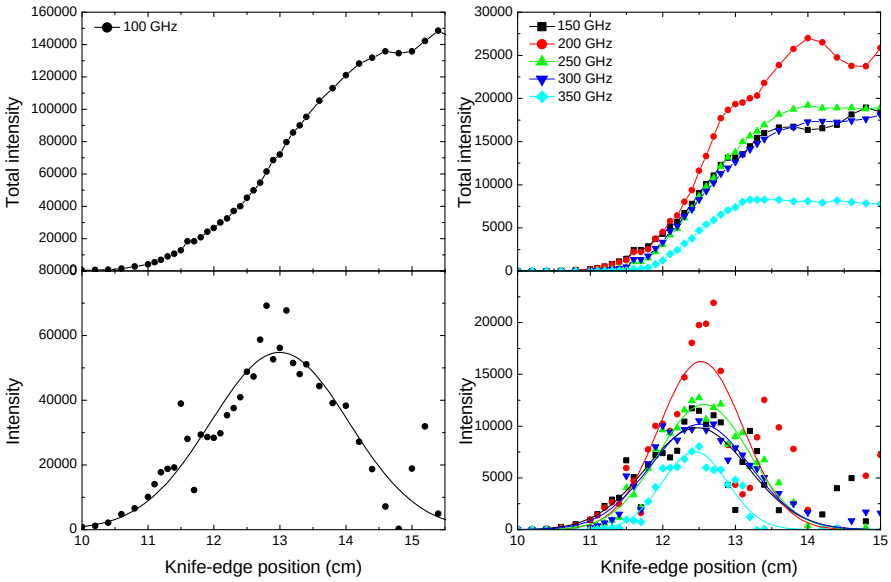

Figure A.12.: Measured intensity and derivative at a distance of 15 cm between photomixer and knife edge.

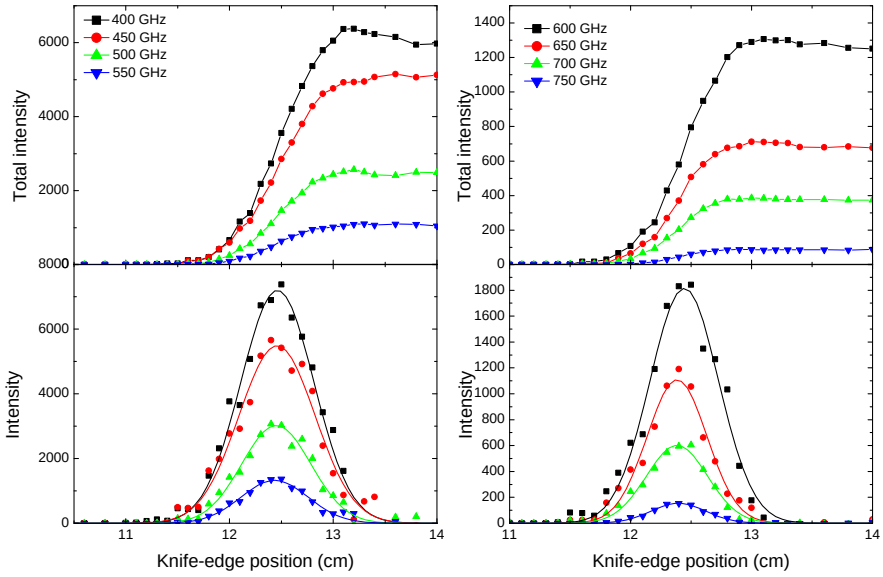

Figure A.13.: Measured intensity and derivative at a distance of 15 cm between photomixer and knife edge.

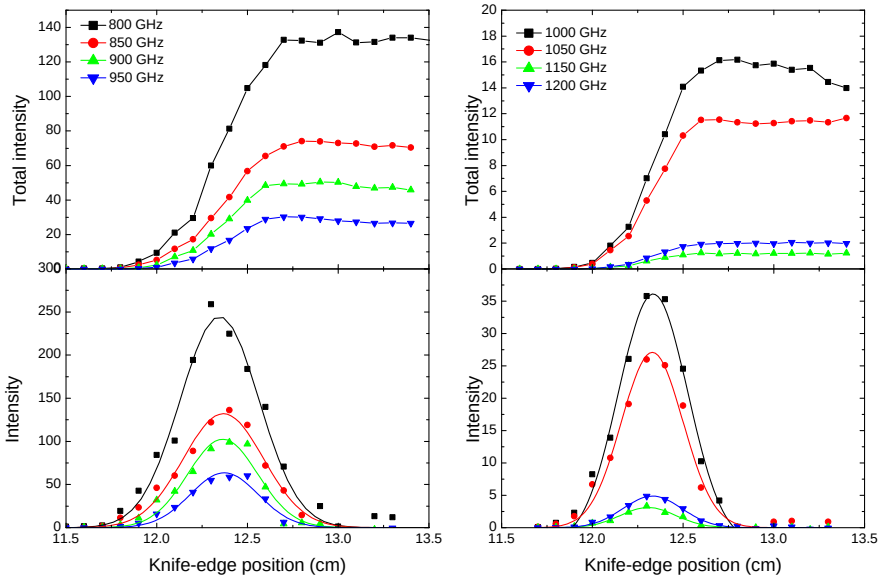

Figure A.14.: Measured intensity and derivative at a distance of 15 cm between photomixer and knife edge.

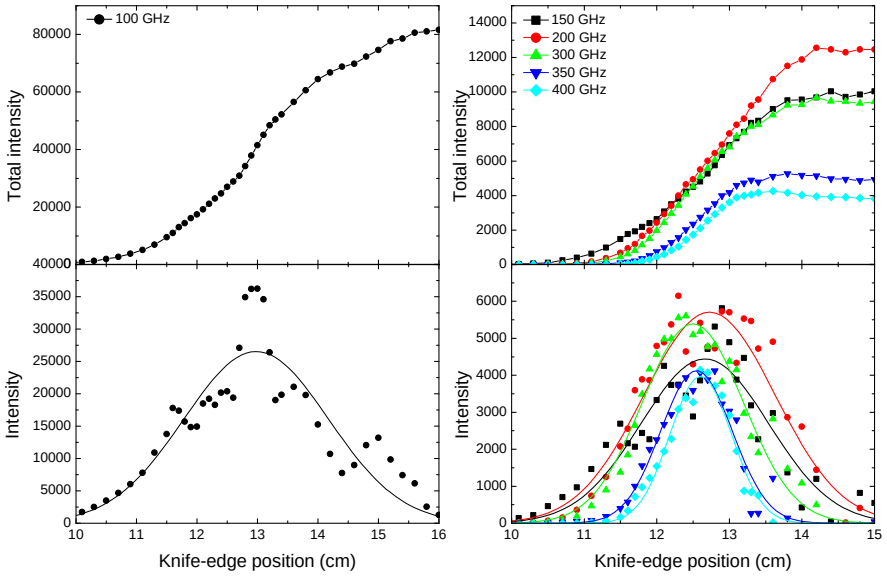

Figure A.15.: Measured intensity and derivative at a distance of 18 cm between photomixer and knife edge.

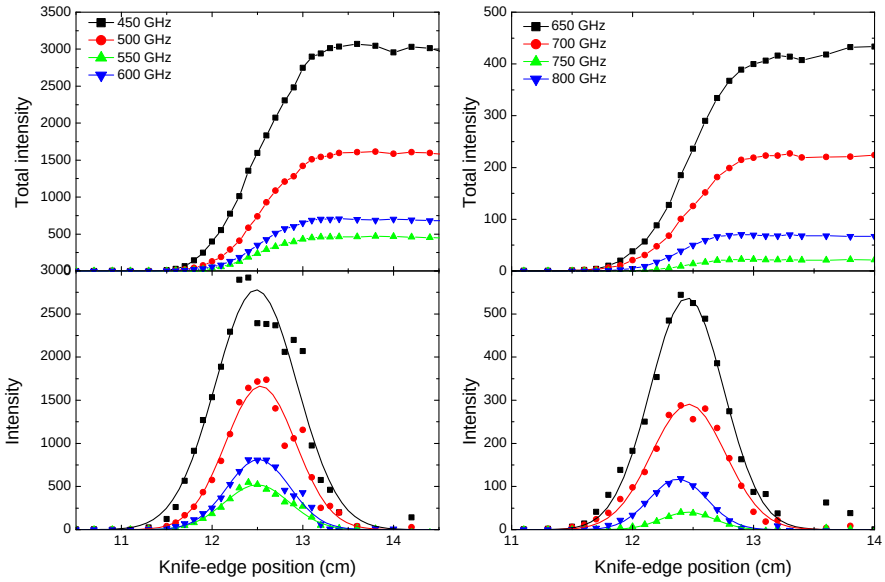

Figure A.16.: Measured intensity and derivative at a distance of 18 cm between photomixer and knife edge.

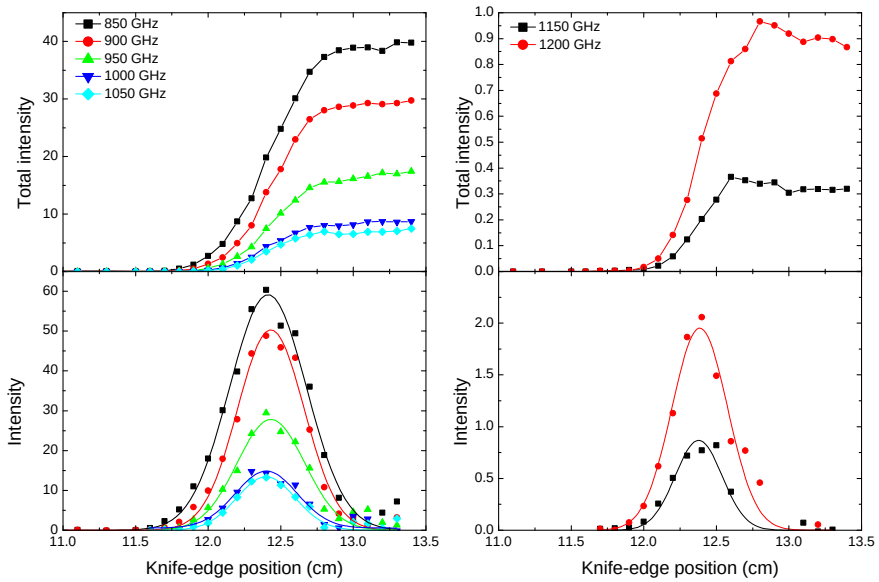

Figure A.17.: Measured intensity and derivative at a distance of 18 cm between photomixer and knife edge.

A.3.2. y-axis beam profile before collimating

Here, the measured beam profiles along the y axis are shown before collimating the beam. The graphs are sorted by the distance between emitter and knife edge.

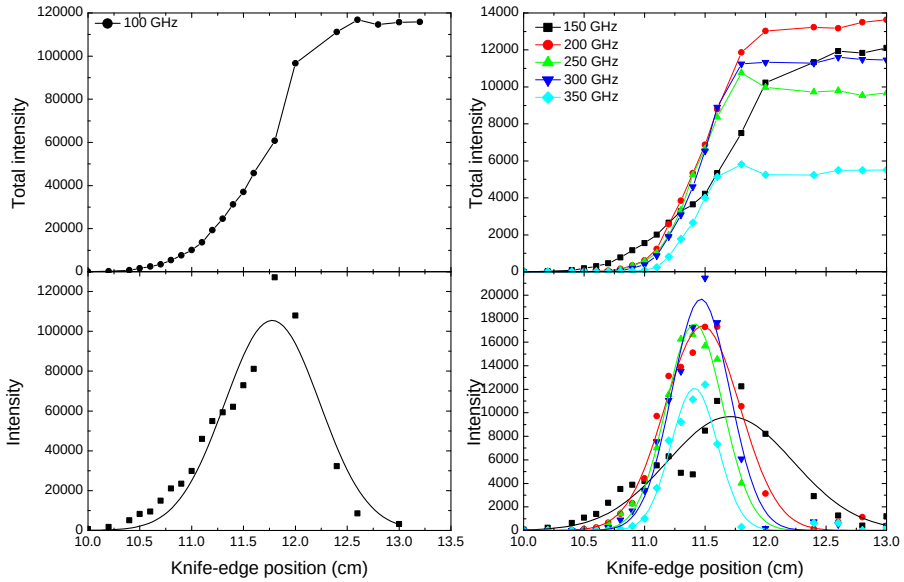

Figure A.18.: Measured intensity and derivative at a distance of 6 cm between photomixer and knife edge.

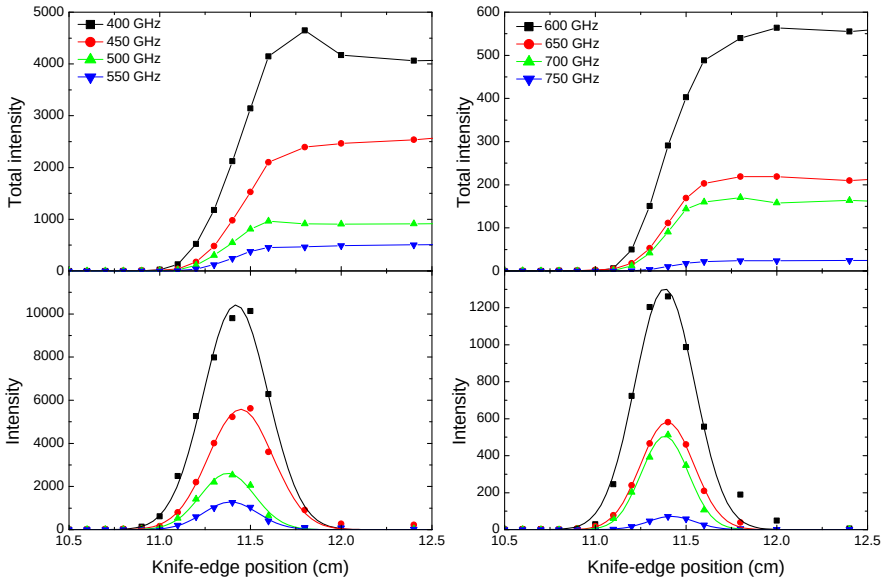

Figure A.19.: Measured intensity and derivative at a distance of 6 cm between photomixer and knife edge.

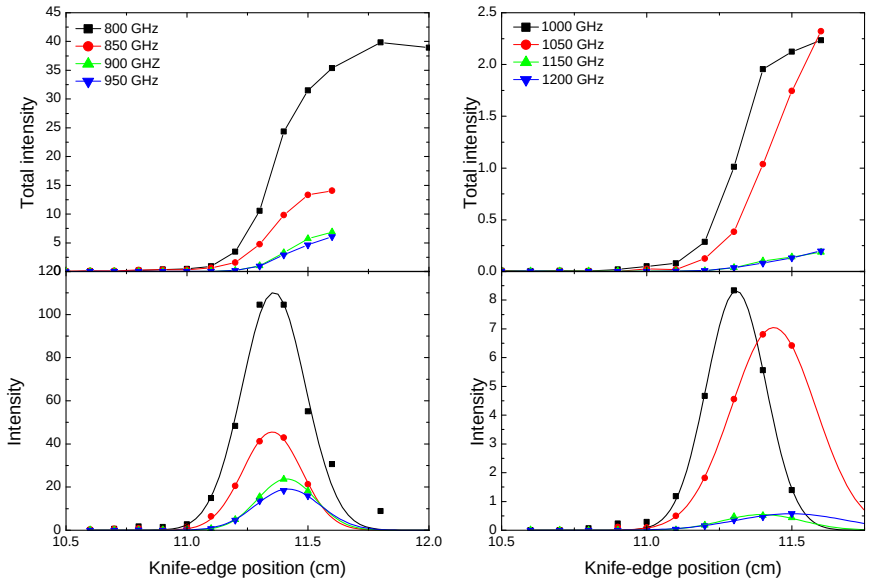

Figure A.20.: Measured intensity and derivative at a distance of 6 cm between photomixer and knife edge.

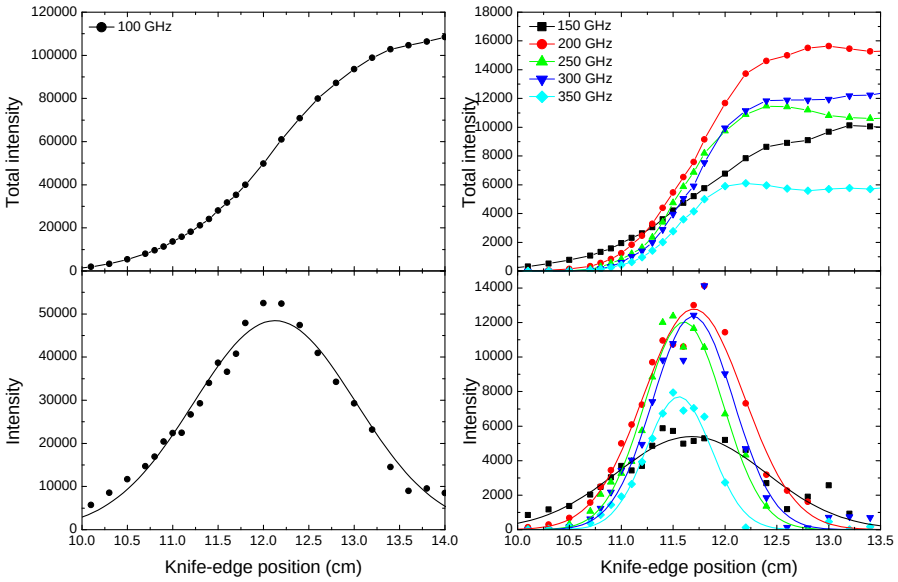

Figure A.21.: Measured intensity and derivative at a distance of 12 cm between photomixer and knife edge.

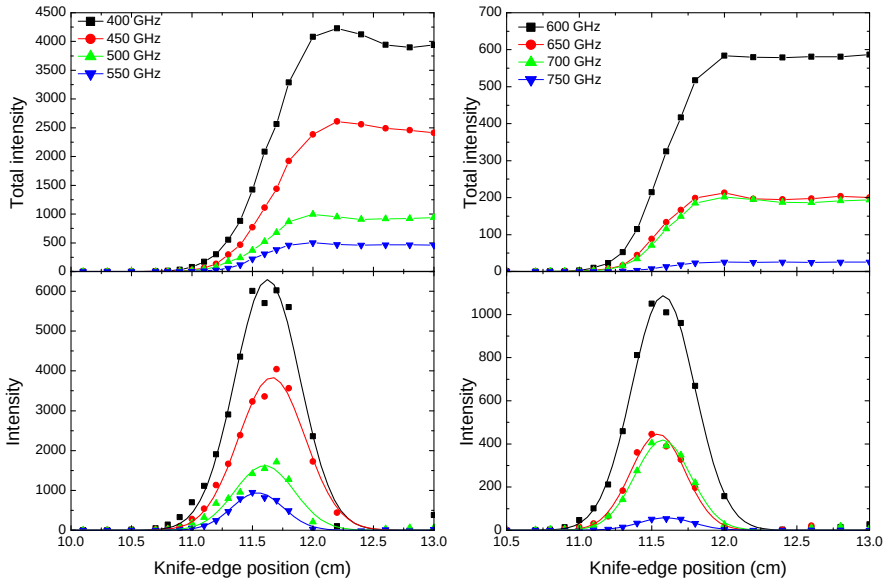

Figure A.22.: Measured intensity and derivative at a distance of 12 cm between photomixer and knife edge.

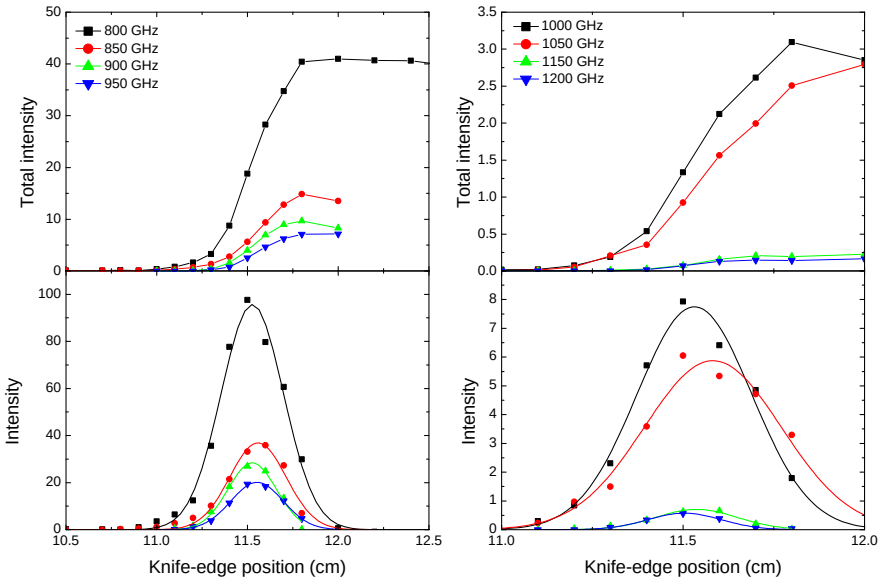

Figure A.23.: Measured intensity and derivative at a distance of 12 cm between photomixer and knife edge.

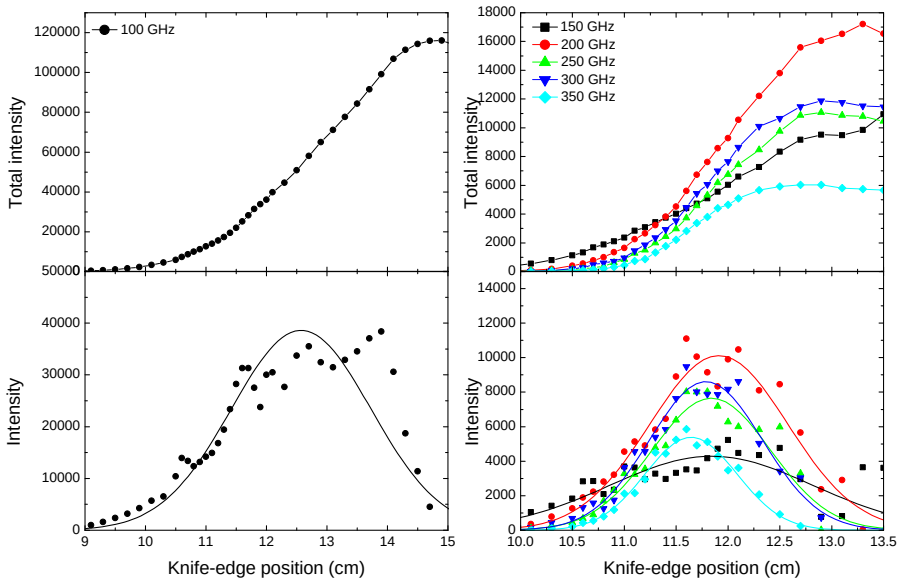

Figure A.24.: Measured intensity and derivative at a distance of 18 cm between photomixer and knife edge.

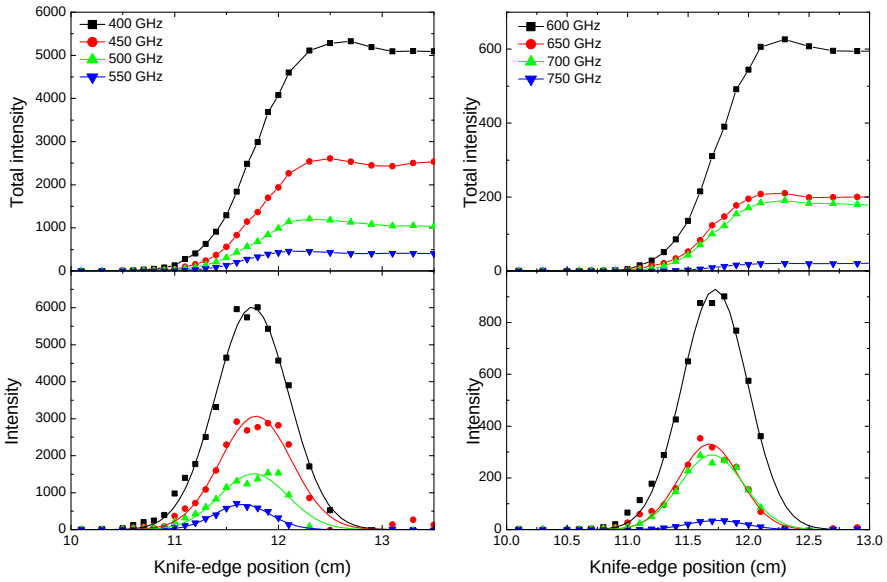

Figure A.25.: Measured intensity and derivative at a distance of 18 cm between photomixer and knife edge.

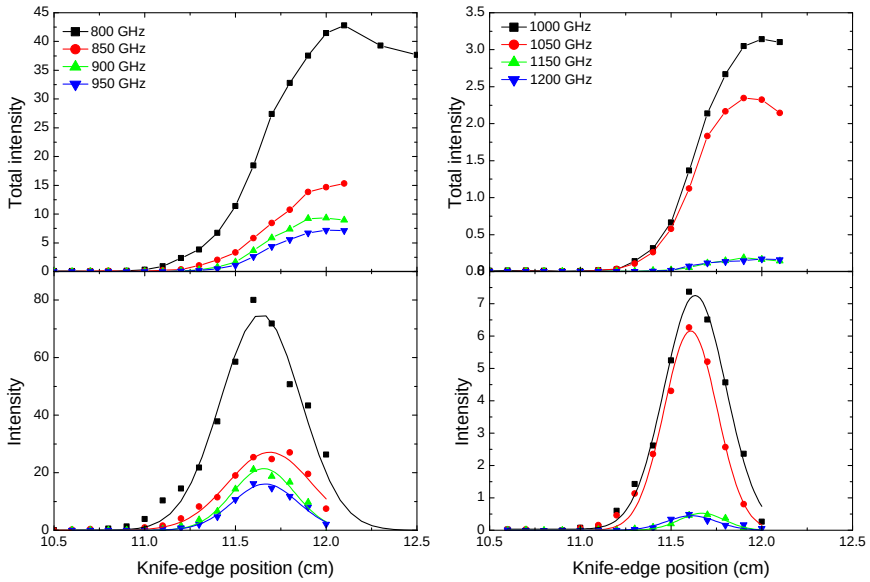

Figure A.26.: Measured intensity and derivative at a distance of 18 cm between photomixer and knife edge.

A.3.3. x-axis beam profile after collimating

Here, the measured beam profiles along the x axis are shown after collimating the beam. The graphs are sorted by the distance between emitter and knife edge.

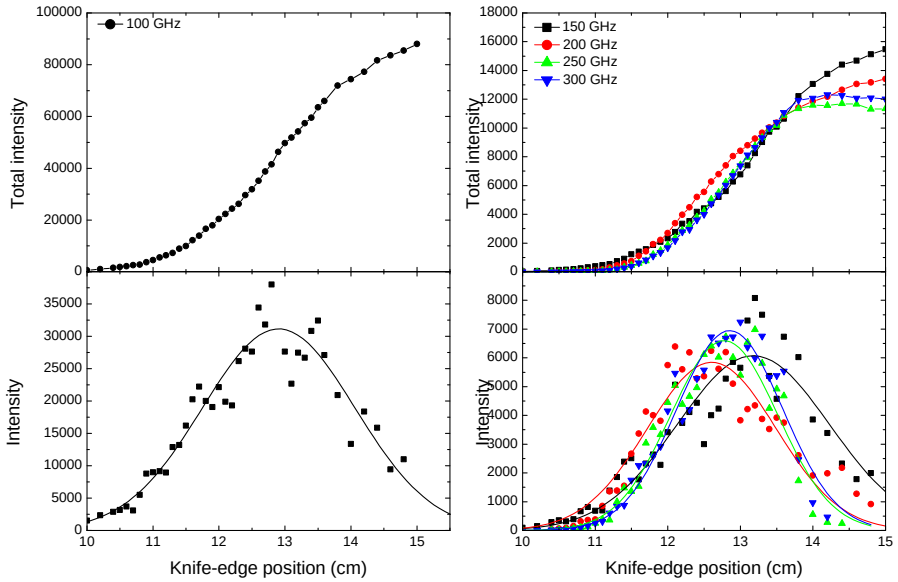

Figure A.27.: Measured intensity and derivative at a distance of 21.4 cm between photomixer and knife edge.

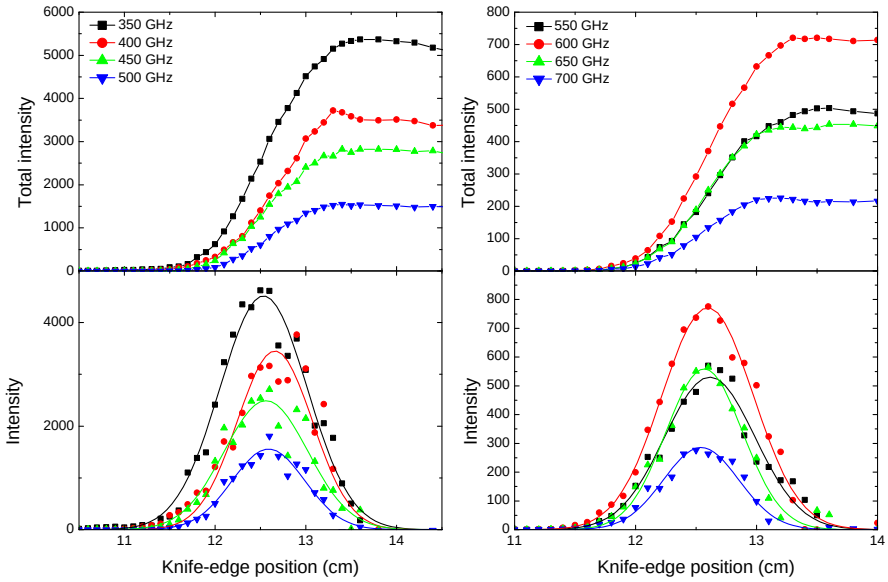

Figure A.28.: Measured intensity and derivative at a distance of 21.4 cm between photomixer and knife edge.

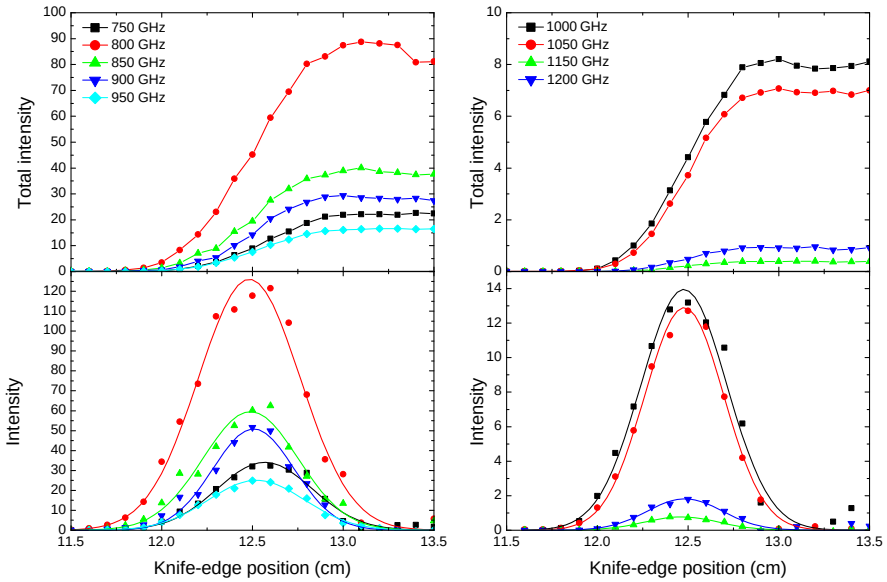

Figure A.29.: Measured intensity and derivative at a distance of 21.4 cm between photomixer and knife edge.

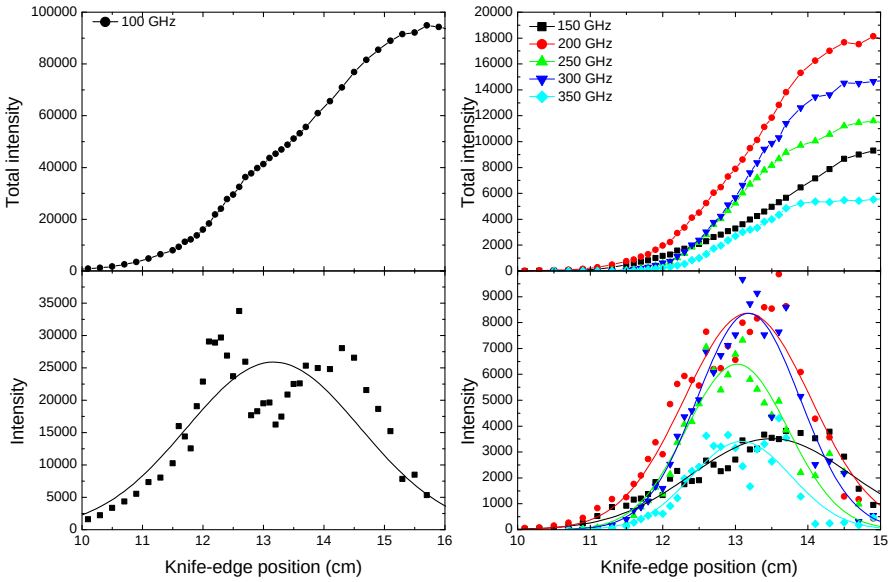

Figure A.30.: Measured intensity and derivative at a distance of 34.4 cm between photomixer and knife edge.

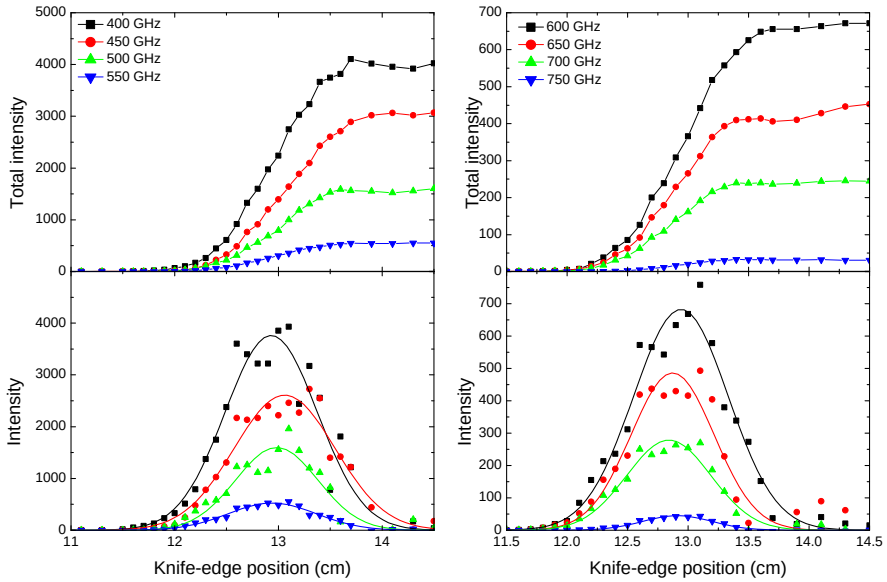

Figure A.31.: Measured intensity and derivative at a distance of 34.4 cm between photomixer and knife edge.

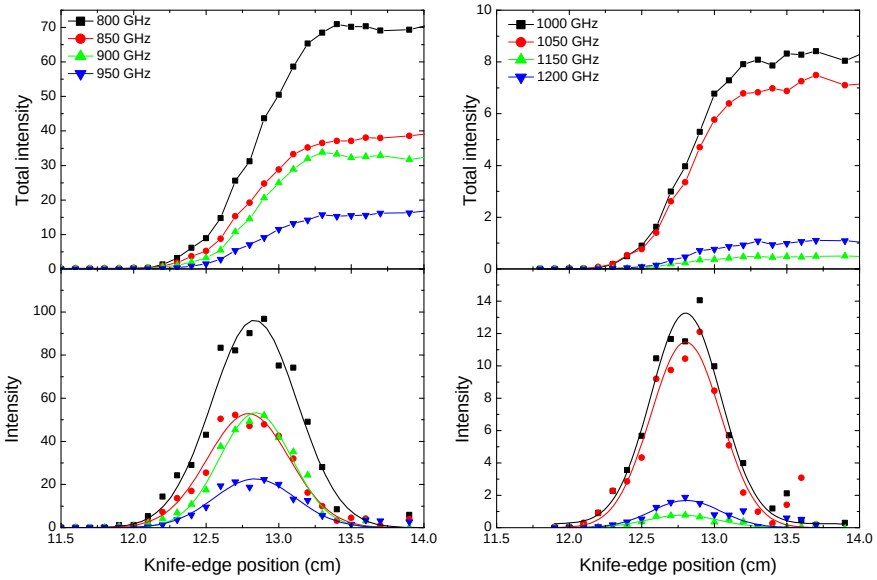

Figure A.32.: Measured intensity and derivative at a distance of 34.4 cm between photomixer and knife edge.

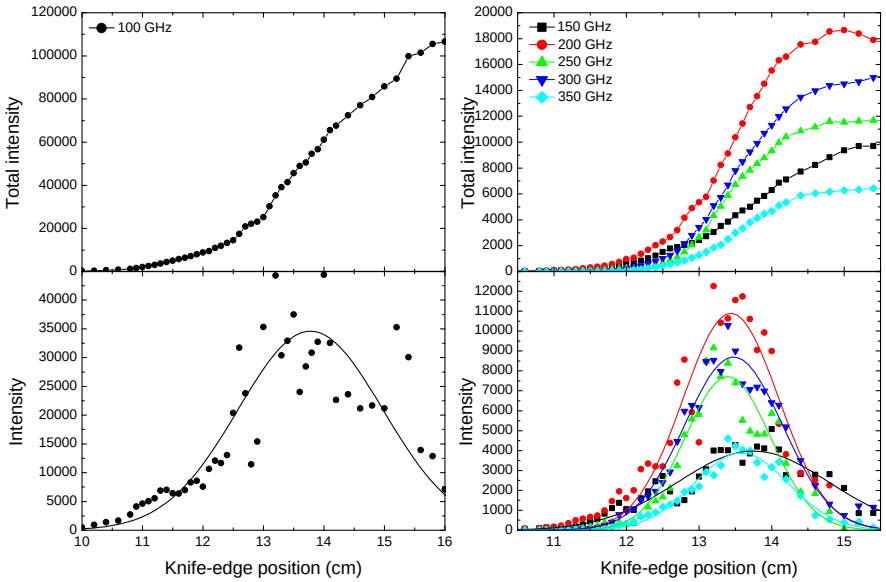

Figure A.33.: Measured intensity and derivative at a distance of 49.4 cm between photomixer and knife edge.

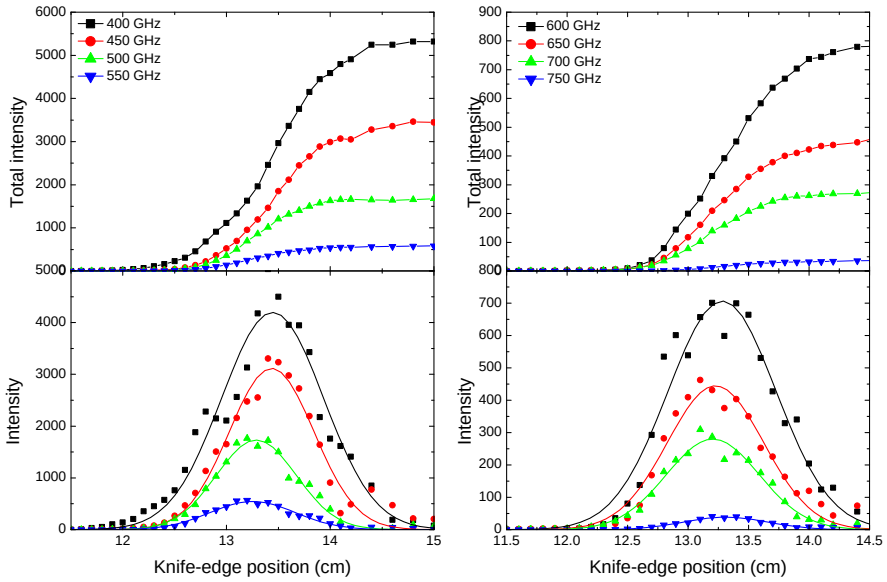

Figure A.34.: Measured intensity and derivative at a distance of 49.4 cm between photomixer and knife edge.

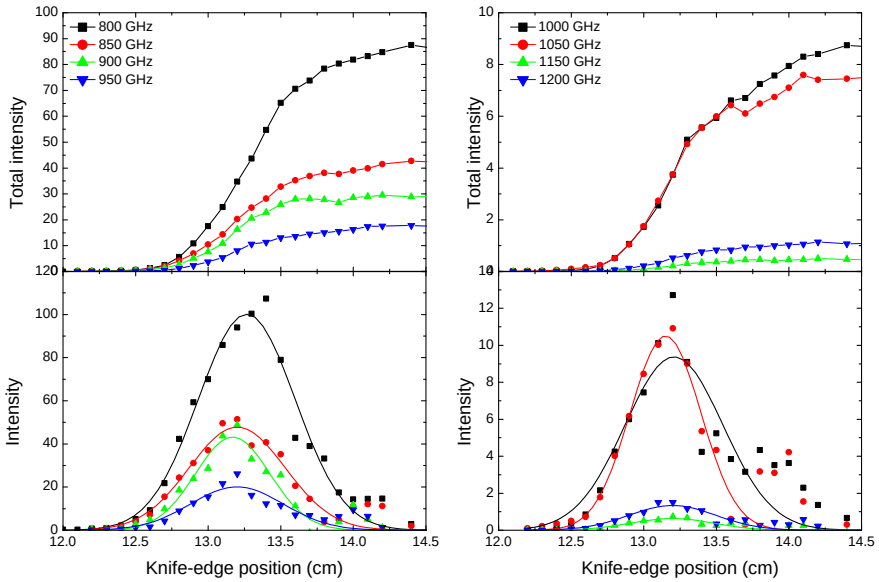

Figure A.35.: Measured intensity and derivative at a distance of 49.4 cm between photomixer and knife edge.

A.3.4. x-axis beam profile at the focal spot

Here, the measured beam profiles along the x axis are shown at the focal spot.

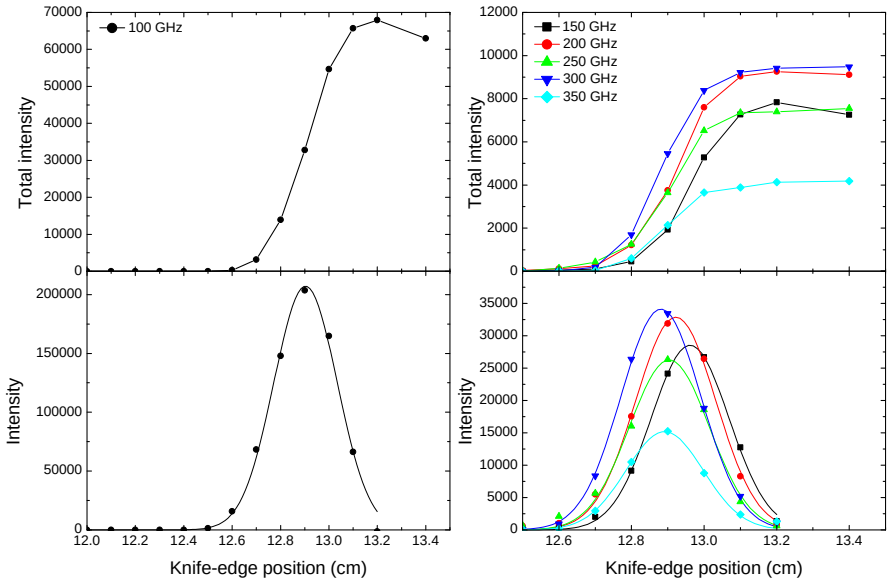

Figure A.36.: Measured intensity and derivative at the focal spot.

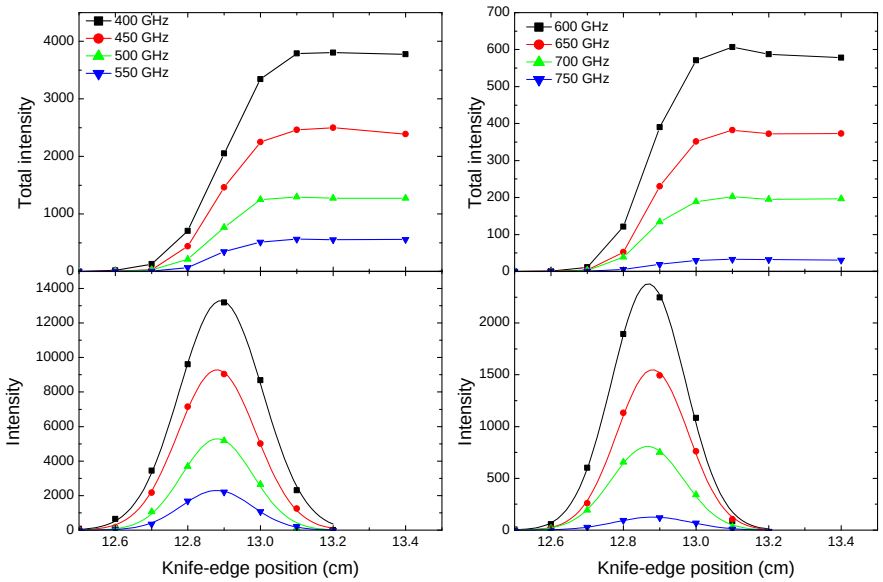

Figure A.37.: Measured intensity and derivative at the focal spot.

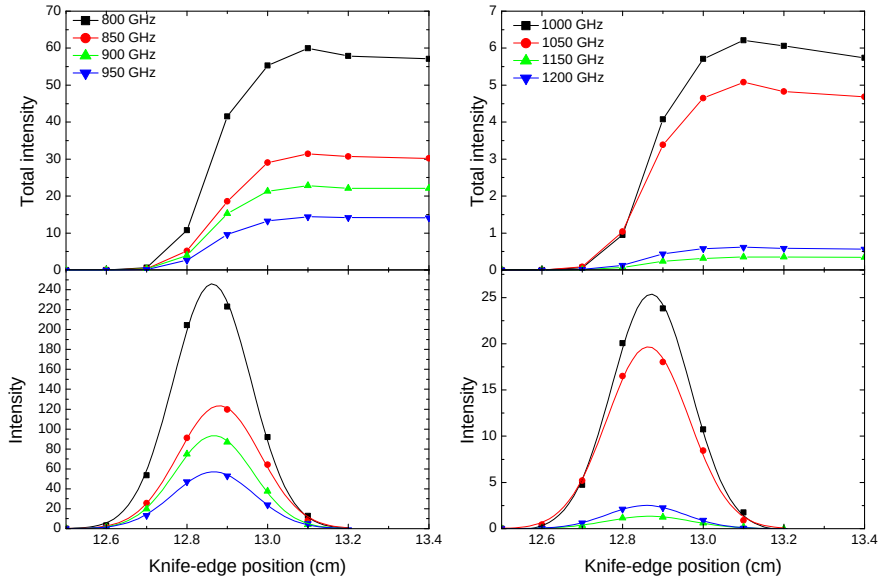

Figure A.38.: Measured intensity and derivative at the focal spot.

Table A.1.: Determined radii of all beam-profile measurements

	before collimating lens					behind collimating lens						
Distance (cm)	6.1	9	12	15	17.9	21.4	34.4	49.4	6	12	17.4	
Frequency (GHz)	Radius on x axis (cm)								Radius on y axis (cm)			Radius of the focal spot (cm)
100	1.07	1.5	1.02	2.09	2.39	2.32	2.88	2.4	0.91	1.79	2.31	0.26
150	0.73	1.4	1.49	1.83	1.76	2.1	2.19	2.09	1.04	1.45	1.96	0.21
200	0.58	0.85	1.31	1.16	1.81	1.77	1.74	1.32	0.62	0.97	1.33	0.22
250	0.54	0.72	0.83	1.26	1.46	1.48	1.41	1.18	0.47	0.76	1.14	0.22
300	0.50	0.63	1.1	1.37	1.39	1.46	1.42	1.35	0.48	0.78	1.09	0.22
350	0.4	0.55	0.69	0.9	0.98	0.96	1.37	1.3	0.39	0.63	0.89	0.21
400	0.39	0.46	0.6	0.71	0.85	0.83	0.89	0.98	0.36	0.54	0.71	0.23
450	0.31	0.49	0.61	0.74	0.9	0.92	0.97	0.82	0.36	0.55	0.69	0.21
500	0.29	0.45	0.48	0.67	0.77	0.8	0.8	0.77	0.3	0.49	0.66	0.2
550	0.26	0.42	0.58	0.65	0.72	0.75	0.85	0.83	0.3	0.43	0.54	0.19
600	0.31	0.45	0.51	0.56	0.69	0.76	0.78	0.9	0.33	0.44	0.54	0.2
650	0.25	0.4	0.48	0.5	0.61	0.64	0.69	0.8	0.29	0.38	0.5	0.2
700	0.24	0.36	0.43	0.51	0.61	0.62	0.70	0.77	0.26	0.39	0.53	0.2
750	0.23	0.31	0.39	0.46	0.44	0.53	0.58	0.7	0.26	0.37	0.48	0.21
800	0.23	0.34	0.38	0.44	0.48	0.56	0.59	0.67	0.26	0.35	0.44	0.19
850	0.21	0.29	0.38	0.44	0.53	0.52	0.57	0.66	0.24	0.31	0.46	0.2
900	0.21	0.26	0.31	0.39	0.46	0.45	0.5	0.51	0.24	0.27	0.35	0.19
950	0.21	0.26	0.33	0.37	0.47	0.53	0.56	0.64	0.27	0.29	0.36	0.2
1000	0.19	0.26	0.29	0.35	0.46	0.47	0.5	0.68	0.21	0.32	0.34	0.19
1050	0.19	0.25	0.31	0.34	0.4	0.44	0.48	0.49	0.29	0.38	0.29	0.2
1150	0.19	0.25	0.27	0.31	0.32	0.41	0.49	0.57	0.27	0.22	0.25	0.21
1200	0.19	0.24	0.28	0.32	0.38	0.42	0.48	0.6	0.37	0.2	0.28	0.19

Table A.2.: Determined opening angles

Frequency (GHz)	angle (degrees)	
	x axis	y axis
100	6.23	7
150	7.16	4.61
200	7.07	3.57
250	4.62	3.38
300	4.89	3.09
350	2.92	2.51
400	2.24	1.75
450	2.78	1.68
500	2.31	1.8
550	2.2	1.2
600	1.7	1.08
650	1.58	1.04
700	1.71	1.36
750	1.43	1.09
800	1.13	0.9
850	1.54	1.09
900	1.22	0.53
950	1.2	0.46
1000	1.22	0.7
1050	0.99	-
1150	0.63	-
1200	0.89	-

A.4. Polarization measurements

In the following section the measured polarization curves and the corresponding fits are shown.

A.4.1. Polarizer angle of 0 °

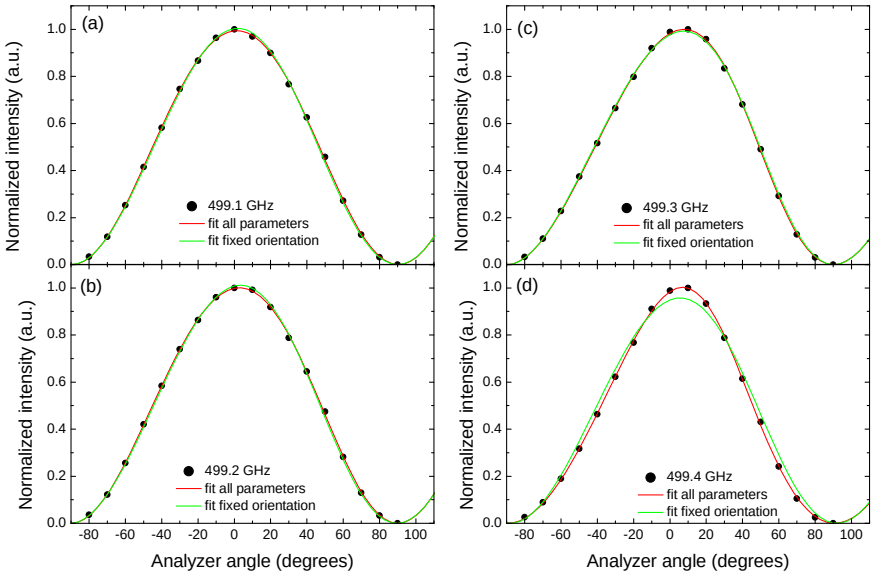

Figure A.39.: Polarization curves measured with a polarizer angle of 0 °. For the fit shown in red the orientaion of the ellipse was fitted while for the fit shown in green Θ was fixed at 40 °.

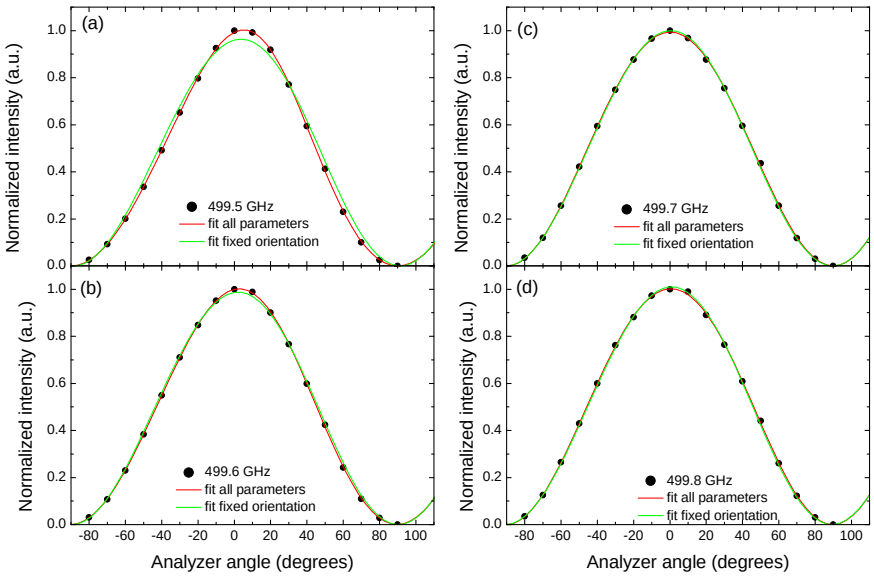

Figure A.40.: Polarization curves measured with a polarizer angle of 0 °. For the fit shown in red the orientaion of the ellipse was fitted while for the fit shown in green Θ was fixed at 40 °.

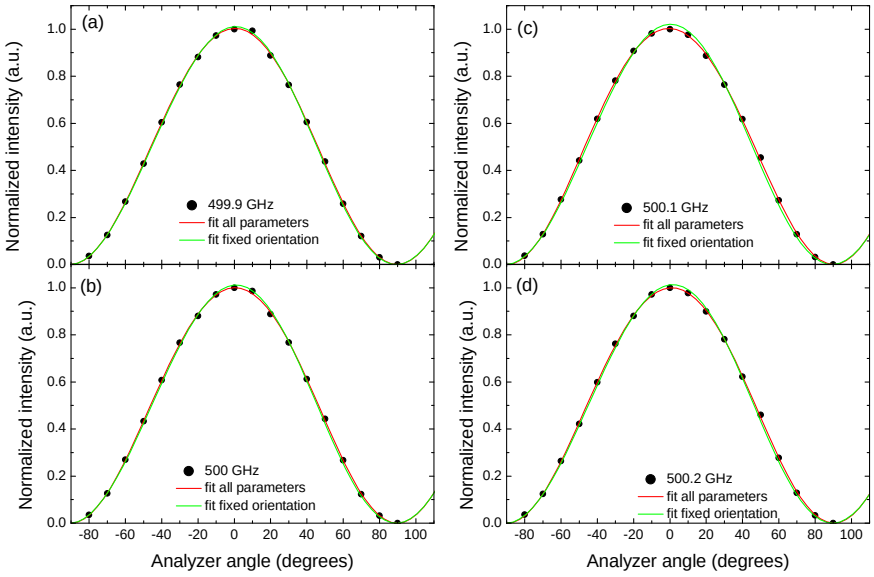

Figure A.41.: Polarization curves measured with a polarizer angle of 0 °. For the fit shown in red the orientaion of the ellipse was fitted while for the fit shown in green Θ was fixed at 40 °.

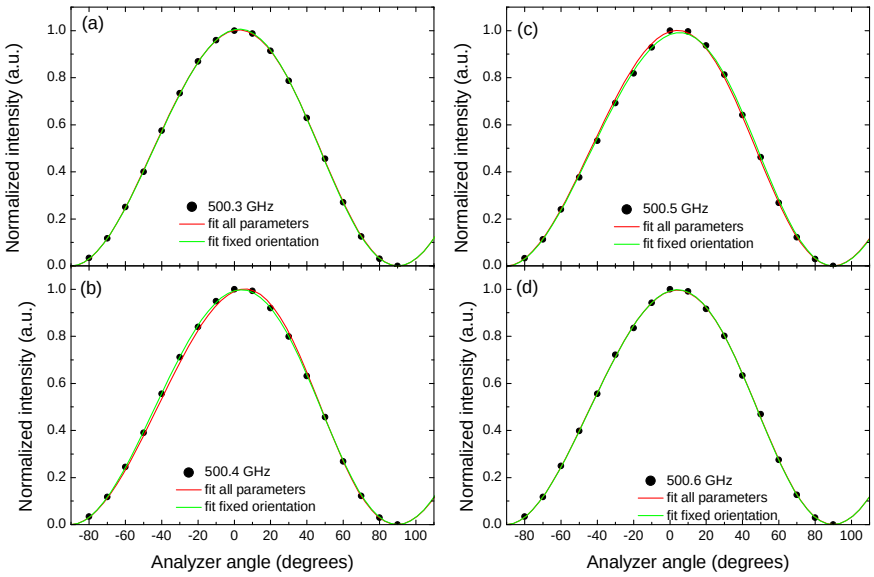

Figure A.42.: Polarization curves measured with a polarizer angle of 0 °. For the fit shown in red the orientaion of the ellipse was fitted while for the fit shown in green Θ was fixed at 40 °.

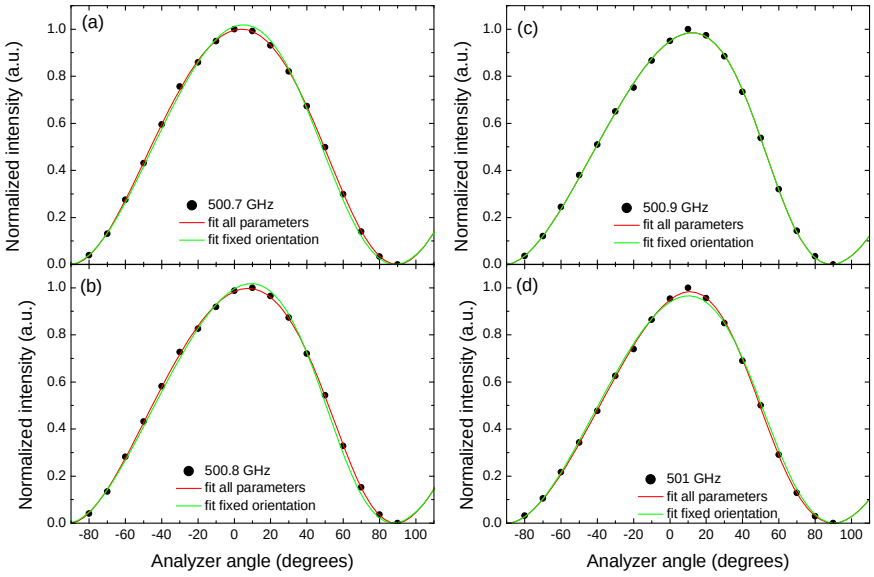

Figure A.43.: Polarization curves measured with a polarizer angle of 0 °. For the fit shown in red the orientaion of the ellipse was fitted while for the fit shown in green Θ was fixed at 40 °.

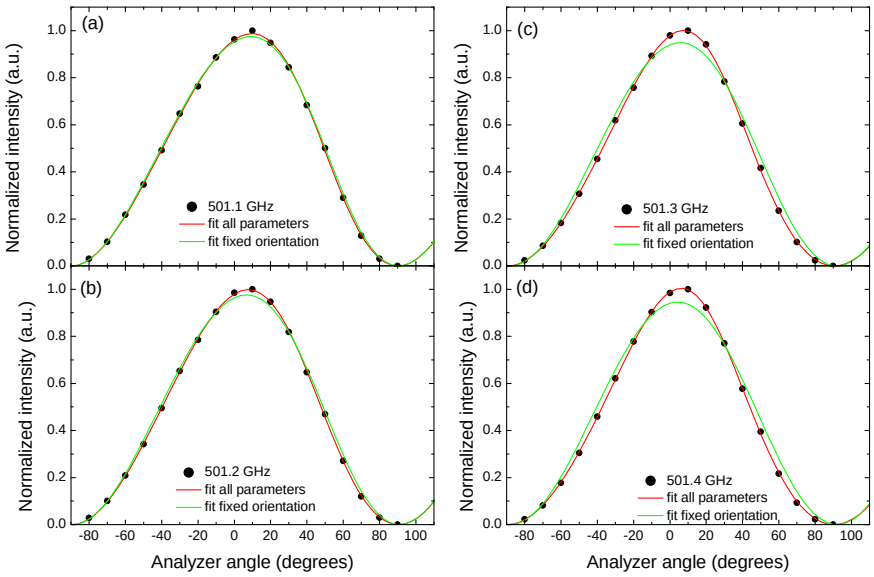

Figure A.44.: Polarization curves measured with a polarizer angle of 0 °. For the fit shown in red the orientaion of the ellipse was fitted while for the fit shown in green Θ was fixed at 40 °.

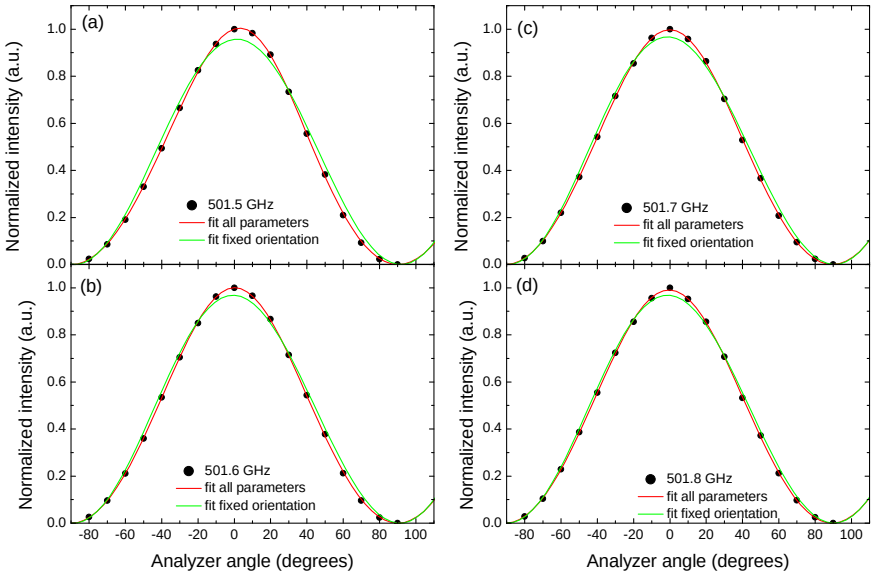

Figure A.45.: Polarization curves measured with a polarizer angle of 0 °. For the fit shown in red the orientaion of the ellipse was fitted while for the fit shown in green Θ was fixed at 40 °.

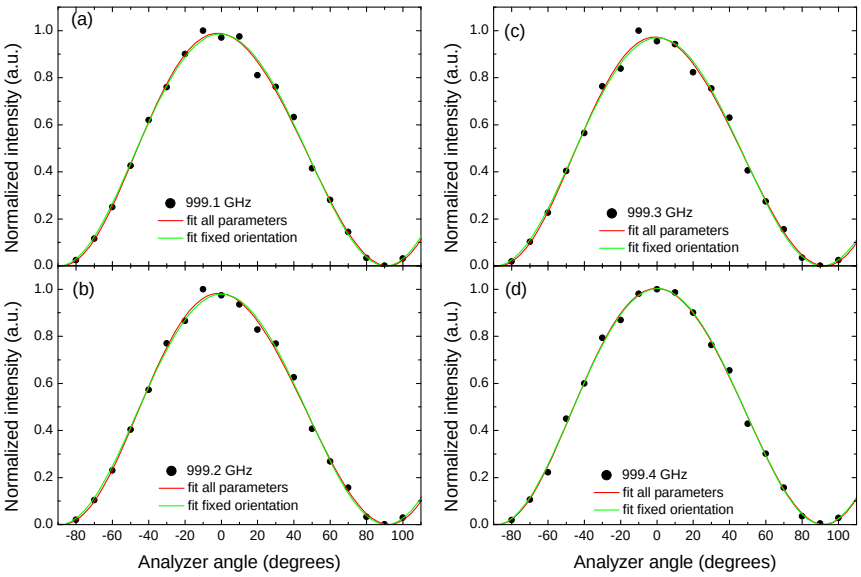

Figure A.46.: Polarization curves measured with a polarizer angle of 0 °. For the fit shown in red the orientaion of the ellipse was fitted while for the fit shown in green Θ was fixed at 80 °.

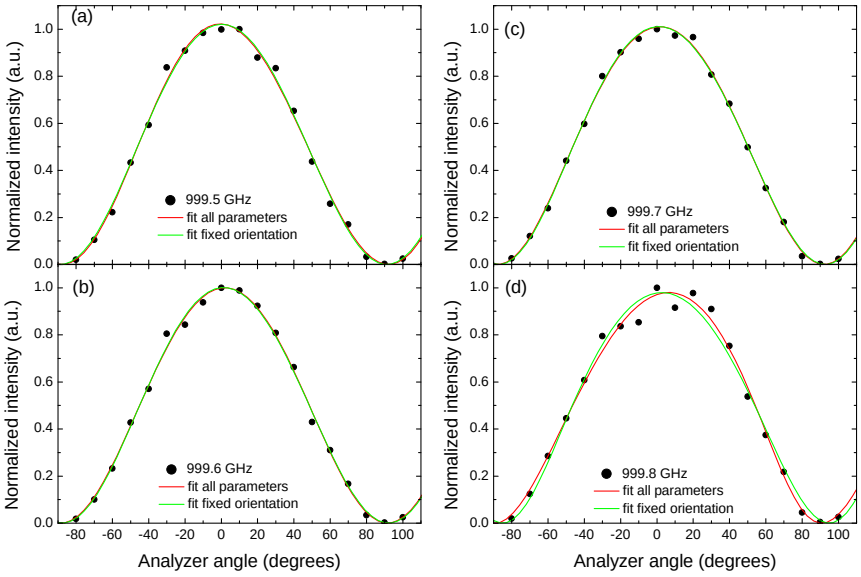

Figure A.47.: Polarization curves measured with a polarizer angle of 0 °. For the fit shown in red the orientaion of the ellipse was fitted while for the fit shown in green Θ was fixed at 80 °.

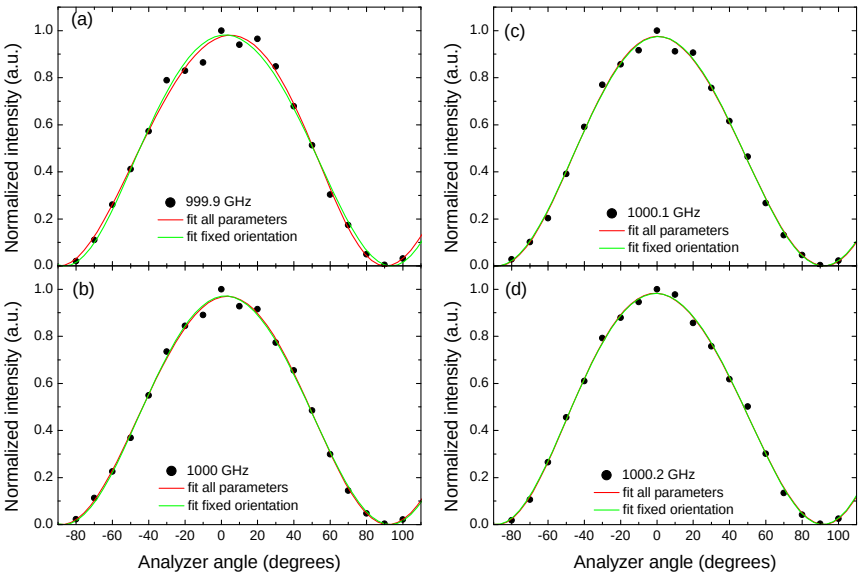

Figure A.48.: Polarization curves measured with a polarizer angle of 0 °. For the fit shown in red the orientaion of the ellipse was fitted while for the fit shown in green Θ was fixed at 80 °.

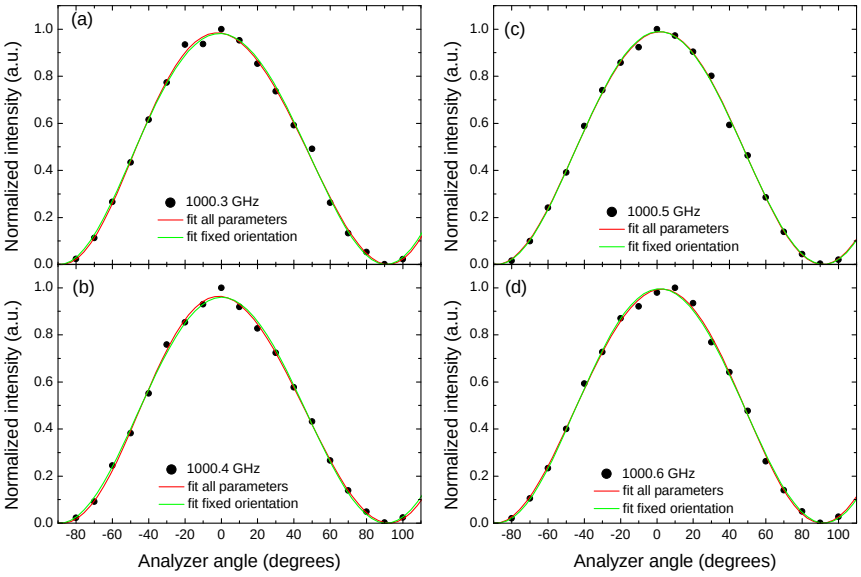

Figure A.49.: Polarization curves measured with a polarizer angle of 0 °. For the fit shown in red the orientaion of the ellipse was fitted while for the fit shown in green Θ was fixed at 80 °.

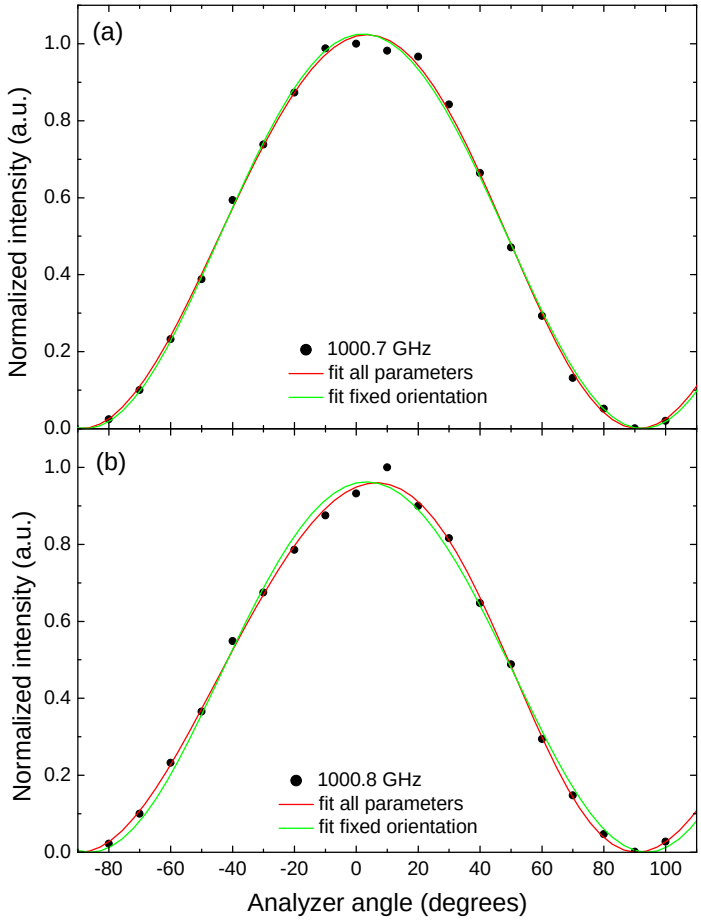

Figure A.50.: Polarization curves measured with a polarizer angle of 0 °. For the fit shown in red the orientaion of the ellipse was fitted while for the fit shown in green Θ was fixed at 80 °.

A.4.2. Polarizer angle of 45 °

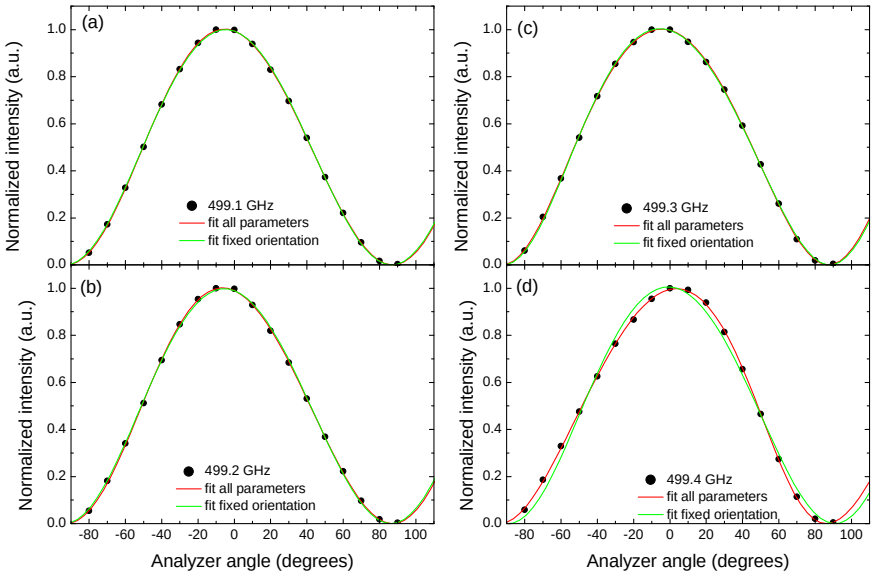

Figure A.51.: Polarization curves measured with a polarizer angle of 45 °. For the fit shown in red the orientaion of the ellipse was fitted while for the fit shown in green Θ was fixed at 40 °.

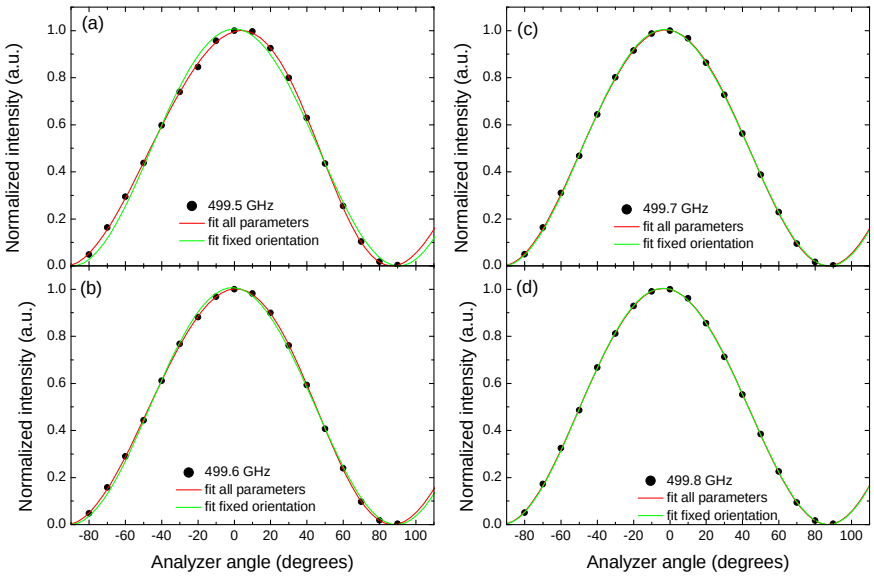

Figure A.52.: Polarization curves measured with a polarizer angle of 45 °. For the fit shown in red the orientaion of the ellipse was fitted while for the fit shown in green Θ was fixed at 40 °.

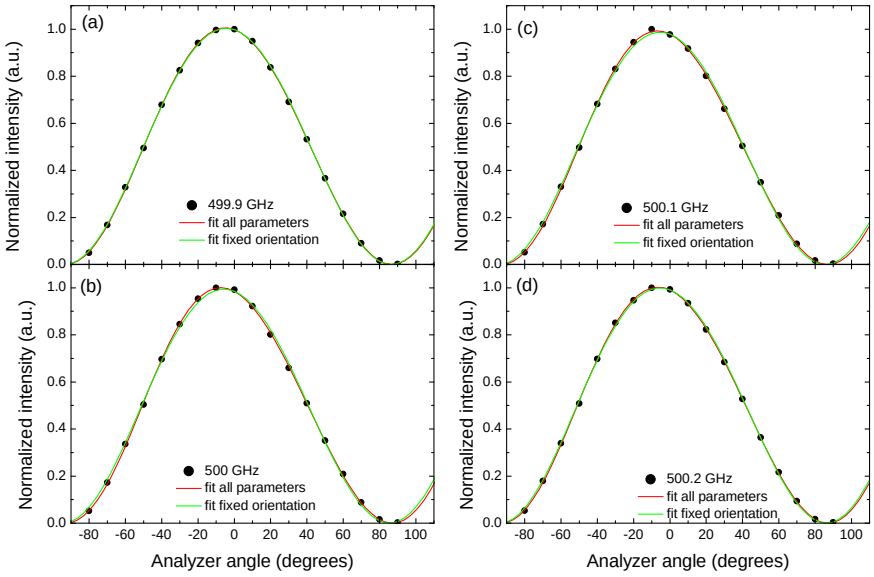

Figure A.53.: Polarization curves measured with a polarizer angle of 45 °. For the fit shown in red the orientaion of the ellipse was fitted while for the fit shown in green Θ was fixed at 40 °.

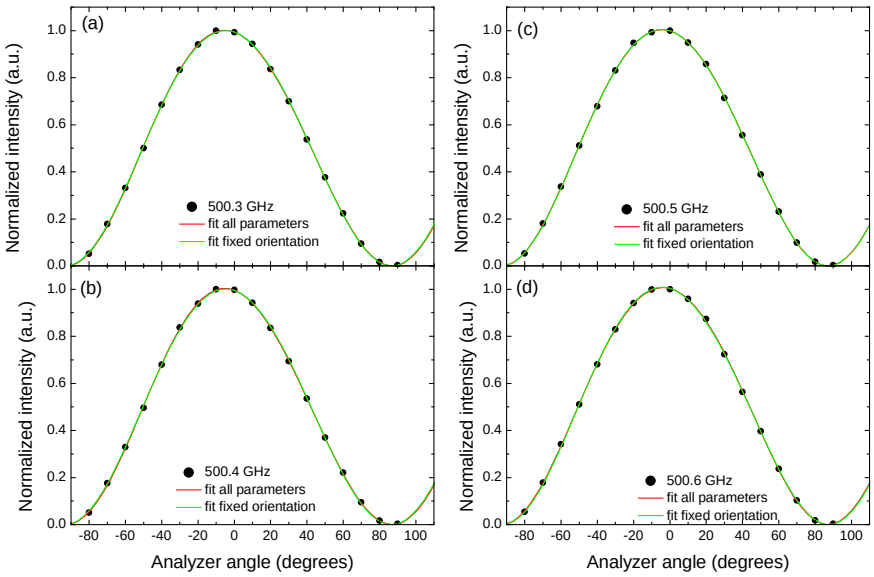

Figure A.54.: Polarization curves measured with a polarizer angle of 45 °. For the fit shown in red the orientaion of the ellipse was fitted while for the fit shown in green Θ was fixed at 40 °.

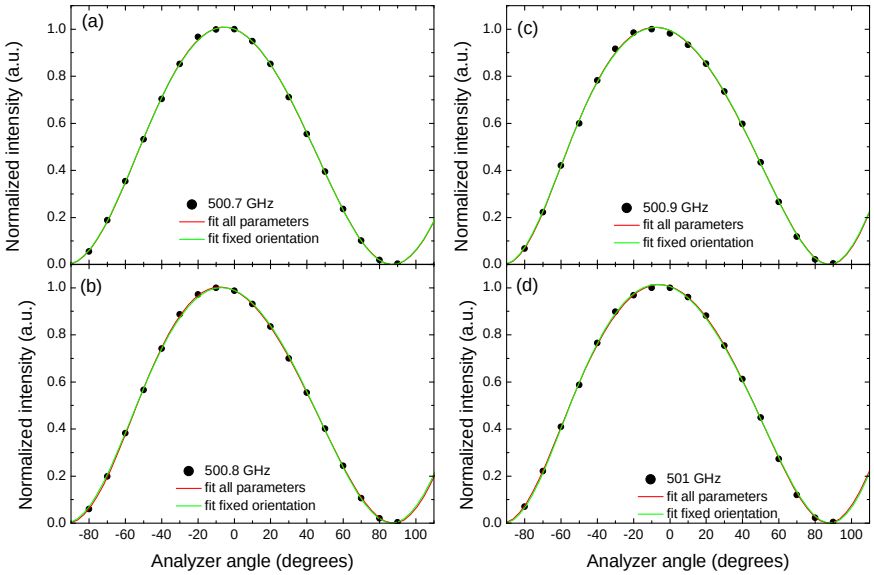

Figure A.55.: Polarization curves measured with a polarizer angle of 45 °. For the fit shown in red the orientaion of the ellipse was fitted while for the fit shown in green Θ was fixed at 40 °.

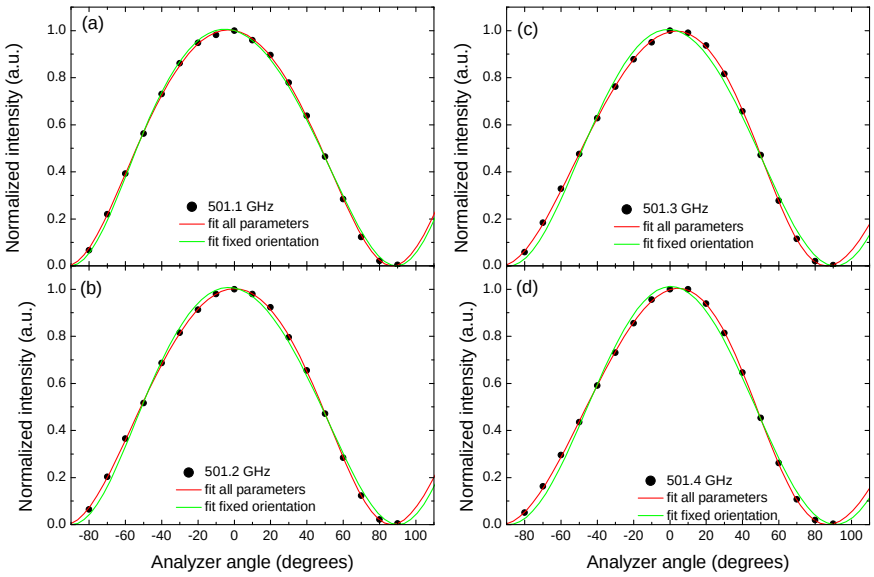

Figure A.56.: Polarization curves measured with a polarizer angle of 45 °. For the fit shown in red the orientaion of the ellipse was fitted while for the fit shown in green Θ was fixed at 40 °.

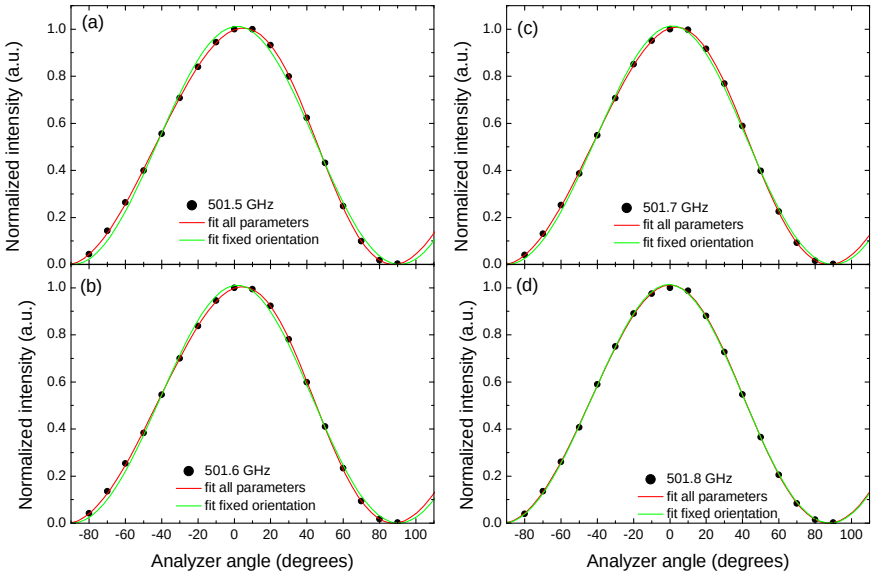

Figure A.57.: Polarization curves measured with a polarizer angle of 45 °. For the fit shown in red the orientaion of the ellipse was fitted while for the fit shown in green Θ was fixed at 40 °.

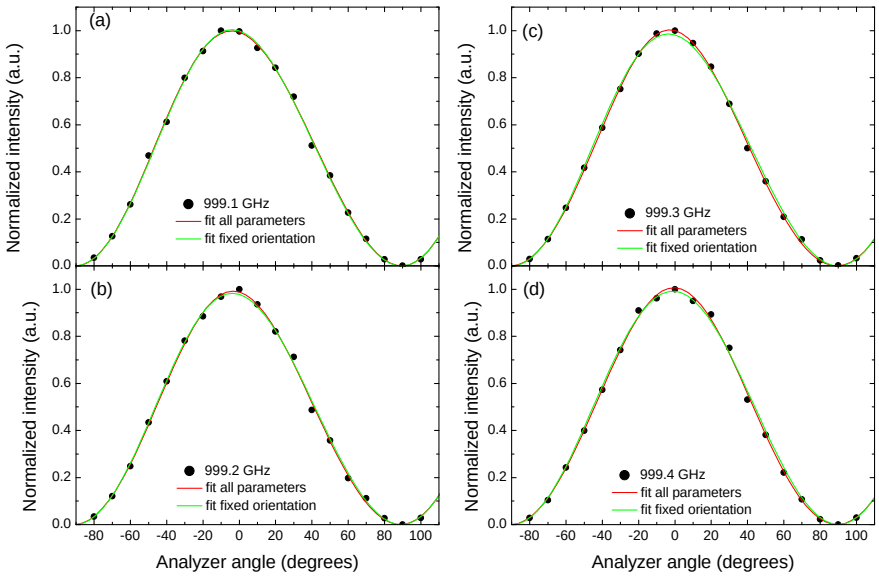

Figure A.58.: Polarization curves measured with a polarizer angle of 45 °. For the fit shown in red the orientaion of the ellipse was fitted while for the fit shown in green Θ was fixed at 80 °.

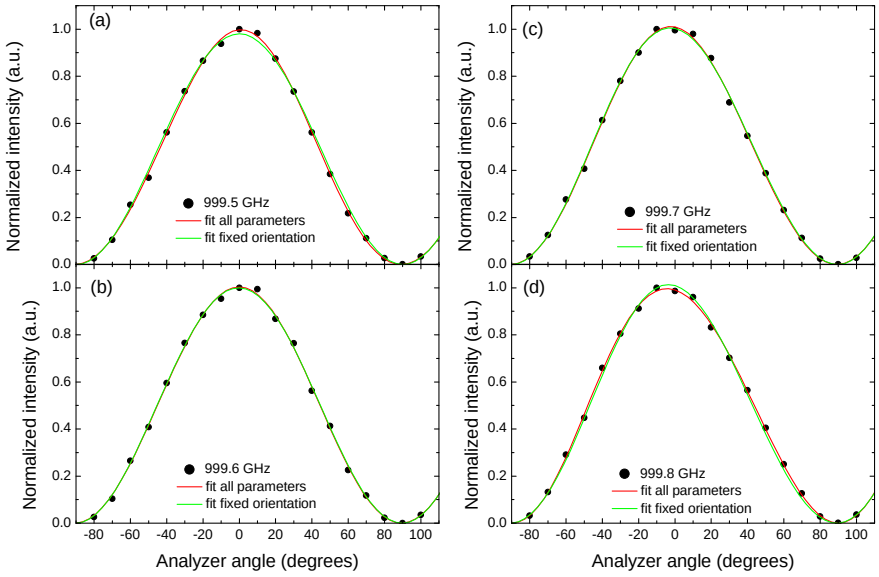

Figure A.59.: Polarization curves measured with a polarizer angle of 45 °. For the fit shown in red the orientaion of the ellipse was fitted while for the fit shown in green Θ was fixed at 80 °.

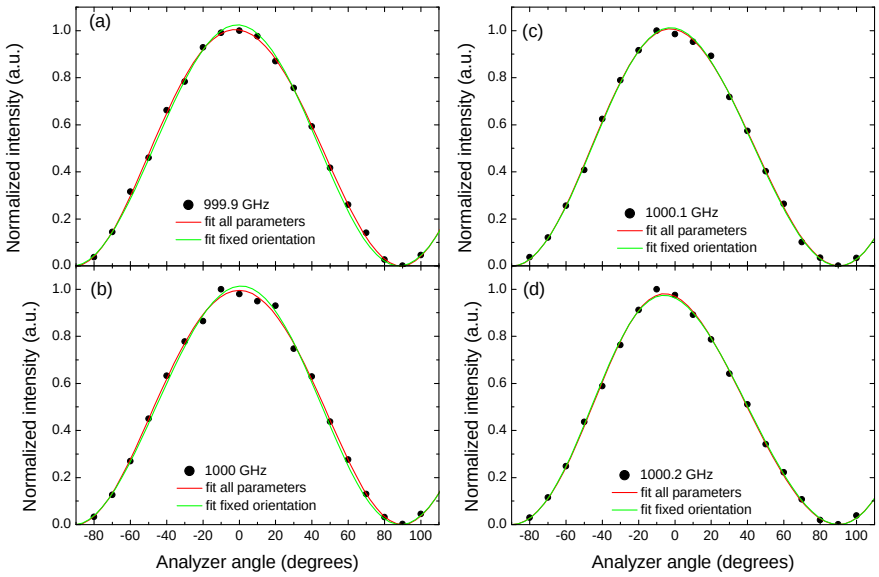

Figure A.60.: Polarization curves measured with a polarizer angle of 45 °. For the fit shown in red the orientaion of the ellipse was fitted while for the fit shown in green Θ was fixed at 80 °.

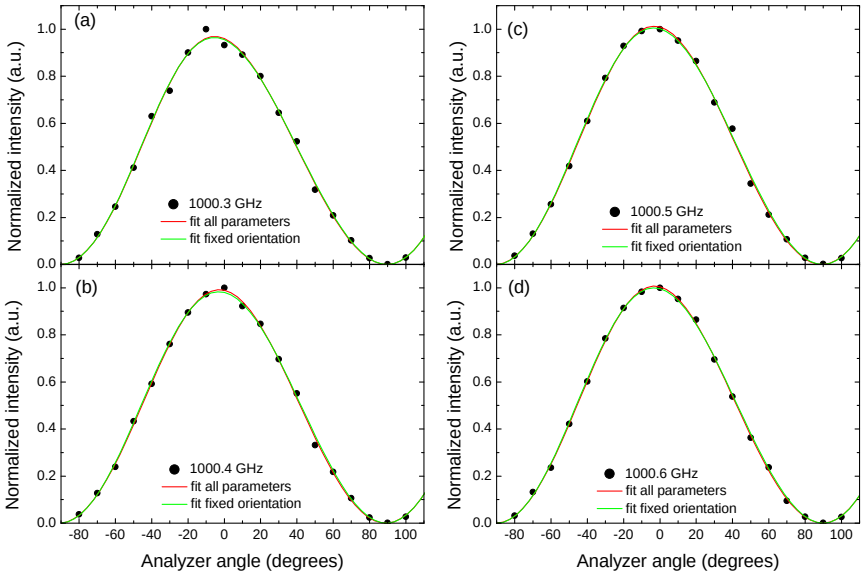

Figure A.61.: Polarization curves measured with a polarizer angle of 45 °. For the fit shown in red the orientaion of the ellipse was fitted while for the fit shown in green Θ was fixed at 80 °.

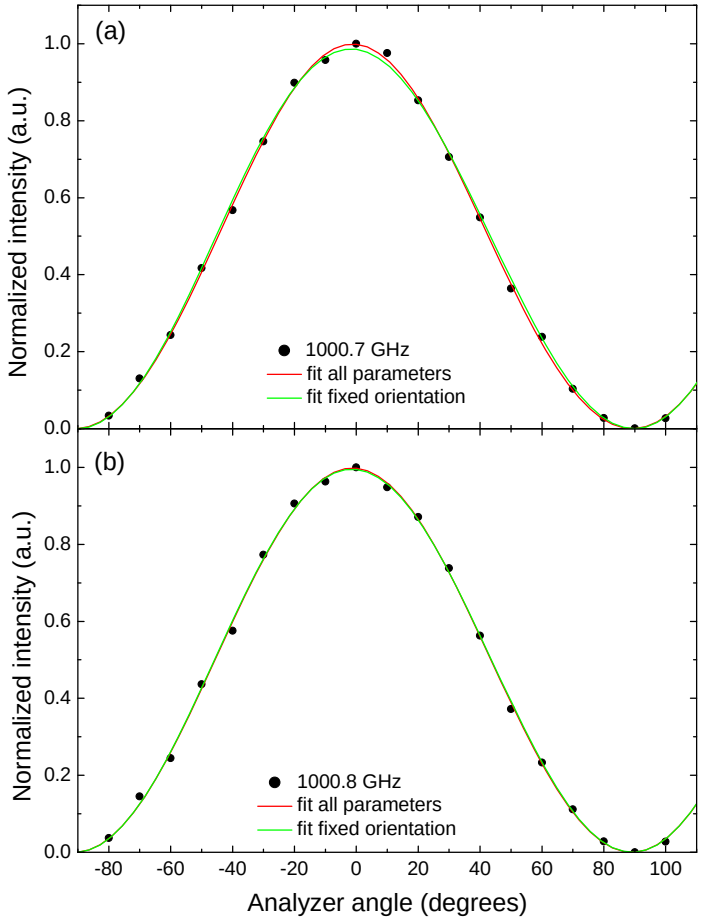

Figure A.62.: Polarization curves measured with a polarizer angle of 45 °. For the fit shown in red the orientaion of the ellipse was fitted while for the fit shown in green Θ was fixed at 80 °.

A.4.3. Polarizer angle of 90 °

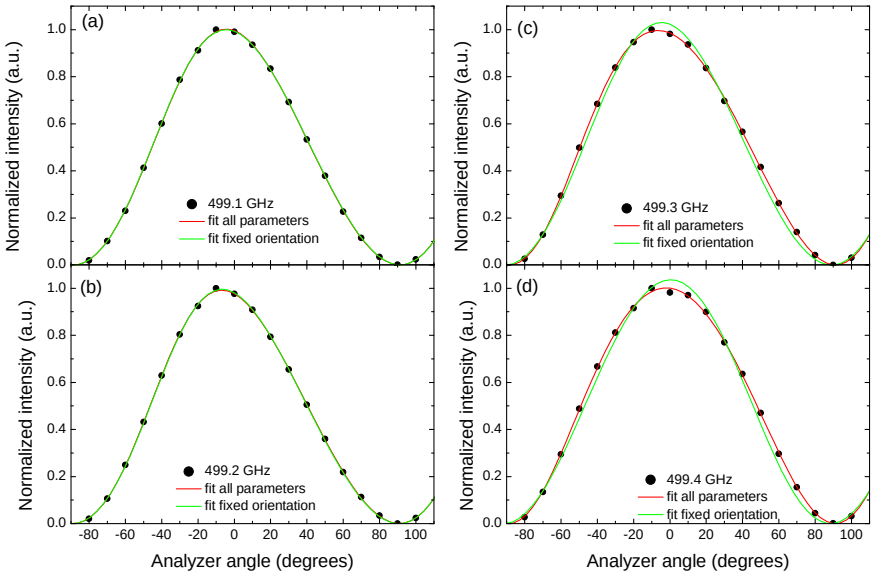

Figure A.63.: Polarization curves measured with a polarizer angle of 90 °. For the fit shown in red the orientaion of the ellipse was fitted while for the fit shown in green Θ was fixed at 40 °.

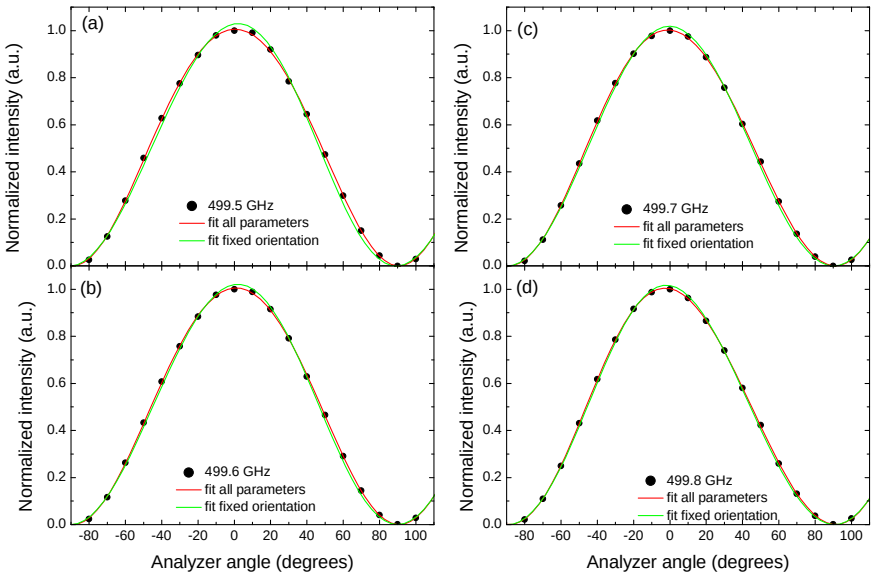

Figure A.64.: Polarization curves measured with a polarizer angle of 90 °. For the fit shown in red the orientaion of the ellipse was fitted while for the fit shown in green Θ was fixed at 40 °.

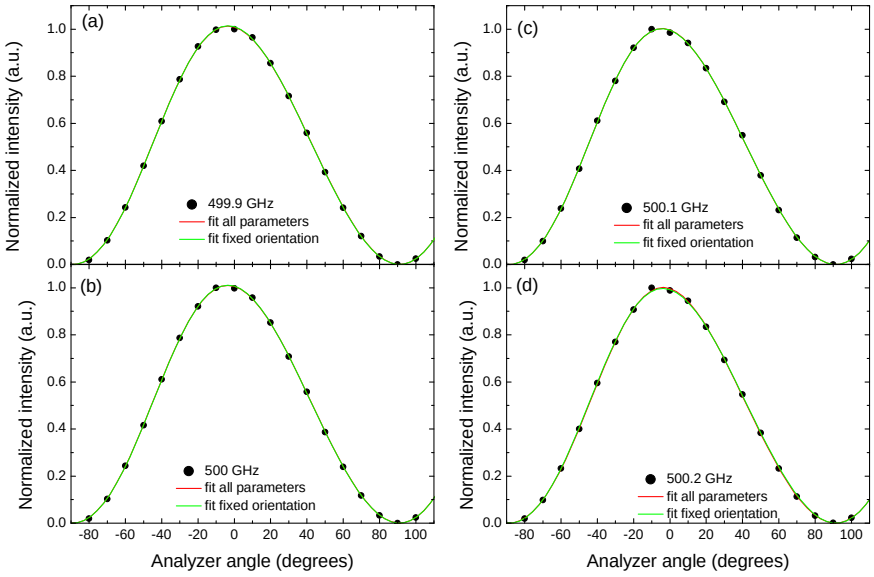

Figure A.65.: Polarization curves measured with a polarizer angle of 90 °. For the fit shown in red the orientaion of the ellipse was fitted while for the fit shown in green Θ was fixed at 40 °.

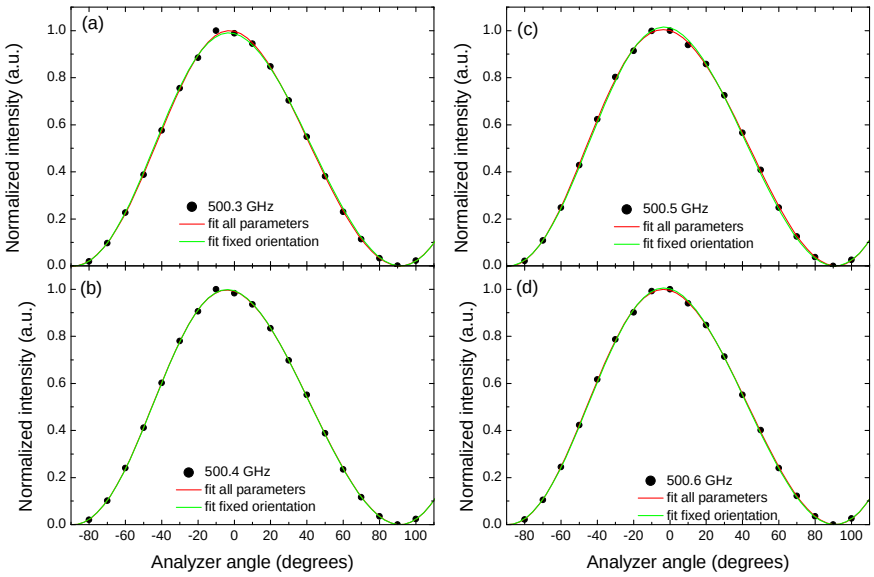

Figure A.66.: Polarization curves measured with a polarizer angle of 90 °. For the fit shown in red the orientaion of the ellipse was fitted while for the fit shown in green Θ was fixed at 40 °.

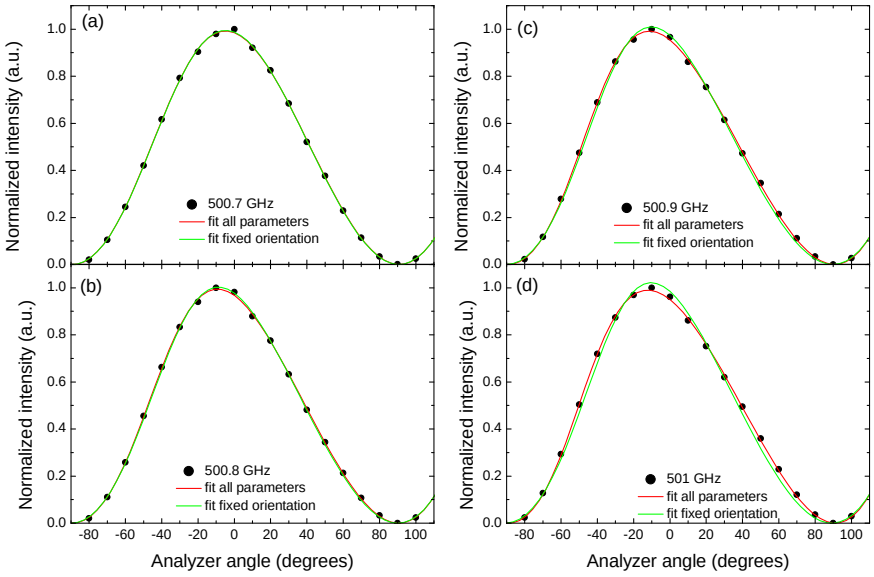

Figure A.67.: Polarization curves measured with a polarizer angle of 90 °. For the fit shown in red the orientaion of the ellipse was fitted while for the fit shown in green Θ was fixed at 40 °.

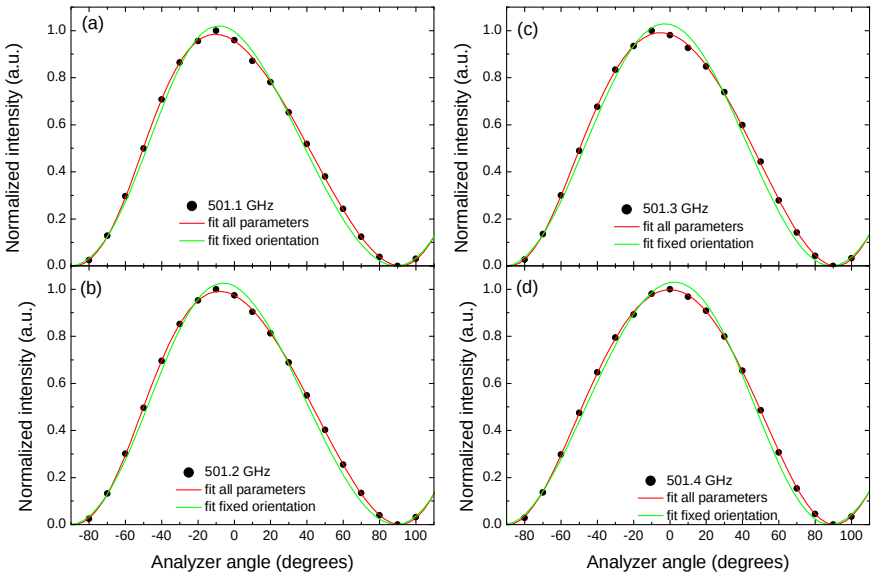

Figure A.68.: Polarization curves measured with a polarizer angle of 90 °. For the fit shown in red the orientaion of the ellipse was fitted while for the fit shown in green Θ was fixed at 40 °.

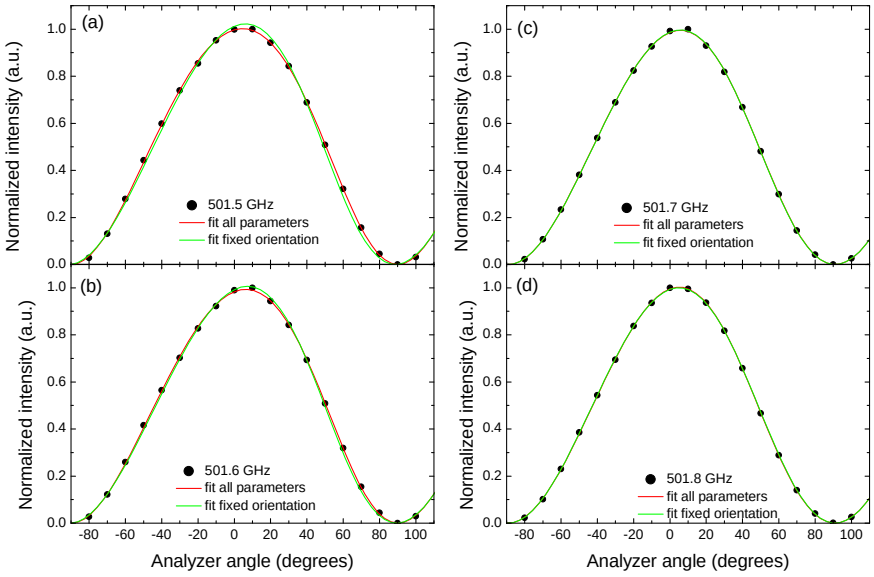

Figure A.69.: Polarization curves measured with a polarizer angle of 90 °. For the fit shown in red the orientaion of the ellipse was fitted while for the fit shown in green Θ was fixed at 40 °.

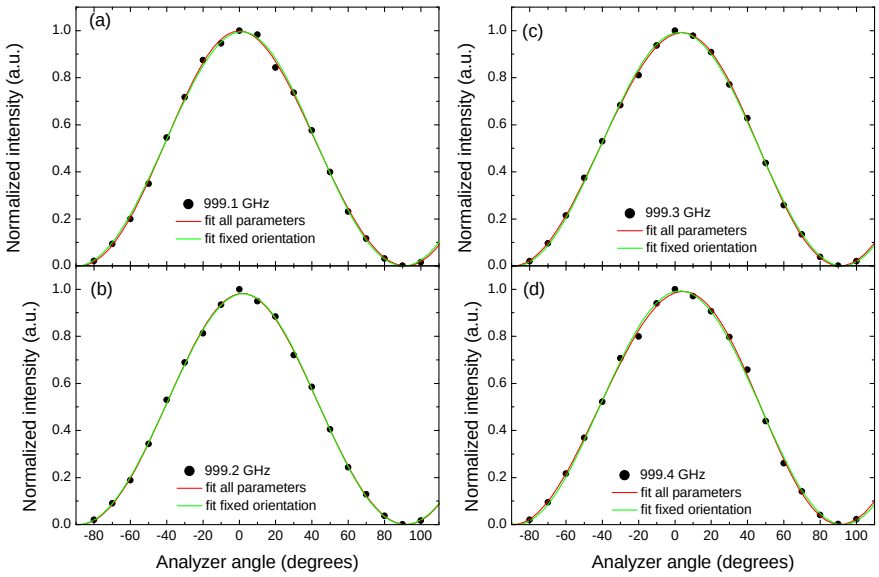

Figure A.70.: Polarization curves measured with a polarizer angle of 90 °. For the fit shown in red the orientaion of the ellipse was fitted while for the fit shown in green Θ was fixed at 80 °.

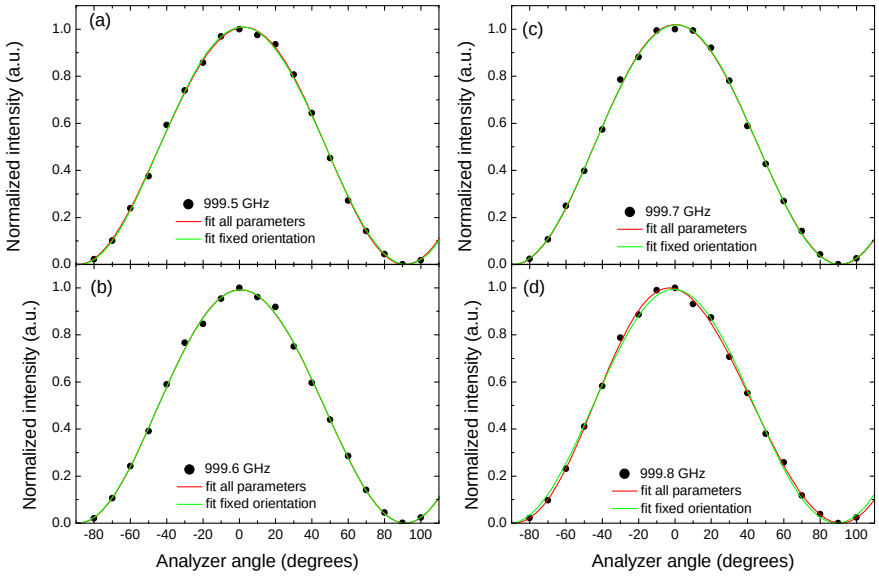

Figure A.71.: Polarization curves measured with a polarizer angle of 90 °. For the fit shown in red the orientaion of the ellipse was fitted while for the fit shown in green Θ was fixed at 80 °.

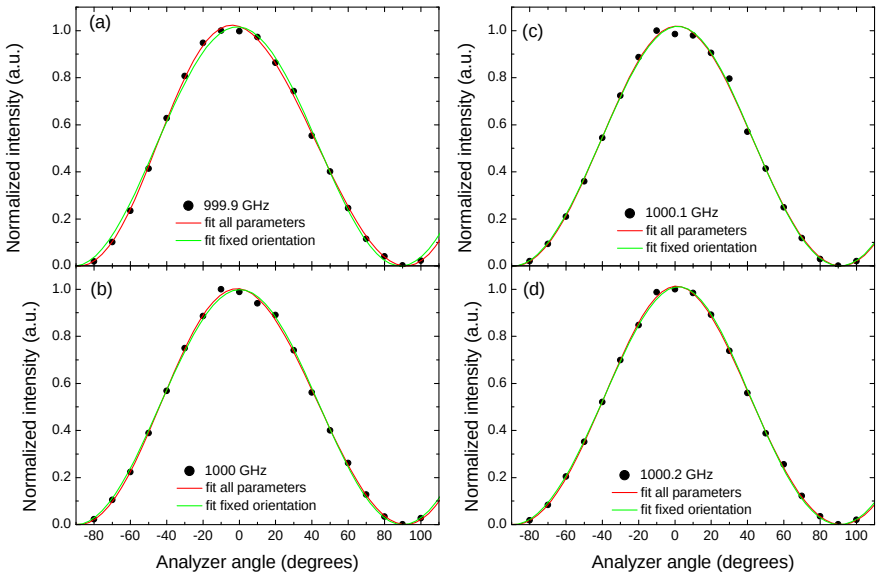

Figure A.72.: Polarization curves measured with a polarizer angle of 90 °. For the fit shown in red the orientaion of the ellipse was fitted while for the fit shown in green Θ was fixed at 80 °.

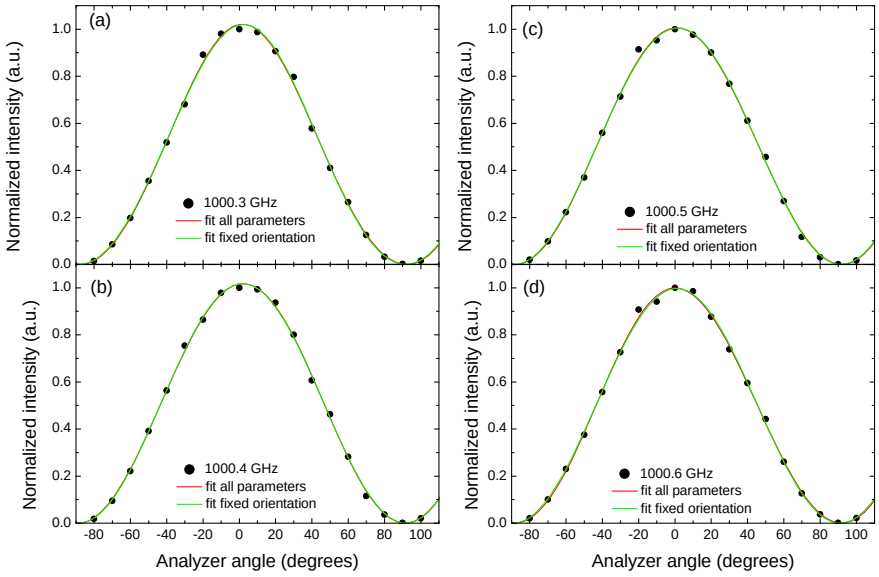

Figure A.73.: Polarization curves measured with a polarizer angle of 90 °. For the fit shown in red the orientaion of the ellipse was fitted while for the fit shown in green Θ was fixed at 80 °.

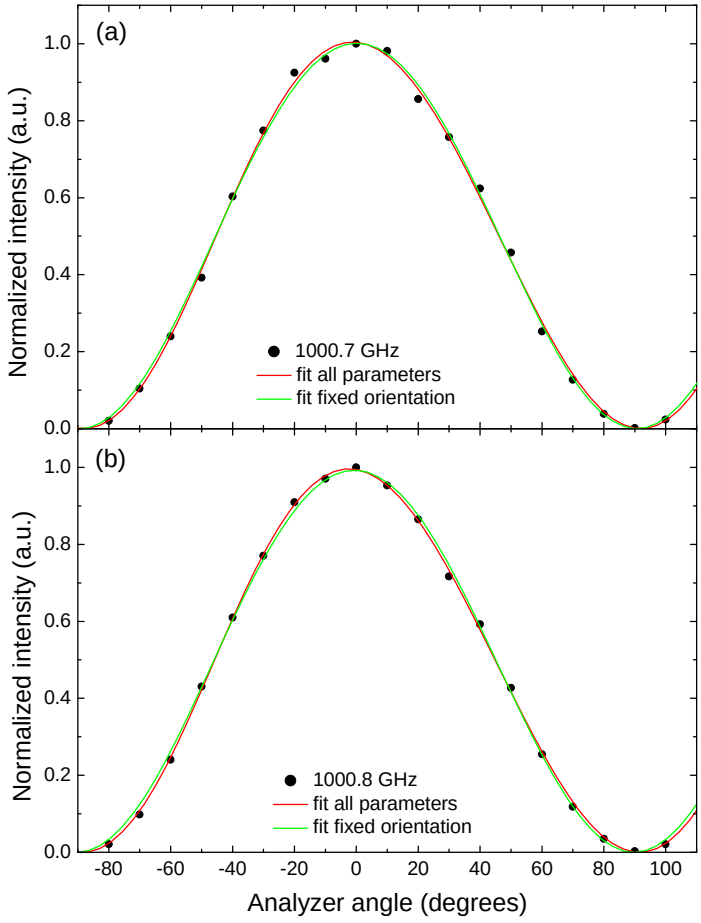

Figure A.74.: Polarization curves measured with a polarizer angle of 90 °. For the fit shown in red the orientaion of the ellipse was fitted while for the fit shown in green Θ was fixed at 80 °.

Table A.3.: Half-axes ratio and orientation of the ellipse, obtained from the fit of all parameters. All Angles are given in degrees.

Analyzer angle	a/b	Θ	a/b	Θ	a/b	Θ
	0^{circ}		45^{circ}		90^{circ}	
499.1	1.092	10.41	1.141	24.29	1.239	32.36
499.2	1.154	20.1	1.183	68.13	1.326	36.77
499.3	1.317	41.26	1.372	41.22	1.378	59.13
499.4	1.353	65.62	1.456	70.44	1.338	77.58
499.5	1.297	68	1.314	80.15	1.218	87.647
499.6	1.124	61.05	1.156	78.86	1.137	90.56
499.7	1.05	4.07	1.07	54.65	1.13	68.14
499.8	1.078	11.64	1.097	42.97	1.156	51.52
499.9	1.073	11.98	1.094	23.5	1.181	35.74
500.0	1.1	6.83	1.118	11.22	1.188	35.28
500.1	1.14	-6.86	1.155	10.98	1.234	34.1
500.2	1.115	6.36	1.168	21.66	1.218	30.55
500.3	1.1	29.16	1.141	28.24	1.188	23.96
500.4	1.163	40.19	1.125	24.54	1.212	36.22
500.5	1.235	44.84	1.162	37.18	1.2	46.12
500.6	1.168	33.54	1.172	42.07	1.18	41.38
500.7	1.288	18.1	1.233	32.9	1.228	36.36
500.8	1.53	24.41	1.4	29.19	1.416	38.78
500.9	1.622	36.02	1.647	33.34	1.517	42.78
501.0	1.468	44.46	1.583	39.47	1.586	55.23
501.1	1.384	43.07	1.592	46.94	1.531	51.69
501.2	1.294	51.97	1.502	57.18	1.44	56.58
501.3	1.408	66.25	1.451	69.1	1.388	71.07
501.4	1.417	71.14	1.351	79.38	1.334	87.22
501.5	1.308	79.46	1.288	90.86	1.339	106.28
501.6	1.214	87.47	1.268	99.08	1.333	113.99
501.7	1.207	88.55	1.244	102.84	1.193	123.19
501.8	1.156	88.45	1.147	166.78	1.162	127.38

Table A.4.: Half-axes ratio and orientation of the ellipse, obtained from the fit of all parameters. All Angles are given in degrees.

Analyzer angle	a/b	Θ	a/b	Θ	a/b	Θ
	0^{circ}		45^{circ}		90^{circ}	
999.1	1.182	62.91	1.141	87.95	1.159	100.33
999.2	1.154	54.75	1.124	23.25	1.137	90
999.3	1.15	57.35	1.168	59.48	1.117	56.32
999.4	1.15	71.26	1.104	45.39	1.125	47.07
999.5	1.143	64.72	1.122	31.54	1.071	22.76
999.6	1.136	91.19	1.026	25.6	1.066	163.29
999.7	1.25	86.06	1.088	22.74	1.03	128.63
999.8	1.68	101.36	1.19	103.26	1.175	124.14
999.9	1.353	105.0	1.163	126.76	1.218	128.73
1000.0	1.147	97.2	1.16	135.43	1.122	177.96
1000.1	1.121	70.45	1.109	91.24	1.124	93.16
1000.2	1.263	76.0	1.25	75.84	1.208	92.92
1000.3	1.231	66.0	1.205	77.04	1.162	90.2
1000.4	1.15	50.5	1.102	63.22	1.028	49.6
1000.5	1.08	94.33	1.121	20.63	1.04	113.45
1000.6	1.112	108.05	1.13	20.72	1.07	118.29
1000.7	1.11	114.18	1.1	50.22	1.131	144.35
1000.8	1.266	119.027	1.027	55.53	1.148	39.23

A.5. Measurements on MgO

Here, the transmittance and effective sample thickness of MgO measured with the 3-laser setup for different choices of ω_{ref} are shown.

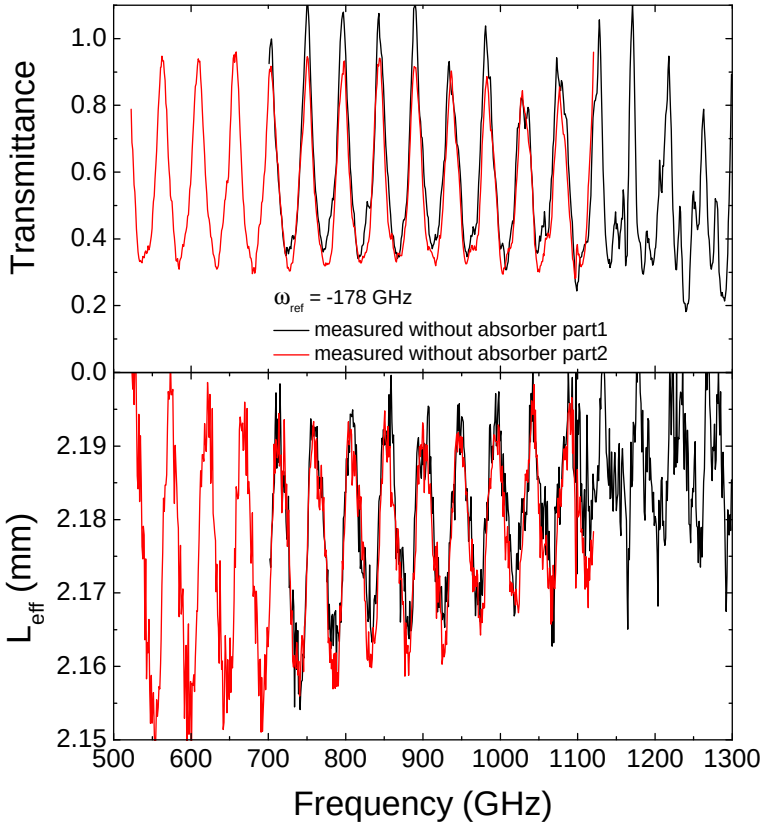

Figure A.75.: Transmittance and effective sample thickness of MgO measured with $\omega_{ref} = -178\ GHz$. The right and the left side show the measurements with and without absorber, respectively.

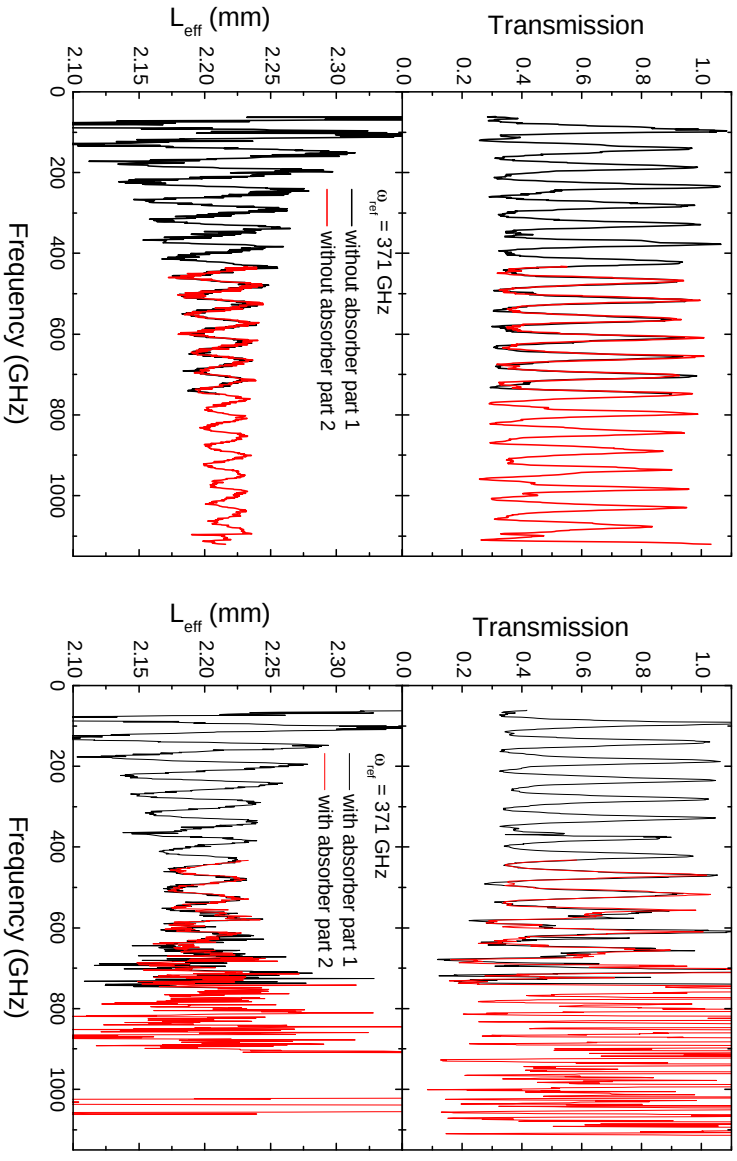

Figure A.76.: Transmittance and effective sample thickness of MgO measured with $\omega_{ref} = 371\ GHz$. The right and the left side show the measurements with and without absorber, respectively.

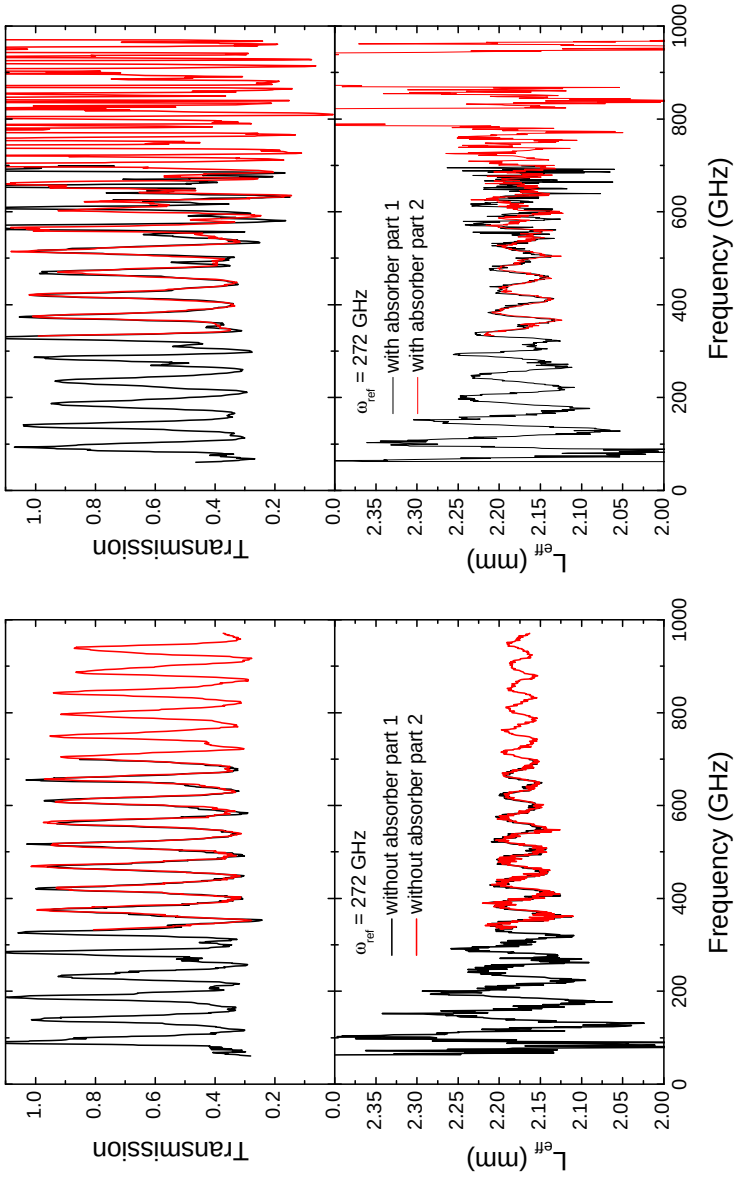

Figure A.77.: Transmittance and effective sample thickness of MgO measured with $\omega_{ref} = 272\ GHz$. The right and the left side show the measurements with and without absorber, respectively.

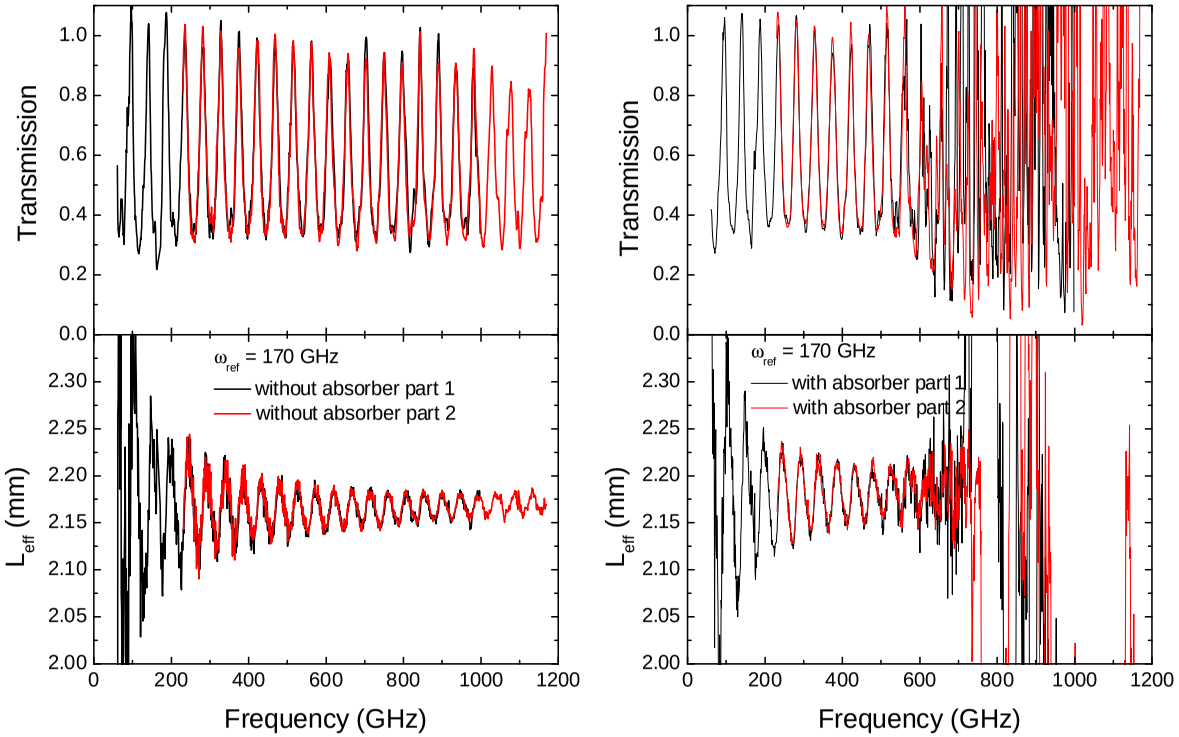

Figure A.78.: Transmittance and effective sample thickness of MgO measured with $\omega_{ref} = 170\ GHz$. The right and the left side show the measurements with and without absorber, respectively.

A.6. Low-temperature data of silicon

A.6.1. Si measurements with the bath cryostat

In this section the measured transmittance and phase data of silicon obtained using the bath cryostat are shown.

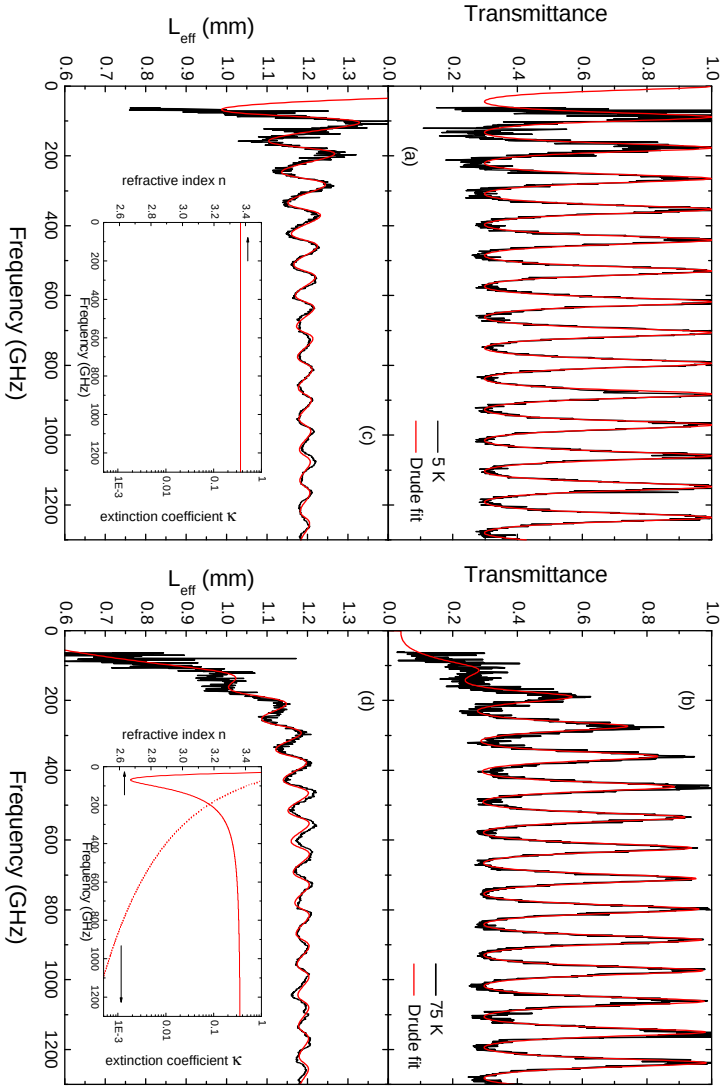

Figure A.79.: Transmittance and effective sample thickness of Si measured at 5 K (left panel) and at 75K (right panel) together with the corresponding fits. Figure

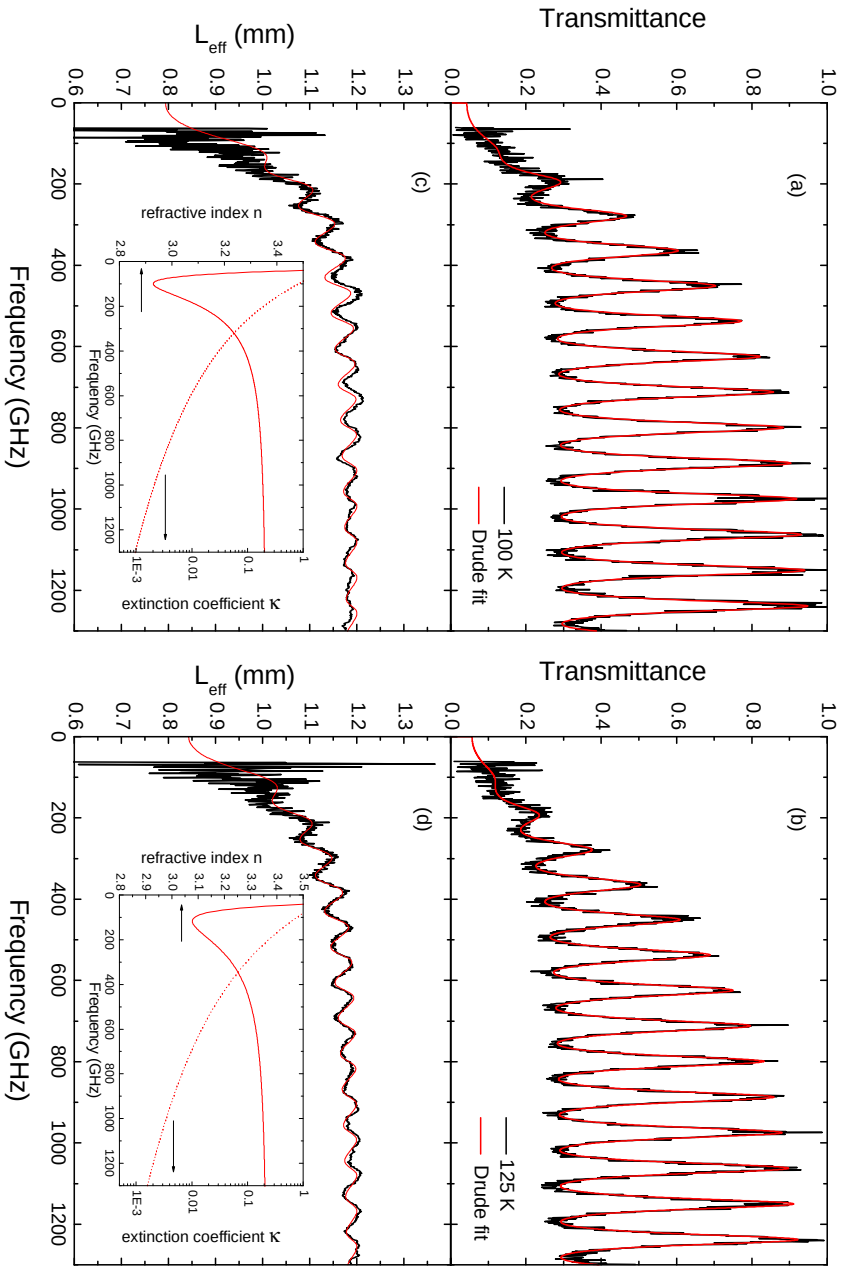

Figure A.80.: Transmittance and effective sample thickness of Si measured at 100 K (left panel) and at 125 K (right panel) together with the corresponding fits. Figure

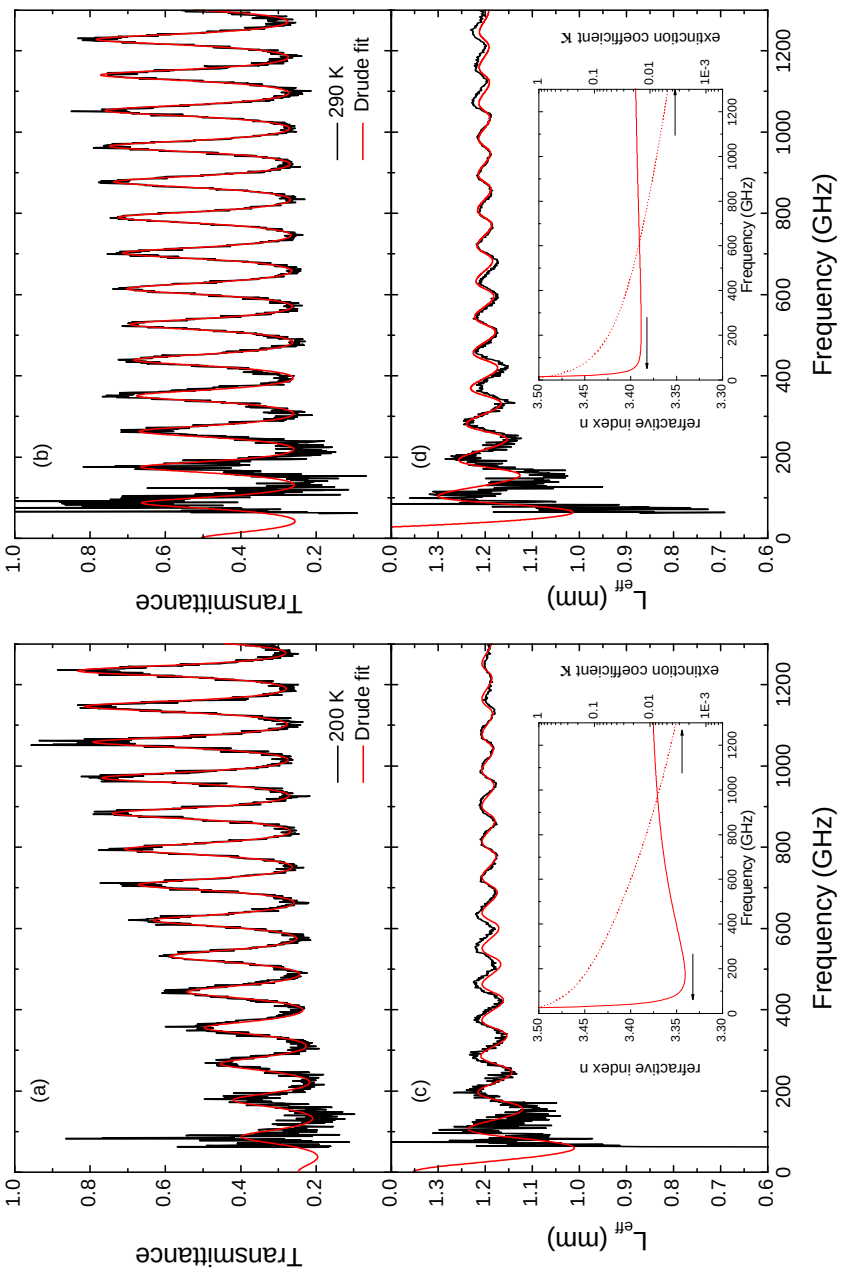

Figure A.81.: Transmittance and effective sample thickness of Si measured at 200 K (left panel) and at 290 K (right panel) together with the corresponding fits. Figure

A.6.2. Si measurements with the cold-finger cryostat

In this section the measured transmittance and phase data of silicon obtained using the cold-finger cryostat are shown.

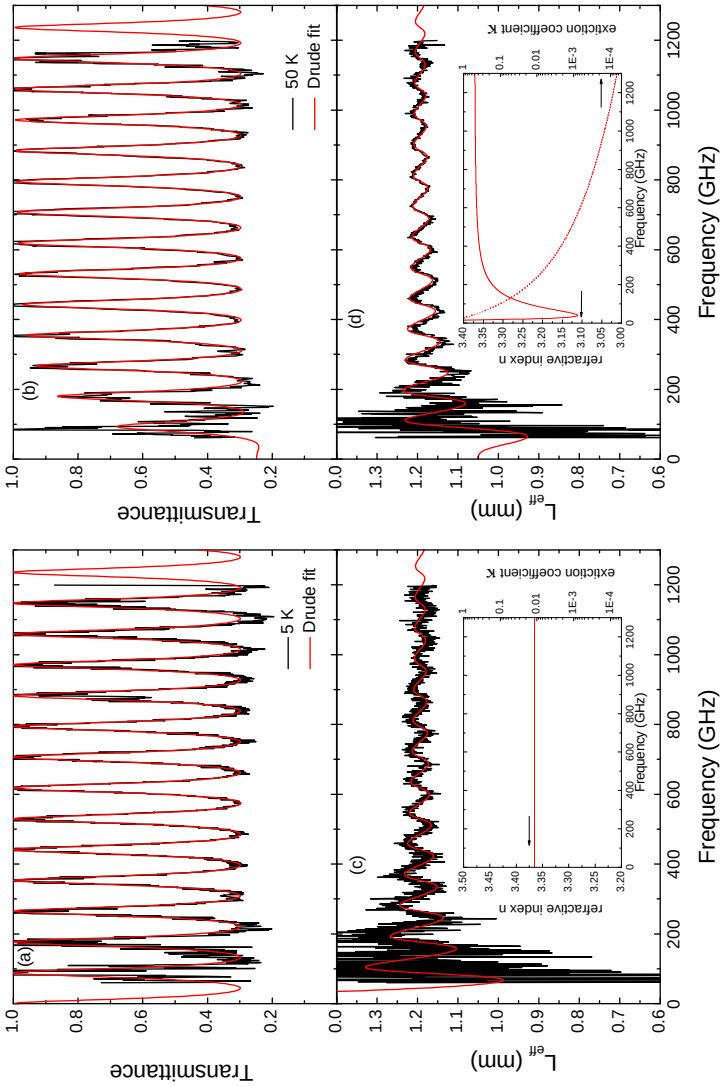

Figure A.82.: Transmittance and effective sample thickness of Si measured at 5 K (left panel) and at 50 K (right panel) together with the corresponding fits. Figure

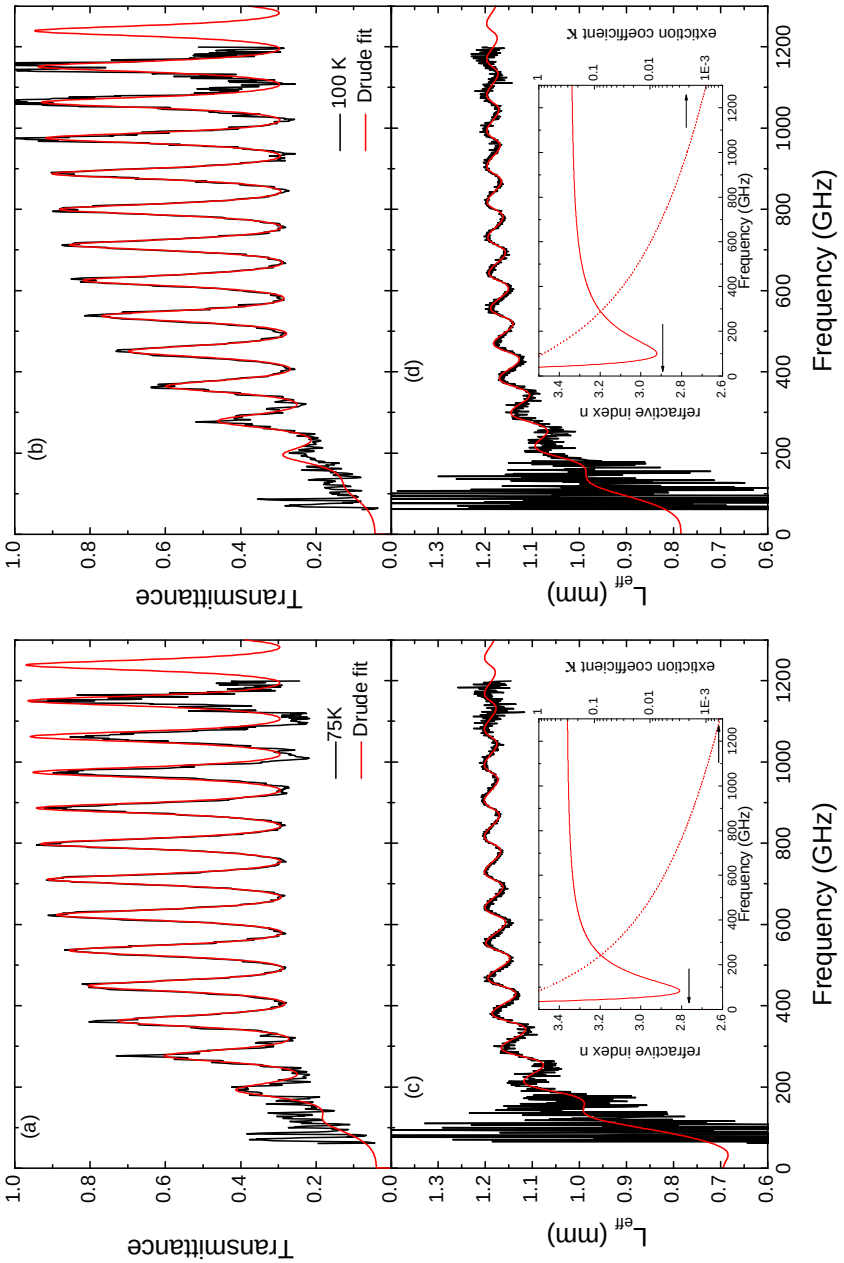

Figure A.83.: Transmittance and effective sample thickness of Si measured at 75 K (left panel) and at 100 K (right panel) together with the corresponding fits. Figure

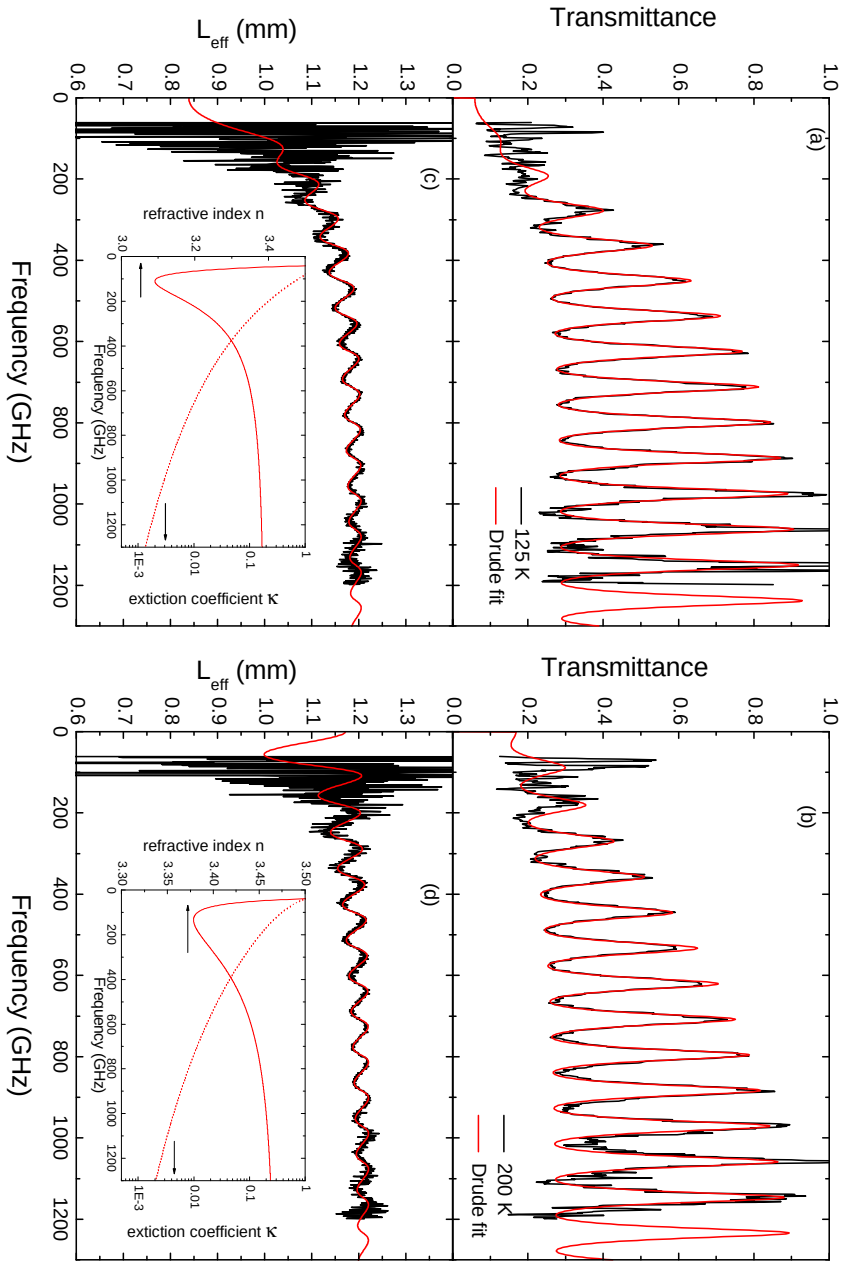

Figure A.84.: Transmittance and effective sample thickness of Si measured at 125 K (left panel) and at 200 K (right panel) together with the corresponding fits. Figure

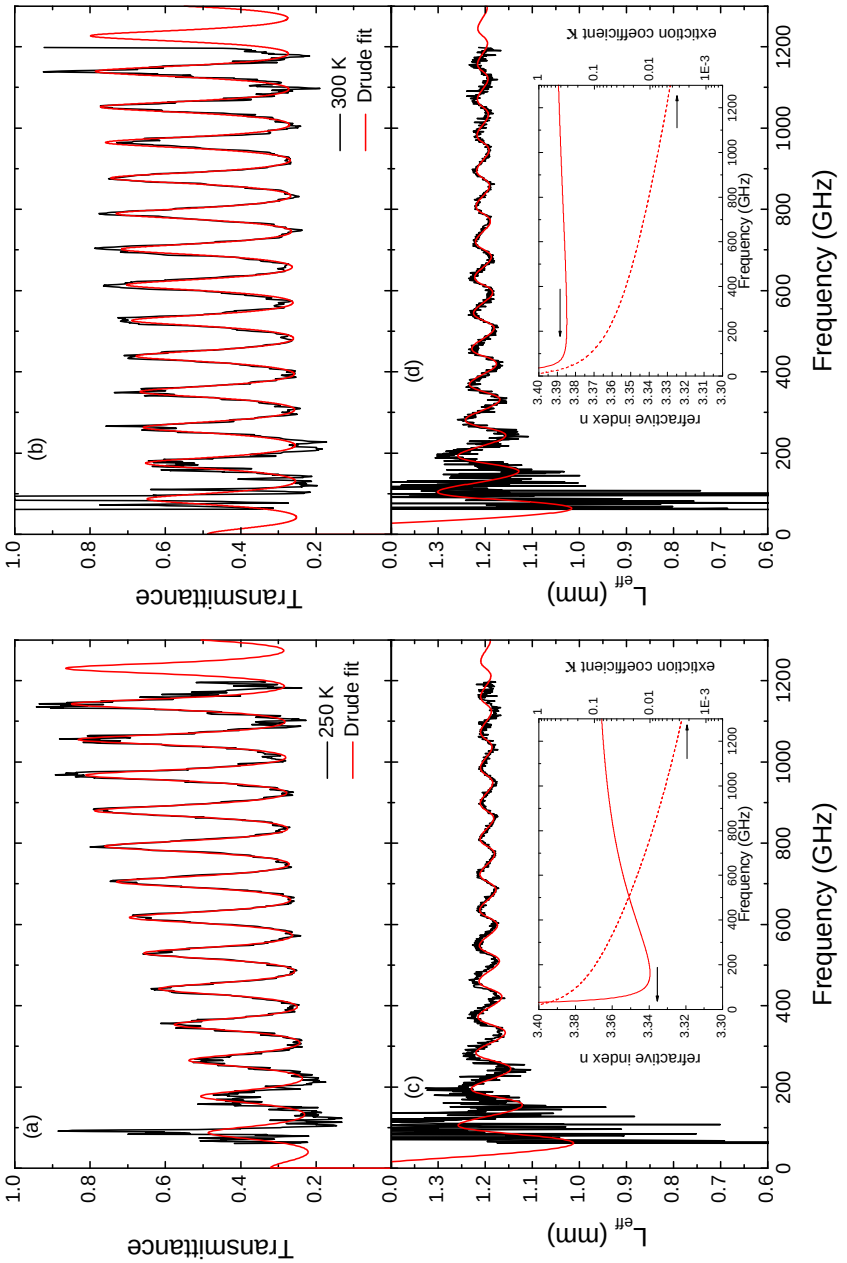

Figure A.85.: Transmittance and effective sample thickness of Si measured at 250 K (left panel) and at 300 K (right panel) together with the corresponding fits. Figure

References

[1] T. M. Korter and D. F. Plusquellic. Continuous-wave terahertz spectroscopy of biotin: vibrational anharmonicity in the far-infrared. *Chemical Physics Letters*, 385:45–51, 2004. 1

[2] Bernd Michael Fischer. *Broadband THz Time-Domain Spectroscopy of Biomolecules*. PhD thesis, Albert-Ludwigs-Universität Freiburg, 2005. 23, 25, 149, 151, 153

[3] J. S. Melinger, S. S. Harsha, N. Laman, and D. Grischkowsky. Guided-wave terahertz spectroscopy of molecular solids. *Journal of the Optical Society of America B*, 26(9):A79–A89, 2009. 1

[4] S. D. Brorson, R. Buhleier, I. E. Trofimov, J. O. White, Ch. Ludwig, F. F. Balakirev, H.-U. Habermeier, and J. Kuhl. Electrodynamics of high-temperature superconductors investigated with coherent terahertz pulse spectroscopy. *Journal of the Optical Society of America B*, 13(9):1979–1993, 1996. 1

[5] J. Orenstein, J. Corson, O. Seongshik, and J. N. Eckstein. Superconducting fluctuations in $Bi_2Sr_2Ca_{1-x}Dy_xCu_2O_{8+\delta}$ as seen by terahertz spectroscopy. *Annalen der Physik*, 15(7-8):596–605, 2006.

[6] P. Calvani, S. Lupi, M. Ortolani, L. Baldassarre, C. Mirri, R. Sopracase, U. Schade, Y. Takano, and T. Tamegai. Study of the optical gap in novel superconductors by coherent THz radiation. *Infrared Physics & Technology*, 51:429–432, 2008.

[7] M. Dressel, N. Drichko, B. Gorshunov, and A. Pimenov. THz spectroscopy of superconductors. *Journal of Selected Topics in Quantumelectronics*, 14(2):399–406, 2008. 18

[8] T. Fischer, A. V. Pronin, J. Wosnitza, K. Iida, F. Kurth, S. Haindl, L. Schultz, B. Holzapfel, and E. Schachinger. Highly anisotropic energy gap in superconducting $Ba(Fe_{0.9}Co_{0.1})_2As_2$ from optical conductivity measurements. *Physical Review B*, 82:224507, 2010. 1

[9] M. Dressel, N. Kasper, K. Petukhov, B. Gorshunov, G. Grüner, M. Huth, and H. Adrian. Nature of heavy quasiparticles in magnetically ordered heavy fermions UPd_2Al_3 and UPt_3. *Physical Review Letters*, 88(18):186404, 2002. 1

[10] J. P. Ostertag, M. Scheffler, M. Dressel, and M. Jourdan. Observing the anisotropic optical response of the heavy-fermion compound UNi_2Al_3. *Physica Status Solidi (b)*, 247(3):760–762, 2010.

[11] J. P. Ostertag, M. Scheffler, and M. Dressel. Terahertz conductivity of the heavy-fermion compound UNi_2Al_3. *Physical Review B*, 84:035132, 2011. 1

[12] N. A. Spaldin and M. Fiebig. The renaissance of magnetoelectric multiferroics. *Science*, 309:391–392, 2005. 1

[13] D. I. Khomskii. Multiferroics: Different ways to combine magnetism and ferroelectricity. *Journal of Magnetism and Magnetic Materials*, 306:1–8, 2006. 1

[14] A. Pimenov, A. A. Mukhin, V. Yu. Ivanov, V. D. Travkin, A. M. Balbashov, and A. Loidl. Possible evidence for electromagnons in multiferroic manganites. *Nature Physics*, 2:97–100, 2006. 2

[15] A. Pimenov, A. M. Shuvaev, A. A. Mukhin, and A. Loidl. Electromagnons in multiferroic manganites. *Journal of Physics: Condensed Matter*, 20:434209, 2008.

[16] A. Pimenov, A. Loidl, A. A. Mukhin, V. D. Travkin, V. Yu. Ivanov, and A. M. Balbashov. Terahertz spectroscopy of electromagnons in $Eu_{1-x}Y_xMnO_3$. *Physical Review B*, 77:014438, 2008.

[17] A. Pimenov, A. M. Shuvaev, A. Loidl, F. Schrettle, A. A. Mukhin, V. D. Travkin, V. Yu. Ivanov, and A. M. Balbashov. Magnetic and magnetoelectric excitations in $TbMnO_3$. *Physical Review Letters*, 102:107203, 2009.

[18] N. Kida, Y. Takahashi, J.S. Lee, R. Shimano, Y. Yamasaki, Y. Kaneko, S. Miyahara, N. Furukawa, T. Arima, and Y. Tokura. Terahertz time-domain spectroscopy of electromagnons in multiferroic perovskite manganites. *Journal of the Optical Society of America B*, 26(9):A35–A51, 2009.

[19] G. A. Komandin, V. I. Torgashev, A. A. Volkov, O. E. Porodinkov, I. E. Spektor, and A. A. Bush. Optical properties of $BiFeO_3$ ceramics in the frequency range 0.3-30.0 THz. *Physics of the Solid State*, 52(4):734–743, 2010.

[20] I. Kézsmárki, N. Kida, H. Murakawa, S. Bord'acs, Y. Onose, and Y. Tokura. Enhanced directional dichroism of terahertz light in resonance with magnetic excitations of the multiferroic $Ba_2CoGe_2O_7$ oxide compound. *Physical Review Letters*, 106:057403, 2011. 2

[21] F. Hindle, A. Cuisset, R. Bocquet, and G. Mouret. Continuous-wave terahertz by photomixing: applications to gas phase pollutant detection and quantification. *Comptes Rendus Physique*, 9:262–275, 2008. 2

[22] B. Fischer, M. Hoffmann, H. Helm, , G. Modjesch, and P. Uhd Jepsen. Chemical recognition in terahertz time-domain spectroscopy and imaging. *Semiconductor Science and Technology*, 20:S246–S253, 2005. 2, 149, 150, 151, 153, 154

[23] M. R. Leahy-Hoppa, M. J. Fitch, X. Zheng, L. M. Hayden, and R. Osiander. Wideband terahertz spectroscopy of explosives. *Chemical Physics Letters*, 434:227–230, 2007.

[24] L. Ho, M. Pepper, and P. Taday. Terahertz spectroscopy - signatures and fingerprints. *Nature Photonics*, 2:541–543, 2008.

[25] J. S. Melinger, S. Sree Harsha, N. Laman, and D. Grischkowsky. Temperature dependent characterization of terahertz vibrations of explosives and related threat materials. *Optics Express*, 18(26):27238–27250, 2010. 2

[26] K. Kawase, Y. Ogawa, Y. Watanabe, and H. Inoue. Non-destructive terahertz imaging of illicit drugs using spectral fingerprints. *Optics Express*, 11(20):2549–2554, 2003. 2

[27] Y. Watanabe, K. Kawase, T. Ikari, H. Ito, Y. Ishikawa, and H. Minamide. Component spatial pattern analysis of chemicals using terahertz spectroscopic imaging. *Applied Physics Letters*, 83:800–802, 2003.

[28] A. W. M. Lee, Q. Qin, S. Kumar, B. S. Williams, and Q. Hu. Real-time terahertz imaging over a standoff distance (>25 meters). *Applied Physics Letters*, 89:141125, 2006.

[29] H. Zhong, A. R. Sanchez, and X.-C. Zhang. Identification and classification of chemicals using terahertz reflective spectroscopic focalplane imaging system. *Optics Express*, 14(20):9130–9141, 2006.

[30] W. L. Chan, J. Deibel, and D. M. Mittleman. Imaging with terahertz radiation. *Reports on Progress in Physics*, 70:1325–1379, 2007. 2

[31] N. Karpowicz, J. Dai, X. Lu, Y. Chen, M. Yamaguchi, H. Zhao, X.-C. Zhang, M. Zhang, , C. Zhang, M. Price-Gallagher, C. Fletcher, O. Mamer, A. Lesimple, and K. Johnson. Coherent heterodyne time-domain spectrometry covering the entire "terahertz gap". *Applied Physics Letters*, 92:011131, 2008. 2, 24

[32] A. H. Saeedkia, D. Majedi, S. Safavi-Naeini, and R. R. Mansour. Analysis and design of a photoconductive integrated photomixer/antenna for terahertz applications. *Journal of Quantum Electronics*, 41(2):234–241, 2005. 3

[33] D. Saeedkia, R. R. Mansour, and S. Safavi-Naeini. The interaction of laser and photoconductor in a continuous-wave terahertz photomixer. *Journal of Quantum Electronics*, 41(9):1188–1196, 2005.

[34] I. S. Gregory, C. Baker, W. R. Tribe, M. J. Evans, H. E. Beere, E. H. Linfield, A. G. Davies, and M. Missous. High resistivity annealed low-temperature GaAs with 100 fs lifetimes. *Applied Physics Letters*, 83(20):4199–4201, 2003. 34

[35] I. S. Gregory, W. R. Tribe, B. E. Cole, M. J. Evans, E. H. Linfield, A. G. Davies, and M. Missous. Resonant dipole antennas for continuous-wave terahertz photomixers. *Applied Physics Letters*, 85(9):1622–1624, 2004. 27

[36] I. S. Gregory, C. Baker, W. R. Tribe, I. V. Bradley, E. H. Evans, M. J. Linfield, A. G. Davies, and M. Missous. Optimization of photomixers and antennas for continuous-wave terahertz emission. *Journal of Quantum Electronics*, 41(5):717–728, 2005. 27, 33, 34, 35, 36, 101, 107

[37] I. S. Gregory, M. J. Evans, H. Page, S. Malik, I. Farrer, and H. E. Beere. Analysis of photomixer receivers for continuous-wave terahertz radiation. *Applied Physics Letters*, 91:154103, 2007.

[38] R Mendis, C. Sydlo, J. Sigmund, M. Feiginov, P. Meissner, and H. L. Hartnagel. Spectral characterization of broadband THz antennas by photoconductive mixing: Toward optimal antenna design. *Antennas and Wireless Propagation Letters*, 4:85–88, 2005.

[39] E. A. Michael. Travelling-wave photonic mixers for increased continuous-wave power beyond 1 THz. *Semiconductor Science and Technology*, 20:164–177, 2005.

[40] E. A. Michael, B. Vowinkel, R. Schieder, M. Mikulics, M. Marso, and P. Kordos. Large-area traveling-wave photonic mixers for increased continuous terahertz power. *Applied Physics Letters*, 86:111120, 2005.

[41] P. Cámara Mayorga, I. Munoz Pradas, E. A. Michael, M. Mikulics, A. Schmitz, P. van der Wal, C. Kaseman, R. Güsten, K. Jacobs, M. Marso, H. Lüth, and P. Kordos. Terahertz photonic mixers as local oscillators for hot electron bolometer and superconductor-insulator-superconductor astronomical receivers. *Journal of Applied Physics*, 100:043116, 2006. 36

[42] I. Cámara Mayorga, E. A. Michael, A. Schmitz, P. van der Wal, R. Güsten, K. Maier, and A. Dewald. Terahertz photomixing in high energy oxygen- and nitrogen-ion-implanted GaAs. *Applied Physics Letters*, 91:031107, 2007. 3, 34, 36

[43] E. R. Brown, J. E. Bjarnason, A. M. Fedor, and T. M. Korter. On the strong and narrow absorption signature in lactose at 0.53 THz. *Applied Physics Letters*, 90:061908, 2007. 4, 149, 151, 152, 153, 159, 255, 258

[44] M. Dressel and G. Grüner. *Electrodynamics of Solids*. Cambridge University Press, 2002. 5, 8

[45] G. Herziger and R. Poprawe. Lasertechnik i. Script for the Lecture: Lasertechnik I, RWTH Aachen, 2006. 9, 12

[46] A. E. Siegman. *Lasers*. University Science Books, 1986. 11

[47] S. Feng and H. G. Winful. Physical origin of the Gouy phase shift. *Optics Letters*, 26(8):485–487, 2001. 11

[48] B. Ferguson and X-C. Zhang. Materials for terahertz science and technology. *Nature Materials*, 1:26–33, 2002. 17

[49] J. M. Chamberlain. Where optics meets electronics: recent progress in decreasing the terahertz gap. *Phil. Trans. R. Soc. Lond. A*, 362:199–213, 2004. 17

[50] G. Grüner, editor. *Millimeter and Submillimeter Wave Spectroscopy of Solids*, volume 74 of *Topics in Applied Physics*. Springer, 1998. 17, 18, 24, 25

[51] M. Abo-Bakr, J. Feikes, K. Holldack, P. Kuske, W. B. Peatman, U. Schade, G. Wüstefeld, and H.-W. Hübers. Brilliant, coherent far-infrared (THz) synchrotron radiation. *Physical Review Letters*, 90(9):094801, 2003. 17

[52] Silvio R. A. Salinas. *Introduction to Statistical Physics*. Springer, 2001. 17

[53] S. Martens, B. Gompf, and M. Dressel. Characterization of continuous-wave terahertz sources: laser mixing versus backward-wave oscillatorso. *Applied Optics*, 48(29):5490–5496, 2009. 18, 101

[54] F. Lewen, R. Gendriesch, I. Pak, D. G. Paveliev, M. Hepp, R. Schieder, and G. Winnewisser. Phase locked backward wave oscillator pulsed beam spectrometer in the submillimeter wave range. *Review of Scientific Instruments*, 69:32–39, 1998. 18

[55] J. B. Gunn. Instabilities of current in III-V semiconductors. *IBM Journal of Research and Development*, 8(2):141–159, 1964. 19

[56] J. B. Gunn. Microwave oscillations of current in III-V semiconductors. *Solid State Communications*, 1:88–91, 1963. 19

[57] R. Köhler, A. Tredicucci, F. Beltram, H. E. Beere, E. H. Linfield, A. G. Davies, D.A. Ritchie, R. C. Iotti, and F. Rossi. Terahertz semiconductor-heterostructure laser. *Nature*, 417:156–159, 2002. 19

[58] Yun-Shik Lee. *Principles of Terahertz Science and Technology*. Springer, 2009. 19, 20

[59] M. A. Belkin, J. A. Fan, S. Homorz, F. Capasso, S. P. Khanna, M. Lachab, A. G. Davies, and E. H. Linfield. Terahertz quantum cascade lasers with copper metal waveguides operating up to 178 K. *Optics Express*, 16:3242–3248, 2008. 20

[60] G. Scalari, C. Walther, J. Faist, H. Beere, and D. Ritchie. Electrically switchable, two-color quantum cascade laser emitting at 1.39 and 2.3 THz. *Applied Physics Letters*, 88:141102, 2006. 20

[61] P. L. Richards. Bolometer for infrared and millimeter waves. *Journal of Applied Physics*, 76:1–24, 1994. 21

[62] M. J. E. Golay. Theoretical consideration in heat and infra-red detection, with particular reference to the pneumatic detector. *Review of Scientific Instruments*, 18(5):347–356, 1947. 22

[63] D. H. Auston, K. P. Cheung, and P. R. Smith. Picosecond photoconducting hertzian dipoles. *Applied Physics Letters*, 45:284–186, 1984. 22

[64] P. Uhd Jepsen, R. H. Jacobsen, and S. R. Keiding. Generation and detection of terahertz pulses from biased semiconductor antennas. *Journal of the Optical Society of America B*, 13(11):2424–2436, 1996. 22

[65] Y. Cai, I. Brener, J. Lopata, J. Wynn, L. Pfeiffer, and J. Federici. Design and performance of singular electric field terahertz photoconducting antennas. *Applied Physics Letters*, 71:2076–2078, 1997.

[66] M. Tani, S. Matsuura, K. Sakai, and S. Nakashima. Emission characteristics of photoconductive antennas based on low-temperature-grown GaAs and semi-insulating GaAs. *Applied Optics*, 36(30):7853–7859, 1997. 22

[67] Ch. Fattinger and D. Grischkowsky. Terahertz beams. *Applied Physics Letters*, 54:490–192, 1989. 24

[68] M. van Exter and D. R. Grischkowsky. Characterization of an optoelectronic terahertz beam system. *Microwave Theory and Techniques*, 38(11):1684–1691, 1990. 24

[69] R. Yano, H. Gotoh, Y. Hirayama, S. Miyashita, Y. Kadoya, and T. Hattori. Terahertz wave detection performance of photoconductive antennas: Role of antenna structure and gate pulse intensity. *Journal of Applied Physics*, 97:103103, 2005. 24

[70] D. M. Mittleman, R. H. Jacobsen, R. Neelamani, R. G. Baraniuk, and M. C. Nuss. Gas sensing using terahertz time-domain spectroscopy. *Applied Physics B*, 67:379–390, 1998. 24

[71] Q. Wu and X.-C. Zhang. Free-space electro-optic sampling of terahertz beams. *Applied Physics Letters*, 67:3523–3525, 1995. 25

[72] A. Nahata, D. H. Auston, T. F. Heinz, and C. Wu. Coherent detection of freely propagating terahertz radiation by electro-optic sampling. *Applied Physics Letters*, 68:150–152, 1996. 25

[73] Y. Cai, I. Brener, J. Lopata, J. Wynn, L. Pfeiffer, J. B. Stark, Q. Wu, X. C. Zhang, and J. F. Federici. Coherent terahertz radiation detection: Direct comparison between free-space electro-optic sampling and antenna detection. *Applied Physics Letters*, 73(4):444–44, 1998. 25

[74] E. R. Brown, F. W. Smith, and K. A. McIntosh. Coherent millimeter-wave generation by heterodyne conversion in low-temperature-grown GaAs photoconductors. *Journal of Applied Physics*, 73:1480, 1993. 27

[75] E. R. Brown, K. A. McIntosh, F. W. Smith, M. J. Manfra, and C. L. Dennis. Measurements of optical-heterodyne conversion in low-temperature-grown GaAs. *Applied Physics Letters*, 62:1206–1208, 1993.

[76] E. R. Brown, K. A. McIntosh, K. B. Nichols, and C. L. Dennis. Photomixing up to 3.8 THz in low-temperature-grown GaAs. *Applied Physics Letters*, 66:285–287, 1995. 36, 101, 107

[77] K. A. McIntosh, E. R. Brown, K. B. Nichols, O. B. McMahon, W. F. Dinatale, and T. M. Lyszczarz. Terahertz photomixing with diode lasers in low-temperature-grown GaAs. *Applied Physics Letters*, 67:3844–3846, 1995.

[78] S. Verghese, K. A. McIntosh, and E. R. Brown. Optical and terahertz power limits in the low-temperature-grown GaAs photomixers. *Applied Physics Letters*, 71:2743–2745, 1997. 27

[79] S. Verghese, K. A. McIntosh, S. Calawa, W. F. Dinatale, E. K. Duerr, and K. A. Molvar. Generation and detection of coherent terahertz waves using two photomixers. *Applied Physics Letters*, 73(26):3824–3826, 1998. 27, 39

[80] S. Matsuura, M. Tani, and K. Sakai. Generation of coherent terahertz radiation by photomixing in dipole photoconductive antennas. *Applied Physics Letters*, 70:559–561, 1997. 27

[81] S. Matsuura, M. Tani, H. Abe, K. Sakai, H. Ozeki, and S. Saito. High-resolution terahertz spectroscopy by a compact radiation source based on photomixing with diode lasers in a photoconductive antenna. *Journal of Molecular Spectroscopy*, 187:97–101, 1998.

[82] I. S. Gregory, W. R. Tribe, C. Baker, Cole B. E., M. J. Evans, L. Spencer, M. Pepper, and M. Missous. Continuous-wave terahertz system with a 60 dB dynamic range. *Applied Physics Letters*, 86:204104, 2005. 27

[83] A. J. Deninger, T. Göbel, D. Schönherr, T. Kinder, A. Roggenbuck, M. Köberle, Lison F., T. Müller-Wirts, and P. Meissner. Precisely tunable continuous-wave terahertz source with interferometric frequency control. *Review of Scientific Instruments*, 79:044702, 2008. 30, 31

[84] Toptica Photonics. Lasers for scientific challenges. Catalog, 2009/2010. 32

[85] S. Preu, G. H. Döhler, S. Malzer, L. J. Wang, and A. C. Gossard. Tunable, continuous-wave terahertz photomixer sources and applications. *Journal of Applied Physics*, 109:061301, 2011. 33

[86] S. Gupta, M. Y. Frankel, J. A. Valdmanis, J. F. Whitaker, G. A. Mourou, F. W. Smith, and A. R. Calawa. Subpicosecond carrier lifetime in GaAs grown by molecular beam epitaxy at low temperatures. *Applied Physics Letters*, 59(25):3276–3278, 1991. 34

[87] S. Gupta, J. F. Whitaker, and G. A. Mourou. Ultrafast carrier dynamics in III-V semiconductors grown by molecular-beam epitaxy at very low substrate temperatures. *Journal of Quantum Electronics*, 28(10):2464–2472, 1992. 34

[88] S. E. Ralph and D. Grischkowsky. Trap-enhanced electric fields in semi-insulators: the role of electrial and optical carrier injection. *Applied Physics Letters*, 59(16):1972–1974, 1991. 35

[89] E. R. Brown. A photoconductive model for superior GaAs THz photomixers. *Applied Physics Letters*, 75:769–771, 1999. 36

[90] K. Sakai, editor. *Terahertz Optoelectronics*, volume 97 of *Topics in Applied Physics*. Springer, 2005. 36

[91] Iván Cámara Mayorga. *Photomixers as tunable terahertz local oscillators*. PhD thesis, Rheinische Friedrich-Wilhelm Universität Bonn, 2008. 36

[92] C. Fattinger and D. Grischkowsky. Point source terahertz optics. *Applied Physics Letters*, 53:1480–1482, 1988. 36

[93] G. Mouret, S. Matton, R. Bocquet, D. Bigourd, F. Hindle, A. Cuisset, J. F. Lampin, K. Blary, and D. Lippens. Thz media characterization by means of coherent homodyne detection, results and potential applications. *Applied Physics B*, 89:395–399, 2007. 39

[94] Roggenbuck. *Entwicklung, Aufbau und Charakterisierung eines spektral hochauflösenden cw THz Spektrometers mit optoelektronischer Signalerzeugung und Detektion.* PhD thesis, Universität Siegen, to be published. 40, 41, 42, 43, 44, 45, 58, 60

[95] A. Roggenbuck, K. Thirunavukkuarasu, H. Schmitz, J. Marx, A. Deninger, I. Cámara Mayorga, R. Güsten, J. Hemberger, and M. Grüninger. Using a fiber stretcher as a fast phase modulator in a continuous wave terahertz spectrometer. *Journal of the Optical Society of America B*, 29(4):614–620, 2012. 40, 60

[96] R. Mendis, C. Sydlo, J. Sigmund, M. Feiginov, P. Meissner, and H. L. Hartnagel. Coherent generation and detection of continuous terahertz waves using two photomixers driven by laser diodes. *International Journal of Infrared and Millimeter Waves*, 26(2):201–207, 2005. 39

[97] G. Mouret, S. Matton, R. Bocquet, D. Bigourd, F. Hindle, A. Cuisset, J. F. Lampin, and D. Lippens. Anomalous dispersion measurement in terahertz frequency region by photomixing. *Applied Physics Letters*, 88:181105, 2006. 39

[98] A. Nahata, T. Yardley, and Heinz T. F. Free-space electro-optic detection of continuous-wave terahertz radiation. *Applied Physics Letters*, 75(17):2524–2526, 1999. 39

[99] K. A. Siebert, H. Quast, R. Leonhardt, T. Löffler, M. Thomson, T. Bauer, H. G. Roskos, and S. Czasch. Continuous-wave all-optoelectronic terahertz imaging. *Applied Physics Letters*, 80(16):3003–3005, 2002.

[100] I.S. Gregory, W.R. Tribe, B.E. Cole, C. Baker, M.J. Evans, I.V. Bradley, E.H. Linfield, A.G. Davies, and M. Missous. Phase sensitive continuous-wave THz imaging using diode lasers. *Electronics Letters*, 40(2):143– 145, 2004. 39

[101] A. M. Sinyukov, Z. Liu, Y. L. Hor, K. Su, R. B. Barat, D. E. Gary, Z.-H. Michalopoulou, I. Zorych, J. F. Federici, and D. Zimdars. Rapid-phase modulation of terahertz radiation for high-speed terahertz imaging and spectroscopy. *Optics Letters*, 33(14):1593–1595, 2008. 40

[102] T. Göbel, D. Schoenherr, C. Sydlo, M. Feiginov, P. Meissner, and H.L. Hartnagel. Continuous-wave terahertz system with electro-optical terahertz phase control. *Electronics Letters*, 44(14):863–864, 2008.

[103] T. Göbel, D. Schoenherr, C. Sydlo, M. Feiginov, P. Meissner, and H. L. Hartnagel. Single-sampling-point coherent detection in continuous-wave photomixing terahertz systems. *Electronics Letters*, 45(1):65–66, 2009. 40

[104] M. Grüninger, J. Hemberger, and A. Roggenbuck. Faserbasierte THz-Fourier-Spektroskopie (Amtl. AZ: DE 10 2010 040 356.3), 2010. 61

[105] Ernesto Uldarico Vidal. Eliminating phase drift in a continuous wave thz spectrometer using three lasers. Master's thesis, Universität zu Köln, 2011. 61, 62, 64, 65, 67, 114

[106] F. R. T. Luna, G. H. Cavalcanti, L. H. Coutinho, and A. G. Trigueiros. A compilation of wavelengths and energy levels for the spectrum of neutral rubidium (Rb I). *Journal of Quantitative Spectroscopy & Radiative Transfer*, 75:559–587, 2002. 62

[107] O. S. Heavens. Radiative transition probabilities of the lower excited states of the alkali metals. *Journal of the Optical Society of America*, 51(10):1058–1061, 1961. 62

[108] D. W. Preston. Doppler-free saturated absorption: Laser spectroscopy. *American Journal of Physics*, 64:1432–1436, 1996. 62

[109] G. A. Komandin, O. E. Porodinkov, I. E. Spector, and A. A. Volkov. Multiphonon absorption in a MgO single crystal in the terahertz range. *Semiconductors and Dielectrics*, 51(10):2045–2050, 2009. 72, 73, 75, 109, 112, 119

[110] M. van Exter, Ch. Fattinger, and D. Grischkowsky. Terahertz time-domain spectroscopy of water vapor. *Optics Letters*, 14(20):1128–1130, 1989. 77, 78

[111] R. L. Pickett, H. M. Poynter, E. A. Cohen, M. L. Delitsky, J. C. Pearson, and H. S. P. Müller. Submillimeter, millimeter, and microwave spectral line catalog. *Journal of Quantitative Spectroscopy and Radiative Transfer*, 60:883–890, 1998. 77, 78

[112] A. Roggenbuck, H. Schmitz, A. Deninger, I. Cámara Mayorga, J. Hemberger, R. Güsten, and M. Grüninger. Coherent broadband continuous-wave terahertz spectroscopy on solid-state samples. *New Journal of Physics*, 12:043017, 2010. 78

[113] C. Z. Tan and J. Arndt. Temperature dependence of refractive index of glassy SiO_2 in the infrared wavelength range. *Journal of Physics and Chemistry of Solids*, 61:1315–1320, 2000. 85

[114] R. B. Sosman. *The Properties of Silica*. Chemical Catalog Company, 1927. 85

[115] Y.-S. Jin, G.-J. Kim, and S.-G. Jeon. Terahertz dielectric properties of polymers. *Journal of the Korean Physical Society*, 49(2):513–517, 2006. 95

[116] M. Naftaly and R. E. Miles. Terahertz time-domain spectroscopy for material characterization. *Proceedings of the IEEE*, 95(8):1658–1665, 2007.

[117] A. Podzorov and G. Gallot. Low-loss polymers for terahertz applications. *Applied Optics*, 47(18):3254–3257, 2008.

[118] M. Naftaly and R. E. Miles. Terahertz time-domain spectroscopy of silicate glasses and the relationship to material properties. *Journal of Applied Physics*, 102:043517, 2007. 95

[119] Paul F. Goldsmith. *Quasioptical Systems: Gaussian beam quasioptical propagation and applications*. IEEE Press, 1997. 95

[120] N. Nagai and R. Fukasawa. Abnormal dispersion of polymer films in the THz frequency region. *Chemical Physics Letters*, 388:479–482, 2004. 96

[121] R. Piesiewicz, C. Jansen, S. Wietzke, D. Mittleman, M. Koch, and T. Kürner. Properties of building and plastic materials in the THz range. *International Journal of Infrared and Millimeter Waves*, 28:363–371, 2007. 96

[122] Y.-S. Jin, D. M. Kim, S.-G. Jeon, C.-H. Shon, and Jung. S.-S. Experimental measurement of the 3d spatio-temporal profile of a pulsed terahertz wave. *Journal of the Korean Physical Society*, 48(4):603–606, 2006. 97

[123] Y. Kitoh, M. Yamashita, N. Nagashima, and M. Hangyo. Terahertz beam profiler using optical transmission modulation in silicon. *Japanese Journal of Applied Physics*, 40:L1113–L1115, 2001. 97

[124] W. Plass, R. Maestle, K. Wittig, A. Voss, and A. Giesen. High-resolution knife-edge laser beam profiling. *Optics Communications*, 134:21–24, 1997. 97

[125] Jennifer Marx. Design and implementation of a liquid helium cryostat for continuous-wave THz spectroscopy. Master's thesis, Universität zu Köln, 2011. 97, 128, 130, 131, 134

[126] Eugene Hecht. *Optics*. Addison Wesley, 4 edition, 2002. 101

[127] C.-W. Chen, T.-T. Tang, S.-H. Lin, J. Y. Huang, C.-S. Chang, P.-K. Chung, S.-T. Yen, and C.-L. Pan. Optical properties and potential applications of ε-GaSe at terahertz frequencies. *Journal of the Optical Society of America B*, 26(9):A58–A65, 2009. 101

[128] M. Scheffler, J. P. Ostertag, and M. Dressel. FabryŰperot resonances in birefringent $yalo_3$ analyzed at terahertz frequencies. *Optics Letters*, 34(22):3520–3522, 2009.

[129] L. Zhang, H. Zhong, C. Deng, C. Zhang, and Y. Zhao. Polarization sensitive terahertz time-domain spectroscopy for birefringent materials. *Applied Physics Letters*, 94:211106, 2009. 101

[130] Iván Cámara Mayorga. privat communication, 2012. 105

[131] D. Grischkowsky and S. Keiding. THz time-domain spectroscopy of high T_C substrates. *Applied Physics Letters*, 57(10):1055–1057, 1990. 109

[132] T. Kiwa and M. Tonouchi. Time-domain terahertz spectroscopy of (100) $(LaAlO_3)_{0.3}$-$(Sr_2AlTaO_6)_{0.7}$ substrate. *Japanese Journal of Applied Physics*, 40:L38–L40, 2001. 109

[133] A. Pimenov, T. Rudolf, F. Mayr, A. Loidl, A. A. Mukhin, and A. M. Balbashov. Coupling of phonons and electromagnons in $GdMnO_3$. *Physical Review B*, 74:100403(R), 2006. 113, 119

[134] M. van Exter and D. Grischkowsky. Optical and electronic properties of doped silicon from 0.1 to 2 THz. *Applied Physics Letters*, 56:1694–1696, 1990. 123

[135] N. Katzenellenbogen and D. Grischkowsky. Electrical characterization to 4 THz of N- and P-type GaAs using THz time-domain spectroscopy. *Applied Physics Letters*, 61:840–842, 1992.

[136] T.-I. Jeon and D. Grischkowsky. Nature of conduction in doped silicon. *Physical Review Letters*, 78(6):1106–1109, 1997. 126

[137] T. Jeon and D. Grischkowsky. Characterization of optically dense, doped semiconductors by reflection THz time domain spectroscopy. *Applied Physics Letters*, 72(23):3032–3034, 1998. 123

[138] O. Morikawa, M. Tonouchi, and M. Hangyo. Sub-THz spectroscopic system using a multimode laser diode and photoconductive antenna. *Applied Physics Letters*, 75(24):3772–3774, 1999. 123

[139] S. Nashima, O. Morikawa, K. Takata, and M. Hangyo. Temperature dependence of optical and electronic properties of moderately doped silicon at terahertz frequencies. *Journal of Applied Physics*, 90(2):837–842, 2001.

[140] T. Nagashima and M. Hangyo. Measurement of complex optical constants of a highly doped Si wafer using terahertz ellipsometry. *Applied Physics Letters*, 79(24):3917–3919, 2001.

[141] S. Nashima, O. Morikawa, K. Takata, and M. Hangyo. Measurement of optical properties of highly doped silicon by terahertz time domain reflection spectroscopy. *Applied Physics Letters*, 79(24):3923–3925, 2001.

[142] M. Hangyo, T. Nagashima, and S. Nashima. Spectroscopy by pulsed terahertz radiation. *Measurement Science and Technology*, 13:1727–1738, 2002. 123

[143] M. Herrmann, M. Tani, K. Sakai, and R. Fukasawa. Terahertz imaging of silicon wafers. *Journal of Applied Physics*, 91(3):1247–1250, 2002. 123

[144] CryoVac. *Bedienungsanleitung He-Konti IT Kryostat Typ Spektro 3*, 2011. 129, 130

[145] K. G. Lyon, G. L. Salinger, C. A. Swenson, and G. K. White. Linear thermal expansion measurements on silicon from 6 to 340 K. *Journal of Applied Physics*, 48:865–868, 1977. 137

[146] F. J. Morin and P. J. Maita. Electrical properties of silicon containing arsenic and boron. *Physical Review*, 96:28, 1954. 141

[147] R. A. Logan and A. J. Peters. Impurity effects upon mobility in silicon. *Journal of Applied Physics*, 31(1):122–124, 1960.

[148] L. Elstner. Die Temperaturabhängigkeit der Defektelektronenbeweglichkeit in Siliziumkristallen. *Physica Status Solidi*, 17:139–150, 1966. 141

[149] M. Asche and J. von Borzeszkowski. On the temperature dependence of hole mobility in silicon. *Physica Status Solidi*, 37:433–438, 1970. 141

[150] K. Takeda, K. Sakui, and M. Sakata. Temperature dependence of mobility and hall coefficient factor for holes of highly pure silicon. *Journal of Physics C: Solid State Physics*, 15:767–776, 1982. 141

[151] Ph. F. Taday. Applications of terahertz spectroscopy to pharmaceutical sciences. *Philosophical Transactions of the Royal Society*, 362:351–364, 2004. 149

[152] M. Walther, M. R. Freeman, and F. A. Hegmann. Metal-wire terahertz time-domain spectroscopy. *Applied Physics Letters*, 87:261107, 2005. 151, 153

[153] E. Jung, J. Kim, Y. Han, K. Moon, M. Lim, and H. Han. Terahertz time domain spectroscopy of crystalline α-lactose monohydrate. *Biochip Journal*, 2(4):296–299, 2008.

[154] M. B. Byrne, J. Cunningham, K. Tych, A.D. Burnett, M. R. Stringer, C. D. Wood, L. Dazhang, M. Lachab, E. H. Linfield, and A. G. Davies. Terahertz vibrational absorption spectroscopy using microstrip-line waveguides. *Applied Physics Letters*, 93:182904, 2008.

[155] W. Withayachumnankul, B. M. Fischer, and D. Abbott. Material thickness optimization for transmission-mode terahertz time-domain spectroscopy. *Optics Express*, 16(10):7382–7396, 2008. 149, 151, 153, 154

[156] S. Saito, T. M. Inerbaev, H. Mizuseki, N. Igarashi, R. Note, and Y. Kawazoe. First principles calculation of terahertz vibrational modes of a disaccharide monohydrate crystal of lactose. *Japanese Journal of Applied Physics*, 45(43):L1156–L1158, 2006. 149

[157] D. G. Allis, A. M. Fedor, T. M. Korter, J. E. Bjarnason, and E. R. Brown. Assignment of the lowest-lying THz absorption signatures in biotin and lactose monohydrate by solid-state density functional theory. *Chemical Physics Letters*, 440:203–209, 2007. 149

[158] John W. Eaton. *GNU Octave Manual*. Network Theory Limited, 2002. 161, 175

List of Publications

1. **Coherent broadband continuous-wave terahertz spectroscopy on solid-state samples**

   A. Roggenbuck, H. Schmitz, A. Deninger, I. Cámara Mayorga, J. Hemberger, R. Güsten, and M. Grüninger
   New Journal of Physics **12**, 043017 (2010)

2. **Using a fiber stretcher as a fast phase modulator in a continuous-wave terahertz spectrometer**

   A. Roggenbuck, K. Thirunavukkuarasu, H. Schmitz, J. Marx, A. Deninger, I. Cámara Mayorga, R. Güsten, J. Hemberger, and M. Grüninger
   Journal of the Optical Society of America B **29**, 614 (2012)

3. **Conference contributions**

   - *Spring meeting of the German Physical Society (DPG)*, division condensed matter, Dresden, 2009, Regensburg, 2010, Dresden, 2011
   - *International workshop on Strongly Correlated Transition Metal Compounds of SFB 608*, Kerkrade, 2009, Cologne, 2010, Cologne, 2011
   - *429. WE-Heraeus Seminar on Microwaves for Condensed Matter Physics*, Bad Honnef, 2009
   - *International Workshop on Terahertz spectroscopy and its high-field applications* of Forschungszentrum Dresden-Rossendorf, 2010

Acknowledgements

An diesem Punkt möchte ich mich bei allen bedanken, die zum Entstehen dieser Arbeit beigetragen haben.

Prof. Grüninger danke ich für die Betreuung dieser Arbeit, für die vielen Ideen und Hilfestellungen. Danke auch für die Geduld gerade während der Korrektur dieser Arbeit.

Dr. Komalavalli Thirunavukkuarasu danke ich für die vielen Diskussionen und nützlichen Tipps. Ich werde die netten Abende mit der Arbeitsguppe und das hervorragende Essen in guter Erinnerung behalten.

Ich danke den Optikern, die da wären: Lius Mäder (jetzt Fels), Julia Küppersbusch (jetzt Reul), Malte Langenbach, Andreas Janssen, Jennifer Marx, Ernesto Vidal, Michael Voigt und Ignacio Vergara für die gute Zusammenarbeit, das lockere Arbeitsklima und Hilfe mit Rat und Tat.

Dr. Anselm Deninger und besonders Axel Roggenbuck von Toptica Photonics danke ich für die Einweisung in das THz Spektrometer und die ausführlichen Diskussionen zur Technik.

Dr. Ivan Cámara Mayorga und Andreas Schmitz für die stete Versorgung mit neuen Photomischern und deren ständige Weiterentwicklung.

Dem Team der Werkstatt der Anorganischen Chemie danke ich für die Fertigung der HDPE Linsen.

Christoph July und Andreas Steffen danke ich für das Korrekturlesen der vorliegenden Arbeit.

Abstract

Within the scope of this thesis a novel continuous-wave terahertz spectrometer was set up and extended to fit the needs of solid-state spectroscopy. The system is based on mixing two near-infrared distributed feedback diode lasers, of which the beat signal can be tuned continuously from 0 to 1.8 THz. The laser beat is converted into THz radiation by a so-called photomixer, which efficiently generates THz radiation from 60 GHz to 1.8 THz. A second photomixer is used for the coherent detection of cw THz radiation. Due to the coherent detection, the phase information is preserved and the measured photocurrent is a product of the THz amplitude and phase. This allows for the determination of both, real and imaginary part of the complex optical functions without the need of Kramers-Kronig transformation.

To separate the amplitude and phase information of the photocurrent an additional phase modulation has to be applied. This can be achieved by modulating the path-length difference at the receiver via a fiber stretcher for a fixed frequency. Conversely the frequency can be varied for a fixed path-length difference. For both techniques suitable methods to precisely extract amplitude and phase from the photocurrent are developed. Different possibilities to determine the complex optical functions from the measured transmittance and phase are presented. To improve the precision of the spectrometer, the stability and reliability of the critical values such as amplitude, phase, and frequency are investigated. As a part of the improvement of the phase stability, a whole new approach to correct for phase fluctuations is presented. For this purpose a third laser is implemented into the setup. Keeping two of the lasers at constant frequency and tuning the third one results in one stable and two tunable beat frequencies. The phase of the fixed frequency is recorded and used to correct phase fluctuations of the tunable beat frequencies. For measurements at low temperatures a cryostat is implemented into the setup. The beam profile and the polarization dependence of the emitter and receiver, respectively, are investigated and optical elements to generate a focused beam are designed and employed.

To test the performance of the setup different solid-state samples are measured. Magnesium oxide is investigated using all different measurement modes. Their performance is discussed based on the results. The temperature dependence of the optical properties of Si are investigated, showing that very good results can be obtained down to lowest temperatures and frequencies while using a cryostat. As third sample α-lactose monohydrate is investigated which has the narrowest absorption line known for solid-state samples. Both resonance frequency and linewidth are determined very accurately removing doubts of previous measurements [43].

Kurzzusammenfassung

Im Rahmen der vorliegenden Doktorarbeit wurde ein neuartiges CW THz Spektrometer aufgebaut und hinsichtlich der Ansprüche der Festkörperspektroskopie erweitert. Das System basiert auf der Überlagerung zweier nahinfraroter Distributed Feedback Laser, deren Schwebungsfrequenz kontinuierlich von 0 bis 1.8 THz variiert werden kann. Die Umwandlung der Schwebung in ein THz Signal geschieht mittels so genannter Photomischer, die effektiv THz Frequenzen zwischen 60 GHz und 1.8 THz generieren können. Ein zweiter Photomischer wird genutzt, um die THz Strahlung zu detektieren. Durch die kohärente Detektion bleibt die Phaseninformation erhalten und der gemessene Photostrom ist ein Produkt aus THz Amplitude und Phase. Dies ermöglicht es, den Real- und Imaginärteil der komplexen optischen Funktionen zu bestimmen ohne auf Kramers-Kronig Transformationen zurückgreifen zu müssen.

Um die Amplituden- und Phaseninformation des Photostroms zu trennen, muss eine zusätzliche Phasenmodulation eingesetzt werden. Dies kann zum einen dadurch erreicht werden, dass der Weglängenunterschied am Detektor bei fester Frequenz mittels eines Faserstretchers variiert wird. Im Gegensatz dazu kann die Frequenz bei festem Weglängenunterschied variiert werden. Für beide Verfahren werden geeignete Methoden entwickelt, Amplituden- und Phaseninformation präzise aus dem Photostrom zu entnehmen. Verschiedene Möglichkeiten die komplexen optischen Funktionen aus der gemessenen Transmission und Phase zu bestimmen werden präsentiert. Um die Präzision des Spektrometers weiter zu verbessern wird die Stabilität kritischer Größen wie beispielsweise Amplitude, Phase und Frequenz untersucht. Im Zuge der Verbesserung der Phasenstabilität wird eine neuartiger Ansatz zur Korrektur von Phasenfluktuationen vorgestellt. Zu diesem Zweck wird ein dritter Laser in den Aufbau integriert. Werden zwei Laser bei konstanter Frequenz gehalten und nur die Frequenz des Dritten variiert, ergeben sich eine konstante und zwei variable Schwebungsfrequenzen. Die Phase der konstanten Schwebung wird aufgezeichnet und zur Korrektur von Phasenfluktuationen der anderen Schwebungsfrequenzen genutzt. Für Messungen bei tiefen Temperaturen wird ein Kryostat in den Aufbau integriert. Das Strahlprofil und die Polarisationsabhängigkeit von Sender bzw. Detektor werden untersucht und optische Elemente zur Fokussierung des Strahls werden entwickelt und eingesetzt.

Zum Test der Leistungsfähigkeit des Spektrometers werden verschiedene Festkörper untersucht. Magnesiumoxid wird unter Verwendung aller Messmethoden untersucht und deren Leistungsfähigkeit anhand der Ergebnisse verglichen. Die Temperaturabhängigkeit der optischen Eigenschaften von Si wird untersucht und gezeigt,

dass mit dem Kryostaten gute Ergebnisse bis hinunter zu tiefen Temperaturen und Frequenzen erzielt werden können. Als dritte Probe wird α-Lactose Monohydrat untersucht, welches die schmalste bekannte Absorptionslinie für Festkörper besitzt. Sowohl die Resonanzfrequenz als auch die Liniebreite werden sehr genau bestimmt und Unsicherheiten früherer Messungen ausgeräumt [43].

Offizielle Erklärung

Ich versichere, dass ich die von mir vorgelegte Dissertation selbstständig angefertigt, die benutzten Quellen und Hilfsmittel vollständig angegeben und die Stellen der Arbeit - einschließlich Tabellen, Karten und Abbildungen -, die anderen Werken im Wortlaut oder dem Sinn nach entnommen sind, in jedem Einzelfall als Entlehnung kenntlich gemacht habe, dass diese Dissertation noch in keiner anderen Fakultät oder Universität zur Prüfung vorgelegen hat, dass sie - abgesehen von den in der Publikationsliste angegebenen Teilpublikationen - noch nicht veröffentlicht worden ist sowie, dass ich eine solche Veröffentlichung vor Abschluss des Promotionsverfahrens nicht vornehmen werde. Die Bestimmungen dieser Promotionsordnung sind mir bekannt. Die von mir vorgelegte Dissertation ist von Prof. Dr. M. Grüninger betreut worden.

Köln, den 13. Februar 2012

Holger Schmitz